New energetic materials based on nanoporous carbon filled with an oxidizing agent

Romuald van Riet

ÉCOLE DOCTORALE *Énergie-Matériaux-Sciences de la Terre et de l'Univers (EMSTU)*

CONDITIONS EXTRÊMES ET MATÉRIAUX : HAUTE TEMPÉRATURE ET IRRADIATION

FACULTÉ *Polytechnique*

DÉPARTEMENT DE CHIMIE

THÈSE EN COTUTELLE INTERNATIONALE présentée par :

Romuald VAN RIET

soutenue : 9 décembre 2021

pour obtenir les grades de :

Docteur de l'Université d'Orléans

Discipline/ Spécialité : Chimie des matériaux

et de Docteur de l'École Royale Militaire

Discipline/ Spécialité : Sciences de l'ingénieur

NEW ENERGETIC MATERIALS BASED ON NANOPOROUS CARBON FILLED WITH AN OXIDIZING AGENT

THÈSE dirigée par :

Mme OVÍN ANIA M. Concepción	Directrice de recherche, CNRS, CEMHTI, France
M. LODEWYCKX Peter	Professeur militaire, École Royale Militaire, Belgique

RAPPORTEURS :

Mme JOB Nathalie	Professeur ordinaire, Université de Liège, Belgique
M. MATYÁŠ Robert	*Associate professor*, *University of Pardubice, Czech Republic*

JURY :

Mme BONNAMY Sylvie	Directrice de recherche, CNRS, ICMN, France Présidente du jury
M. LEFEBVRE Michel	Professeur ordinaire, École Royale Militaire, Belgique
Mme JOB Nathalie	Professeur ordinaire, Université de Liège, Belgique
M. MATYÁŠ Robert	*Associate professor*, *University of Pardubice, Czech Republic*
Mme OVÍN ANIA M. Concepción	Directrice de recherche, CNRS, CEMHTI, France
M. LODEWYCKX Peter	Professeur militaire, École Royale Militaire, Belgique

Remerciements

Je tiens tout d'abord à remercier Madame Conchi O. Ania, directrice de recherche au CEMHTI (CNRS Orléans), et le Colonel IMM Peter Lodewyckx, professeur militaire à l'Ecole Royale Militaire, qui m'ont encadré et guidé tout au long de ma thèse, pour leur disponibilité permanente, la confiance qu'ils m'ont témoignée et les encouragements qu'ils m'ont prodigués.

Je remercie également Madame Catherine Bessada, directrice de recherche et directrice du CEMHTI et Monsieur Michel Lefebvre, professeur ordinaire et chef du département de Chimie de l'Ecole Royale Militaire, pour m'avoir accueilli au sein de leur laboratoire dans le cadre de ma thèse et avoir permis sa réalisation.

J'adresse tous mes remerciements à Madame Nathalie Job, professeur ordinaire à l'Université de Liège, et à Monsieur Robert Matyáš, professeur à l'Université de Pardubice, pour avoir accepter d'être rapporteur de cette thèse.

J'exprime également ma gratitude à Madame Sylvie Bonnamy, directrice de recherche à l'ICMN (CNRS Orléans) et à Monsieur Michel Lefebvre, professeur ordinaire à l'Ecole Royale Miltaire, qui ont accepté d'être examinateurs.

Je tiens à remercier le personnel du Département de Chimie de l'Ecole Royale Militaire pour leur soutien et leur assistance dans le cadre des expériences menées au cours de cette thèse, et en particulier Madame Jessica Laffut, Messieurs Lindsey Couvreur, Joris Flebus, Jacques Lataer et Edouard Nadin, le Major Christophe Van de Velde et l'Adjudant Fabrice Tonnoir. De même, je tiens à remercier le personnel du CEMHTI, et en particulier Madame Rachelle Omnée. J'exprime également ma reconnaissance au Sous-Lieutenant Brian Noiret pour sa contribution au volet expérimental de cette thèse dans le cadre de son mémoire de fin d'étude à l'Ecole Royale Militaire.

Je remercie le laboratoire ICMN, pour avoir effectué les mesures d'analyse élémentaire, et le Département de Mécanique de l'Ecole Royale Militaire, pour avoir fourni les images de microscopie optique.

Finalement, mes remerciements vont à ma famille qui m'a soutenu tout au long de cette thèse.

Acknowledgements

The financial support of the European Research Council (ERC-CoG grant 684181) and of the Belgian Defence is acknowledged.

Contents

Extended summary

Energetic materials are those capable of rapidly releasing energy through a chemical reaction. They have numerous military and civilian applications, as high explosives, propellants or in pyrotechnic compositions. Although plenty of materials show such ability to release energy, only a few combine it with the adequate physicochemical, thermal and mechanical properties that make them safe for storage and use, stable over time and performant. Many of the energetic materials that are in service or are currently produced suffer from serious drawbacks such as hazardous aging, ecotoxicity, poor thermal stability, etc. It is well known that finding a compromise between safety, performance and environmental considerations is complicated and requires trade-offs. Extensive research is therefore performed to develop new energetic materials with enhanced properties. Most efforts are directed towards advanced synthesis of complex organic energetic molecules and energetic nanomaterials. The latter mainly consist of energetic formulations containing nanoparticles. However, both approaches face significant challenges, notably in terms of production cost, safe manufacturing, material homogeneity, toxicity or chemical compatibility.

Within this scope, this work aims at exploring a new family of energetic materials produced by filling the porosity of a nanoporous carbon, acting as a reducing agent (fuel), with a solid oxidizing agent in order to obtain an energetic material which is able to detonate. The filling of a reducing nanoporous matrix with an oxidizing agent allows to retain the potential advantages of a nanoscale mixture in terms of fast decomposition kinetics without having to suffer from the disadvantages of nanoparticles in terms of homogeneity, hazardous handling and potential toxicity. The use of nanoporous carbon as reducing matrix has moreover a lot of advantages with respect to other reducing agents, because its decomposition products are mostly gaseous, it is a robust three-dimensional material, and it is likely to have a desensitization effect on the formulations. This concept is novel and could potentially lead to a new family of energetic materials with promising properties and applications as pyrotechnic composition, propellant or high explosive.

In a preliminary feasibility study, it was determined that a pore volume of 1 cm^3/g is the minimum value from which the concept is theoretically possible, and that higher pore volumes are preferred. This is perfectly in line with the physicochemical properties of widely used and commercially available nanoporous carbons that can have pore volumes as high as 2.5 cm^3/g. The analysis also showed that relatively high degrees of pore filling must be achieved, with a minimal objective of about 60-80 % in function of the porosity. Finally, it was shown that alkali perchlorate salts lead to the best theoretical properties and are therefore the most suitable candidates to investigate the concept.

This work is divided in two main parts. The first part consists of developing a synthesis process in order to efficiently fill the porosity of nanoporous carbons with solid oxidizing agents. The second part then consists of experimentally proving the concept by demonstrating the ability of nanoporous carbons filled with an oxidizing agent to detonate and by assessing their basic properties as energetic materials.

The objectives of the pore filling process consist of achieving a high degree of pore filling of about 60-80 % on the one hand, and of selectively filling the nanopores on the other hand. The latter constraint arises from the fact that the decomposition of oxidizer particles crystallized in wider pores or on the surface of the carbon particles is expected to not be fast enough to efficiently contribute to the detonation process. At the time scale of the detonation wave, this could result in an energy loss and prevent a sustained detonation of the material. In this work, a new process of pore filling by crystallization after solution contraction upon drying is proposed to achieve these objectives. It consists of three subsequent steps. During the infiltration step, a concentrated aqueous solution of oxidizing agent is infiltrated in the porosity of a nanoporous carbon. Most of the interstitial solution is then removed during the filtration step. The purpose of this step consists of keeping the pores filled and forming a surface film with controlled thickness on the carbon particles. During the last step, the solvent is progressively evaporated by heating the mixture on a controlled manner. The solution continuously contracts upon evaporation of the solvent, but does not become immediately supersaturated as the solubility increases with temperature.

It is assumed that the solution preferentially fills the nanopores upon contraction because of capillary effects. Finally, further solvent evaporation leads to the crystallization of the oxidizing agent in the nanopores. This approach should allow a high degree of pore filling to be achieved while preventing homogeneous and heterogeneous nucleation outside of the nanopores. To investigate the efficiency of this pore filling process and to characterize the physicochemical properties of the pristine carbons, different experimental techniques are used including gas adsorption and mercury intrusion porosimetry. The efficiency of the pore filling process was first evaluated for different carbons filled with sodium perchlorate, potassium nitrate and ammonium perchlorate to study the influence of the oxidizing agent. Significant differences in terms of degree and uniformity of pore filling were observed between the different salts. Whereas the results strongly suggest that sodium perchlorate is crystallized in the nanopores at a density close to its theoretical maximal density, significant pore blocking occurred with potassium nitrate and ammonium nitrate. The ability of sodium perchlorate to selectively crystallize in the nanopores of the carbons is a confirmation that the aqueous solution preferentially fills the smallest pores upon solvent evaporation because of capillarity. As only pore filling with sodium perchlorate met the criteria defined in the feasibility study with a pore filling yield exceeding 60 %, this salt was used as oxidizing agent for pursuing the objective of the PhD thesis. In order to investigate the influence of the physicochemical properties of nanoporous carbon on the pore filling process, twelve nanoporous carbons prepared from different precursors and showing varied textural properties and surface chemistries were used. Four of them are commercial activated carbons, and the others are materials obtained upon thermochemical modifications of the former (thermal reduction, chemical oxidation and overactivation). The porosity of the carbons is infiltrated with aqueous solution of sodium perchlorate at four different concentrations ranging from 40 to 60 wt%. The interpretation of the results is quite difficult, as the respective potential contributions of variable density and pore blocking to the pore filling characterization are interdependent and cannot be separately quantified. Whereas higher salt concentrations lead to higher yields, it has no significant impact on the observed extent of nanopore filling. A detailed analysis showed that this results from a combination of pore blocking and larger pore filling. Regarding the influence of the physicochemical properties of the carbons, the yield of the pore filling process is very well correlated with the nanopore volume of the pristine carbons, but both textural properties and surface chemistry appear to have a significant influence on the degree of pore filling. The results suggest that the crystallization of the oxidizing salt occurs selectively in pores of width smaller than 3-4 nm, but the capillary driving force appears to become too weak in larger pores to effectively lead to the preferential filling of these pores when the solvent is progressively evaporated. This is presumably related to the stronger dispersive intermolecular forces in the micropores and the smallest mesopores where the force fields of the opposite walls can superpose to some extent. Finally, the results show that the degree of pore filling is significantly dependent on the nature and the extent of the surface chemistry, as a relatively large amount of polar functional groups appears to be needed to achieve a high degree of pore filling. This is presumably related to an overall lower interfacial free energy between the concentrated salt solution and the pore walls in the presence of polar surface groups which promotes the preferential filling of the nanopores during the drying step. Even if the efficiency of the pore filling process strongly depends on the nature of both the oxidizing salt and the carbon, the criteria fixed in the preliminary feasibility study are met, as this process enables to successfully achieve a high extent of pore filling with a selective filling of the nanopores. Most of the salt crystallized moreover in pores of width smaller than 4 nm, which corresponds to the criteria fixed in this work for ensuring a homogeneous mixture of the oxidizing and the reducing agent at the nanometer scale.

In order to study the energetic properties of the carbons filled with oxidizing agents produced by the previously developed pore filling process, a static thermal characterization is first performed by differential scanning calorimetry and thermogravimetric analysis. The thermogravimetric analysis is performed at different heating rates to allow the kinetics of the decomposition reaction of the filled carbons to be modelled. This characterization is considered as static in contrast to the dynamic detonation process. It was first observed that the onset of the decomposition of carbons filled with sodium perchlorate occurs at temperatures ranging from 250 to 320 °C, where the decomposition of the bare oxidizer starts at 470 °C. Comparable results were obtained with potassium nitrate and ammonium perchlorate as oxidizing agent, with the onset of decomposition of the filled carbons occurring at temperatures about 100 °C lower than the decomposition temperature of the oxidizing agent itself. This suggests that the nature of the oxidizing agent plays a significant role in the decomposition mechanism. The results also show that, although for the same carbon the pore filling yield has no significant influence on the onset of the decomposition and on the decomposition kinetics, these properties strongly depend on the physicochemical properties of the carbon and on the nature of the oxidizing agent. It was observed that

the onset of the decomposition occurs at lower temperatures if the surface of the carbons presents a large amount of oxygen-containing functional groups. This indicated that not only the nature of the oxidizing agent, but also the nature and the thermal stability of the reducing agent play a significant role in the decomposition mechanism. The decomposition kinetics of the carbons filled with sodium perchlorate at the nanometer scale were then compared to that of the corresponding physical mixtures at the micrometer scale. No significant differences were surprisingly observed, suggesting that the decomposition kinetics of the carbon-oxidizing agent mixture is not significantly faster because of the confinement in nanopores with respect to a physical mixture. Qualitatively, it was however observed that the reaction of the filled carbon upon ignition was significantly more violent than that of the physical mixture. To assess their safety features, the sensitivities of different carbons filled with sodium perchlorate to impact and friction and their temperature of ignition were measured. They are all in line with potential applications, with low impact sensitivities ranging from 5 to 20 J and moderate friction sensitivities ranging from 48 to 160 N. The temperatures of ignition are in very good agreement with the onset temperatures measured by differential scanning calorimetry. One carbon filled with sodium perchlorate at a high degree of pore filling was finally chosen to perform a detailed study of its detonability and detonation properties. For this, over 500 g of this energetic material were produced at the laboratory scale. After a preliminary study of detonability, three different densities ranging from 0.85 to 1.40 g/cm^3 were investigated. The results show that, when in a heavy steel confinement, the material is able to detonate for all the densities when initiated by a common detonator. Detonation velocities ranging from 3000 to 4200 m/s were measured. The effect of the charge diameter was investigated, and the results show that in these circumstances the critical diameters are about 6-8 mm and the ideal diameters about 8-10 mm. The overall performances correspond to that of explosives for blasting applications and to about 30-60 % of that of a high explosive for military application such as trinitrotoluene. These properties are very impressive for a composite energetic material with a very significant fraction of solid decomposition products, which denotes very fast dynamic decomposition kinetics promoted by the nanometer scale of the mixture. With respect to the study of the static decomposition kinetics, these detonation properties are presumably strongly related to the fact that the mixture of oxidizing and reducing agents in the nanopores is in the immediate vicinity of the hot spots generated in the material by shock compression, and to the higher density achieved when the carbon particles are filled with the oxidizing agent than for the corresponding physical mixture. These results are an experimental proof of the concept of this work.

In conclusion, the concept of a new family of energetic materials based on nanoporous carbons filled with oxidizers was demonstrated in this work, opening up new horizons in the path towards performant, safe and non-toxic energetic nanomaterials with a broad spectrum of applications. A new efficient pore filling process was first developed and the related influence of the nature of the oxidizing agent and of the physicochemical properties of the nanoporous carbons was deeply investigated. The energetic properties of these new composite materials were then studied and it was notably shown that they can be easily detonated and that they have sensitivities in line with potential applications. Moreover, the unique properties and versatility of nanoporous carbons combined with the large number of degrees of freedom of the pore filling process developed in this work offer promising perspectives in this field.

Résumé étendu

Les matériaux énergétiques sont ceux capables de libérer rapidement de l'énergie par réaction chimique. Ils ont de nombreuses applications militaires et civiles comme explosifs brisants, poudres, propergols ou dans des compositions pyrotechniques. Bien que de nombreux matériaux présentent cette capacité à dégager de l'énergie, seuls quelques-uns la combinent avec les propriétés physico-chimiques, thermiques et mécaniques adéquates qui les rendent sûrs pour le stockage et l'utilisation, stables dans le temps et performants. Beaucoup des matériaux énergétiques en service ou produits actuellement présentent de graves inconvénients tels qu'un vieillissement dangereux, une écotoxicité, une mauvaise stabilité thermique, etc. Il est bien connu que la recherche d'un compromis entre la sécurité, les performances et les considérations environnementales est compliquée et nécessite des compromis. C'est pourquoi des recherches approfondies sont menées afin de développer de nouveaux matériaux énergétiques aux propriétés améliorées. La plupart des efforts sont dirigés vers la synthèse avancée de molécules énergétiques organiques complexes ou vers des nanomatériaux énergétiques. Ces derniers consistent principalement en des formulations énergétiques contenant des nanoparticules. Cependant, ces deux approches sont confrontées à des défis importants, notamment en termes de coût de production, de sécurité de fabrication, d'homogénéité des matériaux, de toxicité ou de compatibilité chimique.

Ce travail vise dans ce cadre à explorer une nouvelle famille de matériaux énergétiques produits en remplissant la porosité d'un carbone nanoporeux, agissant comme agent réducteur (carburant), avec un agent oxydant solide afin d'obtenir un matériau énergétique capable de détoner. Le remplissage d'une matrice nanoporeuse réductrice par un agent oxydant permet de conserver les avantages potentiels d'un mélange nanométrique en matière de cinétique de décomposition rapide sans avoir à subir les inconvénients des nanoparticules en matière d'homogénéité, de manipulation dangereuse et de toxicité potentielle. L'utilisation du carbone nanoporeux comme matrice réductrice présente en outre de nombreux avantages par rapport à d'autres agents réducteurs. En effet, ses produits de décomposition sont essentiellement gazeux, c'est un matériau tridimensionnel robuste et il est susceptible d'avoir un effet de désensibilisation sur les formulations. Ce concept est novateur et pourrait potentiellement conduire à une nouvelle famille de matériaux énergétiques avec des propriétés prometteuses et des applications comme composition pyrotechnique, propergol ou explosif brisant.

Lors d'une étude de faisabilité préliminaire, il a été déterminé qu'un volume poreux de 1 cm^3/g est la valeur minimale à partir de laquelle le concept est théoriquement possible et que des volumes poreux plus élevés sont préférables. Cela correspond parfaitement aux propriétés physico-chimiques des carbones nanoporeux largement utilisés et disponibles dans le commerce, qui peuvent avoir des volumes de pores allant jusqu'à 2,5 cm^3/g. L'analyse a également montré que des taux relativement élevés de remplissage des pores doivent être atteints, avec un objectif minimal d'environ 60-80 % en fonction de la porosité. Enfin, il a été déterminé que les sels de perchlorate de métaux alcalins permettent d'atteindre les meilleures propriétés théoriques et sont donc les candidats les plus appropriés pour étudier le concept.

Ce travail est divisé en deux parties principales. La première partie consiste à développer un procédé de synthèse afin de remplir efficacement la porosité des carbones nanoporeux avec des agents oxydants solides. La deuxième partie consiste ensuite à prouver expérimentalement le concept en démontrant la capacité des carbones nanoporeux remplis d'un agent oxydant à détoner et en étudiant leurs propriétés de base en tant que matériaux énergétiques.

Les objectifs du procédé de remplissage des pores consistent à atteindre un taux élevé de remplissage des pores d'environ 60 à 80 % d'une part, et à remplir sélectivement les nanopores d'autre part. Cette dernière contrainte découle du fait que la décomposition des particules d'oxydant cristallisées dans les pores plus larges ou à la surface des particules de carbone pourrait ne pas être assez rapide pour contribuer efficacement au processus de détonation. À l'échelle de temps de l'onde de détonation, cela pourrait se traduire par une perte d'énergie et empêcher une détonation auto-entretenue du matériau. Dans ce travail, un nouveau procédé de remplissage des pores par cristallisation après contraction de la solution lors

du séchage est proposé afin d'atteindre ces objectifs. Il se compose de trois étapes successives. Au cours de l'étape d'infiltration, une solution aqueuse concentrée d'agent oxydant est infiltrée dans la porosité d'un carbone nanoporeux. La majeure partie de la solution interstitielle est ensuite retirée lors de l'étape de filtration. Le but de cette étape est de maintenir les pores remplis et de former un film surfacique d'épaisseur contrôlée sur les particules de carbone. Lors de la dernière étape, le solvant est progressivement évaporé en chauffant le mélange de manière contrôlée. La solution se contracte continuellement lors de l'évaporation du solvant, mais ne devient pas immédiatement sursaturée car la solubilité augmente avec la température. On fait l'hypothèse que la solution remplit préférentiellement les nanopores lors de la contraction par capillarité. L'évaporation continue du solvant finit par conduire à la cristallisation de l'agent oxydant dans les nanopores. Cette approche est supposée permettre d'atteindre un haut taux de remplissage des pores tout en empêchant la nucléation homogène et hétérogène en dehors des nanopores. Pour étudier l'efficacité de ce procédé de remplissage des pores et pour caractériser les propriétés physico-chimiques des carbones vierges, différentes techniques expérimentales sont utilisées, notamment l'adsorption de gaz et la porosimétrie par intrusion de mercure. L'efficacité du procédé de remplissage des pores a d'abord été évaluée pour différents carbones remplis de perchlorate de sodium, de nitrate de potassium et de perchlorate d'ammonium afin d'étudier l'influence de l'agent oxydant. Des différences significatives en matière de taux et d'uniformité de remplissage des pores ont été observées entre les différents sels. Alors que les résultats suggèrent fortement que le perchlorate de sodium est cristallisé dans les nanopores à une densité proche de sa densité maximale théorique, un blocage significatif des pores est observé avec le nitrate de potassium et le nitrate d'ammonium. La capacité du perchlorate de sodium à cristalliser sélectivement dans les nanopores des carbones confirme que la solution aqueuse remplit préférentiellement les plus petits pores lors de l'évaporation du solvant par capillarité. Puisqu'uniquement le remplissage des pores avec du perchlorate de sodium répondait aux critères définis dans l'étude de faisabilité, avec un taux de remplissage des pores supérieur à 60 %, ce sel a été utilisé comme agent oxydant pour poursuivre l'objectif de la thèse. Afin d'étudier l'influence des propriétés physico-chimiques du carbone nanoporeux sur le procédé de remplissage des pores, douze carbones nanoporeux préparés à partir de différents précurseurs et présentant des textures et des chimies de surface variées ont été utilisés. Quatre d'entre eux sont des charbons actifs commerciaux, et les autres sont des matériaux obtenus par des modifications thermochimiques de ceux-ci (par réduction thermique, oxydation chimique et suractivation). Les pores de ces carbones sont infiltrés avec une solution aqueuse de perchlorate de sodium à quatre concentrations différentes allant de 40 à 60 % massique. L'interprétation des résultats de la caractérisation du remplissage des pores est assez complexe, car les contributions potentielles de la densité variable et du blocage des pores sont interdépendantes et ne peuvent être quantifiées séparément. Alors que des concentrations de sel plus importantes mènent à des rendements plus élevés, elles n'ont pas d'impact significatif sur l'étendue du remplissage des nanopores observée. Une analyse détaillée a montré que cela résulte d'une combinaison du blocage des pores et du remplissage des plus grands pores. En ce qui concerne l'influence des propriétés physico-chimiques des carbones, le rendement du procédé de remplissage des pores est très bien corrélé avec le volume des nanopores des carbones vierges, mais les propriétés texturales et la chimie de surface semblent avoir une influence significative sur le taux de remplissage des pores. Les résultats suggèrent que la cristallisation du sel oxydant se produit sélectivement dans les pores de largeur inférieure à 3-4 nm, mais la force motrice capillaire semble devenir trop faible dans les pores plus grands pour entraîner le remplissage préférentiel de ces pores lorsque le solvant est progressivement évaporé. Ceci est vraisemblablement lié aux forces intermoléculaires dispersives plus fortes dans les micropores et les plus petits mésopores où les champs d'interaction des parois opposées peuvent se superposer dans une certaine mesure. Enfin, les résultats montrent que le taux de remplissage des pores dépend de manière significative de la nature et de l'étendue de la chimie de surface, car une quantité relativement importante de groupes fonctionnels polaires semble être nécessaire pour obtenir un taux élevé de remplissage des pores. Ceci est vraisemblablement lié à une énergie de surface globalement plus faible entre la solution saline concentrée et les parois des pores en présence de groupes de surface polaires, ce qui favorise le remplissage préférentiel des nanopores pendant l'étape de séchage. Même si l'efficacité du procédé de remplissage des pores dépend fortement de la nature du sel oxydant et du carbone, les critères fixés dans l'étude préliminaire de faisabilité sont remplis. Le procédé décrit permet en effet d'atteindre avec succès un haut taux de remplissage des pores avec un remplissage sélectif des nanopores. La majeure partie du sel cristallisé se trouve par ailleurs dans les pores de largeur inférieure à 4 nm, ce qui correspond aux critères fixés dans ce travail pour assurer un mélange homogène de l'agent oxydant et de l'agent réducteur à l'échelle nanométrique.

Afin d'étudier les propriétés énergétiques des carbones remplis d'agents oxydants produits par le procédé de remplissage de pores développé précédemment, les propriétés thermiques statiques des matériaux

sont d'abord analysées par calorimétrie à balayage différentiel et analyse thermogravimétrique. L'analyse thermogravimétrique est réalisée à différentes vitesses de chauffe pour permettre de modéliser la cinétique de la réaction de décomposition des carbones remplis. Cette caractérisation est considérée comme statique par opposition au processus de détonation dynamique. Il a tout d'abord été observé que le début de la décomposition des carbones remplis de perchlorate de sodium se produit à des températures allant de 250 à 320 °C, alors que la décomposition de l'oxydant seul commence à 470 °C. Des résultats comparables ont été obtenus avec du nitrate de potassium et du perchlorate d'ammonium comme agent oxydant, le début de la décomposition des carbones remplis se produisant à des températures inférieures d'environ 100 °C à la température de décomposition de l'agent oxydant lui-même. Cela suggère que la nature de l'agent oxydant joue un rôle important dans le mécanisme de décomposition. Les résultats montrent également que, bien que pour le même carbone le rendement de remplissage des pores n'ait pas d'influence significative sur le début de la décomposition et sur la cinétique de décomposition, ces propriétés dépendent fortement des propriétés physico-chimiques du carbone et de la nature de l'agent oxydant. Il a été observé que le début de la décomposition se produit à des températures plus basses si la surface des carbones présente une grande quantité de groupes fonctionnels contenant de l'oxygène. Cela indique que non seulement la nature de l'agent oxydant, mais aussi la nature et la stabilité thermique de l'agent réducteur jouent un rôle important dans le mécanisme de décomposition. La cinétique de décomposition des carbones remplis de perchlorate de sodium à l'échelle nanométrique a ensuite été comparée à celle des mélanges physiques correspondants à l'échelle micrométrique. De manière surprenante, aucune différence significative n'a été observée, ce qui suggère que la cinétique de décomposition du mélange carbone-agent oxydant n'est pas significativement plus rapide en raison du confinement dans les nanopores par rapport à un mélange physique. D'un point de vue qualitatif, on a toutefois observé que la réaction du carbone rempli à l'allumage était significativement plus violente que celle du mélange physique. Pour évaluer leurs caractéristiques de sécurité, les sensibilités de différents carbones remplis de perchlorate de sodium à l'impact et à la friction ainsi que leurs températures d'ignition ont été mesurées. Elles sont toutes en accord avec les applications potentielles, avec des sensibilités faibles à l'impact allant de 5 à 20 J et des sensibilités modérées à la friction allant de 48 à 160 N. Les températures d'ignition sont en très bon accord avec les températures de début de décomposition déterminées par calorimétrie différentielle à balayage. Un carbone rempli de perchlorate de sodium à un haut taux de remplissage des pores a finalement été choisi pour réaliser une étude détaillée de sa détonabilité et de ses propriétés de détonation. Pour cela, plus de 500 g de ce matériau énergétique ont été produits à l'échelle du laboratoire. Après une étude préliminaire de la détonabilité, trois densités différentes allant de 0,85 à 1,40 g/cm^3 ont été étudiées. Les résultats montrent que, dans un confinement fort en acier, le matériau est capable de détoner pour toutes les densités lorsqu'il est initié par un simple détonateur. Des vitesses de détonation allant de 3000 à 4200 m/s ont été mesurées. L'effet du diamètre de la charge a été étudié, et les résultats montrent que, dans ces circonstances, les diamètres critiques sont d'environ 6 à 8 mm et les diamètres idéaux d'environ 8 à 10 mm. Les performances globales correspondent à celles des explosifs pour des applications en carrière et à environ 30 à 60 % de celles d'un explosif brisant militaire tel que le trinitrotoluène. Ces propriétés sont très impressionnantes pour un matériau énergétique composite comportant une fraction importante de produits de décomposition solides, ce qui dénote une cinétique de décomposition dynamique très rapide favorisée par l'échelle nanométrique du mélange. Mis en parallèle avec l'étude de la cinétique de décomposition statique, ces propriétés de détonation sont vraisemblablement fortement liées au fait que le mélange d'agents oxydant et réducteur dans les nanopores se trouve à proximité immédiate des points chauds générés dans le matériau par la compression par choc, et à la densité plus élevée atteinte lorsque les particules de carbone sont remplies d'agent oxydant par rapport à celle du mélange physique correspondant. Ces résultats constituent une preuve expérimentale du concept de ce travail.

En conclusion, le concept d'une nouvelle famille de matériaux énergétiques basés sur des carbones nanoporeux remplis d'agents oxydants a été démontré dans ce travail, ouvrant par-là de nouveaux horizons vers des nanomatériaux énergétiques performants, sûrs et non toxiques avec un large spectre d'applications. Un nouveau procédé efficace de remplissage des pores a été développé et l'influence de la nature de l'agent oxydant et des propriétés physico-chimiques des carbones nanoporeux a été étudiée en détail. Les propriétés énergétiques de ces nouveaux matériaux composites ont ensuite été étudiées et il a notamment été démontré qu'ils peuvent facilement détoner et qu'ils présentent des sensibilités en phase avec les applications potentielles. Les propriétés uniques et la versatilité des carbones nanoporeux combinées au grand nombre de degrés de liberté du procédé de remplissage des pores développé dans ce travail offrent par ailleurs des perspectives prometteuses dans ce domaine.

Introduction

Energetic materials are those capable of rapidly releasing energy through a chemical reaction. They have numerous military and civilian applications, as high explosives, propellants or in pyrotechnic compositions. Although plenty of materials show such ability to release energy, only a few combine it with the adequate physicochemical, thermal and mechanical properties that make them safe for storage and use, stable over time and performant. Many of the energetic materials that are in service or are currently produced suffer from serious drawbacks such as hazardous aging, ecotoxicity, poor thermal stability, etc. It is well known that finding a compromise between safety, performance and environmental considerations is complicated and requires trade-offs. Extensive research is therefore performed to develop new energetic materials with enhanced properties. Most efforts are directed towards advanced synthesis of complex organic energetic molecules and energetic nanomaterials. The latter mainly consist of energetic formulations containing nanoparticles. However, both approaches face significant challenges, notably in terms of production cost, safe manufacturing, material homogeneity, toxicity or chemical compatibility.

Within this scope, this work aims at exploring a new family of energetic materials produced by filling the porosity of a nanoporous carbon, acting as a reducing agent (fuel), with a solid oxidizing agent in order to obtain an energetic material which is able to detonate. The filling of a reducing nanoporous matrix with an oxidizing agent allows retaining the potential advantages of a nanoscale mixture in terms of fast decomposition kinetics without having to suffer from the disadvantages of nanoparticles in terms of homogeneity, hazardous handling and potential toxicity. The use of nanoporous carbon as reducing matrix has moreover a lot of advantages with respect to other reducing agents, because its decomposition products are mostly gaseous, it is a robust three-dimensional material, and it is likely to have a desensitization effect on the formulations. This concept is novel and could potentially lead to a new family of energetic materials with promising properties and applications as pyrotechnic composition, propellant or high explosive.

In the first chapter of this thesis, introductory concepts and theoretical aspects about energetic materials and carbon materials are first described. Literature studies about the use of carbon materials in energetic materials and energetic materials based on nanoporous materials other than carbon are then presented. The concept of energetic materials based on nanoporous carbon is finally described, and its theoretical feasibility assessed.

The experimental part of this thesis is divided into two chapters. The first experimental chapter describes the development of a synthesis process aiming at filling the porosity of nanoporous carbons with solid oxidizing agents, and discusses the influence of the physicochemical properties of the nanoporous carbon material on the efficiency of this process. The second experimental chapter consists of experimentally proving the concept by demonstrating the ability of nanoporous carbons filled with an oxidizing agent to detonate and by studying their basic properties as energetic materials.

Chapter 1

Theory, literature review and introductory concepts

In this chapter, introductory concepts and theoretical aspects about energetic materials and carbon materials are first described in sections 1.1 and 1.2. Literature studies about the overall use of carbon materials in energetic materials and energetic materials based on nanoporous materials other than carbon are then presented in sections 1.3 and 1.4. The concept of energetic materials based on nanoporous carbon is finally described, and its theoretical feasibility assessed in section 1.5.

1.1 Generalities about energetic materials

1.1.1 Definition and classification

Energetic materials are substances or mixtures of substances that are capable of rapidly releasing energy through chemical reaction [1]. Depending on the application, three types of energetic materials can be distinguished:

- High explosives are designed to undergo a detonation, which is a decomposition reaction in which the zone of chemical reaction propagates through the initial medium at a supersonic velocity behind a shock front [1]. The detonation of high explosives has several effects, like the fragmentation of adjacent materials or the generation of a shock wave in the surrounding medium. The are mostly used in military warheads and in civil explosive formulations for blasting.
- Propellants burn in a controlled manner. They undergo a deflagration reaction which is a combustion propagating through the initial medium at a subsonic velocity, driven by thermal conduction [1]. They are mostly used for propelling projectiles and missiles in gun and rocket propellants, for military and civilian applications, but also for reducing the drag of projectiles, or to generate gases for powering auxiliary devices.
- Pyrotechnic formulations undergo an energetic chemical reaction at a controlled rate intended to produce (on-demand and in various combinations), specific effects such as time delays, or quantities of heat, noise, smoke, light, or infrared radiation [1]. They have numerous military and civilian applications.

Energetic materials are characterized by their performance in their respective application, their sensitivity and their stability or aging properties. The sensitivity of energetic materials is a family of safety features related to its ability to react to external stimuli resulting in its unwanted initiation.

It is important to bear in mind that the application of an energetic material does not only depend on the material itself, but also on the ignition means. If the generation of a shock wave by a pyrotechnic chain in a given energetic material leads to its detonation, it will be considered as a high explosive. However, if the same material is subjected to heat generated by an igniter, it will only deflagrate (in most cases) and will be considered as a propellant. The conditions required for a material to be able to detonate are much more stringent than in the case of a deflagration because the propagation velocity of the decomposition reaction of the former is much faster than in the latter case. Generally speaking, if a material can detonate when subjected to a shock wave, it will deflagrate when subjected to heat. Within the scope of this work, high explosives will be targeted, to study and to demonstrate the concept of energetic materials based on nanoporous carbons. Their application as gun or rocket propellant or as pyrotechnic composition will be part of future work.

The different categories of energetic materials sorted by composition are first discussed and the notion of oxygen balance defined. The theory of the detonation phenomenon is then introduced.

1.1.2 Composition

When sorted by composition, two categories of energetic materials are distinguished:

- **Energetic molecules** contain energetic functionalities, the most well-known being the nitro functional group NO_2. These molecules are metastable and decompose spontaneously at elevated temperature. They contain most of the time enough oxygen (or other oxidizing atom) so that most of the decomposition products are gaseous, and are mainly used as high explosives and propellants. Typical examples are trinitrotoluene (TNT), hexogen (RDX) and nitroglycerine; nitrocellulose is a special case of energetic molecules as it is a polymer. Homogeneous mixtures of energetic molecules are also used in energetic formulations, a typical example being Composition B or double base propellant [2].
- **Composite energetic formulations** are made of at least two distinct phases, one having an oxidizing character (the oxidizer) and the other a reducing character (the fuel). Typical examples are black powder (a mixture of potassium nitrate, charcoal and sulfur), thermite charges (typically, a mixture of iron oxide and aluminum) or composite rocket propellant (oxidizing particles dispersed in a polymeric binder). Most of the pyrotechnic compositions are furthermore composite energetic formulations. The energetic materials based on nanoporous carbons presented in this work are composite energetic materials.

For a material to be energetic, it must contain enough oxidizer (mostly oxygen but also halogen atoms), either within an energetic molecule or in an apart phase, in order to be able to release a significant amount of energy in a short period of time upon ignition. The oxygen balance (denoted Ω) is a measure of the fuel to oxidizer ratio in a compound or a mixture [3]. It basically expresses the deficiency or excess in oxidizing atoms required to oxidize the "fuel" atoms as carbon, hydrogen, metals, etc.; it is usually expressed as a mass fraction. In the case of an energetic material of empirical formula $C_pH_qO_rN_s$, the oxygen balance to CO_2 is defined as follows:

$$\Omega_{CO_2} = \left(r - 2p - \frac{q}{2}\right) \cdot \frac{16}{\mathcal{M}_{EM}}$$

where $\mathcal{M}_{EM}$ is the molar mass of the energetic material. The oxygen balance definition must be corrected if metal (fuel) or halogen (oxidizer) atoms are present, depending on the most stable products which will be formed.

Even if the composition of decomposition gases resulting from a deflagration or a detonation is much more complex, the oxygen balance can be used to provide qualitative guidance about the energetic character of materials. For the most commonly used energetic materials, there are very few propellants or high explosives with oxygen balances to CO_2 lower than approximately -75 wt% [3,4]. There is moreover a correlation between the oxygen balance of an energetic material and its performance as propellant or high explosive [3]. This will be considered when discussing the theoretical feasibility of energetic materials based on nanoporous carbons.

1.1.3 Detonation phenomenon

In order to discuss the potential use of energetic materials based on nanoporous carbons as high explosives, the main theoretical aspects of the detonation phenomenon have to be briefly presented. The ideal detonation model will be first described, and then the limitations of this simplified theory, with the objective of highlighting the main parameters governing the ability of an energetic material to detonate and its performance. As a detonation is defined as a decomposition reaction in which the zone of chemical reaction propagates through the initial medium at a supersonic velocity behind a shock front [1], some concepts about shock compression of materials will be introduced before discussing the detonation phenomenon itself.

Shock compression

The detonation process is closely related to the shock compression caused by a shock wave propagating through an unreacted explosive material and characterized by a discontinuous change in state. The state of a material is characterized by its internal energy (U) or enthalpy (H), temperature (T), pressure (P), specific mass (ρ), and particle velocity (v). The shock wave generated in the material is characterized

by its propagation velocity (D), known as shock velocity. The subscripts "0" denotes the undisturbed material ahead of the shock front. To determine the properties of the material behind the shock front, the Rankine-Hugoniot jump equations are applied by expressing the conservation of mass, momentum and energy through the shock front for a one-dimensional steady shock and considering a material initially at rest ($v_0 = 0$):

$$\rho_0 D = \rho(D - v) \tag{1.1}$$

$$P - P_0 = \rho_0 D v \tag{1.2}$$

$$\Delta U = \frac{1}{2}(P + P_0)\left(\frac{1}{\rho_0} - \frac{1}{\rho}\right) \tag{1.3}$$

For any material, the following thermal (1.4) and caloric (1.5) equations of state can be written:

$$f\left(P, T, \frac{1}{\rho}\right) = 0 \tag{1.4}$$

$$f\left(\Delta U, T, \frac{1}{\rho}\right) = 0 \text{ or } f\left(\Delta H, T, \frac{1}{\rho}\right) = 0 \tag{1.5}$$

By combining equations (1.1) to (1.5), it is possible to determine a relation between any two of the six parameters describing the state of the shocked material. Such a relation is referred to as a Hugoniot locus (a Hugoniot in abbreviated form) and represents the locus of all possible single-shocked states of a material. The expression of the thermal equation of state (1.4) for condensed materials in the considered range of pressures (1 - 100 GPa) is however not straightforward. Notwithstanding, extensive research and experimental work [5–7] have shown that the relation between the shock velocity and the particle velocity is linear for most of the materials in the considered range of pressures, which allows to circumvent this issue by using this empirical relation:

$$D = C_0 + sv \tag{1.6}$$

where the values of the parameters C_0 and s are experimentally determined. By combining this experimental Hugoniot and the equations of conservation of mass (1.1) and momentum (1.2), the Hugoniot of the material in the $\left(P, \frac{1}{\rho}\right)$ plane can be expressed as:

$$P - P_0 = \frac{C_0^2\left(\frac{1}{\rho_0} - \frac{1}{\rho}\right)}{\left[\frac{1}{\rho_0} - s\left(\frac{1}{\rho_0} - \frac{1}{\rho}\right)\right]^2} \tag{1.7}$$

The equations of conservation of mass (1.1) and momentum (1.2) can also be combined, which leads to a straight line in the $\left(P, \frac{1}{\rho}\right)$ plane, known as the Rayleigh line:

$$-\rho_0^2 D^2 = \frac{P - P_0}{\frac{1}{\rho} - \frac{1}{\rho_0}} \tag{1.8}$$

For any shock wave, the initial and final states must therefore lie on both curves, namely at the intersections between the Hugoniot of the material and the Rayleigh line. Whereas the Hugoniot of the material only depends on the initial state and on the empiric parameters of equation (1.6), the slope of the Rayleigh line depends also on the shock velocity, as shown in figure 1.1 for example. Considering that the initial state is completely defined and if one of the parameters of the shocked state is known, all the other parameters can therefore directly be determined.

Behind the shock front, the material will not stay in a stressed state as this state is not in mechanical equilibrium with the undisturbed surroundings. Where the stressed material is in contact with the surrounding medium at rest, it will exert a force on the surrounding medium and will accelerate away from the stressed area, thereby relieving the pressure. The adjacent stressed material will then be suddenly unrestrained, and so on. This phenomenon can be pictured as a rarefaction wave (or relief, or unloading wave) starting at the edges of the stressed material and propagating through it. During the relief of the pressure, the particles are accelerated away from the shocked zone, so that that the

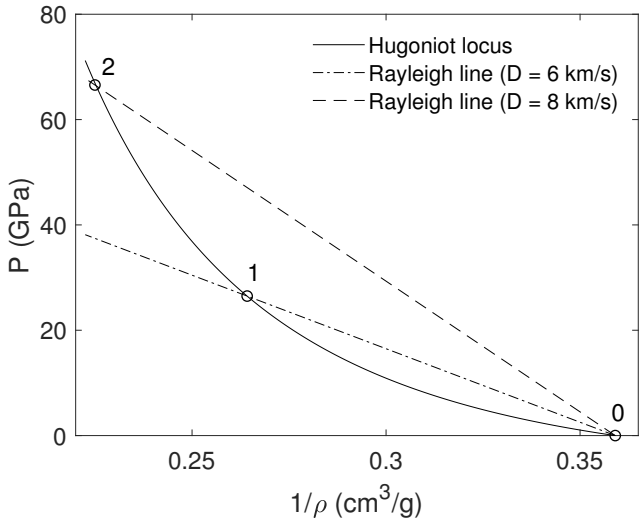

Figure 1.1: Determination of the properties of the shocked state of aluminum. The initial state (0) is characterized by a specific mass of 2.8 g/cm^3. Two shocked states, 1 and 2, are represented as illustrations. Numerical data from the literature [8] were used in equations (1.7) and (1.8).

rarefaction wave propagates in the opposite direction to the particles [8]. In the range of pressures of interest, this rarefaction process is so fast that it can be considered as adiabatic. It is furthermore a continuous relief which does not imply discontinuities, so that it can be considered reversible [8]. The material is therefore relieved isentropically from its shocked state. On the contrary to a shock wave, a rarefaction wave is continuous, and its propagation velocity is characterized by the velocities of its leading and trailing edges. The leading edge velocity depends on the shocked state and on the hydrodynamic properties of the materials, whereas the trailing edge velocity is often approximated by the longitudinal sound speed of the material [8].

Ideal detonation

Whereas an explosive is in metastable equilibrium at room temperature as the rate of the decomposition reaction is negligible, the decomposition reaction will become very fast behind the shock front because of the sharp temperature increase caused by the shock compression. The ideal detonation model is the simplest theory that describes the detonation phenomenon, and it refers to a steady-state one-dimensional detonation process where the thickness of the reaction zone is considered to be zero. This mainly means that the side effects and the reaction kinetics are neglected, and that the unsteady phenomena are not considered. Under these assumptions, the explosive just behind the shock front decomposes instantaneously to form the detonation products. As the nature of the material changes, the final state lies on the Hugoniot curve of the detonation products. In most of the practical applications, the decomposition reaction leads to the formation of gases. For theoretical illustration or a first estimation, the problem can be significantly simplified by using equations of states similar to that of ideal gases. The standard enthalpy of reaction $\Delta_r H^0$ is introduced as a parameter in equation (1.5):

$$\Delta H = \int C_P^0 \mathrm{d}T + \Delta_r H^0 \tag{1.9}$$

where ΔH is the enthalpy difference, C_P^0 the standard specific heat capacity at constant pressure, and T the temperature. By introducing the enthalpy definition in equation (1.3), the conservation of enthalpy through the shock front can also be expressed as:

$$\Delta H = \frac{1}{2}\left(P - P_0\right)\left(\frac{1}{\rho_0} + \frac{1}{\rho}\right) \tag{1.10}$$

The ratio of specific heat capacities is also considered as a parameter, named the polytropic coefficient Γ. This parameters is considered constant on the temperature interval. It lacks classical physical meaning

and aims to reflect the deviation from the ideal gas assumption. By combining equations (1.1), (1.2), (1.10), (1.9) and the ideal gas law as thermal equation of states, the Hugoniot of the detonation gases in the $\left(P, \frac{1}{\rho}\right)$ plane can be expressed as:

$$P - P_0 = \frac{2\Delta_r H^0}{\frac{1}{\rho_0} - \frac{1}{\rho}\frac{\Gamma+1}{\Gamma-1}} \tag{1.11}$$

Three different states are defined

- The initial state (subscript 0), which is the state of the unreacted explosive ahead of the shock front.
- The state of the unreacted explosive just behind the shock front. At this state, the explosive has been shocked and it is at high temperature and pressure, but the decomposition reaction has not started yet. This state is called the von Neumann (VN) state. In the ideal detonation model, this state is actually fictitious as the reaction is instantaneous.
- The state of the decomposition products just after the completion of the decomposition reaction, but before their expansion. This state is called the Chapman-Jouguet (CJ) state.

Since the conservations of mass and momentum are always obeyed, these three states must lie on the same Rayleigh line. To simplify and considering a steady process, this can only happen if the Rayleigh line is tangent to the Hugoniot of the detonation products at the CJ-state, as shown on figure 1.2. Once detonation gases are formed, they will expand through their isentrope via a rarefaction wave, known as the Taylor wave. For the detonation to be in steady state, the detonation gases must expand at the same velocity as they are generated by the decomposition reaction. This means that the leading edge of the rarefaction wave must have the same propagation velocity as the shock front, namely the detonation velocity D. By introducing the definition of the sound velocity, it can be shown that this can only happen if the flow at the CJ-state is sonic with respect to the shock front [9]:

$$\left.\frac{\partial P}{\partial \frac{1}{\rho}}\right|_{\mathrm{CJ}} = -\rho_{CJ}^2 c_{CJ}^2 \tag{1.12}$$

where c is the sound velocity of the gases.

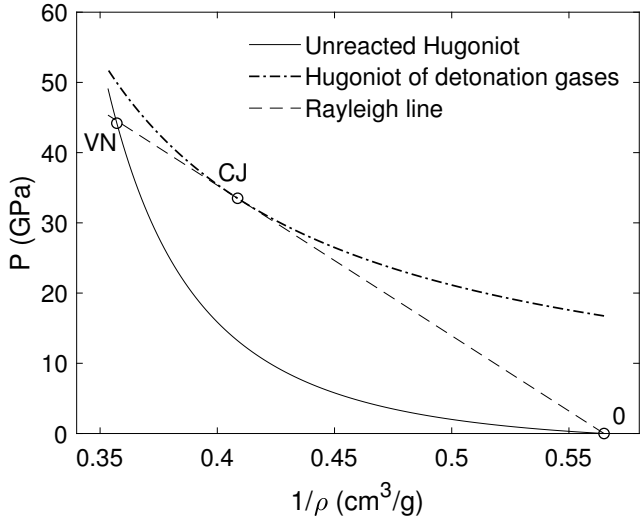

Figure 1.2: Hugoniot curves of pentaerythritol tetranitrate (PETN). The initial state (0) is characterized by a specific mass of 1.77 g/cm^3. The Chapman-Jouguet (CJ) and von Neumann (VN) states are represented. Numerical data from the literature [8] are used in equations (1.7), (1.11), and (1.8).

By expressing that equations (1.8) and (1.11) must be tangent at the CJ-state with the isentrope of the detonation gases, so have the slope given in equation (1.12), the CJ-state can be completely characterized. This is known as the Chapman-Jouguet steady-state condition and has been derived from experimental

results and thermodynamic considerations [9, 10] under the discussed ideal assumptions. The following relevant relations can be derived:

$$\rho_{\mathrm{CJ}} = \rho_0 \frac{\Gamma + 1}{\Gamma} \tag{1.13}$$

$$v_{\mathrm{CJ}} = \frac{D}{\Gamma + 1} \tag{1.14}$$

$$P_{\mathrm{CJ}} = \frac{\rho_0 D^2}{\Gamma + 1} \tag{1.15}$$

Summarizing, after that the shock compresses the explosive, the decomposition reaction is initiated and completed instantaneously, and the detonation gases compress the adjacent explosive and drive the shock front forward. At the CJ-state, the shock front and the leading edge of the rarefaction wave propagate at the same velocity (D) in the material and the process is steady. This means that there is only one possible ideal steady-state state for the detonation products of a given explosive at a given initial density, the CJ-state, which can be experimentally characterized. The energy liberated by the decomposition reaction is partially used to compress the explosive, and the other part is converted to work during the expansion of the detonation gases along their isentrope.

Under these ideal assumptions, the CJ-state can also be determined by thermodynamic calculations. To improve the accuracy of these calculations, equations of state dedicated to detonation products are often used and the equilibrium compositions are calculated by minimizing the free energy of the system [11]. Based on the elementary composition of the explosive and its standard enthalpy of formation, the steady-state detonation parameters are then obtained by iterating until the CJ-condition is fulfilled. It is well known that for some explosives (for instance for most of the military explosives), the calculated CJ detonation parameters are in very good agreement with the experimental results, whereas this is not the case for other explosives (e.g. some explosives for civilian uses). This is caused by significant deviations from the assumptions of the ideal theory, so called real effects. The extent of these real effects will determine if an explosive can be considered as ideal or if the real effects have to be taken into account. Detonation pressures differences of more than 5 GPa and detonation velocities differences of more than 500 m/s between the calculated and the experimental results are considered as an indication of significant real effects affecting the detonation phenomenon [12].

Real detonation

In a real detonation, finite dimensions and decomposition kinetics will play a role. There are also unsteady phenomena which deviate from the ideal theory, but these will not be discussed here.

Once heated by shock compression, the decomposition reaction will be very fast but not instantaneous, and the thickness of the reaction zone will depend on the state of the shocked explosive and on the decomposition kinetics. On the one hand, the expansion of the detonation gases will not be purely axial on the sides of the charge. Radial expansion will occur as well, leading to radial losses as this flow will exert no effect on the adjacent explosive. On the other hand, during the time needed for the completion of the reaction, the shocked but unreacted explosive will be partially relieved from its compressed state through a rarefaction wave before the completion of the reaction. These effects will slow down the decomposition reaction, markedly on the edges of the charge. This leads to a curvature of the shock front as the result of the deviations from the ideal one-dimensional detonation theory. Depending on the reaction kinetics, the charge dimensions and its confinement, these effects can also lead to a lower overall detonation velocity or even prevent the detonation from being sustained. The limiting dimension below with the real effects prevent the detonation from occurring, is called the critical diameter or critical thickness of the material.

The following different cases can be distinguished for illustrative purposes:

- Most military explosives are considered as ideal explosives, since their behavior is properly described by the ideal theory. The order of magnitude of the thickness of their reaction zone is 0.1 - 1 mm for an induction time of 10 - 100 ns [8, 12]. Simply stated, the decomposition reaction is so fast that the finite dimensions have no significant effect on its velocity, and the experimental detonation parameters (detonation velocity, detonation pressure, etc.) are very close to those predicted by the ideal model, except for very small charges, with dimensions in the mm-range.
- For other explosives, as civilian explosives, the real effects are much more pronounced due to reaction zone thickness in the cm-range [8]. In most of the practical applications, the side effects will therefore affect the detonation process and the detonation velocity will be lower than that of the ideal case.

- Finally, some materials are metastable at room temperature and can undergo a decomposition reaction when heated by shock compression, but they are not able to detonate as their decomposition reaction is too slow to allow the reaction to propagate at a supersonic velocity through the material. This is a consequence of the real effects described in this section, but detonation parameters of these materials could be calculated by using the ideal model. In this case, neglecting the reaction kinetics is however an unacceptable assumption.

In the particular case of composite explosives, for instance explosive mixed with aluminum as additive, the reaction pattern is even much more complex, as the kinetics of the aluminum oxidation is controlled by the diffusion through the alumina layer [4]. These composite explosives can therefore also be subject to intrinsic significant deviation from the ideal theory.

To further discuss the decomposition kinetics, the heterogeneity of the explosive materials needs to be considered. Even if an explosive is homogeneous in terms of chemical composition, it is most of the time heterogeneous in terms of structure and contains density discontinuities such as voids, pores, defects, etc. Exceptions are liquid explosives and solid single crystals, but they have very limited practical applications. When a shock wave reaches such a discontinuity, the interaction results in local high temperature and pressure regions known as hot spots [12]. It has been shown that these hot spots play a key role in the propagation of a detonation wave in a heterogeneous explosive [13]. This makes the detonation phenomenon even more difficult to study, as the overall decomposition kinetics depends on local and dynamic features.

Performance

The performance of a high explosive is characterized by its brisance, namely its ability to create a strong shattering or fragmenting effect in the surroundings of the explosive charge [14, 15]. The relation between the brisance and the fundamental detonation parameters of an explosive is not straightforward and different interpretations have been given through the past [14]. However, it is now commonly accepted that the brisance of an explosive is primarily governed by its detonation pressure [12, 15].

The experimental determination of the detonation pressure of an explosive is however difficult. Under the ideal assumptions, equation (1.15) shows that this detonation pressure, and thus the brisance of an explosive, depends on its initial density, the square of its detonation velocity, and its polytropic coefficient. As this coefficient is almost constant for most of the common explosives [8], it is generally stated that the brisance is mainly governed by the initial density of an explosive and the square of its detonation velocity:

$$\text{Brisance} \sim \rho_0 D^2 \tag{1.16}$$

It can also be observed in figure 1.2 and in equation (1.8) that the higher the initial density, the higher the detonation velocity of the explosive. For a given explosive material, the initial density plays therefore a key role in determining its performances.

Initiation

Because this section only aims to highlight the main parameters governing the ability of a material to detonate, the unsteady features of the detonation phenomenon have not been considered. They will however play a key role during the initiation of the explosive. Within the scope of the considered applications, the explosive is initiated by a shock wave generated by the detonation of explosive adjacent to it in a pyrotechnic chain, called the donor charge. The shock sensitivity of an explosive determines the minimal shock stimulus that is needed to allow the explosive to undergo a sustained detonation. This shock sensitivity is intimately related to all the aforementioned parameters governing the detonation properties of an explosive (namely its decomposition kinetics and its hydrodynamic properties), but also its density, dimensions, degree of confinement, and local features as hot spots. The donor charge is characterized by its performance in terms of brisance, but also by its whole Taylor wave, which is governed by the isentrope of its detonation gases, its size, and its degree of confinement [8]. One important classification is related to whether or not an explosive charge can be detonated by a standard detonator (usually a No. 8 detonator or equivalent [2]). In this case, the explosive is considered as cap-sensitive. The cap-sensitivity is not a requirement for an explosive to be able to detonate as it can be initiated by an additional booster, as for most of the civilian explosives. It is however a good indication that the shock sensitivity is in line with potential military applications.

Summary

This section aimed to highlight the main parameters governing the ability of an explosive to detonate and its performances, and to provide guidance for assessing new energetic materials. It has been showed that the ideal theory allows to predict the ideal performance of an explosive based on thermodynamic calculations, and that the performance of an explosive is mainly governed by its initial density and detonation velocity. The real effects, related to the finite reaction kinetics, the finite dimensions of the charge and its degree of confinement, as well as local dynamic features (hot spots) and the means of initiation also have to be considered when studying the ability of a material to detonate. In particular, the hot spots generated by the interaction of a shock wave with density discontinuities in the material during its compressive heating play a key role in the propagation of a detonation wave and their dynamic and local nature makes their effect very difficult to quantify by performing static experiments. Simply stated, to study the ability of a material to detonate and its related performance, dynamic detonation experiments have to be carried out while keeping in mind that all the aforementioned real effects. Furthermore, the mean of initiation has also to be considered when designing the experimental set-up. It should be pointed out that it is practically impossible to demonstrate that a material cannot detonate in any circumstances, as infinite charge dimensions and initiation means would be needed. Hence the purpose of this work is to study the ability of energetic materials based on nanoporous carbons to detonate for charge sizes and initiation means in line with potential practical applications.

1.2 Generalities about carbon materials and nanoporous carbons

1.2.1 Carbon materials

Carbon materials are unique ones that have been extensively used in many specialized applications from gas adsorption and separation, environmental remediation, catalysis, and energy storage [16–20]. Such variety of applications is mostly due to the flexible coordination chemistry of carbon atoms that allows almost infinite possibilities of three-dimensional structures and to their ability to react with other heteroatoms (e.g., oxygen, nitrogen, boron) to incorporate specific functionalities [19, 20].

From a structural point of view, most carbon materials are composed of sp^2-hybridized carbon atoms arranged in a two-dimensional structure and grouped in layers of fused aromatic rings (graphene sheets) with varied degree of planarity. These graphene-like layers are stacked by weak Van der Waals forces either in an ordered (i.e., graphite and graphitizable carbons) or turbostratic –disordered stacking- structure (i.e. activated carbons, carbon blacks) with different degrees of planarity depending on the graphitization extent of the materials [20, 21]. The latter strongly disordered carbon materials can be seen as built of segments of graphene sheets of different size and perfection bonded in a very large number of ways. The defects in those layers are notably due to holes, non-planarity, dangling bonds, topological defects and the presence of heteroatoms. The imperfect packing of those randomly bonded defective and distorted graphene layers creates pores with sizes ranging from a fraction of a nanometer to micrometers [20]. Figure 1.3 shows a schematic representation of such a structure and highlights the presence of porosity.

An example of the richness of carbon materials due to the flexible coordination chemistry of carbon atoms is seen in the number of allotropic forms of carbon (e.g., diamond, graphite, graphene, fullerenes, glassy carbon); among the most representative:

1. Diamond is a rigid and isotropic three-dimensional structure, where carbon atoms present sp^3 hybridization with tetrahedral stereochemistry and form a face-centered cubic structure, as shown in figure 1.4a. It is the hardest solid material and has a very high thermal conductivity but low electronic conductivity [20].
2. Graphite consists of a layered structure of sp^2 carbon atoms with a planar trigonal stereochemistry forming a flat condensed system of fused aromatic rings (hexagonal arrangement). These sp^2-based sheets (graphenes) are bound to each other along the z-axis direction by weak dispersive and Van der Waals forces, which confer a high degree of anisotropy to this material. An example of graphite structure is shown in figure 1.4b. As an example, in plane graphite (sp^2 sheets) has higher thermal conductivity than diamond, good electrical conductivity and practically negligible reactivity; on the other hand, edge-plane graphite regions have high reactivity [20].
3. Graphene is a two-dimensional sheet of sp^2 carbon atoms. This configuration provides this material with extraordinary properties such as large surface area (theoretical value of ca. 2600 $m^2 \cdot g^{-1}$ for a single layer), excellent thermal and electrical conductivity, optical transparency, high mechanical

Figure 1.3: Schematic representation of a disordered carbon material highlighting the presence of porosity between the defective and distorted graphene layers [22].

strength and high elasticity [20]. Graphene has no gap between conduction and valance bands (zero-gap semiconductor), so it can be considered a semiconductor or a metal [19].

4. Fullerenes are empty cages made of carbon atoms bonded with 3 neighboring carbon atoms in rings of 5, 6 and 7 atoms [23], as shown in figure 1.4c for the typical example of C_{60}.

In addition to these allotropic forms of carbon, molecular forms of carbon related to graphite exist, as carbon nanotubes (CNT), which can be pictured as graphene sheets rolled to form hollow tubes [24], as seen in figure 1.4d. CNT can be classified attending to different criteria such as their electronic conductivity (metallic, semimetallic) or the arrangement of the tubes in single or multi-wall configuration, or open and close-ended CNTs [24].

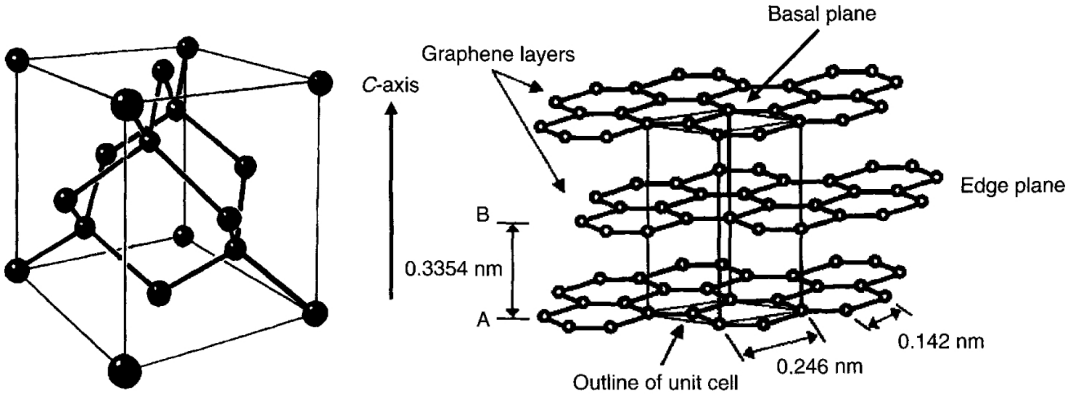

(a) Diamond [20].

(b) Example of graphite [20].

(c) C_{60} fullerene (adapted from [25]).

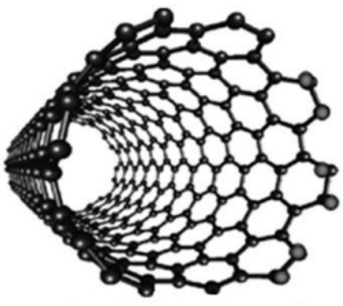

(d) Example of carbon nanotube (adapted from [25]).

Figure 1.4: Schematic representation of the structures of the main allotropic forms of carbon.

Carbon materials can also be shaped to or synthesized as nanosized particles. Carbon blacks and carbon dots are examples related to the graphite structure [20], where nanodiamonds are nanoparticles of diamond.

Other important type of carbon materials is the nanoporous carbons. They will be described in the next section, as these will be the materials used in this PhD thesis.

1.2.2 Nanoporous carbon

Nanoporous carbons are carbon materials containing nanopores, i.e. pores of width below 100 nm [26]. A short description of their main properties and of the related synthesis methods is given in this section.

Properties

The structure of nanoporous carbons is composed by distorted graphene-like layers of sp^2 domains of carbon atoms, with heteroatoms and sp^3 carbon atoms arranged in graphene layers with varied degree of planarity and dimensionality. The different degrees of the staked layers define the graphitization extent of the material. Thus, the structure of the carbon skeleton in porous carbons can be considered as a non-organized carbon phase composed of complex aromatic-aliphatic forms and twisted/distorted graphitic sheets, with randomly oriented crystallites, and defects and interstices between those crystallites that generate pores of nanometric dimensions [19, 20].

The pores in carbon materials are historically divided in three different categories depending on their size and according to IUPAC recommendations [26]:

- The term micropore refers to pores of widths smaller than 2 nm.
- The term mesopore refers to pores of widths between 2 and 50 nm.
- The term macropore refers to pores of widths larger than 50 nm.

This classification is based on the different gas phase adsorption mechanisms as a function of the pore width. Even if this distinction is of little interest for applications other than adsorption, it is very widely used.

Different experimental techniques are used to characterize the porosity with respect to this classification. The micropore and the mesopore volumes are mainly determined from equilibrium physisorption isotherms of nitrogen or argon at their boiling point under atmospheric pressure, while the macropore volume is determined by mercury intrusion porosimetry [16]. Different models can be applied to these experimental equilibrium adsorption isotherms to determine surface areas, pore volumes and pore size distributions of the materials [20,26]. Besides these macroscopic physicochemical properties related to the porosity of the nanoporous carbon, there are other aspects of the porous structure which are difficult to quantify at this scale. The porous structure or the texture of the nanoporous carbon is also characterized by microscopic features as the structure of the carbon skeleton, the way the pores are interconnected and their shapes [16, 26].

Nanoporous carbons are also mainly characterized by their surface chemistry. The defects in the carbon matrix and the large number of edge carbon atoms in disordered carbon materials are active sites that have a great tendency to react with heteroatoms to form stable surface compounds [16]. The most common heteroatoms are oxygen, hydrogen, nitrogen and sulfur. The nature, the concentration and the distribution of surface groups in a carbon material characterize its surface chemistry, and it strongly depends on the precursor material and the synthesis process. The oxygen-containing groups are the most common surface functionalities and are obtained by oxidation treatment of the carbon, mostly in air or in oxidizing solution. They are schematically shown in figure 1.5. The surface chemistry of a carbon material can be directly or indirectly characterized to some extent by different techniques, as elemental analysis, titrations, spectroscopic methods or thermal analysis (e.g., temperature programmed desorption) [16]. Some carbons also contain variable amounts of metal oxides or inorganic impurities (ashes) that come from the precursor material or the synthesis process.

Synthesis

Nanoporous carbons can be prepared from various carbon-rich precursors or synthesized in different ways. Char and activated carbon are the oldest known nanoporous carbon materials. Activated carbons are defined by IUPAC as "a porous carbon material, a char which has been subjected to reaction with gases, sometimes with the addition of chemicals, e.g. ZnCl2, before, during or after carbonization in order to increase its adsorptive properties" [27]. It is produced at industrial scale since the beginning of the 20-th century [16], mainly from coal, wood charcoal and coconut shell charcoal, either by physical or

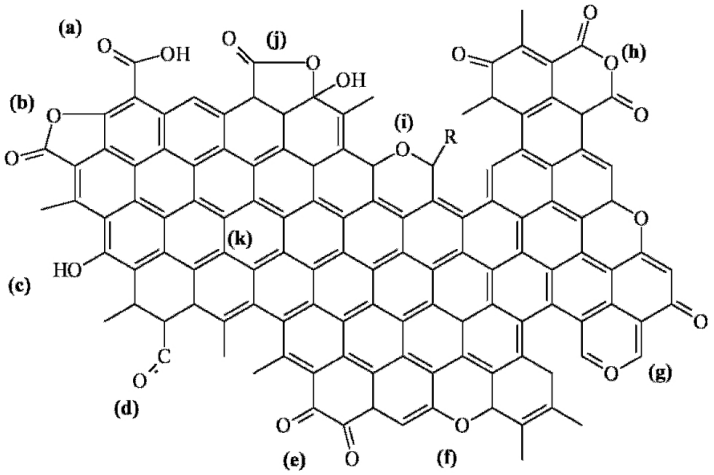

Figure 1.5: Examples of oxygen-containing groups on carbon surface: (a) carboxyl groups, (b) lactone, (c) hydrogyl, (d) carbonyl, (e) quinone, (f) ether, (g) pyrone, (h) carboxylic anhydride, (i) chromene, and (j) lactol [16].

chemical activation processes [28]. These conventional methods are widely used at industrial and basic research scale to produced nanoporous carbons.

Physical (or thermal) activation usually consists of two consecutive steps, namely a carbonization followed by an activation. The carbonization is first performed under inert atmosphere at a moderate temperature between 400 and 800 °C to remove the volatiles from the precursor material. The activation then consists of exposing the material to gaseous oxidizing agents (mainly steam or carbon dioxide, to prevent too exothermic reactions) at elevated temperatures between 800 and 1000 °C in order to selectively oxidize carbon atoms and expand the porous structure [20, 28].

The chemical activation is a one-step process, consisting of adding an activating agent (mainly $ZnCl_2$, H_3PO_4 and KOH) to the precursor material and heating the mixture under inert atmosphere at temperatures ranging from 400 to 900 °C [20, 28]. During the process, a significant porosity is formed in the carbon material by removal of water molecules or selective removal of carbon atoms [20,28]. The residues of the oxidizing agent are washed after the heat treatment.

Typically, activated carbons are highly disordered and exhibit a well-developed porosity in the micro- and mesoporous range. Activated carbon with a volume of pores of widths smaller than 50 nm larger than 1 cm^3/g are common, and values as high as 2.5 cm^3/g have been reported [20].

Some alternatives to the conventional synthetic methods have been emerged for the preparation of nanoporous carbons, aiming at controlling the porosity and the surface chemistry. Among most relevant methodologies, several strategies can be considered such as hydrothermal/solvothermal carbonization, nanocasting techniques (hard-, soft-templating), sol-gel approaches, self-activation of certain precursors, etc. [19, 20].

The thermal exfoliation of graphite and graphite oxide to produce expanded graphite and reduced graphene oxide (rGO), respectively, can also lead to the generation of a significant nanoporosity, with volumes of pores of width smaller than 50 nm of about 0.75 cm^3/g [29].

1.3 Use of carbon materials in energetic materials

Carbon materials have been and are used in many composite energetic formulations as a reducing agent (fuel). The oxidation of carbon is highly exothermic and the combustion products are gaseous. The ability of a fuel to be oxidized in gaseous products is very important for applications as propellant and high explosive, so that composite energetic formulations based on carbon materials can be used in the whole scope of energetic materials. This section aims to review the different energetic formulations that contain carbon materials and to highlight the effect of their physicochemical properties and their role in the combustion process. As black powder is the first known energetic material and as it has been extensively studied, it is discussed as first. Then, the various historical energetic materials containing carbon materials are described. Finally, the modern energetic formulations that contain carbon materials and the recent developments of these formulations are discussed.

1.3.1 Black powder

Black powder, also known as gunpowder, is a mixture of a carbon material, typically charcoal, potassium nitrate and sulfur [30]. It is used in Europe since the 13th-century, mainly as gun propellant and pyrotechnic formulations [30, 31]. It has been widely replaced as gun propellant by propellant based on nitrocellulose since the beginning of the 20th-century, but it is still widely used as igniter formulations for its ease of ignition and its high burning rate at low pressure [32].

The formulation of black powder is merely complex and has long been considered as an art rather than a science [32,33]. Even with the most recent manufacturing techniques, the process is only partially standardized and large deviation in combustion properties between batches are still observed [32, 33]. Various authors have studied the potential causes of these unexplained deviations, but without going beyond the stage of assumptions [32–35]. It therefore remains an open question today. The charcoal has however been considered in most of the cases as the most probable source of deviation [32–37] due to its very variable physico-chemical properties. Nonetheless, it should be noted that the area of expertise of these authors for much of such studied is energetic materials, thus no modern characterisation techniques of nanoporous carbon materials appear to have been used and very little information is available about the porosity or the surface chemistry of the charcoals.

It has been known for a very long time that only certain carbon materials can be used as black powder ingredients and that the type of charcoal has a significant influence on its performance [38]. For instance, charcoals made of light wood with an open structure and carbonized at low temperature (circa. 500 °C) are recommended [34, 37]. While not using the same terminology, different authors have shown that the surface chemistry of the carbon materials (mainly charcoals but also carbon blacks) plays a key role in the combustion properties of black powder [34–37]. In sum, their data show that, the higher the volatile content of the carbon materials, the lower the ignition temperature and the activation energy of the decomposition reaction [34–37]. Even if this can be related to the extent of the surface chemistry of the carbon materials, the role of the nature of the surface groups has not yet been clarified due to the lack of appropriate surface characterization. Some authors showed also that, when the charcoals and the carbon black are thermally treated at 950 °C in inert atmosphere, the nature of the carbon material still had an influence on the combustion properties of the black powders [35], suggesting that not only the surface chemistry but also the porosity and the precursor material are crucial. The role of the limited surface area of the charcoal (i.e. ranging from 1 to 3 m^2/g) has also been pointed out as an important parameter for the combustion of black powder [4], with little detailed discussion about its influence on the combustion mechanism. The ash content of the carbon materials were also investigated and found to not influence significantly the combustion properties of the investigated black powders, indicating that the ashes do not act as catalyst during the combustion [35]. Overall, the mechanism of combustion of black powder and the precise role of each ingredient is still a matter of debate [39], despite numerous studies [33, 39–42]. This is more pronounced for the role of the carbon material component in the combustion process. Indeed, despite being the oldest propellant known [30], little is known about the influence of the physicochemical properties of the carbon materials on the combustion properties of black powder and on its combustion mechanism in general. This is probably related to the difficult observation of a dynamic process as combustion of a composite material at the microscropic level, and to heterogeneity of disordered porous carbon materials in terms of reactivity and thermal stability at this scale.

1.3.2 Historical of energetic materials

The history of energetic materials is very rich. Whereas black powder was used in most of the applications up to the middle of the 19-th century, the progress of chemistry progressively led to the discovery of novel energetic substances or mixtures of substances. In parallel to the development of new organic or inorganic compounds (as fulminates, azides, nitrated organic molecules, etc.), oxidizing substances (mainly salts of chlorate, perchlorate and nitrate) were widely used in a great variety of energetic formulations for military and civilian applications.

Carbon materials, under the form of charcoal, coal, carbon black, coke or even activated carbon, have long been used as reducing agents in some of these formulations [30, 43, 44]. Most of them have however been progressively replaced as propellants and high explosives by safer formulations with higher performances, and only a very few were still in use after the Second World War. However, during the First World War, due to a lack of chemical precursors, many of those energetic mixtures were used in ammunition.

The energetic formulations containing carbon material are shortly described in this section. For the

sake of clarity, it should be note that those formulations for which too little information is available or into which the role of carbon material is only marginal have been omitted.

Amide powder (*amidpulver* in German) is a German smokeless artillery propellant that was used from the late 19-th century and during the First World War. It was composed of 37 wt% NH_4NO_3, 14 wt% KNO_3 and 49 wt% charcoal [45, 46]. ***Ammonpulver*** is also a German gun propellant based on NH_4NO_3 and used during the First World War. It contained 85 wt% NH_4NO_3 and 15 wt% charcoal. It was reported as cheap, insensitive, powerful, flashless and smokeless, but difficult to ignite [45]. **Hebler powder** or **wellite** is a comparable Swiss smokeless propellant containing 62.3 wt% KNO_3, 15.8 wt% NH_4NO_3, 11.5 wt% charcoal and 9.5 wt% sulfur. It was abandoned because it was too hygroscopic for practical use [47]. These formulations can be seen as attempts to use ammonium nitrate to develop new propellants to replace black powder, mainly in order to make smokeless and flashless gun propellants for artillery. Their main drawbacks are their difficult ignition and their hygroscopic character.

Ammoniakkrut is the first known explosive based on NH_4NO_3, patented in 1867 [45]. The original formulation consisted of 80 wt% NH_4NO_3 and 20 wt% charcoal. This formulation was however very difficult to detonate and 10-14 wt% nitroglycerine (NGl) was quickly added to sensitize it. This formulation was finally considered as too hygroscopic and exudable for practical applications [45]. The family of **dynammons** was used in many countries and also contained NH_4NO_3 finely mixed with a fuel, notably charcoal [48]. A German dynammon containing 90 wt% NH_4NO_3 and 10 wt% red charcoal is reported to have a density of 1.01 and a detonation velocity of 4100-4200 m/s [44, 46]. **Astralit**, **titanites** and **fulmenit** are other examples of civilian and military high explosives used until the First World War and based on NH_4NO_3, mixed with trinitrotoluene and nitroglycerine or nitrocellulose, and containing a small amount (1-10 wt%) of charcoal [45, 49, 50].

Ammonals are mixtures of NH_4NO_3 and aluminum which were used in different countries as civilian and military high explosives. The first ammonal formulations, from the early 20-th century to the First World War, also contained charcoal as additional fuel [44, 45]. A great variety of composition, with 70-90 wt% NH_4NO_3, 4-25 wt% Al and 2-6 wt% charcoal is reported [44, 45]. For a formulation made of 72 wt% NH_4NO_3, 23.5 wt% Al and 4.5 wt% charcoal, a detonation velocity of 3450 m/s was reported [44]. After the First World War, charcoal was progressively omitted in the ammonal formulations and trinitrotoluene added, in order to make the formulations easier to detonate [45]. **Lithofracteur** are civilian high explosives of the late 19-th century used in many countries. In some versions of this explosive, carbon materials were used. An other version, named lithofracteur of Newton, contained 77 wt% $Ba(NO_3)_2$, 2 wt% KNO_3 and 21 wt% charcoal [47]. Just before the Second World War, a particular ammonal formulation containing 85 wt% NH_4NO_3, 10 wt% activated carbon and 5 wt% aluminum was reported [30]. Based on the limited available information, it seems that this formulation was significantly easier to detonate than the other high explosives made of NH_4NO_3 and charcoal [30].

Liquid oxygen explosives are a special case of explosive for which the oxidizer is liquid oxygen (liquid air has also been used in the very first versions), and which was developed at the end of the 19-th century. It consisted of combustible materials impregnated with liquid oxygen just before the firing of the charge. The delay between the soaking and the firing had to be shorter than 15 minutes [47]. These explosives have been extensively used in many countries for blasting application, up to the 1950's in US, before being progressively replaced by more practical ammonium nitrate emulsion and ammonium nitrate-fuel oil explosives [47]. Various carbon materials have been used as combustible material, notably charcoal and different grades of carbon black, lamp black being the most widely used. Detonation velocities of 4000-6000 m/s were reported and the mixtures were cap-sensitive [47]. Despite extensive research on the subject until the Second World War, no mention to activated carbon as porous fuel was found.

Whereas the historical dynamite contains nitroglycerine absorbed in *kieselguhr* (a natural porous diatomaceous silica) to desensitize it [48], a great variety of other absorbent materials and additives were used. In some cases, carbon materials was used as nitroglycerine absorbent in early developments of the late 19-th century. **Carbondynamites**, patented in 1886, consisted of nitroglycerine absorbed on cork charcoal [30], and a German version of **lithofracteur** contained 52 wt% nitroglycerine, 12 wt% pulverized coal, 2 wt% sulfur, 4 wt% $NaNO_3$ and 30 wt% kieselguhr [46, 47].

The **Bellford powder** was patented in 1853. It consisted of a regular black powder impregnated by an aqueous saturated solution of potassium chlorate and then dried at 38 °C for 4 days [43, 51]. Unfortunately, very little is known about this formulation, but it can be assumed that potassium chlorate at least partially crystallized in the porosity of the charcoal upon drying. This is potentially the first reported use of a porous carbon material filled with an oxidizer, even if the confinement of the salt in the porosity of the carbon material was not emphasized.

Very interestingly, one attempt to use **activated carbon as a porous reducing matrix filled**

with oxidizing agents was reported in the patent literature [52] in 1938; three different methods were described:

1. The first method consists of filling the porosity with an energetic substance prepared in-situ. For instance, the porosity is filled with glycerol, and the obtained material is treated with a mixture of nitric and sulfuric acid in order to obtain an activated carbon filled with nitroglycerine. The degree of nitration is not reported, but it can be assumed that some of the adsorbed glycerine remained inaccessible for the nitrating treatment. This is essentially comparable to the historical Nobel's dynamite, where nitroglycerine is absorbed in natural porous silica to reduce its sensitivity. The main advantage of the proposed process is the safety, as nitroglycerine does not have to be handled in a hazardous liquid form. No information is available about the physicochemical properties of the activated carbon and the resulting material is described only qualitatively as "an explosive substance adhesively bonded to the carbon". It can only be presumed that nitroglycerine was to some extent physically adsorbed on the surface of the activated carbon by dispersive forces and/or specific interactions with polar surface groups. Another explosive molecule potentially synthesized in situ in the activated carbon porosity is tetranitromethane. There is no report on study of exudation upon heating and aging, and the power (quantified according to the Trauzl test [14]) of the obtained materials is reported "lower than that of dynamite", without mention of the ability of this material to detonate.
2. In describing a second method, the author claims to make use of the adsorptive and "catalytic" properties of activated carbon to promote the formation of perchloric acid or nitric acid in the porosity, followed by the "adhesive bonding" of the acid to the carbon surface. Essentially, a physical mixture of activated carbon and particles of ammonium nitrate or ammonium perchlorate are exposed to overheated steam. In these conditions, formed aqueous solutions of the salts at least partially decomposes in volatile ammonia and nitric or perchloric acid, respectively. It is assumed that part of the formed acidic aqueous solution and/or gaseous acid enters the porosity of the carbon during the process, leading to a strong oxidation of the carbon surface. The pretended role of activated carbon in the acid formation is unclear, as the thermal decomposition of aqueous solutions of ammonium nitrate and ammonium perchlorate are known to notably lead to formation of ammonia and nitric or perchloric acid, respectively. Presumably, the whole process can be considered as a safe process to strongly oxidize the carbon surface, potentially by decorating the surface with explosive functions as nitro groups, without handling concentrated acid solutions or risking run-away thermal behavior. The author mentions that it is subsequently possible to fill the porosity of the oxidized activated carbon with nitrate or perchlorate salts. This part of the process consists of mixing the activated carbon with a saturated solution of the salts under vacuum. He also proposed to impregnate the activated carbon with perchloric or nitric acid and to subsequently expose it to a flow of ammonia, in order to synthesize ammonium nitrate or ammonium perchlorate into the porosity. For both methods, no direct observation of the filling of the porosity is reported, and there is no mention of the performance of these materials or of their ability to detonate.
3. The third method consists of soaking activated carbon in molten salts, notably a eutectic mixture of ammonium nitrate and ammonium perchlorate. The author mentioned an immediate and significant release of ammonia when some activated carbons were used, presumably related to the catalytic properties of the surface of these activated carbons promoting the decomposition. The material obtained following this synthesis method is reported to be cap-sensitive and able to detonate but no direct quantitative observation of a detonation was reported.

Of these three methods, only the third was considered as suitable for the synthesis of high explosive for military application. The ability of this material to detonate is attributed by the author to "the intimate contact between the activated carbon and [...] the oxidizing substances". Even if this is definitely the closest research to the present work, no actual results or quantitative observations were presented. To the best of our knowledge, this work was not followed up with additional research and remained at the concept level.

1.3.3 Modern energetic materials

After the Second World War, the large number of energetic materials in use was significantly reduced, as a result of standardization and modern research work. In the field of secondary high explosives for military applications, the vast majority of the formulations are based on nitrated benzene derivatives (e.g. TNT, tetryl and picric acid), nitrate esters (e.g. PETN) or nitramines (e.g. RDX and HMX) [2,53]. Emulsion slurries and ANFO (*Ammonium Nitrate Fuel Oil*) are currently the most common types of high

explosives for civilian applications [53]. With regard to gun propellants, virtually all formulations are based on nitrate esters (e.g. nitrocellulose, sometimes gelatized by nitroglycerine), with some containing also nitroguanidine. Modern rocket propellants are either based on nitrate esters (nitrocellulose gelatized by nitroglyrine), or contain inorganic oxidizing particles (e.g. ammonium perchlorate) dispersed in a polymeric matrix [2]. As a result of these developments, the historical high explosives and propellants containing carbon materials as main ingredients are no longer in use. As the field of pyrotechnic formulations has been much less subject to such rationalisation, a large number of different formulations are still used nowadays. Black powder, and its derivatives as benite, is still extensively used for pyrotechnic applications, as igniters for instance. Apart from this exception, it can be considered that carbon materials are not used as main ingredients in modern energetic materials.

In contract, carbon materials are extensively used as additives in modern energetic materials. For instance, carbon black or powdered graphite are added to translucent rocket propellants to increase the opacity and to prevent radiation heating in other places than on the burning surface [54]. A few high explosives contain 1-2 wt% of carbon black for the same reason. Carbon black, powdered graphite and activated carbon are also considered as burning rate catalysts in rocket propellants, but their precise role in the combustion process is rather unclear [4, 55]. Gun propellant and pyrotechnic formulations are often "graphitized" (i.e. coated with powdered graphite, or sometimes carbon black) to improve their pourability and limit their sensitivity to electrostatic discharges [2].

1.3.4 Recent developments

Most recently, different carbon nanomaterials have attracted a lot of attention in the scientific world as the result of their superior electrical, mechanical and thermal properties, and they have been extensively studied as additives in energetic materials, mostly to reduce their sensitivity and improve their thermal stability in order to make their use safer [25]. Nanodiamonds have been studied as reducing agent in combination with potassium chlorate, in an attempt to reduce the sensitivity of the formulation and to improve its thermal stability [56]. However and to the best of our knowledge, the detonability of these formulations has not been demonstrated [56]. A large number of "energetic fullerenes" were produced by functionalizing fullerenes with energetic functional groups [25] and were studied as energetic binder in combination with polymer, as burning rate modifier and even as energetic material [25, 57]. Graphene-based nanocomposites produced by sol-gel synthesis have also been used as a matrix containing oxidizer (ammonium nitrate and perchlorate), although is seems that the intrinsic potential energetic properties of this material were not considered [25, 58]. They are namely mostly studied as combustion catalyst or oxidizer with a lower sensitivity. Graphite oxide (GO) has been considered to some extent as an energetic material on its own. Due to its high molar C/O ratio of 2:1 [29], this material has however an oxygen balance to CO_2 of about -120 %, which makes it unsuitable for most of the practical applications [3]. Hence, it has mostly been studied as an additive in order to decrease the sensitivity of high explosives such as HMX [59]. For this kind of application, its relatively high oxygen content makes it a better candidate than graphite in order to limit the effect on the performance of the composite energetic materials [25]. Reduced graphene oxide (rGO) has also been used as a coated additive on CL-20 high explosive crystals to decrease their sensitivity [60], and carbon nanotubes (CNT) have been extensively studied as carriers of combustion catalysts, as additives to decrease the sensitivity of formulations and as supports for metal fuel [25]. Different carbon nanomaterials, but mostly carbon black, have also been dispersed in energetic formulations to make them more sensible to laser ignition [25]. Even if some of these carbon materials are porous and if the desensitization mechanism is most of the time unclear, their role in the resulting energetic composite has been mainly discussed in terms of the electrical, mechanical and thermal properties of the carbon material used as additive [25], rather than of their porosity.

Interestingly, there are some recently reported cases of the use of carbon nanomaterials as carrier for energetic materials and oxidizing agents. Most of them result from an attempt to encapsulate energetic materials in a carbon matrix in order to decrease the sensitivity of the formulation. The hollow cavities of multi-wall carbon nanotubes (MWCNT) were filled with crystalline potassium nitrate by a wet chemical process using potassium nitrate mixed with highly concentrated nitric acid, during which the textural properties and the surface chemistry of the MWCNTs were modified [61]. After this treatment, crystallized potassium nitrate was observed in the cavities of the MWCNTs. However, volumetric ratio between MWCNT and potassium nitrate of about 10:1 was observed [61]. It therefore appears that the oxygen balance of this material is too negative for being used as an energetic material on its own. It has however been studied in pyrotechnic formulation in combination with other energetic materials [61].

Some attempts to embed energetic materials, as FOX-7 and RDX, in different types of nanoporous

carbons [62, 63] have also been reported. In both cases the explosive is reported to be recrystallized in the porous structure of the carbons after solvent evaporation. However, the ratio of high explosives in the obtained composites ranged from 50 to 70 wt% [62, 63], which corresponds to oxygen balances to CO_2 of -100 wt% at the best. It therefore appears that the decrease of sensitivity has a strong impact on performances. The energetic properties of these composite materials were moreover not thoroughly investigated as the focus was on sensitivity features.

The thermal properties and the burning rate of a hydroxylammonium nitrate (HAN) aqueous solution (95 wt% HAN) in the presence of activated carbon was studied as a propellant candidate [64–66]. Even if the activated carbon additive has been described as a combustion catalyst in these studies, the reported concentrations actually correspond to almost stoichiometric mixtures and the activated carbon acts most probably as a reducing agent in the combustion process. As the oxidizing solution is liquid, the pores of the activated carbon are filled to some extent by the solution during the preparation process, ensuring an intimate mixture at the nanometer scale of the oxidizing and the reducing agent. Interestingly, the onset of the decomposition is reported to occur at a significantly lower temperature in the presence of activated carbon than for the pure solution (i.e. at 86 °C instead of 185 °C [64]). To the best of our knowledge, the detonation properties of this material have not yet been studied.

It has also been reported that when ammonium nitrate is mixed with activated carbon or carbon nanotubes, "violent reactions" take places just after its melting [67]. It can be expected that the molten ammonium nitrate is able to enter the porosity of the nanoporous carbon, and that the decomposition temperature of this composite material is lower than the melting point of ammonium nitrate.

1.4 Energetic materials based on nanoporous materials other than carbon filled with an oxidizer

It is interesting to note that other porous materials filled with oxidizers were studied as potential energetic materials. Porous silicon filled with an oxidizer was reported as a potential energetic material in 2002 [68], and it subsequently became a new field of investigation at the intersection of semiconductors and energetic materials science. Several types of oxidizer were used to fill the porosity of the silicon, mostly perchlorate and nitrate salts and sulfur [69]. The impregnation of the pores was performed by filling the porosity with a solution containing the oxidizer and subsequently evaporating the solvent. In the particular case of sulfur, molten sulfur was directly filled in the pores as well [69, 70]. Porous silicon filled with sodium perchlorate is considered as a possible detonable energetic material, and its detonability was theoretically predicted [71]. However, to the best of our knowledge, this has not been yet experimentally confirmed. The main drawbacks that currently limit the applications of energetic materials based on porous silicon to pyrotechnic compositions seem to be the solid nature of the decomposition products, and the fact that this material is synthesized as a thin porous film with a thickness of around 25-50 μm on a silicon substrate. It is therefore greatly subjected to the non-ideal effect affecting the detonation phenomenon described in section 1.1.3.

Metal organic frameworks, consisting of metal ions coordinated to organic ligands to form three dimensional crystalline structures, are another type of nanoporous material which was investigated as potential base of composite energetic materials [72]. As an example, the energetic properties of zeolitic imidazolate frameworks (ZIF) filled with a liquid oxidizing agent (tetranitromethane) have been studied by thermal analysis. The theoretical predictions for these composite materials are in line with potential applications as high explosive, but the detonability of the material has not been experimentally demonstrated [72]. The use of a liquid oxidizing agent as tetranitromethane also raises questions about exudation of the oxidizer or compatibility issues with contact materials.

1.5 Energetic materials based on nanoporous carbon

1.5.1 Concept description

The concept of this thesis consists of filling the porosity of a nanoporous carbon, acting as a reducing agent (fuel), with a solid oxidizing agent in order to obtain an energetic material which is able to detonate. Even if a related approach was suggested just before the Second World War in the patent literature [52], it seems that no actual results or quantitative observations have yet been reported. In general, and even if the concept of energetic materials based on nanoporous carbons filled with an oxidizing agent has

been marginally mentioned in the past, it has not been deeply investigated and no experimental proof of concept has been provided.

The design of composite energetic nanomaterials is based on a simple observation, namely that the rate limiting step of the decomposition mechanism of a composite energetic material has the tendency to depend on transfer phenomena [73], and will therefore be much faster for nanomaterials than for conventional physical mixtures of oxidizing and reducing agents at the micrometer scale. As discussed in section 1.1, a faster kinetics is a key to open the door to applications as high explosives, but propellant and pyrotechnic composition with fast burning rate are also highly attractive. A physical mixture at the nanometer scale of reducing and oxidizing agents is however far from simple, mostly because it is very difficult to properly disperse both phases at this scale without forming agglomerates [73]. Free nanoparticles can moreover cause health issues. Bearing all this in mind, the use of a nanoporous matrix is an elegant solution to these issues. The filling of the nanopores with the oxidizing agent ensures its homogeneous dispersion at the nanometer scale, and there are no free nanoparticles.

In addition, the use of nanoporous carbon as reducing matrix has a lot of advantages with respect to other reducing agents. First of all, of all the potential reducing agents, only carbon and sulfur oxidation leads to the formation of decomposition products which are gaseous at moderated temperature [4]. They can therefore perform significant work during their expansion and generate high pressures, which are key features of propellants and high explosives, respectively. Another advantage of nanoporous carbon is that it is a robust three-dimensional material and its production at the industrial scale is mature. The versatile nature of the carbon atoms moreover can lead to the development of a variety of nanoporous carbon materials with unique properties, hereby extending the scope of the possibilities offered by these materials.

From the thermodynamic point of view, the use of pure carbon, or with a limited amount of heteroatoms, is very favorable as the oxidation of carbon is highly exothermic. This is a great advantage with respect to other carbonaceous materials such as carbons gels synthesized through the polymerisation of hydroxybenzenes with aldehydes for instance, where a significant extent of the carbon atoms are already bonded to oxygen atoms (under the form of ether and hydroxyl functional groups), hereby limiting the heat of decomposition of the material. Carbon materials are also generally considered as relatively inert when in contact with other materials found in ammunition, as metal alloys, polymers, glues, etc. Moreover, numerous examples of the use of carbon nanomaterials as additives to decrease the sensitivity of energetic materials were given in the previous literature study. Even if the desensitization mechanism is not very clear [25], it is related with the superior mechanical, electrical and thermal properties of graphene and its derivatives, and these attractive features can be expected to be at least to some extent retained when using nanoporous carbons, despite their lower degree of order with respect to these materials. However, even if nanoporous carbon has been used as fuel or combustion catalyst in many energetic formulations and if its large surface area has been identified as a key parameter of its interesting combustion properties [4, 64–66], it is very difficult to predict the detonability of these composite energetic materials as it depends on dynamic phenomena and local features as described in section 1.1.3.

In summary, the concept of an energetic material made of a nanoporous carbon reducing matrix filled with an oxidizing agent is a very promising and novel concept, which still has to be investigated and demonstrated. The filling of a reducing nanoporous matrix with an oxidizing agent allows the potential advantages of a nanoscale mixture in terms of faster decomposition kinetics to be retained without having to suffer the disadvantages in terms of homogeneity and possible toxicity.

1.5.2 Theoretical feasibility

The very first step of the study of the concept of energetic materials made of a nanoporous carbon matrix filled with an oxidizing agent consists of assessing its theoretical feasibility. As described in section 1.1.2, the oxygen balance is a theoretical parameter which only depends on the elemental composition of a formulation and that can be used to qualitatively assess its potential use as energetic material. Within the scope of this analysis, an oxygen balance to CO_2 of -75 wt% has been used as a threshold to consider that a material can have acceptable performance for practical applications (see section 1.1.2). Moreover only the volume of pores of the nanoporous carbon smaller than 50 nm, i.e. the micro- and the mesopores has been considered. Even if wider pores could be interesting from an energetic point of view, this choice is related to the different characterization techniques of the porosity. In practice and in most cases, most of the pores of these materials have nevertheless a width smaller than 10 nm. As discussed in section 1.2.2, nanoporous carbons with a volume of pores of width smaller than 50 nm of 1 cm^3/g is common,

and values higher than 2 cm^3/g have been reported.

The choice of the oxidizer is also crucial. As the volume of the porous matrix is limited, the relevant parameter is a volumetric expression of the oxygen balance. Considering as first that the density of the oxidizer is equal to its theoretical maximal density (TMD), the volumetric oxygen balance to CO_2 is defined as:

$$\Omega^V_{CO_2} = \Omega_{CO_2} \times \text{TMD} \tag{1.17}$$

where the oxygen balance to CO_2 expressed as a mass fraction is defined in section 1.1.2. The units of this volumetric oxygen balance are g of oxygen per cm^3 of oxidizing agent when the TMD is expressed in g/cm^3. It can be seen as an density of oxidizing species "available" to react with the nanoporous carbon matrix. This definition is useful to perform a semi-quantitative analysis of the oxidizing agents, as shown in table 1.1 where the most common oxidizing agents in pyrotechnic applications are considered.

Table 1.1: Properties of the most common oxidizing agents. The so-called volumetric oxygen balance ($\Omega^V_{CO_2}$) is calculated with equation (1.17) and represents the density of available oxidizing species. [a] TMD : Theoretical Maximal Density [74]. [b] ADN : Ammonium dinitramide.

Oxidizer	Ω_{CO_2} (wt%)	TMD[a] (g/cm^3)	$\Omega^V_{CO_2}$ (g/cm^3)
$NaClO_4$	52.3	2.54	1.33
$KClO_4$	46.2	2.52	1.16
$NaClO_3$	45.1	2.49	1.12
$NaNO_3$	47.1	2.26	1.06
$KClO_3$	39.2	2.34	0.92
KNO_3	39.6	2.11	0.83
NH_4ClO_4	34.0	1.95	0.66
ADN[b]	25.8	1.81	0.47
NH_4NO_3	20.0	1.73	0.34

Not surprisingly, the alkali perchlorate salts are the best candidates to reach acceptable oxygen balances. The chlorate and nitrate alkali salts have quite comparable volumetric oxygen balances, of about one third lower than that of the perchlorate equivalents. In general, the sodium salts have higher volumetric oxygen balances than the potassium salts for the same oxidizing anion, which is related to their denser packing. The ammonium cation leads to a significant decrease of the volumetric oxygen balances, as a result of the lower oxygen balance of these salts and of their lower density with respect to the alkali salts. Finally, ammonium dinitramide (ADN) has also been considered as an example of solid organic oxidizer, but its relatively low oxygen balance and density confer it a volumetric oxygen balance of one third of that of the best inorganic candidate. It has been observed that, for this particular application, not only the oxidizing character of the agent plays a key role, but also its density as the pore volume of the nanoporous materials is limited.

In order to quantitatively evaluate the theoretical feasibility of the concept, the resulting oxygen balance of the composite materials obtained when the nanoporous carbon matrix is filled with an oxidizing agent has been calculated. As a complete filling of the porosity is unlikely, the volumetric filled fraction of the porosity has been considered as a parameter. Figures 1.6a, 1.6b and 1.6c show the resulting oxygen balance to CO_2 in function of the volumetric filled fraction of the porosity for nanoporous carbon with a volume of pore of width smaller than 50 nm equal to 1.0, 1.5 and 2.0 g/cm^3, respectively. For the sake of clarity, only some of the oxidizing agents listed in table 1.1 are shown. The nanoporous carbon is considered as made of pure carbon and the presence of heteroatoms is neglected at this stage. This approach is actually conservative when considering the theoretical feasibility of the concept, as the presence of heteroatoms as O, H, N and S will increase the oxygen balance of the nanoporous carbon matrix.

It can be observed in figure 1.6 that an oxygen balance to CO_2 higher than -75 wt% is achievable in some cases, which means that the concept is theoretically feasible. For nanoporous carbons with a volume of pores of width smaller than 50 nm equal to 1.0 cm^3/g, it can however only be achieved with alkali perchlorate and nitrate salts at very high degree of pore filling. The necessary fraction of pore filling decreases for all oxidizing agent when the pore volume is increased to 1.5 cm^3/g. For a pore volume of 2.0 cm^3/g, low to moderate degrees of pore filling are sufficient to exceed the threshold in terms of oxygen

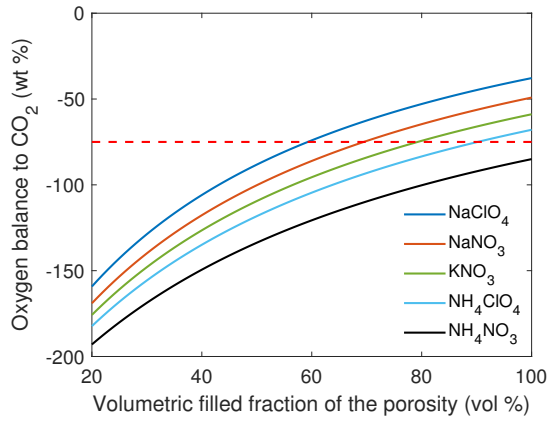

(a) Pore volume of 1.0 cm^3/g.

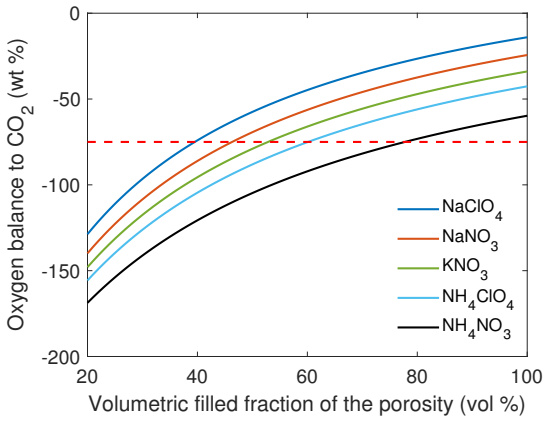

(b) Pore volume of 1.5 cm^3/g.

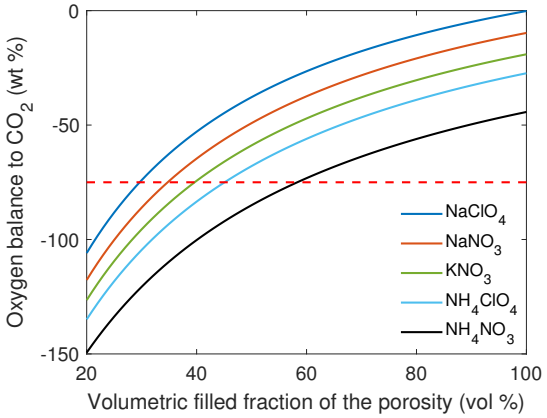

(c) Pore volume of 2.0 cm^3/g.

Figure 1.6: Assessment of the theoretical feasibility of the concept of nanoporous carbon filled with an oxidizing agent as energetic material. The red dashed line represents the minimal requirement of an oxygen balance to CO_2 higher than -75 wt%. Three different volumes of pores of width smaller than 50 nm are shown. The resulting oxygen balance to CO_2 is calculated by considering that density of the oxidizing agent is equal to its theoretical maximal density, in function of the volumetric filled fraction of the porosity.

balance, and stoichiometric mixtures can even be achieved with alkali perchlorate salts at fraction of pore filling close to 100 %.

Even if this analysis is very limited and neglects a lot of practical aspects as the hygroscopicity of the oxidizing salts or the density of the obtained material, it gives some guidance within the scope of the exploration of the considered concept. It can be observed that a pore volume of 1.0 cm^3/g is the minimum level for which the concept is theoretically possible, and that higher pore volumes are preferred. The analysis also shows that relatively high filling rate will have to be achieved, with a minimal objective of about 60 - 80 vol% depending on the porosity. Finally, the alkali perchlorate salts lead to the best theoretical energetic properties and are therefore suitable candidates to investigate the concept.

1.5.3 Scope of present work

Now that the concept of an energetic material made of a nanoporous carbon reducing matrix filled with an oxidizing agent has been shown to be a very promising and novel concept, and that it is theoretically feasible based on nanoporous carbons commercially available or reported in the literature and oxidizing agents commonly used in pyrotechnic applications, the scope of the present work can be defined.

This work is divided in two main parts. The first part consists of developing a synthesis process in order to efficiently fill the porosity of nanoporous carbons with solid oxidizing agents. The experimentally achievable filling rates will then allow the feasibility to be better assessed. However, as described in section 1.1.3, the ability of a composite energetic material to detonate is very difficult to predict as it depends on dynamic phenomena and local features. Therefore the second part of this work consists of experimentally proving the concept by demonstrating the ability of nanoporous carbons filled with an oxidizing agent to detonate and by studying their properties as energetic materials.

Chapter 2

Materials and methods

In this chapter, the materials and the experimental methods used in this PhD thesis are detailed. The chemicals and activated carbons are first described in section 2.1. In section 2.2, the different processes carried out to modify the properties of activated carbons are presented. The different methods used to characterize the porosity, the surface chemistry and the elemental composition of nanoporous carbons are described in sections 2.3 and 2.4. In section 2.5, the different techniques of thermal analysis applied to energetic materials in this work are described. The experimental methods used to determine their sensitivities are detailed in section 2.6. Finally, the details of the experiments performed to characterize the basic detonation properties of these energetic materials are presented in section 2.7.

2.1 Materials

The aqueous solutions are prepared with distilled water and the chemicals listed in table 2.1, and the four commercial activated carbons used in this work are listed in table 2.2.

Table 2.1: Supplier and purity of the chemicals used in this work.

Chemical	Supplier	Purity
Sodium perchlorate (anhydrous)	Acros Organics	$\geq$ 98 wt%
Potassium nitrate	Acros Organics	$\geq$ 99 wt%
Ammonium perchlorate	Fluka	$\geq$ 99.5 wt%
Ammonium nitrate	Acros Organics	$\geq$ 99 wt%

Table 2.2: Supplier and particle size of the commercial activated carbons used in this work.

Activated carbon	Commercial name	Supplier	Form	Particle size
C	C Gran	Cabot Norit	Grains	0.42 - 1.70 mm
F5001	F5001	Blücher	Beads	120 μm
BPL	BPL 12x30	Calgon Carbon Corporation	Grains	0.56 - 1.70 mm
FY5	Filtracarb FY5	CPL activated carbons	Grains	0.21 - 0.71 mm

2.2 Activated carbon modification

2.2.1 Thermal reduction

Activated carbons were reduced by thermal treatment at different temperatures (i.e. 300 and 600 °C) in a flow of inert gas (500 Nml/min N_2) in a horizontal tubular oven. The samples (about 5 g) were first dried at 120 °C under moderate vacuum (1 Pa) to constant mass (mass difference smaller than 0.01 g after 60 minutes). The N_2 flow rate was controlled with a variable area flow meter. The N_2 has a purity higher than 99.9995 vol% and is afterwards filtered by a molecular sieve containing oxygen-removing

catalysts to lower the oxygen and water content to the ppb level. The sample were placed in an alumina crucible in a closed quartz reactor operated under a slight overpressure (10 mbar). After sample insertion and closure, the reactor was flushed with N_2 at 500 Nml/min at room temperature for 60 minutes. The sample was then heated to the treatment temperature at 10 °C/min and kept at this temperature for 60 minutes before being cooled down to 100 °C at 10 °C/min. The oven was then opened, and the samples were allowed to cool to room temperature under inert gas flow before being extracted from the reactor.

2.2.2 Chemical oxidation

Activated carbons were oxidized by chemical wet oxidation treatment with ammonium persulfate or nitric acid solutions. The samples were first dried at 120 °C under moderate vacuum (1 Pa) to constant mass (mass difference smaller than 0.01 g after 60 minutes).

The oxidation with ammonium persulfate was performed by slowly adding 5 g of activated carbon to an acidified aqueous solution of ammonium persulfate prepared by adding 32 g of ammonium persulfate to 50 ml of a solution of H_2SO_4 2 M. The mixture was stirred for 17 hours at room temperature. The solution was then removed by Büchner filtration on a sintered glass filter crucible, and the carbon was rinsed three times with 100 ml of distilled water. The carbon was then transferred to a beaker containing 700 ml of distilled water and the mixture was stirred at 75 °C for 4 hours. The water was then removed by Büchner filtration on a sintered glass filter crucible, and the carbon was rinsed once with 100 ml of distilled water. The neutrality of the filtrate was controlled with pH paper, and the absence of sulphate ion in the filtrate was controlled by observing the absence of precipitation when 1 ml of an acidified $BaCl_2$ solution (25 wt%) is added to 5 ml of filtrate. The carbon was subsequently dried to constant mass, first in a forced convection oven under atmospheric pressure at 120 °C during 2 hours and then at the same temperature under moderate vacuum (1 Pa) to constant mass (mass difference smaller than 0.01 g after 60 minutes).

The oxidation with nitric acid was performed by slowly adding 2 g of activated carbon to 20 ml of an aqueous solution of nitric acid (10 M). The mixture was stirred for 2 hours at room temperature. The solution was then removed by Büchner filtration on a sintered glass filter crucible and the carbon was rinsed with 1000 ml of distilled water. The neutrality of the filtrate was controlled with pH paper. The carbon was subsequently dried to constant mass, first in a forced convection oven under atmospheric pressure at 120 °C during 2 hours and then at the same temperature under moderate vacuum (1 Pa) to constant mass (mass difference smaller than 0.01 g after 60 minutes).

2.2.3 Overactivation

Activated carbons BPL and FY5 were overactivated under CO_2 flow. Before this, the overactivation temperatures were selected by following the guidelines of the literature [75] (see Annex A for details). Temperatures of 875 °C and 840 °C were selected for carbons BPL and FY5, respectively. The samples were first dried at 120 °C under moderate vacuum (1 Pa) to constant mass (mass difference smaller than 0.01 g after 60 minutes).

About 5 g of carbon were placed in a quartz holder provided with a porous frit end and immersed inside a closed quartz jacket; this set-up allows the gas to flow through the bed of carbon. The reactor is operated under a slight overpressure (10 mbar) and placed in a horizontal tubular oven. The reactor is first flushed with N_2 at 500 Nml/min at room temperature for 60 minutes. The N_2 flow rate is controlled with a variable area flow meter. The N_2 has a purity higher than 99.9995 vol% and is afterwards filtered by a molecular sieve containing oxygen-removing catalysts to lower the oxygen and water content to the ppb level. The sample was then heated to the overactivation temperature at 10 °C/min under a 500 Nml/min N_2 flow. When the overactivation temperature was reached, the gas flow was switched to a 10 Nml/min flow of CO_2 (99.99 vol%) during variable periods of time. The CO_2 flow was controlled with a thermal mass flow controller with an accuracy of ± 0.07 Nml/min. Afterwards, the flow was switched back to 500 Nml/min of N_2 during the cooling down step (10 °C/min) up to 100 °C at 10 °C/min. The oven was then opened, and the samples were allowed to cool to room temperature under inert flow before being extracted from the reactor.

2.3 Porosity characterization

2.3.1 Gas adsorption

The micro and mesoporosity of the materials were characterized by means of gas adsorption using an Autosorb iQ manometric instrument (Quantachrome Instruments). This is a well-established technique to characterize the porous structure of nanoporous materials [26].

The onward and converse processes of adsorption are denoted by the terms *adsorption* and *desorption*, respectively. During the desorption phase, the amount adsorbed progressively decreases as the relative pressure of the adsorptive is reduced. The shape of the adsorption/desorption isotherm contains information about the texture of the material (see Annex A).

In this work, adsorption isotherms of N_2 at 77 K, Ar at 87 K and CO_2 at 273 K were measured. About 150 mg of nanoporous carbon was used to perform the analyses; for the filled carbons, the mass of sample was recalculated to have ca. 150 mg of carbon in the analyzed aliquot. The samples were degassed at 120 °C for 17 hours under high vacuum (10^{-3} - 10^{-4} Pa) before being analyzed. The dead volume of the sample holders was measured prior to each analysis with helium gas, and corrections for deviations from ideal gas at cryogenic temperature were applied according to the manufacturer's guidelines. For N_2 and Ar, the saturated vapor pressure of the adsorbate was continuously measured by means of a separated station containing liquid adsorptive dipped in the cryogenic bath. For CO_2, the temperature of the cells was kept to 273 K by means of a bath circulator, and the calculated saturated vapor pressure at this temperature (3.48 MPa [76]) was used. The amount adsorbed was measured at different relative pressures ranging from 10^{-5} to 0.985 for N_2 and Ar, and from 10^{-4} to $3 \cdot 10^{-2}$ for CO_2. The equilibration time was set at 5 minutes and the equilibration criterion defined by the manufacturer used. Thermal transpiration corrections were applied to account for the Knudsen effect at relative pressures lower than 10^{-4}, according to the manufacturer's guidelines.

To characterize the textural properties of nanoporous materials, different post-processing methods and models were applied to the adsorption/desorption isotherm data, following the IUPAC general guidelines on the subject [26]:

- The total pore volume was calculated by expressing the amount adsorbed at the relative pressure of 0.985 as a specific volume. The amount adsorbed is originally determined based on a pressure difference and is expressed as a gas volume in standard conditions of temperature and pressure (STP). To convert this adsorbed amount in a specific volume, it is generally assumed that the pores are filled with the adsorptive at a density corresponding to its liquid density at the analysis temperature (0.806, 1.400 and 1.044 g/cm^3 for N_2, Ar and CO_2, respectively) [26].
- The evaluation of the microporous volume is performed by applying the Dubinin-Radushkevich model of micropore filling [77–79]. This model determines the total mass of adsorbate filling the micropores, and this mass is converted to a microporous volume by using the liquid density of the adsorbate, in the same way as for determination of the total pore volume.
- The modelling of the pore size distribution in the micro and mesoporous range is performed by applying models based on density functional theory (DFT). This method correlates the experimental adsorption/desorption isotherm with a kernel of theoretical isotherms for different pore sizes modelled by DFT [26]. Two kernels provided by the instrument's manufacturer were used. A quenched solid density functional theory (QSDFT) carbon equilibrium kernel based on a slit-pore model [80] is applied to the N_2 and Ar isotherms, and a non-linear density functional theory (NLDFT) carbon equilibrium kernel based on a slit-pore model is applied to the CO_2 isotherms to model the pore size distribution function. Based on this function, the microporous and mesoporous volumes are calculated by interpolation. The same model is applied to the N_2 and Ar isotherms to evaluate the surface area of the adsorbents.

2.3.2 Mercury intrusion

Mercury intrusion is considered as the standard method to characterize the macroporosity of porous materials [79,81]. As mercury is a non-wetting liquid, pressure must be applied to force it into the pores. The volume of mercury intruded in function of the applied pressure is measured. The filling pressure is converted to pore size by applying the Washburn equation (here shown in the case of cylindrical pores):

$$d_p = -\frac{4\gamma}{P}\cos\theta \tag{2.1}$$

where d_p is the pore diameter, γ the surface tension of mercury, P the pressure and θ the contact angle between the solid sample and mercury.

In this work, this method is used to determine the apparent density of the nanoporous carbon particles and their macroporous volume. Generic recommended values [81] for mercury surface tension at 25 °C (484 $mN \cdot m^{-1}$) and contact angle (140°) are used, and independent cylindrical pores are considered. In these conditions, the apparent density was calculated by a gravimetric method at 0.10 MPa, so that the pores of width higher than 14.8 μm were excluded (i.e. considered as part of the external surface). The macroporous volume was determined by measuring the volume of mercury intruded between 0.10 MPa and 29.66 MPa, the latter pressure corresponding to a pore diameter of 50 nm under the considered assumptions.

About 250 mg of nanoporous carbon was used to perform the analysis. If the carbon was filled with an oxidizing agent, the amount of oxidizing agent was taken into account to determine the sample mass so that there was about 250 mg of carbon in the sample. The samples were first dried at 120 °C under moderate vacuum (1 Pa) to constant mass (mass difference smaller than 0.5 mg after 60 minutes) before being analyzed. The analyses were performed with a Pore Master 33 instrument (Quantachrome Instruments) with electronic grade mercury (99.9998 wt%).

This technique has some limitations which should be taken into account to analyze the results. In particular, for disordered materials as activated carbons, the assumption that the porous structure consists of independent cylindrical pores is questionable. Furthermore, the intrusion pressure is governed by the size of the pore entrances and not by the pore size. This can lead to significant deviation in the case of materials with a complex pore network. To intrude the smallest macropores, a high pressure must moreover be applied (around 30 MPa) at which reversible or irreversible structural change may occur by compression or fracture of the material. The latter point is experimentally verified in this work (see Annex B), but the other assumptions remain questionable. The macroporous volume calculated by this method is however useful in comparative studies of materials with similar porosity [81]. In this work, it is therefore only used to compare macroporous volumes of empty and filled nanoporous carbon to estimate the part of the macroporosity filled with an oxidizing agent.

2.4 Surface chemistry and composition

2.4.1 Temperature-programmed desorption

Even if there is no experimental technique that allows a straightforward quantitative analysis of the surface chemistry of nanoporous carbons, temperature-programmed desorption (TPD) is the preferred method for characterizing the oxygen functional groups on microporous carbons [82]. All the oxygen-containing surface groups are decomposed upon heating under an inert atmosphere, releasing CO and/or CO_2 at different temperatures. The nature of the groups is evaluated based on their decomposition temperature and the type of gas released (as shown in figure 2.1), and the amounts can be quantified based on the areas of the peaks [83]. The major difficulty of this technique consists of identifying each surface groups, as the spectra show overlapping of peaks, which must therefore be deconvoluted. As the decomposition peaks result of a random distribution of binding energies of the functional groups, they are well described by Gaussian functions [82, 83].

In this work, the gases released by the decomposition of the oxygen-containing surface groups (e.g. CO, CO_2 and H_2O) are measured by a mass spectrometer (GSD 301 T ThermoStar, Pfeiffer Vacuum) coupled to a thermogravimetric analyser (TGA/DSC 3+, Mettler Toledo). The mass spectrometer is equipped with an electron ionisation source, a quadrupole mass analyser, and a secondary electron multiplier detector. The thermogravimetric analysis (TGA) is performed in the same way as described in section 2.5.2, excepted that the samples were not crushed, that 70 μl alumina crucibles (supplied by Mettler Toledo) are used and that the heating rate is set at 10 K/min. After the sample insertion, the TGA furnace is first flushed with Ar at 70 Nml/min for 50 minutes at room temperature to avoid interference with atmospheric N_2, CO and CO_2 during the measurement. The baseline of the signals is determined by using the last 10 minutes of the flushing step. As this technique is only applied on non-energetic materials, sample masses ranging from 10 to 15 mg were used, corresponding to crucibles approximately filled to half height.

The determination of the nature of the decomposed functional groups is performed by following the guidelines of the literature [82, 83].

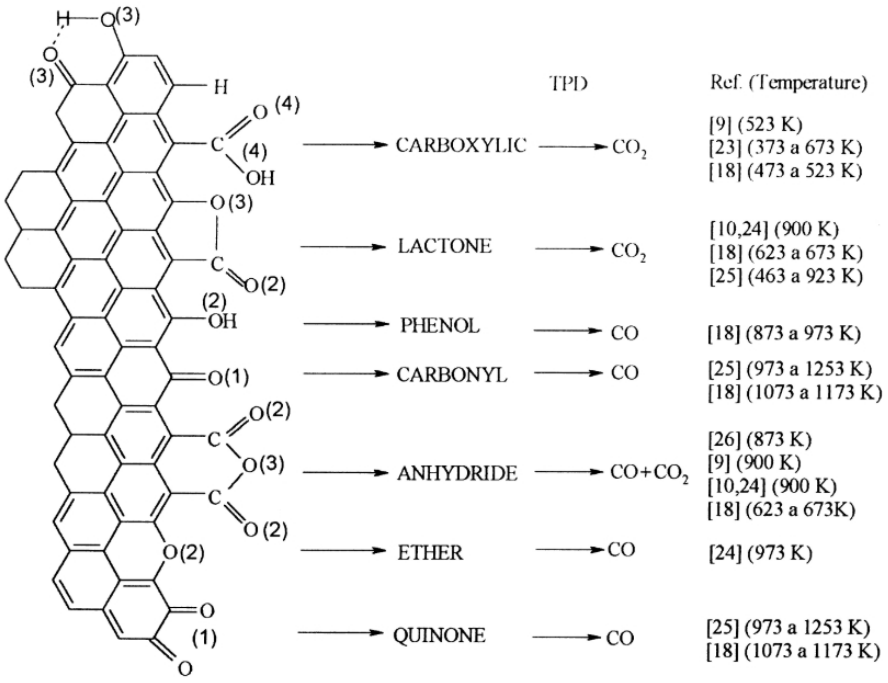

Figure 2.1: Decomposition temperatures of the oxygen-containing functional groups on a carbon surface [83].

2.4.2 Elemental analysis

Elemental analysis is used to determine the total amount (wt%) of carbon (C), oxygen (O), hydrogen (H), nitrogen (N) and sulfur (S). This analytical technique is based on the complete combustion of a sample applying a thermal treatment at high temperature, about 950 °C, in a stream of oxygen. The combustion products (commonly CO_2, H_2O, N_2 and SO_2) are measured generally using infrared spectroscopy. In the case of the determination of the oxygen content, the sample is heated up to 1070 °C under inert atmosphere, releasing different gas molecules (CO, CO_2, H_2O). This gas mixture is passed through a bed of graphite powder to reduce them to CO, then, CO is oxidized to CO_2 in a CuO catalyst, and it is detected by a chatarometric detector. In this work, the determination of C, H, N, S and O contents was carried out by an analyser (Thermo Scientific Flash 2000). For comparative purposes and to eliminate the moisture, all the samples were previously dried under primary vacuum at 60 °C for 24 h.

2.4.3 Ash content

The ash content of the carbons was determined by a gravimetric method after pyrolysis at 1000 °C for 1 h in air. About 1 g of carbon was used, and the samples were first dried at 120 °C under moderate vacuum (1 Pa) to constant mass (mass difference smaller than 0.01 g after 60 minutes).

2.5 Thermal properties

2.5.1 Differential scanning calorimetry

The differential scanning calorimetry (DSC) is a method widely used to characterize the thermal properties of energetic materials. This technique measures the difference between the heat flow to an inert reference and the heat flow to the sample while the temperature is controlled. A signal is measured that is directly proportional to the difference between the heat input to the sample and that of the reference [84]. This signal is converted to power by a calibration based on a known phase transition of reference materials (typically the melting point of pure metals). Any phase transition or decomposition reaction that has either an exothermic or an endothermic character is recorded. In this work, the thermodynamic convention of sign is followed, i.e. the exothermic phenomena correspond to negative peaks.

The general NATO guidelines about the thermal characterization of energetic materials [84] were followed. The analyses were performed on a Q20 DSC (TA Instruments) equipped with a refrigerated cooling system RCS90 (TA Instruments). Calibration was performed based on the melting point of pure indium and zinc pills (supplied by Mettler Toledo) and baseline corrections applied, according to the manufacturer's guidelines. About 1 g of the material to be analyzed was dried at 120 °C under moderate vacuum (1 Pa) to constant mass (mass difference smaller than 0.5 mg after 60 minutes), and subsequently finely crushed with a mortar and pestle to achieve good thermal contact between the sample and the crucibles. The sample mass was measured with a XPR2U/M microbalance (Mettler Toledo) with a readability of 0.1 μg. Sample mass of about 1 mg was used to prevent overheating of the energetic samples and leaking of the crucibles. 30 μl hermetically sealed stainless steel crucibles closed with a gold-plated sealing pan (both supplied by Mettler Toledo) were used. After each analysis, the sealing of the crucibles was controlled according to the manufacturer's guidelines (i.e., a mass loss smaller than 50 μg during the experiment). The analyses were performed at a heating rate of 2 K/min. It was observed that the empty crucible mass follows a normal distribution with a mean of 610.26 mg and a standard deviation of 6.00 mg (based on 82 sample points). With respect to the energetic sample mass (around 1 mg), the mass dispersion of the crucible is significant. A manual baseline correction is therefore applied to account for the heat capacity of stainless steel, owing to the mass difference between the reference crucible and the sample empty crucible. The onset temperature is measured as the point of intersection of a tangent line drawn to the curve before the beginning of the decomposition and another tangent line drawn to a point on the steepest part of the decomposition peak [84]. The peak temperature is also reported. The heat of decomposition is calculated by numerical integration of the signal by using a sigmoid baseline.

2.5.2 Thermogravimetric analysis

The thermogravimetric analysis (TGA) is also a widely used technique to investigate the thermal properties of energetic materials. This method measures the evolution of the sample mass while it is heated in a controlled atmosphere. The decomposition reactions, the reaction with the atmosphere, and the phase transitions can be recorded if they lead to a mass loss or a mass gain. In this work, this technique is used to study decomposition reactions leading to mass losses as gases are evolved.

The general NATO guidelines about the thermal characterization of energetic materials [84] were followed. The analyses were performed with a TGA/DSC 3+ (Mettler Toledo). The calibration was performed based on the melting point of pure indium and zinc pills (supplied by Mettler Toledo), according to the manufacturer's guidelines. Prior to each run, a blank was measured in the same conditions as the analyses to correct for buoyancy. The blank curve was directly subtracted from the measured curves. The samples were prepared by following the same method as for DSC experiments (see section 2.5.1). 100 μl aluminum crucibles (supplied by Mettler Toledo) were used. The purge gas is Ar (99.9995 vol%) at a flow rate of 70 Nml/min. The purge gas is filtered by a molecular sieve containing oxygen-removing catalysts to lower the oxygen and water content to the ppb level. The same gas is used a balance protective gas at a flow rate of 20 Nml/min. As an autosampler was used and some nanoporous carbons and oxidizing agents are hygroscopic, significant water intakes could occur during the waiting times between the different analyses. To prevent any influence on the results, the samples were dried again in the instrument just after their insertion at 120 °C under the purge gas flow during minimum 5 minutes and until a constant mass was reached. The analyses were performed at a heating rate of 2 K/min. As the instrument is equipped with thermocouples on the sample holder, this temperature is used as the sample temperature in the analysis. This is more accurate and allows the absence of overheating to be controlled. The differential thermogravimetric analysis (DTG) is calculated by numerical derivation of the TGA data. The TGA data are first numerically smoothed by using a Gaussian-weighted moving average over windows of 500 s or 16.7 K (sampling rate is 1 s^{-1}). The derivative is then calculated by applying a first-order divided difference method.

2.5.3 Kinetic analysis

The Kissinger method for kinetic analysis [85] was used, as it is one of the most widely used method for estimating the kinetic parameters of energetic materials [84, 86]. As comparable non-isothermal techniques, the Kissinger method relies on a series of experiments performed at different heating rates by using thermal analysis techniques as DSC or TGA. In this work, the TGA method was used, as the dispersion of peak temperatures between replicated analyses is generally significantly lower than in DSC. The method assumes that the rate constant of the reaction follows an Arrhenius equation, that

decomposition is a first order reaction, and that the pre-exponential factor and the activation energy are constant and independent of the extent of the reaction. Under these assumptions, the following equation can be expressed:

$$\ln\left(\frac{\beta}{T_m^2}\right) = \ln\left(\frac{AR}{E_a}\right) - \frac{E_a}{RT_m} \tag{2.2}$$

where β is the heating rate, T_m is the peak temperature, A and E_a the pre-exponential factor and the activation energy of the Arrhenius equation, respectively, and R the universal gas constant. The Kissinger method is usually applied by plotting $\ln\left(\frac{\beta}{T_m^2}\right)$ in function of $\frac{1}{T_m}$, which allows the values of A and E_a to be calculated by linear regression.

This method has the advantages of being very simple and of leading to single values of kinetic parameters that can be easily compared between materials. More complex methods, as the differential isoconversional method of Friedman [87], may be applied to perform kinetic analysis without having to assume that the pre-exponential factor and the activation energy are independent of the extent of the reaction and that the decomposition is a first order reaction. This method is generally considered as more suitable for complex decomposition reaction involving multiple elementary mechanisms, but leads to a more complex set of results as A and E_a are expressed in function of the extent of the reaction. Furthermore, all methods of kinetic analysis have intrinsic limitations, as they are only strictly valid in the measured range of extent of reaction and in the temperature interval of the analysis. For comparison purposes and while keeping in mind its limitations, the Kissinger method is therefore considered as suitable in this work.

In this work, 17 TGA experiments at 5 different heating rates (2 at 0.5 K/min, 2 at 1.0 K/min, 3 at 2.0 K/min, 4 at 4.0 K/min and 6 at 7.0 K/min) were performed on each material to analyze its decomposition kinetics. The heating rates were selected according to the NATO guidelines [84] that recommend trying to achieve a 10-fold variation of the heating rate. At the maximum heating rate of 7.0 K/min, no sign of overheating was detected by calculating the derivative of the sample temperature with respect to the time. At the minimum heating rate of 0.5 K/min, it was still possible to precisely identify the peak temperature. The experiments were repeated and the mean values of the peak temperature used at each heating rate in equation (2.2). The TGA experiments were performed by following the method described in section 2.5.2, where only the heating rate is adapted.

2.6 Sensitivities

2.6.1 Impact sensitivity

The impact sensitivity of energetic materials is measured by dropping a weight of known mass onto a sample of energetic material, following the procedure of the related European Standard [88]. The used apparatus is a BAM fall-hammer (Reichel und Partner GmbH), as schematically shown in figure 2.2.

The materials were finely crushed with a mortar and pestle in order to pass through a sieve with an aperture size of 0.5 mm. A sample volume of 40 mm^3 is used for each test and inserted between the two steel cylinders shown in figure 2.2. According to the standard [88], weights of 1, 5 and 10 kg are used and dropped from heights ranging from 10 to 60 cm in order to achieve impact energy ranging from 1 to 50 J in a series of discrete steps described in the standard [88]. When the weight is released on the sample with a given impact energy, the behavior of the sample is observed and classified as reaction (occurrence of report or flame) or no reaction. The impact sensitivity is defined as the lowest impact energy at which a reaction is observed at least once out of six trials [88].

2.6.2 Friction sensitivity

The friction sensitivity of energetic materials is measured by placing a sample of energetic material on a porcelain plate, pressing a porcelain peg onto the sample under a specific load and moving the plate to apply a friction stimulus to the sample. The procedure of the related European Standard [89] is followed. The used apparatus is a BAM friction apparatus (Reichel und Partner GmbH), as schematically shown in figure 2.3.

The materials were finely crushed with a mortar and pestle in order to pass through a sieve with an aperture size of 0.5 mm. A sample volume of 10 mm^3 is used for each test and placed under the porcelain peg on the porcelain plate, as shown in figure 2.3. According to the standard [89], loads ranging from 5 to 360 N are applied on the sample in a series of discrete steps described in the standard [89]. When

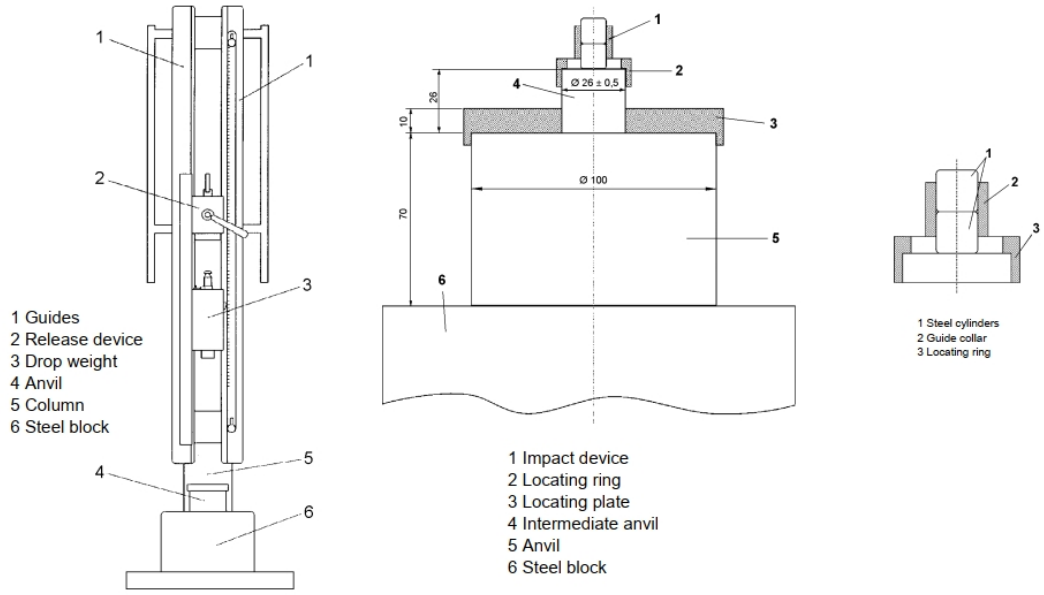

Figure 2.2: Schematic representation of the BAM fall-hammer apparatus for determination of the impact sensitivity of energetic materials [88].

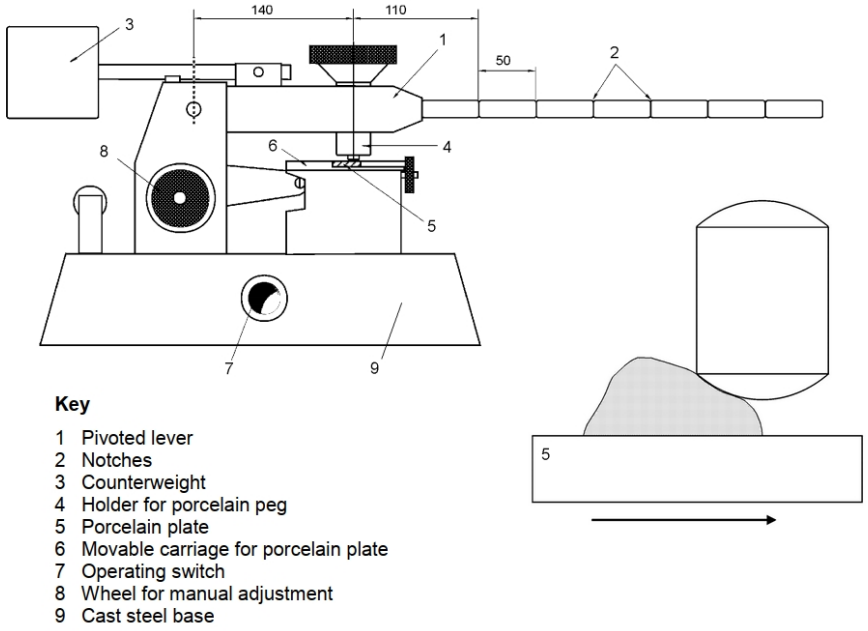

Figure 2.3: Schematic representation of the BAM friction apparatus for determination of the impact sensitivity of energetic materials [88].

the porcelain plate is moved and a friction stimulus applied to the sample, its behavior is observed and classified as reaction (occurrence of report, crackling, sparking or flame) or no reaction. The friction sensitivity is defined as the lowest load at which a reaction is observed at least once out of six trials [89].

2.6.3 Temperature of ignition

The temperature of ignition is measured by heating small quantities of energetic materials at 5 °C/min until an event occurs. The guidelines of the NATO standard about thermal sensitiveness [90] are followed to determine the temperature of ignition. 200 mg of the test material are loaded into glass tubes and

inserted into a heat sink (Reichel und Partner GmbH), the temperature of which is controlled so that it increases from 100 °C to 400 °C at 5 °C/min. The ignition temperature is determined as the temperature at which a reaction occurs. Reaction can take the form of burning with a flame, rapid decomposition or explosion, and are accordingly described as decomposition, ignition, explosion or detonation.

2.7 Detonation properties

Excepted the few experiments performed on bare oxidizing agent and physical mixtures described in Annex I where an additional booster of Comp C-4 was used, all the charges were only initiated by a standard military detonator (E-1 electric detonator supplied by Expal) placed in direct contact with the charge. This detonator has an external diameter of 7.5 mm, a thin aluminum case, and contains a secondary charge made of 0.75 g of PETN (No 8 standard detonator).

The composite energetic material was first finely crushed with a mortar and pestle, and then shaped into steel tubes either by pressing with a hydraulic press or loosely. In the latter case, a sieve shaker was used to vibrate the charge in order to reach a reproducible tapped density. The material was in both cases loaded in the tubes in steps in order to achieve a homogeneous density.

2.7.1 Indent depth

To measure the indent depth, the tubes filled with the composite energetic material were placed on a witness plate made of Al 6082 T651 alloy. For charge diameter up to 10 mm, a 1 cm thick plate was used. For larger diameter, a 3 cm thick plate was used. After the initiation, the depth of the indent is measured with a digital depth micrometer with an accuracy of 10 μm.

2.7.2 Velocity of detonation

Detonation velocities are determined by measuring the arrival times of a detonation wave at 8 different points in a high explosive charge with an Optimex 64 instrument (OZM Research). The probes are passive optical fibres placed in blind holes drilled in the steel tube walls. A light signal is emitted when air is ionized as the shock wave generated in the steel walls by the detonation of the adjacent explosive reaches the bottom of the hole. This light signal is transmitted to the instrument by means of glass optical fibres and sampled at 250 MHz. The relative arrival times are then measured by determining the times at which a steep rise of the light signal is observed. The holes are precisely machined, with an accuracy on the axial distances of $\pm$ 50 μm. The first hole is located at an axial distance from the initiation point equal to three times the diameter of the charge, and the other holes are equally spaced on four times the diameter of the charge. The detailed plans of the tubes are shown in annex A. An example of the experimental set-up (without the detonator, later placed on the top of the charge) is shown in figure 2.4. The velocity of detonation is calculated by linear regression, as the slope of the known relative distances in function of the measured arrival times. Examples of recorded light signal and linear regression performed to determine the velocity of detonation are shown in Annex A.

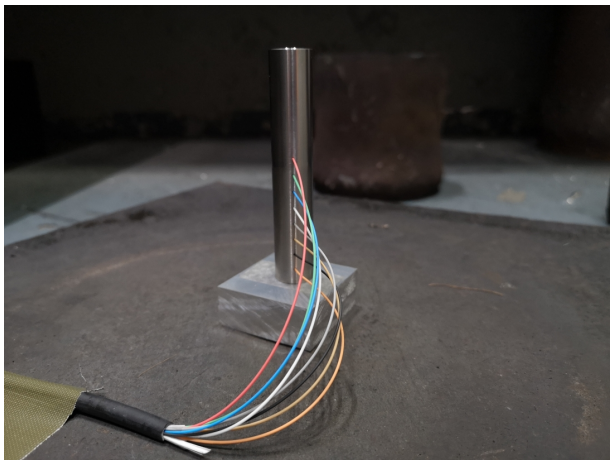

Figure 2.4: Example of the experimental set-up used to measure the velocity of detonation of a charge confined in a steel tube.

Chapter 3

Pore filling process development

In this chapter, the different steps of the development of the pore filling process are presented. The process is first described in details in section 3.1. In section 3.2, the properties of the different nanoporous carbons used in this work to analyze the influence of the properties of the carbon materials on the pore filling process are presented. The methodology used to characterize the efficiency of this process is then described in section 3.3. The influence of the main process parameters is evaluated in section 3.4. The effect of the properties of the nanoporous carbons on the efficiency of the pore filling process is discussed in section 3.5, and partial conclusions (section 3.6) complete the chapter.

3.1 Process description

3.1.1 Generalities

As discussed in section 1.5.2 about the theoretical feasibility of the use of nanoporous carbon filled with an oxidizing agent as potential energetic material, a minimal degree of pore filling of 60 to 80 vol% is required for practical applications. Furthermore, only the micro- and the mesopores must be filled, and it must be avoided that oxidizing agents crystallize in large macropores and on the surface of the carbon particles. This constraint arises from the considerations described in section 1.1.3 about the key role played by the decomposition kinetics in the detonation process. The concept of this work relies on the principle that the decomposition will be significantly faster when the oxidizing and the reducing agent are mixed at the nanometer scale in nanopores. As the decomposition of oxidizing particles on the surface or in the large macropore is therefore expected to be significantly slower, a part of the detonation energy would be used to compress these oxidizing particles but their decomposition would not be fast enough to contribute to the shock compression of the adjacent material which drives the shock front forward. At the time scale of the shock front, this can be considered as an energy loss which may prevent the detonation wave from being sustained in the material. It is interesting to note that this constraint does not apply to static characterization of energetic materials, and was therefore not discussed in the other attempts to fill nanoporous materials with oxidizing agents that are described in section 1.4.

As the considered oxidizing agents are solids at room temperature, they must either be molten or solubilized before being able to infiltrate the carbon porosity. However, the liquid form of the oxidizing agents listed in table 1.1 is not stable enough for this use as their decomposition takes place shortly after melting or even simultaneously [2]. The use of a liquid solution is therefore preferred. Once the liquid solution has been infiltrated in the porosity, a supersaturation state is generated in order to lead to the crystallization of the oxidizing agent in the pores. This supersaturation can be generated by different methods, as by evaporating the solvent, cooling the solution, adding an antisolvent, adding another salt to use the common ion effect, etc. All the methods of crystallisation engineering could actually be used. There are however important differences with regular crystallization. On the one hand, homogeneous nucleation and heterogeneous nucleation on the surface or in the macropores must be avoided. On the other hand, the nanoporous structure of the material makes it necessary to allow the oxidizing substances to diffuse into the porous network to the smallest pores. From a kinetic point of view, these two constraints are actually in conflict as giving more time to the solution to diffuse through the porous network will increase the nucleation probability.

Within the scope of this work and as described in the preliminary feasibility study (see section 1.5.2), the oxidizing character but also the density of the oxidizing agents play a key role, and the oxidizer agent

must be solid to prevent compatibility and safety issues. Only oxidizing salts are therefore considered in this first investigation of the concept. It seems reasonable to assume that it will be easier to achieve a higher degree of pore filling if the concentration of the infiltrated solution of oxidizing salt is very high. Most of the oxidizing salts described in table 1.1 present high solubility in water and/or in dimethyl sulfoxide (DMSO). This latter solvent is however very difficult to remove because of its high boiling point, and thus has not been investigated in this work. As sodium perchlorate has been identified as the best of these candidates in section 1.5.2, and because of its very high solubility in water (66 wt% at 20 °C [76]), most of the preliminary work on the pore filling process is performed with this salt.

3.1.2 Failed attempts and lessons identified

In the very first stage of the development of the pore filling process, the pore volume was infiltrated with a saturated solution of oxidizing salt (in this case KNO_3 and $NaClO_4$), and a supersaturation was generated by different methods: water was very slowly evaporated; methanol as antisolvent was gradually added to the solution; the solution was progressively cooled to decrease the solubility of the salt; and in the case of a solution of $NaClO_4$, a KNO_3 solution was added to crystallize $KClO_4$ by counter-ion effect. In all cases, homogeneous nucleation and/or heterogeneous nucleation on the surface or at the meniscus was however observed. A surfactant (didodecyldimethylammonium bromide) was also added to the saturated solutions to try to prevent heterogeneous nucleation, without noticeable effect. These first attempts have demonstrated that the conflicting constraints related to the diffusion in the porous network and the heterogeneous nucleation on the surface are very difficult to conciliate. A proposed solution then consists in circumventing this issue by first removing the aqueous solution from the interstitial space and from the macropores by filtration before generating a supersaturation, in order to force the salt to crystallize in the micro- and the mesopores. Such a controlled filtration is however not simple, and the yield of the process would be quite low, as the porosity is initially filled with the aqueous solution. For instance, if the porosity was filled with a saturated aqueous solution of sodium perchlorate at room temperature, which has a density of about 1.7 g/cm^3, a maximal degree of micro and mesopores filling of about 45 vol% could be achieved. This does not allow the defined objectives to be met. It could be possible to achieve a higher degree of pore filling by infiltrating a solution saturated at a higher temperature, but this is practically very difficult as any cold spot will lead to very fast heterogeneous nucleation.

3.1.3 Pore filling by crystallization after solution contraction upon drying

Based on the lessons identified from the failed attempts and in order to achieve a high degree of pore filling, a pore filling process by crystallization after solution contraction upon drying has been developed in this work. To the best of our knowledge, it has not been described elsewhere. This process consists of three subsequent steps:

1. An **infiltration step**, during which a concentrated aqueous solution of oxidizing agent is infiltrated in the porosity of the nanoporous carbon at room temperature. The solution is in excess, so that the interstitial space between the nanoporous carbon particles is filled as well. The mixture is then stirred for some time to allow the aqueous solution to fill all the accessible porosity. As the considered aqueous solutions have a strong ionic character (e.g., a saturated solution of sodium perchlorate at 20 °C has a ionic strength of 16 mol/kg [76]), its diffusion through the porous network is supposed to be relatively slow as the carbon materials are globally hydrophobic. After this step, the micro-, the meso- and the macropores are filled with a concentrated solution of oxidizing agent, as well as the interstitial space.
2. A **controlled filtration step**, during which most of the interstitial solution is removed by vacuum filtration. The purpose of this step is to keep the micro-, meso- and macropores filled with the solution, and to form a surface film of controlled thickness on the particles. The thickness of this surface film and the degree of filling of the macropores are mainly governed by the viscosity of the solution, the granulometry of the nanoporous carbons, the air superficial velocity through the bed and the filtration time.
3. A **controlled drying step**, during which the solvent is progressively evaporated by heating the mixture on a controlled manner. When the temperature is increased, the solvent evaporates, but the solubility also increases. The solution therefore contracts as its density becomes higher, without supersaturation. The solution then continuously contracts upon drying, until a saturated solution at elevated temperature fills the micro- and the mesoporosity of the material. It is assumed that the solution will preferentially fill the smallest pores upon contraction because of the capillary effect. Evaporation leads finally to a supersaturation and to the crystallization of the salt in the micro- and

mesopores. The parameters of the process must be tailored so that a supersaturation is generated precisely when the solution fills the micro- and the mesoporosity.

This approach is supposed to allow a high degree of pore filling to be achieved while avoiding to have to handle saturated solution at elevated temperature and while preventing homogeneous and heterogeneous nucleation outside of the micro- and the mesopores. The macropores and the surface film act as a reservoir during solution contraction upon drying, in order to increase the achievable filling rate. The whole process relies on the assumption that the aqueous solution will preferentially fill the micro- and the mesopores upon contraction because of capillarity.

In the first attempts to apply this method, the carbon was filtered on a cellulose filter paper, and subsequently dried directly on the filter placed on a watch glass. This method was applied within the scope of the publication related to this PhD thesis [91]. The results obtained by this method were however not reproducible and difficult to interpretate. It appeared that this was related to the hydrophilic character of the filter, as the solution was "pumped" out of the carbon particles by capillarity. In the present work, the drying is performed in fritted glass crucibles and the wet carbon is then transferred to a PTFE beaker to prevent any capillary effect.

3.2 Pristine nanoporous carbons and derivatives

Even if carbon materials and some nanoporous carbons were used in energetic materials in the past and are investigated in current works (see section 1.3), there is no clear trend about the desirable physicochemical properties of nanoporous carbons that emerges for the application considered in this work. Nanoporous carbons with different textural properties and surface chemistry are therefore used in order to cover a broad spectrum of physicochemical properties.

The physicochemical properties of the pristine carbons and their derivatives studied to investigate the pore filling process are summarized in the following sections and detailed in Annex C. The origin of the pristine materials and the modification methods are detailed in chapter 2.

3.2.1 C and derivatives

Carbon C is an activated carbon obtained by chemical activation of wood with H_3PO_4 at 550 °C [92]. It has a large micro- and mesoporous volume and its surface presents a large amount of oxygen-containing functional groups. In this work, the pristine carbon C and its derivatives resulting from a thermal treatment to promote a gradual de-functionalization are used to highlight the influence of the surface chemistry on the pore filling process. Thermal treatment is performed at 300 and 600 °C to obtain the carbons C-R300 and C-R600, respectively. The N_2 adsorption isotherms and the modelled pore size distribution of these carbons are shown in figures 3.1 and 3.2. Their textural properties are summarized in table 3.1, and the results of the TPDMS analysis are shown in figure 3.3.

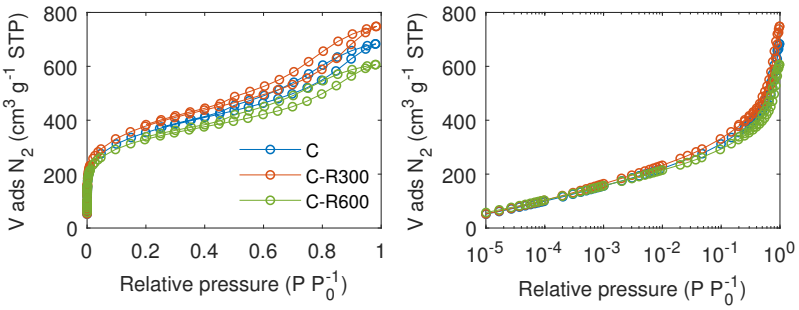

Figure 3.1: N_2 adsorption isotherm measured at 77 K of carbon C and its derivatives obtained by thermal treatment.

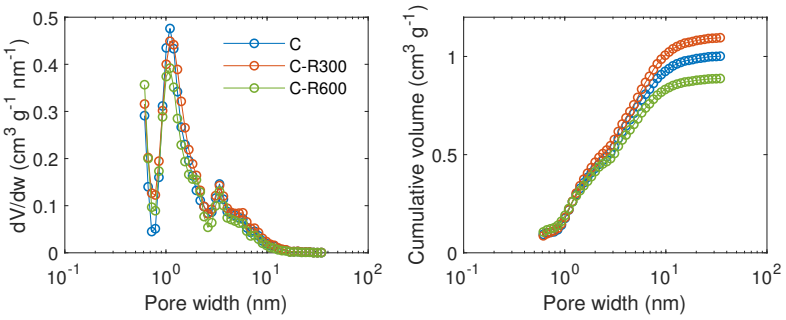

Figure 3.2: Pore size distribution modelled by QSDFT based on N_2 isotherm of carbon C and its derivatives obtained by thermal treatment.

Table 3.1: Selected properties of carbon C and its derivatives obtained by thermal treatment; (a) total pore volume at $P/P_0 = 0.985$; (b) by equilibrium QSDFT model; (c) by DR model; (d) based on MIP data.

Carbon	C	C-R300	C-R600
TPV^a (cm^3/g)	1.06	1.16	0.94
Surface area^b (m^2/g)	1160	1215	1131
V^b_{micro} (cm^3/g)	0.43	0.46	0.41
W^c_0 (cm^3/g)	0.44	0.45	0.40
V^b_{meso} (cm^3/g)	0.57	0.63	0.47
V^d_{macro} (cm^3/g)	0.67	0.93	0.78
Apparent density^d (g/cm^3)	0.41	0.40	0.46

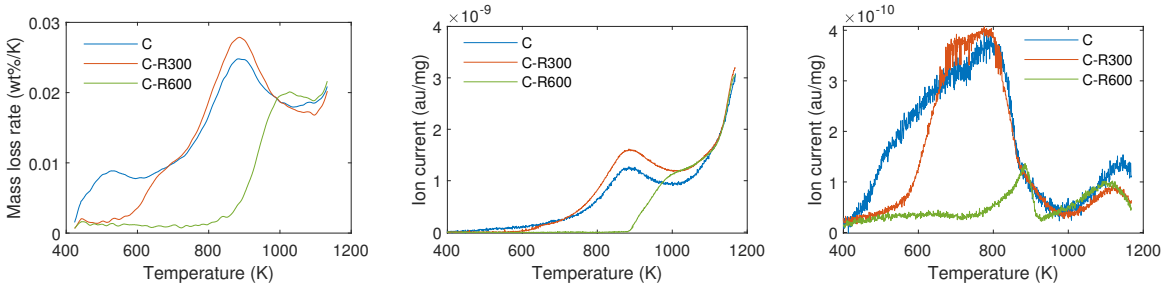

(a) DTG. (b) CO profile. (c) CO_2 profile.

Figure 3.3: TPDMS analysis of carbon C and its derivatives obtained by thermal treatment.

These results show that the textural properties of the carbon C are mostly preserved during its thermal reduction at 300 and 600 °C, while the thermal treatment efficiently modified its surface chemistry, as reflected by the change in the DTG curve, and CO and CO_2 profile, as shown in figure 3.3. Pristine carbon C has a relatively high oxygen content (7.5 wt%) and the TPDMS analysis (see details in Annex C) has shown that carboxylic acid, carbonyl (decomposed in α-substituted ketone and aldehyde), carboxylic anhydride, phenol and carbonyl/quinone functional groups are present on its surface. The sharp increase of the amount of CO evolved from 700 °C and the corresponding CO_2 peak are attributed to the decomposition of volatiles. It is likely that the decomposition of volatiles interferes with the evolution of CO and CO_2 resulting from the decomposition of functional groups usually observed at high temperatures, such as lactones and carbonyl/quinones. Hence the quantification of the amount of carbonyl/quinone functional group is difficult. For the same reason, the absence of lactone groups on the surface must be nuanced, as a small amount could be present. Upon heat treatment at 300 °C, the oxygen content slightly decreases to 6.6 wt%, and the amount of carboxylic acid and carbonyl functional groups is significantly reduced (by approximately 30 and 50 %, respectively), while the amount of other functional groups remains unchanged. This is in line with the TPDMS analysis of carbon C, where only two low temperature peaks attributed to carboxylic acid and carbonyl (decomposed in α-substituted ketone and aldehyde)

have a component below 300 °C. When the heat treatment is carried out at 600 °C, the oxygen content drops to 4.6 wt% and much more functional groups are affected. The carboxylic acid and the carbonyl (decomposed in α-substituted ketone and aldehyde) functional groups are removed from the surface, and the amount of carboxylic anhydride and phenol groups is significantly reduced (by approximately 20 and 30 %, respectively) while the amount of carbonyl/quinone groups remains unchanged. This corresponds to the TPDMS analysis of the pristine carbon C, where only the peak attributed to the carbonyl/quinone functional groups has no component below 600 °C. The desired effect of the treatment has therefore been achieved, since the surface chemistry of the carbon C has been extensively modified by the thermal treatment without significantly affecting its textural properties.

3.2.2 F5001 and derivatives

Carbon F5001 is an activated carbon obtained by physical activation of synthetic polymer [93]. It has a very large micro- and mesoporous volume and has a very low oxygen content. In this work, the pristine carbon F5001 and its derivatives resulting from chemical oxidation are used to highlight the influence of the surface chemistry on the pore filling process. Chemical oxidation is performed with ammonium persulfate (APS) aqueous solution and concentrated nitric acid to obtain the carbons F5001-APS and F5001-HN, respectively. The N_2 adsorption isotherms and the modelled pore size distribution of these carbons are shown in figures 3.4 and 3.5. Their textural properties are summarized in table 3.2, and the results of the TPDMS analysis are shown in figure 3.6.

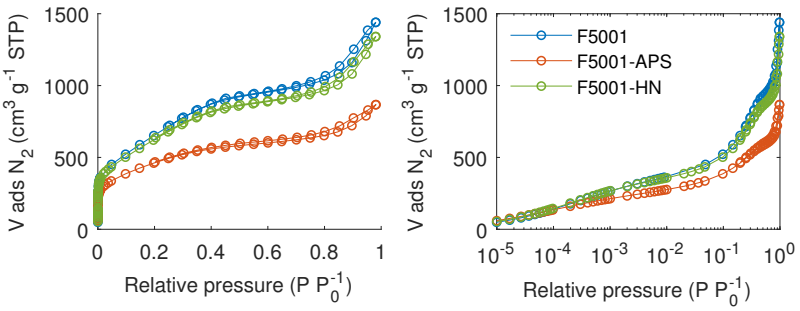

Figure 3.4: N_2 adsorption isotherm measured at 77 K of carbon F5001 and its derivatives obtained by chemical oxidation.

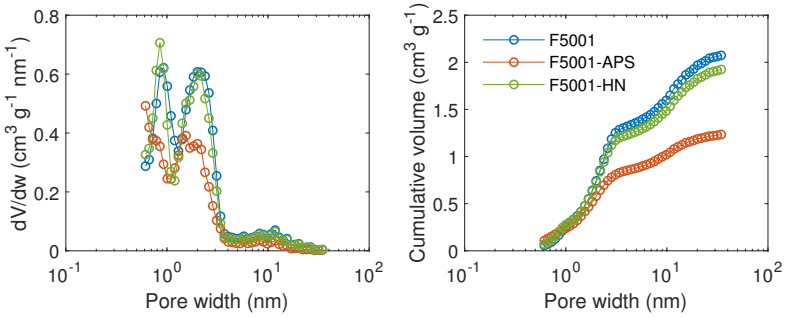

Figure 3.5: Pore size distribution modelled by QSDFT based on N_2 isotherm of carbon F5001 and its derivatives obtained by chemical oxidation.

Table 3.2: Selected properties of carbon F5001 and its derivatives obtained by chemical oxidation; (a) total pore volume at $P/P_0 = 0.985$; (b) by equilibrium QSDFT model; (c) by DR model; (d) based on MIP data.

Carbon	F5001	F5001-APS	F5001-HN
TPV^a (cm^3/g)	2.23	1.34	2.07
Surface area^b (m^2/g)	1890	1258	1850
V^b_{micro} (cm^3/g)	0.74	0.58	0.73
W^c_0 (cm^3/g)	0.99	0.63	0.96
V^b_{meso} (cm^3/g)	1.33	0.65	1.19
V^d_{macro} (cm^3/g)	0.43	0.21	0.37
Apparent density^d (g/cm^3)	0.37	0.61	0.41

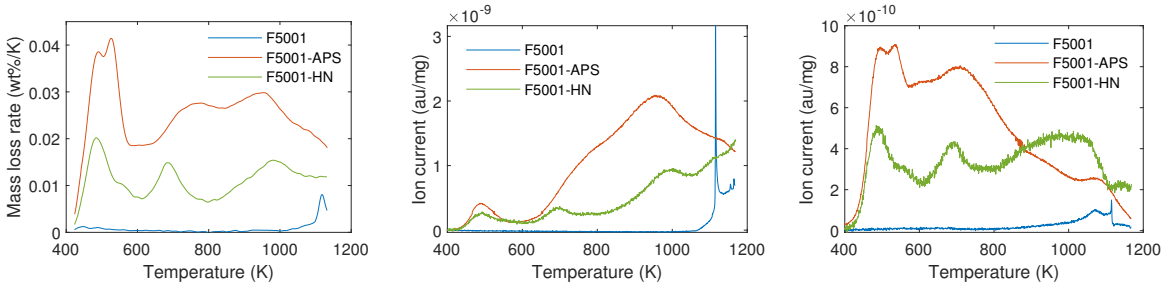

(a) DTG. (b) CO profile. (c) CO_2 profile.

Figure 3.6: TPDMS analysis of carbon F5001 and its derivatives obtained by chemical oxidation.

These results show that the textural properties of the carbon F5001 are mostly preserved during the chemical oxidation with nitric acid, while the porosity is significantly reduced (by 40 %, based on the TPV) by the chemical oxidation with ammonium persulfate. Whereas pristine carbon F5001 has a very low oxygen content (1.6 wt%), the oxidization leads to significantly higher amounts of 14.8 wt% for carbon F5001-APS and 4.5 wt% for carbon F5001-HN. The strong oxidation of the carbon F5001-APS is likely to have led to the blocking of a part of the porosity of the pristine carbon. The difference in oxygen content is also reflected by the observed differences in the DTG curves, and CO and CO_2 profiles in figure 3.6. The TPDMS analysis (see details in Annex C) has shown that carbons F5001-APS and F5001-HN contain functional groups of the same nature (i.e., carboxylic acid, carbonyl, carboxylic anhydride, phenol, lactone and quinone), whereas the difference between the carbons lies in the amount of these functional groups. Carbon F5001-APS presents significantly more carboxylic acid and phenol groups (2 and 2.5 times more, respectively), and significantly less lactone (1.5 times less) than carbon F5001-HN, while the amounts of the other functional groups are comparable. For carbon F5001-HN, the desired effect of the treatment has therefore been achieved, since a significant amount of oxygen-containing groups have been added to the surface without significantly affecting the textural properties of the carbon.

3.2.3 BPL and derivatives

Carbon BPL is an activated carbon obtained by physical activation of bituminous coal [93]. It has a large microporous volume and a very small mesoporous volume, and presents a moderate amount of oxygen-containing functional groups on its surface. In this work, the pristine carbon BPL and its derivatives resulting from CO_2 overactivation are used to highlight the influence of the textural properties on the synthesis process. Overactivation is performed during different times to obtain carbons BPL-18 and BPL-37 with burn-off ratios of 18 and 37 wt%, respectively. The N_2 adsorption isotherms and the modelled pore size distribution of these carbons are shown in figures 3.7 and 3.8. Their textural properties are summarized in table 3.3 and the results of the TPDMS analysis are shown in figure 3.9.

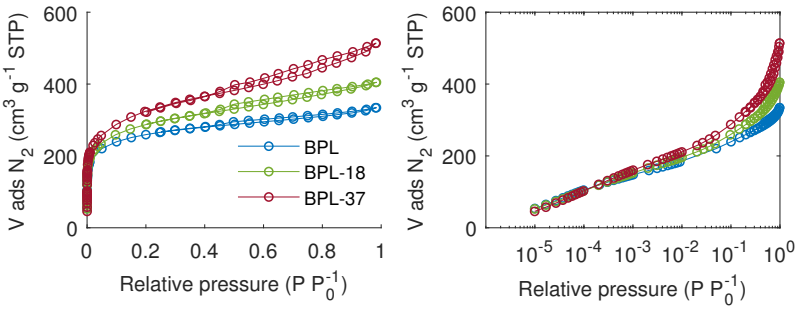

Figure 3.7: N_2 adsorption isotherm measured at 77 K of carbon BPL and its overactivated derivatives.

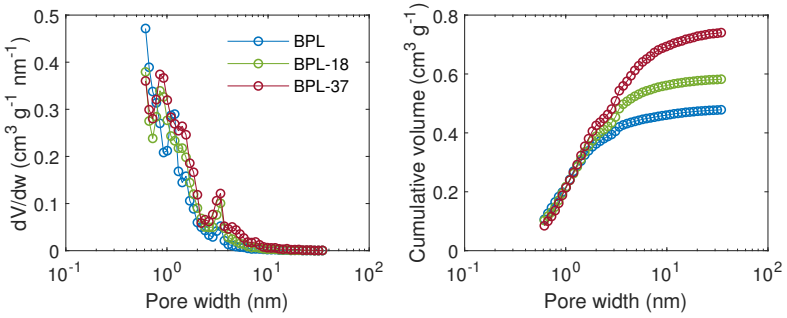

Figure 3.8: Pore size distribution modelled by QSDFT based on N_2 isotherm of carbon BPL and its overactivated derivatives.

Table 3.3: Selected properties of carbon BPL and its overactivated derivatives; (a) total pore volume at $P/P_0 = 0.985$; (b) by equilibrium QSDFT model; (c) by DR model; (d) based on MIP data.

Carbon	BPL	BPL-18	BPL-37
TPV^a (cm^3/g)	0.58	0.63	0.79
Surface area^b (m^2/g)	955	1015	1075
V^b_{micro} (cm^3/g)	0.40	0.39	0.43
W^c_0 (cm^3/g)	0.40	0.40	0.45
V^b_{meso} (cm^3/g)	0.14	0.19	0.31
V^d_{macro} (cm^3/g)	0.31	0.32	0.48
Apparent density^d (g/cm^3)	0.73	0.70	0.57

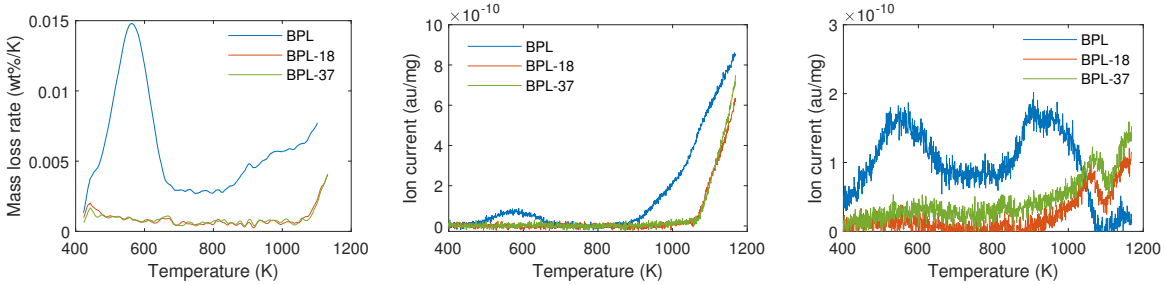

(a) DTG. (b) CO profile. (c) CO_2 profile.

Figure 3.9: TPDMS analysis of carbon BPL and its derivatives obtained by overactivation.

These results show that the textural properties of the carbon BPL are significantly modified by the overactivation treatment, with an increasing porosity with the degree of burn-off. Whereas the micro-

porous volume is almost constant, the mesoporous volume increases significantly upon overactivation. The lower part of the pore size distribution modelled by QSDFT lacks accuracy as the isotherms were measured from a relative pressure of 10^{-5}, which makes it more difficult to compare the micropore size distribution of the carbons. The three isotherms are of type I(b), and the knee seems comparable. This indicates that the micropore size distribution is quite broad and includes large micropore, and that the overactivation treatment does not significantly affect the size distribution of the micropores. The comparison between BPL and its overactivated derivatives remains interesting within the scope of the study of the influence of the textural properties of carbon on the efficiency of the pore filling process, as it will allow the contribution of the small mesopores to be evaluated. Pristine carbon BPL has a relatively low oxygen content of 2.6 wt%, but TPDMS analysis (see details in Annex C) has shown that its surface contains a variety of functional groups (i.e., carboxylic acid, carbonyl, carboxylic anhydride, phenol, lactone and quinone), although the amounts of these groups are relatively small. Upon overactivation, it is observed that the oxygen content drops significantly (to 1.0 wt%) and that the surface chemistry is affected, as shown on the DTG curve, and CO and CO_2 profiles in figure 3.9. The TPDMS analysis has shown that all the groups were removed from the surface, excepted the lactones and carbonyl/quinone, the amounts of which remaining approximately unchanged. This is in line with the physical activation treatment carried out at a relatively high temperature (i.e., 875 °C), at which most of the oxygen-containing surface groups are not stable.

3.2.4 FY5 and derivatives

Carbon FY5 is an activated carbon obtained by physical activation (steam) of coconut shell [94]. It is characterized by a narrow microporosity and a negligible mesoporous volume, and presents a small amount of oxygen-containing functional groups on its surface. In this work, the pristine carbon FY5 and its derivatives resulting from CO_2 overactivation are used to highlight the influence of the textural properties on the synthesis process. Overactivation is performed during different times to obtain carbons FY5-21 and FY5-57 with burn-off ratios of 21 and 57 wt%, respectively. The N_2 adsorption isotherms and the modelled pore size distribution of these carbons are shown in figures 3.10 and 3.11. Their textural properties are summarized in table 3.4 and the results of the TPDMS analysis is shown in figure 3.12.

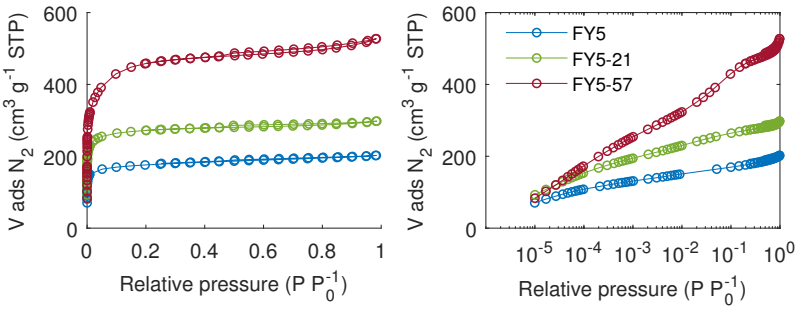

Figure 3.10: N_2 adsorption isotherm measured at 77 K of carbon FY5 and its overactivated derivatives.

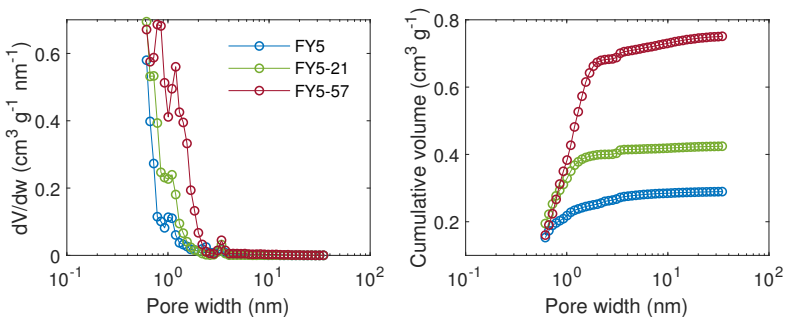

Figure 3.11: Pore size distribution modelled by QSDFT based on N_2 isotherm of carbon FY5 and its overactivated derivatives.

Table 3.4: Selected properties of carbon FY5 and its overactivated derivatives; (a) total pore volume at $P/P_0 = 0.985$; (b) by equilibrium QSDFT model; (c) by DR model; (d) based on MIP data.

Carbon	FY5	FY5-21	FY5-57
TPV[a] (cm^3/g)	0.31	0.46	0.82
Surface area[b] (m^2/g)	835	1188	1369
V^b_{micro} (cm^3/g)	0.25	0.40	0.67
W^c_0 (cm^3/g)	0.27	0.42	0.68
V^b_{meso} (cm^3/g)	0.04	0.03	0.08
V^d_{macro} (cm^3/g)	0.18	0.23	0.29
Apparent density[d] (g/cm^3)	0.98	0.83	0.64

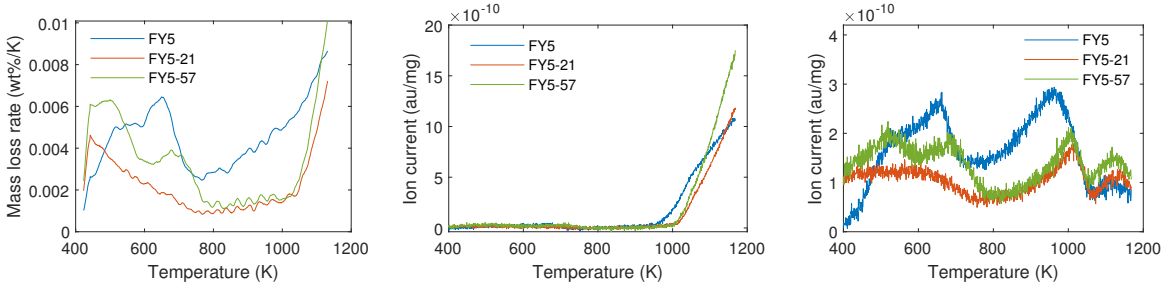

(a) DTG. (b) CO profile. (c) CO_2 profile.

Figure 3.12: TPDMS analysis of carbon FY5 and its derivatives obtained by overactivation.

As indicated by these results, the textural properties of the carbon FY5 were significantly modified by the overactivation treatment. Due to the fact that the lower part of the pore size distribution modelled by QSDFT lacks accuracy as the isotherms were measured from a relative pressure of 10^{-5}, the comparison of the micropore size distributions of the carbons is difficult. It is however observed that the knee of the isotherm becomes less sharp upon overactivation. Whereas the adsorption isotherm of the pristine carbon FY5 is clearly an isotherm of type I(a), characterized by a narrow distribution of micropores of width of ca. 1 nm, the adsorption isotherm progressively changes to a type I(b), characterized by a wider distribution of pore size and large micropores. This is also qualitatively shown on the pore size distribution in figure 3.11, where a shift to wider micropores is observed upon overactivation. This is overall clearly reflected in the increasing micropore volume. As the enlargement of the pores remains in the micropore domain, the mesopore volume remains very small. The comparison between FY5 and its overactivated derivatives will allow the effect of the micropore size distribution on the efficiency of the pore filling process to be evaluated. Pristine carbon FY5 has a relatively low oxygen content of 2.2 wt%, but TPDMS analysis (see details in Annex C) has shown that its surface contains a variety of functional groups (i.e., carboxylic acid, phenol, lactone and quinone), although the amounts of these groups remain relatively small. The presence of carboxylic acid functional groups on carbon FY5 and its derivatives obtained by overactivation, despite the fact that this group is not stable at the temperature of the thermal treatment, is attributed to an oxidation at room temperature occurring after the thermal treatment and owing to the very reactive nature of this biomass-derived carbon. This is likely the reason why the surface chemistry does not seem significantly affected by the thermal treatment; the oxygen content only moderately decreases (to 1.3-1.8 wt%), and the amounts of functional groups remain unchanged, except for the amount of phenol groups which is 4 times lower for the carbons obtained by overactivation than for the pristine BPL. This latter observation is presumably related to small differences between the physical activation method applied to produce pristine carbon FY5 and the overactivation method used in this work.

3.3 Methodology for process characterization

3.3.1 Generalities

In order to characterize the efficiency of the pore filling process, it is necessary to be able to quantify the amount of oxidizing agent in the porosity and to determine in which part of the porous network the oxidizing agent is crystallized. It is also interesting to quantify the mass of salt outside of the porosity, and to investigate the density of the salts in the pores.

The quantity of oxidizing agent after the pore filling process is expressed in this work by a mass yield defined as follows:

$$\text{yield} = \frac{\text{mass of oxidizing agent}}{\text{mass of carbon}} \ (\text{g/g}) \tag{3.1}$$

To determine where is the oxidizing agent in the porosity, the filled fraction is defined as follows:

$$\text{filled fraction} = \frac{\begin{pmatrix}\text{pore volume}\\ \text{of pristine carbon}\end{pmatrix} - \begin{pmatrix}\text{residual pore volume}\\ \text{of filled carbon}\end{pmatrix} \times (\text{yield} + 1)}{\begin{pmatrix}\text{pore volume}\\ \text{of pristine carbon}\end{pmatrix}} \ (\text{vol \%}) \tag{3.2}$$

where the pore volumes are expressed in cm^3/g.

Three different cases are considered for the calculation of the filled fraction:

- considering the pore volume of pristine carbon as the total pore volume (TPV) determined by N_2 adsorption,
- considering the pore volume of pristine carbon as the micro- and the mesopore volumes obtained by QSDFT modelling of the N_2 isotherm data,
- considering the pore volume of pristine carbon as the macroporous volume extracted from the mercury intrusion porosimetry (MIP) data.

The precision of the small filled fractions is intrinsically limited, as the experimental errors become significant when pore volumes of the same order of magnitude are subtracted.

It is also interesting to compare the apparent density of the filled carbon measured by mercury intrusion porosimetry with the calculated apparent density based on the degree of filling and assuming that the oxidizing agent is crystallized inside of the particles. Hence, the calculated apparent density of filled carbons is determined as follows:

$$\begin{pmatrix}\text{Calculated apparent}\\ \text{density of filled carbon}\end{pmatrix} = \begin{pmatrix}\text{Apparent density}\\ \text{of pristine carbon}\end{pmatrix} \times (\text{yield} + 1) \ (\text{g/cm}^3) \tag{3.3}$$

Furthermore, these data can also be used to quantify the amount of oxidizing agent on the surface of the carbon particles, i.e. outside of the porosity:

$$\begin{pmatrix}\text{Mass of oxidizer}\\ \text{on the surface}\end{pmatrix} = \left((\text{yield} + 1) - \frac{\begin{pmatrix}\text{Calculated apparent}\\ \text{density of filled carbon}\end{pmatrix}}{\begin{pmatrix}\text{Apparent density}\\ \text{of pristine carbon}\end{pmatrix}} \right) \times \frac{\text{Oxidizer TMD}}{\begin{pmatrix}\text{Apparent density}\\ \text{of pristine carbon}\end{pmatrix}} \ (\text{g/g}) \tag{3.4}$$

where the oxidizing agent outside of the porosity is assumed to have a density equal to its theoretical maximal density (TMD).

It is also interesting to compare the experimental yield with the yield calculated by assuming that the difference in total pore volume determined by N_2 adsorption between the filled and the pristine carbon is occupied by the oxidizing agent at its TMD. A calculated yield higher than the experimental yield indicates the presence of oxidizing agent in the macropores or on the surface, whereas the opposite indicates that a part of the porosity is blocked and/or that the density of the oxidizing agent in the porosity is lower than its TMD. The calculated yield is obtained as follows:

$$\begin{pmatrix}\text{Calculated}\\ \text{yield}\end{pmatrix} = \begin{pmatrix}\text{Total pore volume}\\ \text{of pristine carbon}\end{pmatrix} \times \begin{pmatrix}\text{Filled fraction of}\\ \text{total pore volume}\end{pmatrix} \times (\text{Oxidizer TMD}) \ (\text{g/cm}^3) \tag{3.5}$$

Based on this assumption, a calculated yield smaller than the experimental one indicates the presence of oxidizing agent in the macropores or on the surface, whereas the opposite indicates that a part of

the porosity is blocked and/or that the density of the oxidizing agent in the porosity is lower than its theoretical maximal density (TMD).

The comparison of the experimental adsorption isotherm and pore size distribution analysis of the filled carbon and those corresponding to the physical mixture (carbon and oxidizing agent in identical ratio) is interesting to demonstrate the filling of the porosity. Even if the oxidizing agent is outside of the porosity, a decrease in the pore volumes is expected because of the mass dilution effect as they are expressed by mass unit of material. Smaller residual pore volumes for the filled carbon than for the theoretical physical mixture indicates that the micro and the mesopores are at least partially filled, as shown in figure 3.13 and 3.14 for instance. The adsorption isotherms of the physical mixtures are calculated based on the adsorption isotherm of the pristine carbon and by assuming the the salt are non-porous. This assumption is verified in Annex E.

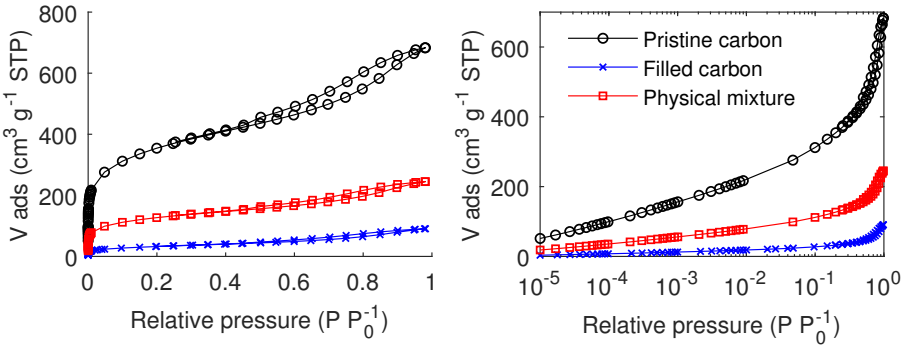

Figure 3.13: N_2 adsorption isotherm measured at 77 K. Example of the comparison between a pristine carbon, a filled carbon and the corresponding theoretical physical mixture.

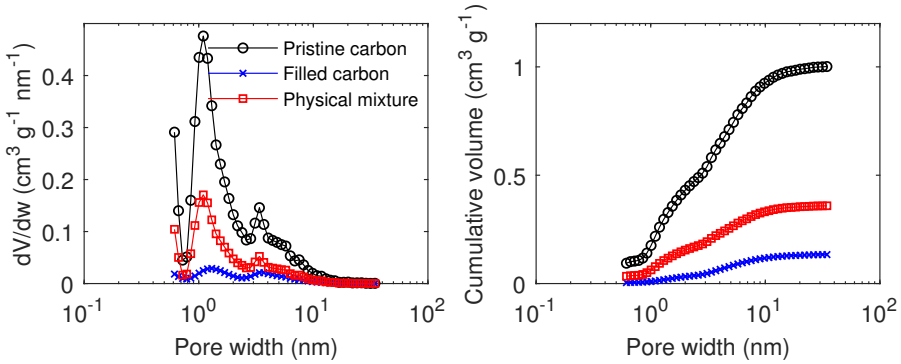

Figure 3.14: Pore size distribution modelled by QSDFT. Example of the comparison between a pristine carbon, a filled carbon and the corresponding theoretical physical mixture.

Finally, the degree of pore filling as a function of the pore width is important to characterize the pore filling efficiency. The pore volume modelled by QSDFT is shown by steps of 1 nm to highlight the degree of pore filling of each part of the porosity. An example is shown in figure 3.15.

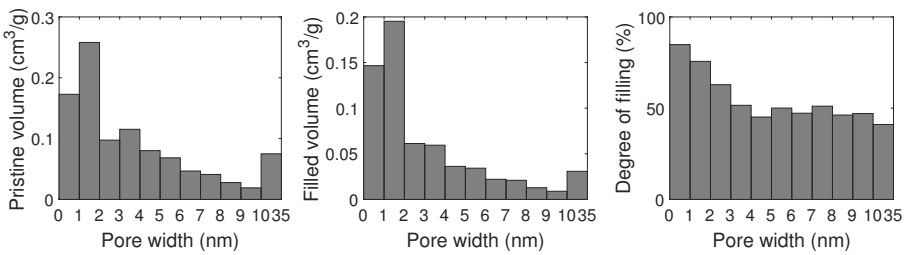

Figure 3.15: Example of degree of pore filling in function of the pore width.

3.3.2 Influence of specific gas-host intermolecular interactions on pore size analysis

The determination of the residual pore volume of carbons filled with an oxidizing agent is based on the measurement of their N_2 adsorption isotherm at 77 K. These results are used to determine the pore size distribution by using the QSDFT model and the residual micro and mesoporous volume are directly obtained from the modelled cumulative pore volume in function of the pore width. N_2 is widely used to study the textural properties of porous carbon, mainly because liquid nitrogen is cheap and easily available in most countries, and because for many adsorbents the nitrogen adsorption isotherms exhibit a well-defined Point B that facilitates the determination of the surface area. However, the use of Ar at 87 K is considered to be more reliable and is now recommended by IUPAC over N_2 at 77 K [26] because of the significant molecular quadrupole of nitrogen that gives rise to strong specific intermolecular interactions (other than dispersive) with polar surface groups (this is not the case of argon) [95]. However, liquid Ar is quite expensive and non-easily accessible.

As only the dispersive intermolecular interactions between the surface and the adsorbate are considered to model the solid-fluid intermolecular interactions in the QSDFT model [80], significant specific surface interactions between the adsorbate and the adsorbent could affect the determination of the pore volumes. In this PhD thesis, even if surface functionalities on the surface of nanoporous carbons can act as polar sites, the QSDFT model was widely applied to characterize these carbons without noticing any significant influence of specific interactions. This is also observed in annex C where the pore size distributions of the commercial pristine activated carbons modelled by QSDFT from the N_2 adsorption data are in very good agreement with that modelled from the Ar adsorption data. The only exception is the FY5 carbon, which is characterized by a very narrow microporosity which makes the measurement of its adsorption isotherms difficult because of a very slow diffusion kinetics. The observed difference is therefore probably the results of kinetic effects and not of specific interactions with the surface (in agreement with the low surface functionalization extent of this carbon).

However, the oxidizing agents considered in this work are salts, as listed in table 1.1. When the carbons are filled with these oxidizing salts of ionic nature, strong ion-quadrupole interactions with N_2 could affect the determination of the residual pore volume of the filled carbons and prevent N_2 adsorption data to be used to characterize the pore filling process. A selection of filled carbons was chosen to investigate this potential issue, and their Ar adsorption isotherm at 87 K was measured. The modelled porosity was then compared to that modelled from the N_2 adsorption data. The detailed results are shown in annex D. Generally speaking, no significant differences were observed, which suggests that the specific interactions between N_2 and the polar sites on the surface are not significant enough to affect the modelling of the textural properties of the filled carbons in a greater extent that the experimental error.

This could be explained by two factors, or by a combination of both. On the one hand, considerations about the stability of the surface of ionic crystals show that surfaces with perpendicular dipole moments producing a polarising electric field in the environment are unstable and therefore are not preferred from a thermodynamic point of view [96]. On the contrary, the other recombined surface types which are stable do not produce a polarizing electric field in the environment [96]. Even if these considerations are theoretically valid for unconfined bulk ionic crystals in equilibrium and must be carefully nuanced when investigating salt crystallized in nanopores, they may contribute to the fact that no significant influence of specific interactions was observed. On the other hand, even if the volume of crystallized salt in the porosity of the carbons can be very large, the adsorbate only interacts with the surface of the oxidizing salt. If the salt crystallizes as aggregates inside of the porosity, it would only present a very small surface to the adsorbate for which the overall interactions would not be significant enough to affect the characterization of the porosity. From a thermodynamic point of view, this situation is very favorable as the ionic interactions inside the salt crystals are much stronger than the dispersive interactions between the salt and the carbon surface, so that the salt will have the tendency to agglomerate inside of the porosity instead of being uniformly dispersed into it to minimize its surface energy. Keeping in mind that the surface of the used nanoporous carbon is heterogeneous from the energetic point of view, it seems reasonable to assume that some polar or energetic sites in the porous network could act as active sites for heterogeneous nucleation, triggering the crystallisation of the salt in their vicinity. The fact, that will be later discussed, that the crystallisation process is carried out progressively and slowly also supports this assumption. In summary, the characterization of the textural properties of nanoporous carbons filled with oxidizing salts based on N_2 adsorption data is considered as not significantly affected by the presence of the salt in the porosity and is used in this work to characterize the efficiency of the pore filling process.

3.4 Influence of process parameters

The pore filling process described in this work is quite complex and depends on a large number of parameters. Table 3.5 lists the main parameters that govern the pore filling process. In this section, the influence of some of these parameters is investigated to define the optimal conditions for the pore filling. The large number of degrees of freedom and some practical limitations prevent all the parameters from being studied. Only the influence of the parameters in bold in table 3.5 is therefore investigated in this work.

Table 3.5: Main parameters of the pore filling process.

General	1. Infiltration	2. Filtering	3. Drying
Oxidizing agent	**Time**	Superficial velocity	Temperature
Solvent	Temperature	Time	**Heating rate**
Solution concentration	Pressure	Bed depth	Dwell time
	Stirring		

Regarding the parameters that have a global influence on the process, the influence of the nature of the oxidizing agent and of the solution concentration is investigated in this work, but only aqueous solutions are used as water is a very good solvent for most of the considered oxidizing salts.

The infiltration step is performed at room temperature and atmospheric pressure on a plate shaker ensuring sufficient agitation of the solution. An excess of aqueous solution of 20 g of solution per g of pristine nanoporous carbon is used in order to submerge the nanoporous carbon completely. As the diffusion of the highly concentrated salt aqueous solution in the nanoporous carbon is expected to be slow, the infiltration time is an important parameter and is investigated in this part.

The filtration step is performed with a Büchner filter connected to a vacuum pump. The diameter of the filter is chosen so that it is completely covered with carbon particles while the depth of the bed is very thin (a few mm) in order to prevent the pressure drop through the bed to lead to inhomogeneity in the material. The filtering efficiency is governed by the filtering time and the superficial velocity of air flowing through the bed due to the pressure difference generated by the vacuum pump [97]. In this case, the downstream pressure was measured and was about 900 mbar in all cases. The air flow rate, and the corresponding superficial velocity, is then determined by the pump maximal flow rate at this pressure and was therefore kept constant during all the experiments. Based on visual observation, the duration of the filtering step was set at one minute. The improvement of the filtration step will be discussed in the perspectives of this work.

Finally, the drying step is performed in a non-ventilated natural convection oven. Forced convection was not used to avoid a too fast drying of the upper layers of the carbon grains which was observed to lead to crystallization on the surface of the grains. The filtered grains were transferred to PTFE beakers before the drying to avoid capillary effects on glass walls. The optimal drying rate corresponds to a balance between two phenomena. It should be slow enough to allow the ions to diffuse to the crystallisation sites in the porous network, while being fast enough so that the temperature increase delays the generation of a supersaturation state by increasing the solubility. The temperature of the drying step was set at 120 °C, the same temperature as that of the degassing of the carbon samples before measurement of their adsorption isotherm. Based on visual observations, the duration of the drying step was set at 2 hours in the natural convection oven, followed by a drying to constant mass in an oven under moderate vacuum at the same temperature. The heating rate of the natural convection oven is investigated in this part to optimize the rate of the drying process.

3.4.1 Oxidizing agent

Initially, four representative oxidizing agents were selected, based on the theoretical feasibility study (see section 1.5.2) and on their properties:

- Sodium perchlorate ($NaClO_4$), which is the best candidate of all common oxidizing agents in terms of volumetric oxygen content and has a very high solubility in water at room temperature.
- Potassium nitrate (KNO_3), which is one of the most widely used oxidizing agents in pyrotechnics and is highly soluble in water. One of its main advantages is its relatively low hygroscopic character with respect to other oxidizing agents such as sodium salts.

- Ammonium perchlorate (NH_4ClO_4), which is the most widely used oxidizing agent in propellant applications, as no solid products are formed during its reaction with a carbonaceous reducing agent. It is furthermore highly soluble in water and has a relatively low hygroscopic character.
- Ammonium nitrate (NH_4NO_3), which has an extremely high water solubility which could allow high yield to be achieved, despite its relatively low volumetric oxygen content.

A preliminary safety study at the mg scale discards the use of ammonium nitrate as oxidizing agent because the nanoporous carbons filled with ammonium nitrate had ignition temperatures of about 80 °C, which was considered as too dangerous for handling.

To study the influence of the oxidizing agent on the pore filling process, carbons C and F5001 were filled with $NaClO_4$, KNO_3 and NH_4ClO_4. The water solubilities of these salts at room temperature are very different, as shown in table 3.6. The solubility of $NaClO_4$ is much higher than that of the two other salts.

Table 3.6: Properties of saturated aqueous solution of the oxidizing salts at 20 °C [76].

	$NaClO_4$	KNO_3	NH_4ClO_4
Weight fraction (wt%)	66.2	24.2	17.8
Molarity (mol/kg)	16.0	3.16	1.40
Solubility (g/100 g H_2O)	195.9	31.9	21.6

The influence of the other parameters will be discussed later. In this section, carbons C and F5001 filled with solutions of KNO_3 and NH_4ClO_4 saturated at room temperature, and with a 56 wt% solution of $NaClO_4$ are compared. The duration of the infiltration step was set at 66 hours for all samples, and they were immediately placed in the natural convection oven pre-heated at 120 °C for the drying step.

Sodium perchlorate

The yield of the pore filling process of carbon C with $NaClO_4$ is 1.79 g/g and the filled carbon looks exactly as the pristine one, without any trace of salt on the surface (see Annex G for examples of microscope pictures). The comparison of the pore size analysis between the filled carbon and the corresponding theoretical physical mixture is shown in figure 3.16 and detailed in table 3.7. The degree of pore filling with respect to the pristine carbon is shown in figure 3.17 and detailed in table 3.8. The apparent density of the filled carbon is 1.20 g/cm^3.

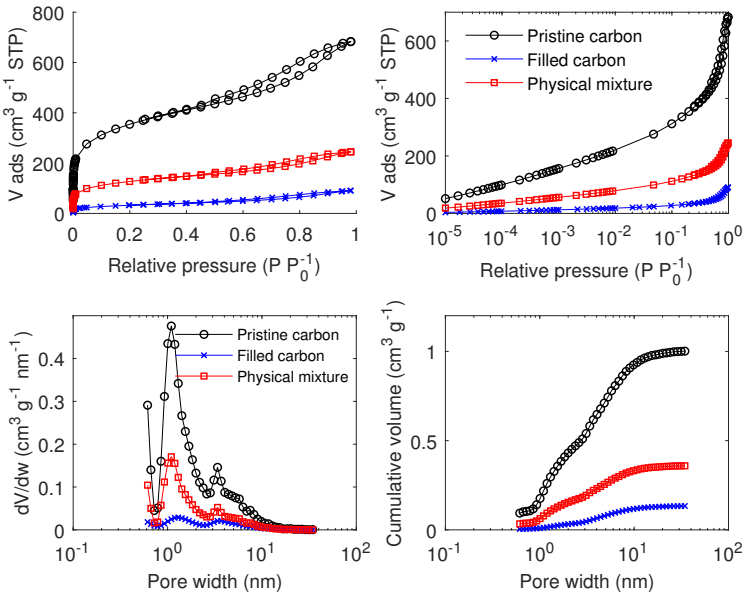

Figure 3.16: Comparison between N_2 adsorption isotherm and pore size analysis of the pristine carbon, the filled carbon and the corresponding theoretical physical mixture for carbon C filled with $NaClO_4$.

Table 3.7: Selected textural properties of carbon C filled with $NaClO_4$ at 1.79 g/g based on N_2 isotherm at 77 K; (a) total pore volume at $P/P_0 = 0.985$; (b) by equilibrium QSDFT model; (1) theoretical values.

Carbon	Pristine carbon	Physical mixture[1]	Filled carbon
TPV[a] (cm^3/g)	1.06	0.38	0.14
V^b_{micro} (cm^3/g)	0.43	0.15	0.03
V^b_{meso} (cm^3/g)	0.57	0.20	0.10

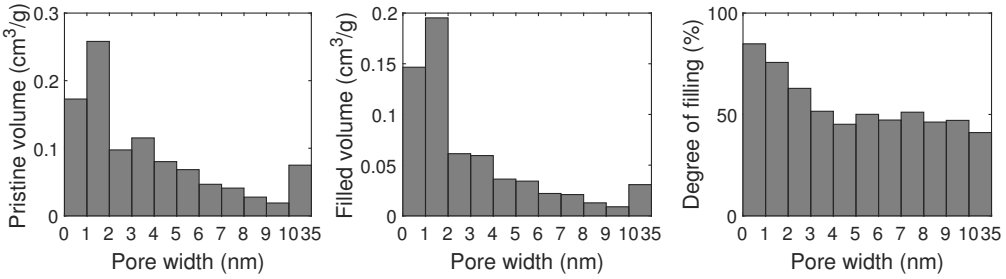

Figure 3.17: Degree of pore filling with respect to the pristine carbon for carbon C filled with $NaClO_4$.

Table 3.8: Characterization of the pore filling efficiency for carbon C filled with $NaClO_4$; (a) total pore volume at $P/P_0 = 0.985$; (b) by equilibrium QSDFT model; (c) based on MIP data.

Fraction of TPV filled[a] (%)	63
Fraction of micropores filled[b] (cm^3/g)	79
Fraction of mesopores filled[b]	50
Fraction of macropores filled[c]	20

When comparing the pore size analysis of the filled carbon with the predicted residual porosity of the corresponding theoretical physical mixture, we observe that the residual porosity of the filled carbon is significantly lower than that of the theoretical mixture. This indicates that the salt has crystallized in the carbon porosity. The analysis of the pore filling efficiency shows that the degree of pore filling is high. The pores are however not uniformly filled. The degree of pore filling is about 80 % in the smallest pores and then progressively drops to about 50 % for pores wider than 3 nm. This indicates that the pore width has an important influence on the degree of pore filling. If the difference of total pore volume determined by N_2 adsorption between the filled and the pristine carbon was filled with sodium perchlorate at its theoretical maximal density (TMD), the yield would be equal to 1.67 g/g. This value is slightly lower than the measured yield of 1.79 g/g. As it appears very unlikely that the density of the salt in the porosity exceeds its TMD, this indicates the presence of a fraction of the salt in the macropores. In this case, the degree of macropore filling was about 20 %, which corresponds to a mass of salt in the macropores of about 0.3 g/g. Furthermore, the measured apparent density (1.20 g/cm^3) is in very good agreement with the apparent density assuming that all the salt is inside the particle (1.15 g/cm^3), hereby confirming the qualitative observation that there is no significant amount of salt on the surface. The reported amount of salt in the macropores is of the same order of magnitude than the difference between the experimental and the calculated yield based on the micro and the mesopore analysis. This suggests that most of the salt is well crystallized in the micro- and the mesopores and that it has a density close to its TMD. Pore blocking cannot be completely excluded on this basis, but the results show that its contribution is not significant.

The yield of the pore filling process of carbon F5001 with $NaClO_4$ is 2.15 g/g and some white traces are observed on the surface of the filled carbon grains, indicating the presence of a small fraction of the salt on the surface. The comparison of the pore size analysis between the filled carbon and the corresponding theoretical physical mixture is shown in figure 3.18 and detailed in table 3.9. The degree of pore filling with respect to the pristine carbon is shown in figure 3.19 and detailed in table 3.10. The apparent density of the filled carbon is 1.06 g/cm^3.

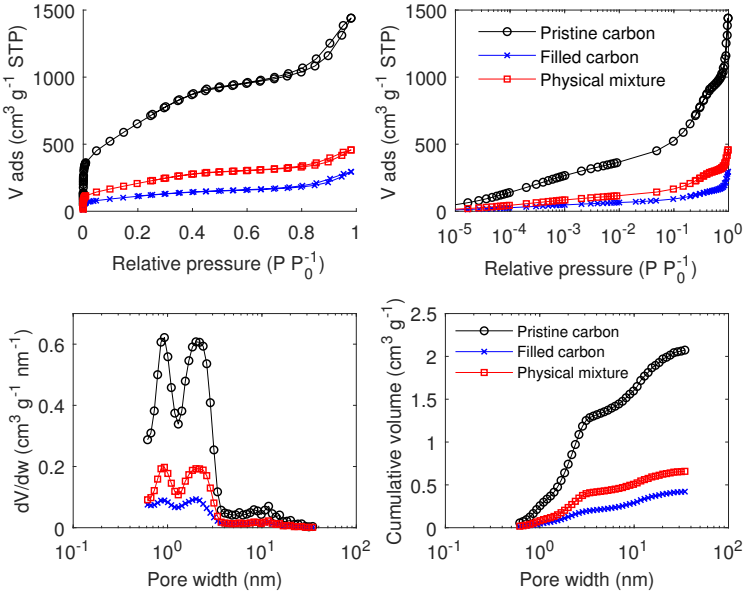

Figure 3.18: Comparison between N_2 adsorption isotherm and pore size analysis of the pristine carbon, the filled carbon and the corresponding theoretical physical mixture for carbon F5001 filled with $NaClO_4$.

Table 3.9: Selected textural properties based on N_2 isotherm at 77 K for carbon F5001 filled with $NaClO_4$;(a) total pore volume at $P/P_0 = 0.985$; (b) by equilibrium QSDFT model; (1) theoretical values.

Carbon	Pristine carbon	Physical mixture[1]	Filled carbon
TPV^a (cm^3/g)	2.23	0.71	0.46
V^b_{micro} (cm^3/g)	0.74	0.23	0.13
V^b_{meso} (cm^3/g)	1.33	0.42	0.29

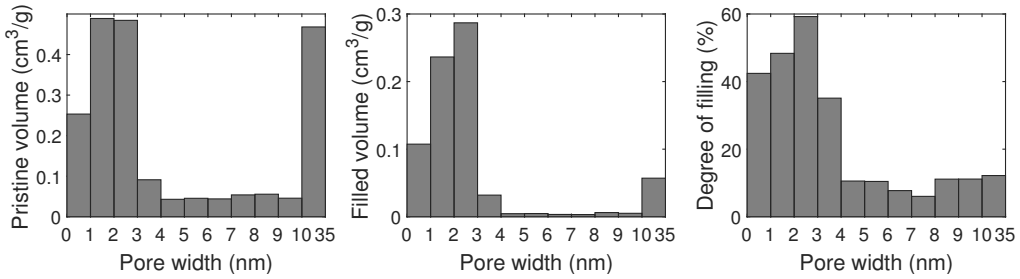

Figure 3.19: Degree of pore filling with respect to the pristine carbon for carbon F5001 filled with $NaClO_4$.

Table 3.10: Characterization of the pore filling efficiency for carbon F5001 filled with $NaClO_4$; (a) total pore volume at $P/P_0 = 0.985$; (b) by equilibrium QSDFT model; (d) based on MIP data.

Fraction of TPV filled^a (%)	36
Fraction of micropores filled^b (cm^3/g)	50
Fraction of mesopores filled^b	30
Fraction of macropores filled^c	16

As in the case of carbon C, the predicted residual porosity of the theoretical physical mixture is higher than that of the experimental residual porosity of the filled carbon, demonstrating that the salt has crystallized in the carbon porosity. The degree of pore filling for this carbon is moderate. The pores are however not uniformly filled. The degree of pore filling first increases with the pore width to about 60 % in the smallest mesopores. It then suddenly drops to reach a very low value of about 10 % in pores wider than 4 nm.

A yield of 2.15 g/g was obtained for this carbon, which is higher than the value obtained considering that the difference of total pore volume determined by N_2 adsorption between the filled and the pristine carbon was filled with sodium perchlorate at its TMD (1.92 g/g). As mentioned above, this indicates the presence of a small fraction of the salt in the macropores and/or on the surface. The observation of small white traces on the surface of the filled carbon confirms the latter assumption (see Annex G for examples of microscope pictures). The degree of macropore filling was about 16 %, which corresponds to a mass of salt in the macropores of about 0.2 g/g. The amount of salt on the surface was estimated to 0.1 g/g by comparing the apparent density determined by MIP (1.06 g/cm^3) and the apparent density calculated by assuming that all the salt is within the carbon particles (1.18 g/cm^3). The sum of these contributions is in very good agreement with the observed difference between the experimental and the calculated yield based on the micro and the mesopores analysis. This strongly suggests that most of the salt is well crystallized in the micro and the mesopores and that it has a density close to its TMD. As mentioned above for carbon C, pore blocking contribution is considered not significant.

Potassium nitrate

The yield of the pore filling process of carbon C with KNO_3 is 0.59 g/g and the filled carbon looks exactly as the pristine one, without traces of salt on the surface. The comparison of the pore size analysis between the filled carbon and the corresponding theoretical physical mixture is shown in figure 3.20 and detailed in table 3.11. The degree of pore filling with respect to the pristine carbon is shown in figure 3.21 and detailed in table 3.12.

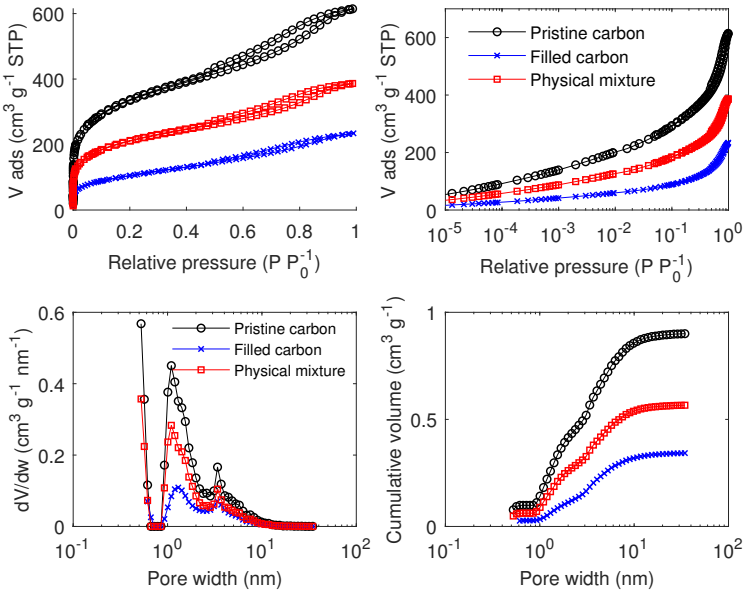

Figure 3.20: Comparison between N_2 adsorption isotherm and pore size analysis of the pristine carbon, the filled carbon and the corresponding theoretical physical mixture for carbon C filled with KNO_3.

Table 3.11: Selected textural properties based on N_2 isotherm at 77 K of carbon C filled with KNO_3; (a) total pore volume at $P/P_0 = 0.985$; (b) by equilibrium QSDFT model; (1) theoretical values.

Carbon	Pristine carbon	Physical mixture[1]	Filled carbon
TPV[a] (cm^3/g)	0.95	0.60	0.36
V^b_{micro} (cm^3/g)	0.41	0.26	0.11
V^b_{meso} (cm^3/g)	0.48	0.30	0.23

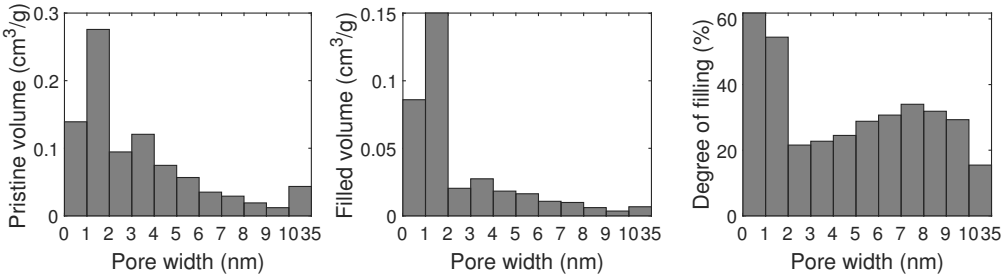

Figure 3.21: Degree of pore filling with respect to the pristine carbon for carbon C filled with KNO_3.

Table 3.12: Characterization of the pore filling efficiency for carbon C filled with KNO_3; (a) total pore volume at $P/P_0 = 0.985$; (b) by equilibrium QSDFT model.

Fraction of TPV filled[a] (%)	40
Fraction of micropores filled[b] (cm^3/g)	57
Fraction of mesopores filled[b]	24

These results are to some extent comparable to that obtained when carbon C was filled with sodium perchlorate. It is observed that potassium nitrate has crystallized in the carbon porosity and that the pore are not uniformly filled. The degree of filling is almost constant in the micropores (ca. 55-60 %), but it suddenly decreases to 20 % in pores of widths larger than 2 nm. Moreover, the comparison between the measured (0.59 g/g) and the calculated yield (0.79 g/g) suggests that a part of the porosity was blocked by the crystallization of potassium nitrate in the porous network and/or that its density in the porosity was smaller than its TMD.

The yield of the pore filling process of carbon F5001 with KNO_3 is 0.50 g/g and some white traces are observed on the surface of the filled carbon grain, indicating the presence of fraction of the salt on the surface. The comparison of the pore size analysis between the filled carbon and the corresponding theoretical physical mixture is shown in figure 3.22 and detailed in table 3.13. The degree of pore filling with respect to the pristine carbon is shown in figure 3.23 and detailed in table 3.14.

Table 3.13: Selected textural properties based on N_2 isotherm at 77 K for carbon F5001 filled with KNO_3; (a) total pore volume at $P/P_0 = 0.985$; (b) by equilibrium QSDFT model; (1) theoretical values.

Carbon	Pristine carbon	Physical mixture[1]	Filled carbon
TPV[a] (cm^3/g)	2.23	1.49	1.46
V^b_{micro} (cm^3/g)	0.74	0.49	0.43
V^b_{meso} (cm^3/g)	1.33	0.89	0.90

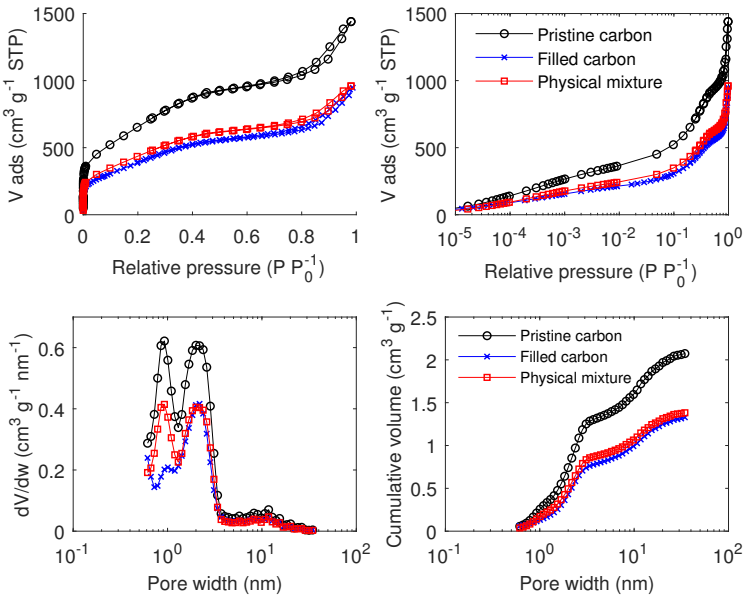

Figure 3.22: Comparison between N_2 adsorption isotherm and pore size analysis of the pristine carbon, the filled carbon and the corresponding theoretical physical mixture for carbon F5001 filled with KNO_3.

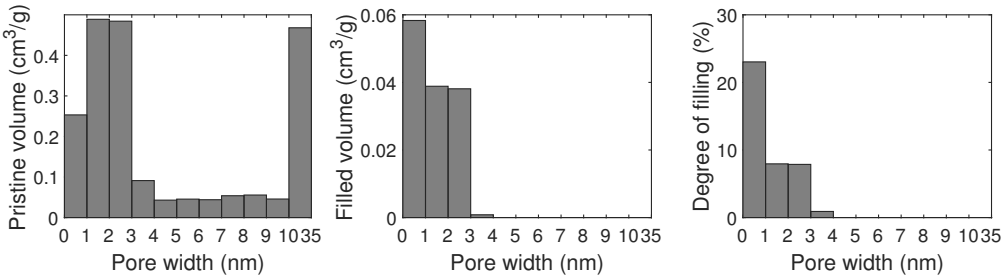

Figure 3.23: Degree of pore filling with respect to the pristine carbon for carbon F5001 filled with KNO_3.

Table 3.14: Characterization of the pore filling efficiency for carbon F5001 filled with KNO_3; (a) total pore volume at $P/P_0 = 0.985$; (b) by equilibrium QSDFT model.

Fraction of TPV filled[a] (%)	2
Fraction of micropores filled[b] (cm^3/g)	13
Fraction of mesopores filled[b]	-1

In contrast with the previous observations, the residual porosity of the filled carbon is in very good agreement with that of the theoretical physical mixture. This indicates that no significant amount of potassium nitrate has crystallized in the carbon porosity. The analysis of the pore filling efficiency confirms that the degree of pore filling is very low, as the calculated yield is ca. 0.1 g/g, which is significantly lower than the measured yield (0.50 g/g). This indicates that most of the potassium nitrate is crystallized in the macropores or on the surface.

Ammonium perchlorate

The yield of the pore filling process of carbon C with NH_4ClO_4 is 0.40 g/g and the filled carbon looks exactly as the pristine one, without any trace of salt on the surface. The comparison of the pore size analysis between the filled carbon and the corresponding theoretical physical mixture is shown in figure 3.24 and detailed in table 3.15. The degree of pore filling with respect to the pristine carbon is shown in figure 3.25 and detailed in table 3.16.

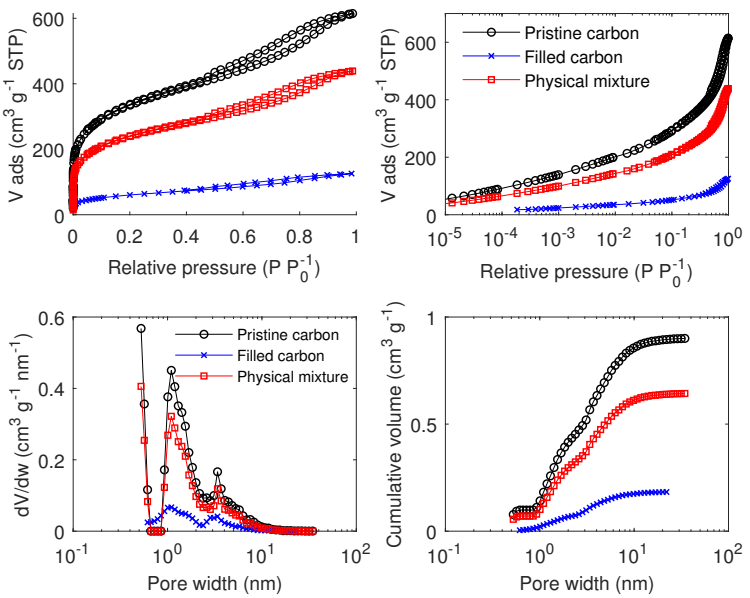

Figure 3.24: Comparison between N_2 adsorption isotherm and pore size analysis of the pristine carbon, the filled carbon and the corresponding theoretical physical mixture for carbon C filled with NH_4ClO_4.

Table 3.15: Selected textural properties based on N_2 isotherm at 77 K of carbon C filled with NH_4ClO_4; (a) total pore volume at $P/P_0 = 0.985$; (b) by equilibrium QSDFT model; (1) theoretical values.

Carbon	Pristine carbon	Physical mixture[1]	Filled carbon
TPV^a (cm^3/g)	0.95	0.68	0.19
V^b_{micro} (cm^3/g)	0.41	0.29	0.07
V^b_{meso} (cm^3/g)	0.48	0.34	0.11

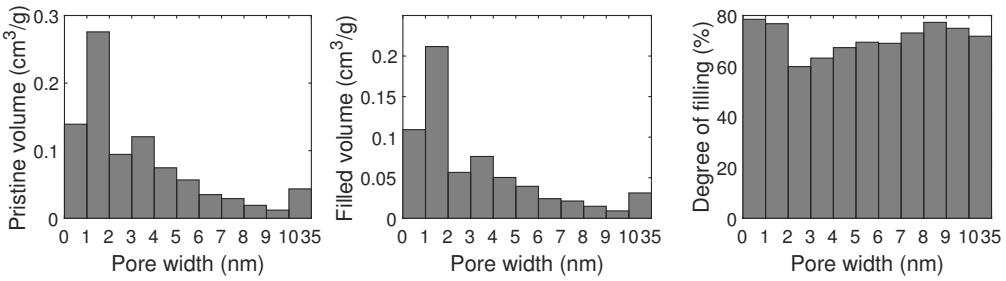

Figure 3.25: Degree of pore filling with respect to the pristine carbon for carbon C filled with NH_4ClO_4.

Table 3.16: Characterization of the pore filling efficiency for carbon C filled with NH_4ClO_4; (a) total pore volume at $P/P_0 = 0.985$; (b) by equilibrium QSDFT model.

Fraction of TPV filled^a (%)	72
Fraction of micropores filled^b (cm^3/g)	76
Fraction of mesopores filled^b	68

As already mentioned for sodium perchlorate and potassium nitrate, the comparison of the adsorption isotherm of the filled carbon C with the corresponding theoretical mixture shows that ammonium perchlorate is also effectively crystallized in the porous structure. The degree of pore filling is very high

with respect to the experimental yield (0.40 g/g), as it appears that the calculated yield is equal to 1.33 g/g. This suggests that a large part of the porosity was blocked by the crystallization of ammonium perchlorate in the porous network and/or that its density in the porosity was smaller than its TMD. As a mean density in the porosity of less than one third of the TMD seems unlikely, this strongly suggests that pore blocking is significant.

The yield of the pore filling process of carbon F5001 with NH_4ClO_4 is 0.50 g/g and the filled carbon looks exactly as the pristine one, without any trace of salt on the surface. The comparison of the pore size analysis between the filled carbon and the corresponding theoretical physical mixture is shown in figure 3.26 and detailed in table 3.17. The degree of pore filling with respect to the pristine carbon is shown in figure 3.27 and detailed in table 3.18.

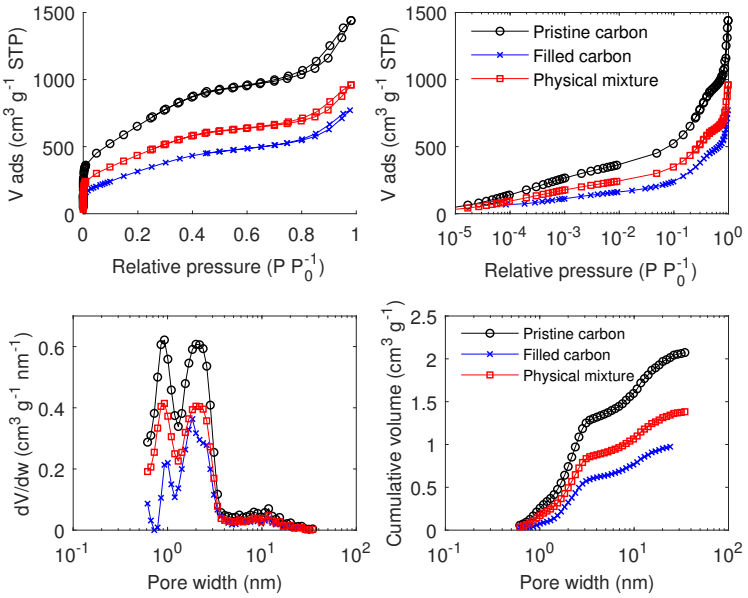

Figure 3.26: Comparison between N_2 adsorption isotherm and pore size analysis of the pristine carbon, the filled carbon and the corresponding theoretical physical mixture for carbon F5001 filled with NH_4ClO_4.

Table 3.17: Textural properties based on N_2 isotherm at 77 K of carbon F5001 filled with NH_4ClO_4; (a) total pore volume at $P/P_0 = 0.985$; (b) by equilibrium QSDFT model; (1) theoretical values.

Carbon	Pristine carbon	Physical mixture[1]	Filled carbon
TPV[a] (cm^3/g)	2.23	1.49	1.19
V^b_{micro} (cm^3/g)	0.74	0.49	0.32
V^b_{meso} (cm^3/g)	1.33	0.89	0.65

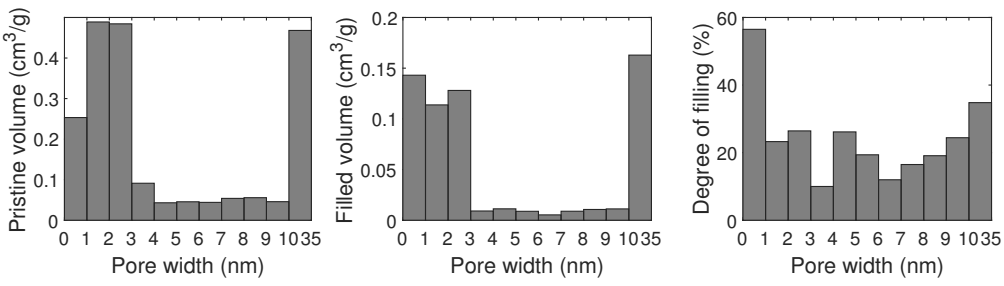

Figure 3.27: Cumulative fraction of pore filled for carbon F5001 filled with NH_4ClO_4.

Table 3.18: Characterization of the pore filling efficiency for carbon F5001 filled with NH_4ClO_4; (a) total pore volume at $P/P_0 = 0.985$; (b) by equilibrium QSDFT model.

Fraction of TPV filled[a] (%)	20
Fraction of micropores filled[b] (cm^3/g)	35
Fraction of mesopores filled[b]	27

As already observed with the same carbon filled with $NaClO_4$ and for carbon C, some NH_4ClO_4 crystallized also in the porous network of carbon F5001 but the degree of pore filling is moderate. The degree of pore filling of the small micropores (ca. 60 %) is moreover significantly higher than that of the larger pores (ca. 20 %). The calculated yield (0.84 g/g) is significantly larger than the measured yield of 0.50 g/g, suggesting that a part of the porosity was blocked by the crystallization of NH_4ClO_4 in the porous network and/or that its density in the porosity was smaller than its TMD.

Summary

The pore filling with sodium perchlorate was successful for both carbons and especially for carbon C for which the degree of pore filling is high. It was shown that the micro and mesopores of both carbons were effectively filled with crystallized salt and that most of the oxidizer is crystallized in pores of widths smaller than 4 nm for both carbons. In both cases, the results strongly suggest that about 90 % of the salt is crystallized in the micro and the mesopores at a density close to its theoretical maximal density (TMD). Small amounts of salt were reported in the macropores for carbon C and in the macropores and on the surface for carbon F5001.

The pore filling with potassium nitrate and ammonium nitrate was less successful as the yields and degrees of pore filling are generally low or moderate. The analysis of the degree of pore filling of carbon F5001 filled with potassium nitrate showed that no significant amount of salt crystallized in the micro and mesopores. For carbon C filled with both oxidizing agents and carbon F5001 filled with ammonium perchlorate, the analysis of the degree of pore filling strongly suggests that a large part of the porosity of the carbons was blocked by the crystallization of the salt in the porous network. The density of the oxidizing agents in the pore may also be lower than their theoretical maximal density. This effect is very significant for carbon C filled with ammonium perchlorate.

The ability of sodium perchlorate to selectively crystallize in the micro and the mesopores of carbons C and F5001 is a confirmation of the main assumption of the pore filling process, namely that the aqueous solution will preferentially fill the micro and the mesopores upon solvent evaporation because of capillarity.

It seems very likely that the significant difference of yield between the three salts is related to their very different solubilities. As the filtering is performed in the same way in all cases, the volume of aqueous solution after this step is more or less the same in all cases. Due to concentration and density effects, this volume contains a much larger amount of sodium perchlorate than of the other salts, which explains the significantly higher yields obtained with sodium perchlorate.

When comparing the yields of the pore filling process with the thresholds defined in the theoretical feasibility study (see section 1.5.2), we observe that both carbons filled with sodium perchlorate are potential energetic materials. However, the amount of potassium nitrate and ammonium perchlorate is very too low for practical applications. As the scope of this work consists in investigating and demonstrating the concept of energetic materials based on nanoporous carbon filled with a solid oxidizing agent, only sodium perchlorate is therefore considered in the rest of this work. Based on the discussed experimental results and the study of the theoretical feasibility, it appears that this salt is the most likely to lead to filled carbons with an energetic character.

3.4.2 Infiltration time

During the infiltration step, the aqueous solution of oxidizing salt must diffuse in the porous network to fill it. This diffusion is expected to be very slow, especially in micropores, as commonly observed in liquid phase adsorption [98]. Even if this may be mitigated locally by the presence of polar surface functional groups for some studied materials, nanoporous carbons are globally hydrophobic, whereas most of the used aqueous solutions have an extremely high ionic strength (of about 16 mol/kg for sodium perchlorate). The interfacial free energy between the carbon surface and the aqueous solution is therefore expected to be high. The consequences on the wetting of the carbon surface by the aqueous solutions

are however difficult to predict, but the overall process of infiltration of the porosity by a concentrated aqueous solution of an oxidizing salt is excepted to be very slow.

This parameter is studied by comparing the degree of pore filling after different infiltration times. Carbon C is arbitrarily chosen as the starting material for this analysis. The degrees of filling of the N_2 adsorption total pore volume and of the micro and the mesoporous volume are shown in figure 3.28 for infiltration times of 17, 42, 66 and 90 hours. Carbon C is filled with a 56 wt% aqueous solution of $NaClO_4$. After the filtration, the samples were immediately placed in a natural convection over pre-heated at 120 °C for drying. No significant influence of infiltration time on the yield of the pore filling process is observed, and the mean yield is equal to 1.78 ± 0.02 g/g. We observe that the degree of pore filling seems quite constant for all infiltration times, with only a slight increase of the degree of micropore filling between infiltration times of 17 and 42 hours. From an infiltration time of 42 hours, a plateau is reached. The second point of the plateau (66 hours) is conservatively chosen as the infiltration time of the process.

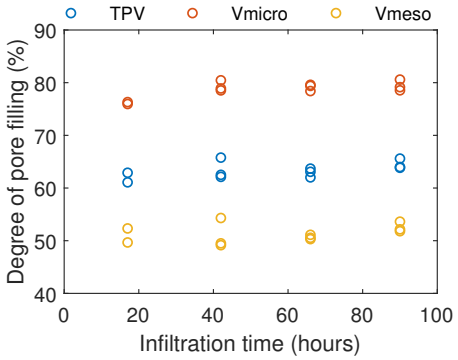

Figure 3.28: Carbon C filled with $NaClO_4$. Influence of the infiltration time on the degree of pore filling.

The influence of the infiltration time on the degree of pore filling was further investigated in three other commercial activated carbons: namely F5001, BPL and FY5. The carbons were chosen upon the textural features (e.g., FY5 has a narrow microporosity where diffusion restrictions upon infiltration may be expected). In order to confirm that the optimal infiltration time is 66 h, only the degrees of pore filling after 66 and 90 hours are compared. No significant difference of yield is observed. Data in Figure 3.29 shows that there is no significant evolution of the degree of pore filling for all the carbons between infiltration times of 66 and 90 hours, the infiltration time of 66 hours is considered as optimal and is used in the rest of this work. As this parameter was conservatively defined and validated for carbons with different textural properties, the same infiltration time is also used for the carbon derivatives.

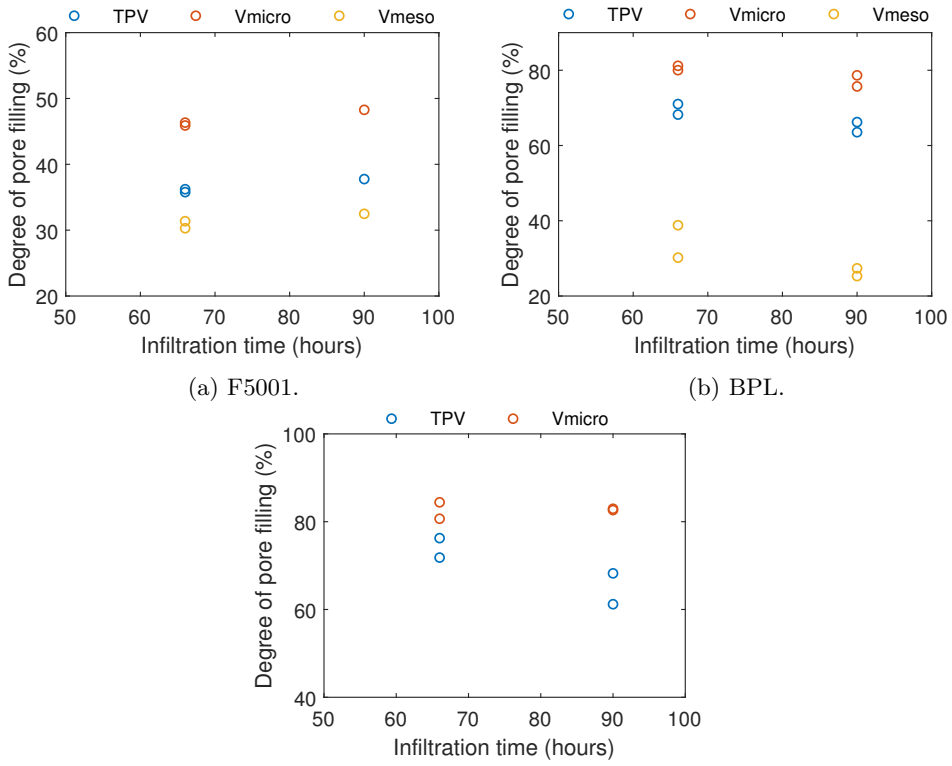

(a) F5001.

(b) BPL.

(c) FY5.

Figure 3.29: Carbons F5001, BPL and FY5 filled with $NaClO_4$. Influence of the infiltration time on the degree of pore filling.

3.4.3 Heating rate

During the drying step, the heating rate must be precisely controlled; it must be sufficiently slow to allow ions to diffuse in the porous network to the crystallization nuclei and water to diffuse out of the pores. In contrast, as the aqueous solubility of the salts increases with temperature, the temperature of the solution must rise fast enough to avoid a too early generation of a supersaturated solution as water is evaporated. To evaluate this parameter, the impact on the degree of pore filling was analyzed for carbon C infiltrated with a 56 wt% solution of $NaClO_4$ during 66 hours and subsequently filtered, and then dried at three different heating rates. The results are shown in figure 3.30, where the immediate heating rate corresponds to a sample directly placed in an oven pre-heated at 120 °C. No significant differences on degree of pore filling were observed, which suggests that the heating rate has a negligible influence. Hence, a drying step by placing the sample directly in the oven pre-heated at 120 °C was selected for the further studies on this PhD thesis.

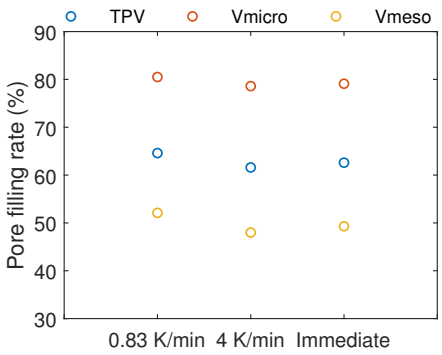

Figure 3.30: Carbon C filled with $NaClO_4$. Influence of the heating rate on the degree of pore filling.

3.5 Influence of the properties of the nanoporous carbons

In order to investigate the influence of the physicochemical properties of nanoporous carbon on the pore filling process, nanoporous carbons with different precursors, textural properties and surface chemistry are considered. The properties of these carbons are detailed in section 3.2. To clarify the discussions, the analysis is divided in three parts. First, the four commercial activated carbons are compared. The carbons C and F5001 and their derivatives with modified surface chemistry are then discussed. Finally, the carbons BPL and FY5 and their overactivated derivatives are compared. The experimental results and the textural properties of all filled carbons discussed in this section are presented in annex F, where it can be observed that the reproducibility of the pore filling process is very good.

3.5.1 Commercial activated carbons

In this section, the influence of the carbon physicochemical properties on the pore filling process is investigated by analyzing the degree of pore filling of carbons C, F5001, BPL and FY5 infiltrated with 40, 50, 56 and 60 wt% sodium perchlorate aqueous solutions. The results are first presented for each carbon and then globally discussed. As discussed above, the infiltration time is set at 66 h, and the filtered samples are directly placed in a natural convection oven pre-heated at 120 °C. The other experimental parameters are described in section 3.4. Optical microscope pictures of the pristine and filled carbons with sodium perchlorate from a 56 wt% aqueous solution are shown in Annex G.

Results

Figure 3.31 and table 3.19 show the degree of pore filling of carbon C infiltrated with 40, 50, 56 and 60 wt% sodium perchlorate aqueous solutions.

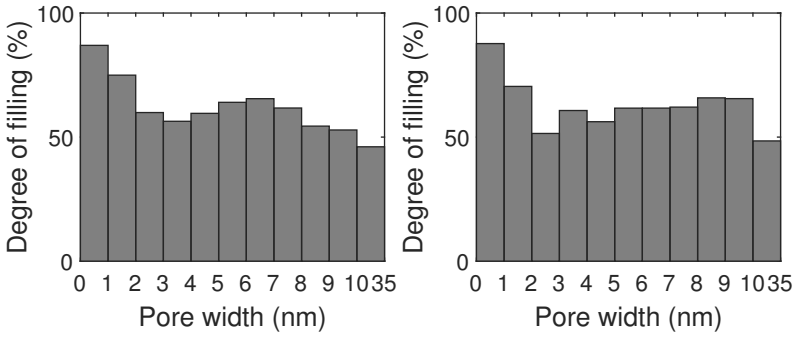

(a) 40 wt%.

(b) 50 wt%.

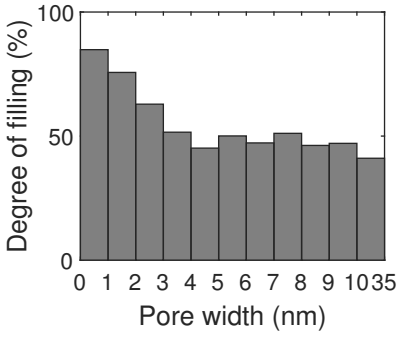

(c) 56 wt%.

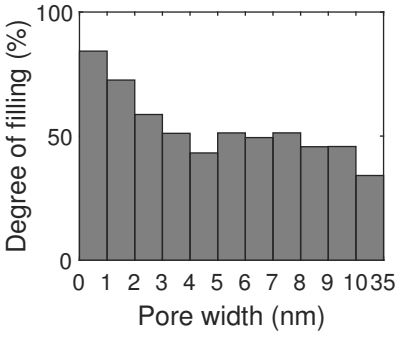

(d) 60 wt%.

Figure 3.31: Influence of the solution concentration on the degree of pore filling for carbon C filled with $NaClO_4$.

Table 3.19: Influence of the solution concentration on the degree of pore filling for carbon C filled with $NaClO_4$; (a) total pore volume at $P/P_0 = 0.985$; (b) by equilibrium QSDFT model; (c) based on MIP data; (d) assuming that the difference of total pore volume determined by N_2 adsorption between the filled and the pristine carbon is filled with $NaClO_4$ at its TMD; (e) assuming that all the salt is in the carbon particles.

Concentration (wt%)	40	50	56	60
Yield (g/g)	1.21	1.52	1.79	2.03
Fraction of TPV filled[a] (%)	66	65	63	60
Fraction of micropores filled[b] (cm^3/g)	79	77	79	77
Fraction of mesopores filled[b]	56	54	51	47
Fraction of macropores filled[c]	8	5	20	12
Apparent density[c] (g/cm^3)	1.04	1.10	1.18	1.22
Calculated yield (g/g)[d]	1.75	1.72	1.67	1.59
Calculated apparent density[e] (g/cm^3)	0.91	1.04	1.15	1.25

Figure 3.32 and table 3.20 show the degree of pore filling of carbon F5001 infiltrated with 40, 50, 56 and 60 wt% sodium perchlorate aqueous solutions.

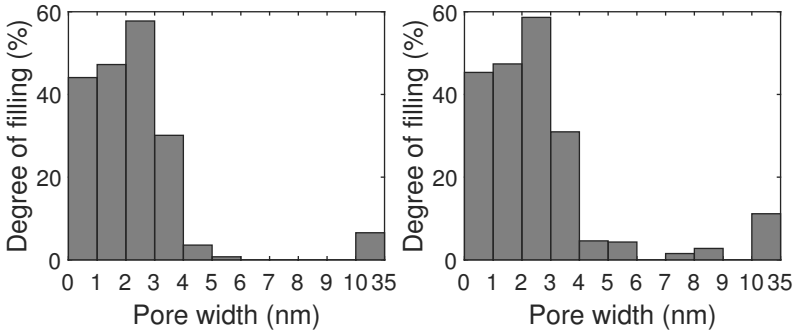

(a) 40 wt%.

(b) 50 wt%.

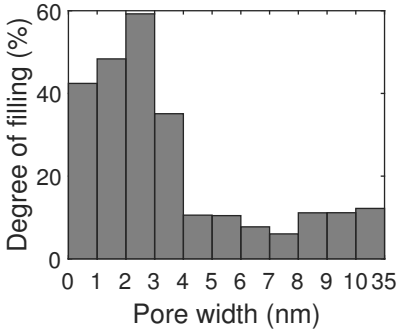

(c) 56 wt%.

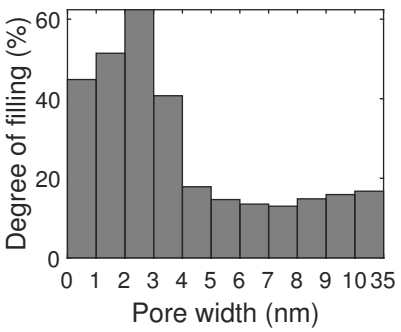

(d) 60 wt%.

Figure 3.32: Influence of the solution concentration on the degree of pore filling for carbon F5001 filled with $NaClO_4$.

Table 3.20: Influence of the solution concentration on the degree of pore filling for carbon F5001 filled with $NaClO_4$; (a) total pore volume at $P/P_0 = 0.985$; (b) by equilibrium QSDFT model; (c) based on MIP data; (d) assuming that the difference of total pore volume determined by N_2 adsorption between the filled and the pristine carbon is filled with $NaClO_4$ at its TMD; (e) assuming that all the salt is in the carbon particles.

Concentration (wt%)	40	50	56	60
Yield (g/g)	1.38	1.77	2.15	2.27
Fraction of TPV filled[a] (%)	32	34	36	39
Fraction of micropores filled[b] (cm^3/g)	46	47	46	49
Fraction of mesopores filled[b]	25	28	30	35
Fraction of macropores filled[c]	3	2	16	29
Apparent density[c] (g/cm^3)	0.88	0.95	1.06	1.11
Calculated yield (g/g)[d]	1.78	1.90	2.00	2.17
Calculated apparent density[e] (g/cm^3)	0.89	1.04	1.18	1.23

Figure 3.33 and table 3.21 show the degree of pore filling of carbon BPL infiltrated with 40, 50, 56 and 60 wt% sodium perchlorate aqueous solutions. No trace of salt on the surface was observed for any of the samples.

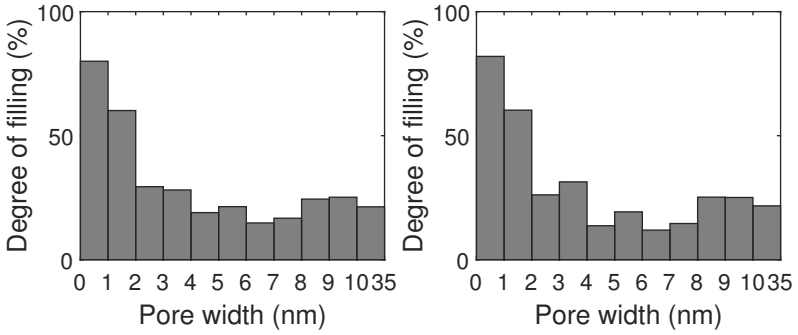

(a) 40 wt%.

(b) 50 wt%.

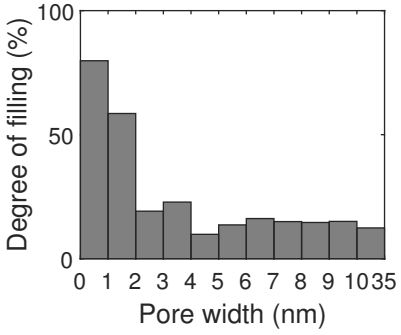

(c) 56 wt%.

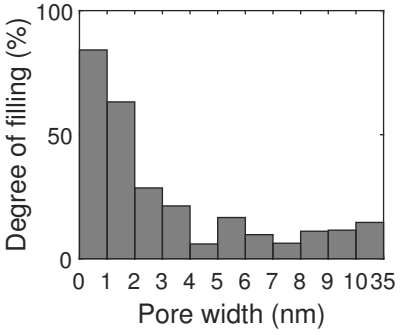

(d) 60 wt%.

Figure 3.33: Influence of the solution concentration on the degree of pore filling for carbon BPL filled with $NaClO_4$.

Table 3.21: Influence of the solution concentration on the degree of pore filling for carbon BPL filled with $NaClO_4$; (a) total pore volume at $P/P_0 = 0.985$; (b) by equilibrium QSDFT model; (c) based on MIP data; (d) assuming that the difference of total pore volume determined by N_2 adsorption between the filled and the pristine carbon is filled with $NaClO_4$ at its TMD; (e) assuming that all the salt is in the carbon particles.

Concentration (wt%)	40	50	56	60
Yield (g/g)	0.53	0.67	0.67	0.81
Fraction of TPV filled[a] (%)	58	60	58	63
Fraction of micropores filled[b] (cm^3/g)	71	72	70	75
Fraction of mesopores filled[b]	19	23	20	23
Fraction of macropores filled[c]	0	6	27	31
Apparent density[c] (g/cm^3)	1.21	1.30	1.34	1.42
Calculated yield (g/g)[d]	0.84	0.87	0.84	0.91
Calculated apparent density[e] (g/cm^3)	1.22	1.34	1.34	1.45

Figure 3.34 and table 3.22 show the degree of pore filling of carbon FY5 infiltrated with 40, 50, 56 and 60 wt% sodium perchlorate aqueous solutions. No trace of salt on the surface was observed for any of the samples.

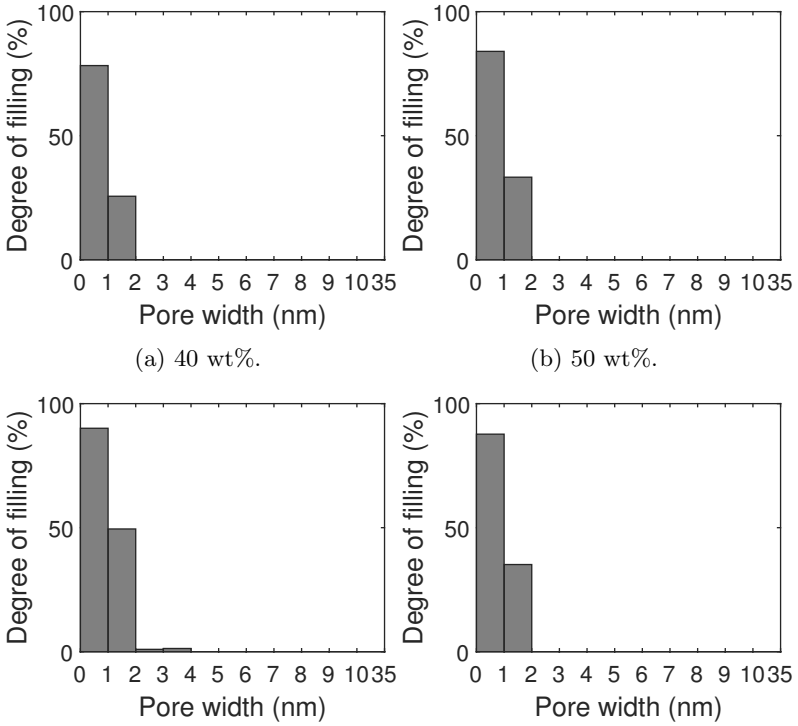

(a) 40 wt%. (b) 50 wt%.

(c) 56 wt%. (d) 60 wt%.

Figure 3.34: Influence of the solution concentration on the degree of pore filling for carbon FY5 filled with $NaClO_4$.

Table 3.22: Influence of the solution concentration on the degree of pore filling for carbon FY5 filled with $NaClO_4$; (a) total pore volume at $P/P_0 = 0.985$; (b) by equilibrium QSDFT model; (c) based on MIP data; (d) assuming that the difference of total pore volume determined by N_2 adsorption between the filled and the pristine carbon is filled with $NaClO_4$ at its TMD; (e) assuming that all the salt is in the carbon particles.

Concentration (wt%)	40	50	56	60
Yield (g/g)	0.32	0.38	0.46	0.54
Fraction of TPV filled[a] (%)	63	64	74	68
Fraction of micropores filled[b] (cm^3/g)	78	80	82	82
Fraction of macropores filled[c]	37	47	58	53
Apparent density[c] (g/cm^3)	1.38	1.49	1.51	1.53
Calculated yield (g/g)[d]	0.49	0.50	0.57	0.53
Calculated apparent density[e] (g/cm^3)	1.30	1.36	1.44	1.52

Discussion

The interpretation of these results is quite complex. On the one hand, the respective potential contributions of variable density and pore blocking to the pore filling characterization are interdependent and cannot be separately quantified. On the other hand, the carbons differ in terms of textural properties and surface chemistries and both effects are difficult to discuss independently. This latter issue motivated the synthesis of modified carbons to isolate the influences of these parameters, which is discussed in the next sections. However, some general trends can be observed when comparing the difference in pore filling of the commercial activated carbons with different solution concentrations.

The difference in yield observed between the carbons is directly related to their respective pore volume. As the filtering step is always performed in the same way, the volume of the retained solution mainly depends on the pore volume of the carbon particles. For the same reason, the difference in yield observed between the different concentrations is directly related to the increasing amount of salt with the concentration in the same volume.

For all carbons, the observed degree of pore filling does not seem to depend on the concentration of the solution and the related yield, as intuitively expected given the significant differences in yield. The comparison between the experimental yield and that calculated by assuming that the difference in total pore volume (as determined by N_2 adsorption) between the filled and the pristine carbon is filled with $NaClO_4$ at its TMD is an useful tool to discuss this point. For carbons C and F5001 at the lowest concentrations and for carbons BPL and FY5 at all concentrations, pore blocking appears to be significant. At high concentrations for carbons C, F5001 and BPL, some salt crystallized in the macropores whereas it is the case for all concentrations for FY5. This is the combination of pore blocking and macropore filling that leads to the same observed degree of pore filling for all concentrations, despite the difference in yield. The presence of salt in the porosity at a very different density than its TMD cannot be excluded but is unlikely to be significant.

The degree of pore filling globally appears to depend on the pore width and is significantly higher for micropores and small mesopores than for wider pores. This shows that the assumption of a preferential contraction of the solution in the micro and the mesopores upon solvent evaporation must be nuanced. The driving force of the diffusion of the solution into these pores is the capillary effect resulting from the intermolecular interactions with the pore walls. With the exception of the carbon F5001 that will be later discussed, the degree of pore filling progressively decreases with pore width. It drops moreover significantly from pore widths of 3-4 nm for all carbons. This suggests that, whereas the assumption of capillary contraction seems globally to be valid for the smallest pores, the capillary driving force becomes too weak from pores wider than 3-4 nm to effectively lead to selective crystallization in the whole micro and mesoporosity. The presence of salt in the macropores and on the surface of the grains, while all the pores are not optimally filled, is the consequence of this limitation. This could be related to the origin of the definition of a micropore, i.e. a pore into which the dispersion force fields of the opposite walls superposes and lead to strong intermolecular interactions with the adsorbate [77]. Even if the effect is progressive and effective up to pore widths of 3-4 nm, the same reason can be proposed to justify the higher degree of pore filling in the micropores and the smallest mesopores than in the rest of the porosity observed in this work. For carbon FY5, significant macropore filling is also observed for all concentrations. This suggests that the assumption of preferential contraction in the micropores is not

relevant for this carbon, probably due to its very narrow microporosity which slows down or prevents the diffusion of the salt in the micropores when the solvent is evaporated.

The textural properties seem to have an influence on pore blocking, as it appears to be more significant for microporous carbons in general and especially for FY5 which has the narrowest microporosity, whereas no evidence of significant pore blocking is observed for carbons C and F5001 excepted for the lowest concentrations. This confirms the intuitive assumption that pore blocking is more prone to be significant for tortuous microporous network than for carbons with a more opened porous network and a well developed mesoporosity.

The surface chemistry also appears to play a role in the pore filling process. Carbon C, which has a surface containing a large number of oxygen-containing groups, presents a higher degree of mesoporous filling than carbon F5001 which has a surface with virtually no functional groups. The lower degree of pore filling of the micropores than of the small mesopores observed for carbon F5001 could furthermore be related to the strongly hydrophobic nature of its surface. It therefore appears that the surface chemistry also influences the preferential contraction of the solution in the micro and mesopores upon solvent evaporation, most likely via specific intermolecular interactions between the aqueous solution and the polar functional groups on the surface which reinforces the capillary effect. This is related to the concept of wettability of carbon pore walls. It can also not be excluded that the smallest pores of carbon F5001 were not filled by the solution during the infiltration step as the result of a high interfacial free energy between the solution of high ionic strength and the highly hydrophobic carbon surface.

3.5.2 Derivatives with modified surface chemistry

In this section, the influence of the surface chemistry on the pore filling process is investigated by analyzing the degree of pore filling of carbons C and its thermally reduced derivatives and of carbon F5001 and its chemically oxidized derivatives with a 56 wt% sodium perchlorate aqueous solution. This intermediate concentration was chosen based on the results of section 3.5.1. The results are first presented and then discussed. The infiltration time is set at 66 h, and the filtered samples are directly placed in a natural convection oven pre-heated at 120 °C. The other experimental parameters are described in section 3.4.

Results

Figure 3.35 and table 3.23 show the degree of pore filling of carbons C and its thermally reduced derivatives at 300 and 600 °C (C-R300 and C-R600) infiltrated with a 56 wt% sodium perchlorate aqueous solution. No traces of salt were observed on the surface of the grains.

Table 3.23: Characterization of the degree of pore filling of carbon C and its derivatives filled with $NaClO_4$; (a) total pore volume at $P/P_0 = 0.985$; (b) by equilibrium QSDFT model; (c) based on MIP data; (d) assuming that the difference in total pore volume determined by N_2 adsorption between the filled and the pristine carbon is filled with $NaClO_4$ at its TMD; (e) assuming that all the salt is in the carbon particles.

Carbon	C	C-R300	C-R600
Yield (g/g)	1.79	2.12	1.50
Fraction of TPV filled[a] (%)	63	44	26
Fraction of micropores filled[b] (cm^3/g)	79	57	39
Fraction of mesopores filled[b] (cm^3/g)	51	34	15
Fraction of macropores filled[c]	20	20	19
Apparent density[c] (g/cm^3)	1.18	1.27	1.06
Calculated yield (g/g)[d]	1.67	1.23	0.61
Calculated apparent density[e] (g/cm^3)	1.15	1.25	1.15

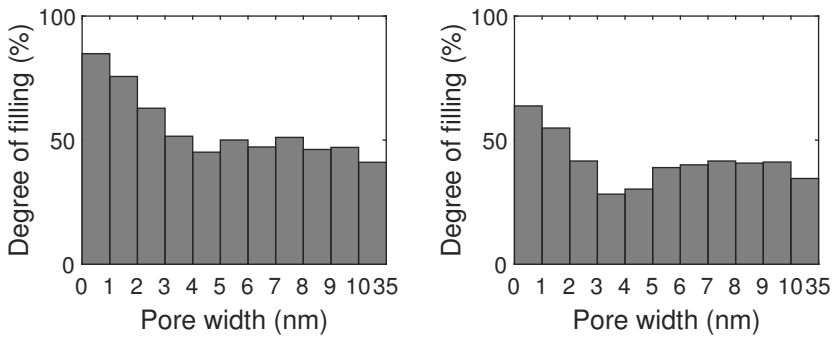

(a) Pristine carbon C.

(b) C-R300.

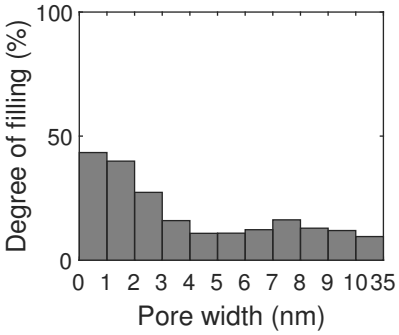

(c) C-R600.

Figure 3.35: Degree of pore filling of carbon C and its derivatives filled with $NaClO_4$.

Figure 3.36 and table 3.24 show the degree of pore filling of carbon F5001 and its chemically oxidized derivatives with ammonium persulfate and nitric acid (F5001-APS and F5001-HN) infiltrated with a 56 wt% sodium perchlorate aqueous solution. Whereas sodium perchlorate crystals were visible on the surface of carbon F5001, the other filled carbons look exactly as the empty ones.

Table 3.24: Characterization of the degree of pore filling of carbon F5001 and its derivatives filled with $NaClO_4$. (a) total pore volume at $P/P_0 = 0.985$. (b) by equilibrium QSDFT model. (c) based on MIP data. (d) assuming that the difference of TPV determined by N_2 adsorption between the filled and the pristine carbon is filled with $NaClO_4$ at its TMD. (e) assuming that all the salt is in the carbon particles.

Carbon	F5001	F5001-APS	F5001-HN
Yield (g/g)	2.15	1.69	2.04
Fraction of TPV filled[a] (%)	36	88	47
Fraction of micropores filled[b] (cm^3/g)	46	99	58
Fraction of mesopores filled[b] (cm^3/g)	30	79	40
Fraction of macropores filled[c]	16	84	52
Apparent density[c] (g/cm^3)	1.06	1.87	1.28
Calculated yield (g/g)[d]	2.00	2.94	2.43
Calculated apparent density[e] (g/cm^3)	1.18	1.69	1.24

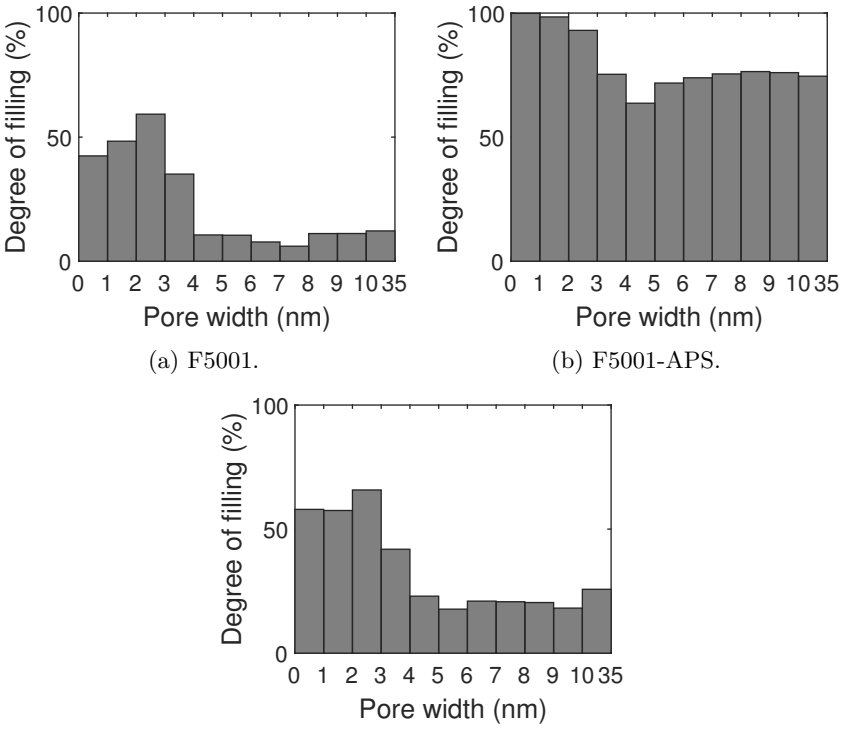

(a) F5001.

(b) F5001-APS.

(c) F5001-HN.

Figure 3.36: Degree of pore filling of carbon F5001 and its derivatives filled with $NaClO_4$.

Discussion

The influence of the surface chemistry is demonstrated as the results globally show that a more developed surface chemistry leads to a higher degree of pore filling. The moderate differences in yield between the pristine carbons and their derivatives are in good agreement with the slight difference in textural properties caused by the treatments. Therefore the influence of the surface chemistry on the degree of pore filling is discussed in this section.

Carbon C-R300 differs from carbon C as its surface presents less carboxylic acid and low-temperature decomposing carbonyl groups, but the overall difference in oxygen content and amount of oxygen-containing functional groups is rather limited. However, this small difference in surface chemistry leads to a significant decrease of the degree of pore filling. As it is likely to be governed by the effectiveness of the preferential contraction of the solution in the nanopores upon drying, a higher degree of pore filling is presumably related to an increased wettability of the pore walls due to the presence of polar functional groups on the surface. Even if all the polar groups contribute to this phenomenon to some extent, they will most likely have different affinity for the aqueous solution, depending on their geometry and of their environment. It is interesting to point out that carboxylic acid has been reported as having the highest affinity towards water molecules from all the typical oxygen-containing functional groups present on carbon materials [99]. This was attributed to the accessibility of the carboxylic groups to water molecules to the one hand, and to the perfect match between the water molecule and the carboxylic group for hydrogen bond formation [99]. Even if this should be nuanced when applied to the present case, these results support the assumption that carboxylic acid may play an important role in the pore filling process. However, although carbon F5001-HN contains almost twice as much carboxylic acid groups than carbon C, significantly more carbonyl groups decomposing at low temperature and while the amounts of the other functional groups are comparable, its overall degree of pore filling significantly lower and exhibit only a slight improvement with respect to the carbon F5001 which presents almost no oxygen-containing surface functional groups. This reflects the complexity of the pore filling process and the role of the process parameters and the other properties of the carbon materials (i.e., their textural properties and precursor).

Carbon C-R600 is significantly de-functionalized with respect to carbon C, and this results in a very low degree of pore filling, in overall comparable to that of carbon F5001. Whereas it is difficult to attribute this feature to a particular surface functional groups as a variety of them was removed during

the heat treatment of carbon C to synthesized carbon C-R600, this suggests that some extent of surface polar groups is needed to achieve high degrees of pore filling.

For carbon F5001-APS which is strongly oxidized, the calculated yield is dramatically higher than the measured yield, certainly taking into account the amount of salt in the macropores of about 0.4 g/g. This indicates that pore blocking is significant and makes the analysis of the degree of pore filling difficult. The same feature is observed for carbon F5001-HN, but to a lesser extent. The wet oxidization process may promote pore blocking during the pore filling process, presumably as the result of interaction with residues of the treatment. The presence of these residues is supported by the non-identified elemental in the elemental analysis.

These results support the assumption, already mentioned in section 3.5.1, that the polar functional groups on the surface play an important role by promoting the diffusion of the solution in the micro and mesopores during solvent evaporation, hereby leading to a higher degree of filling of these pores. However, they do not allow to determine the respective affinity of the different surface functional groups.

3.5.3 Derivatives with modified textural properties

In this section, the influence of the textural properties on the pore filling process is investigated by analyzing the degree of pore filling of carbons BPL and FY5 and their overactivated derivatives with a 56 wt% sodium perchlorate aqueous solution. This intermediate concentration was chosen based on the results of section 3.5.1. The results are first presented for each carbon and then globally discussed. The infiltration time is set at 66 h, and the filtered samples are directly placed in a natural convection oven pre-heated at 120 °C. The other experimental parameters are described in section 3.4.

Results

Figure 3.37 and table 3.25 show the degree of pore filling of carbons BPL and its overactivated derivatives with burn-off of 18 and 37 wt% (BPL-18 and BPL-37) infiltrated with a 56 wt% sodium perchlorate aqueous solution.

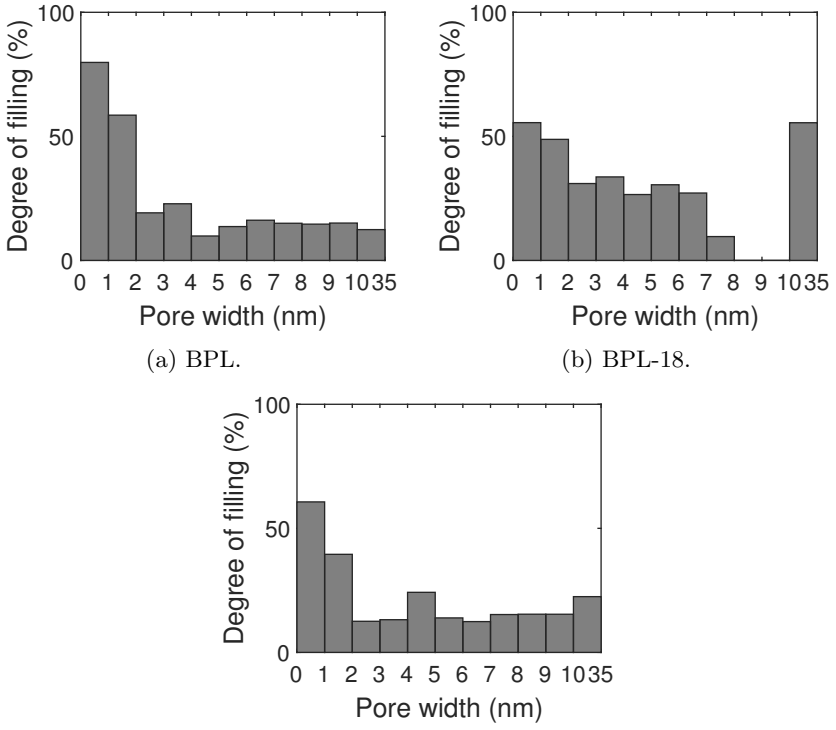

(a) BPL.

(b) BPL-18.

(c) BPL-37.

Figure 3.37: Degree of pore filling of carbon BPL and its derivatives filled with $NaClO_4$.

Table 3.25: Characterization of the degree of pore filling of carbon BPL and its derivatives filled with $NaClO_4$; (a) total pore volume at $P/P_0 = 0.985$; (b) by equilibrium QSDFT model; (c) based on MIP data; (d) assuming that the difference in total pore volume determined by N_2 adsorption between the filled and the pristine carbon is filled with $NaClO_4$ at its TMD; (e) assuming that all the salt is in the carbon particles.

Carbon	BPL	BPL-18	BPL-37
Yield (g/g)	0.67	0.98	1.28
Fraction of TPV filled[a] (%)	58	44	38
Fraction of micropores filled[b] (cm^3/g)	70	49	53
Fraction of mesopores filled[b] (cm^3/g)	20	34	18
Fraction of macropores filled[c]	27	30	39
Apparent density[c] (g/cm^3)	1.34	1.35	1.25
Calculated yield (g/g)[d]	0.84	0.69	0.77
Calculated apparent density[e] (g/cm^3)	1.34	1.38	1.30

Figure 3.38 and table 3.26 show the degree of pore filling of carbons FY5 and its overactivated derivatives with burn-off of 21 and 57 wt% (FY5-21 and FY5-57) infiltrated with a 56 wt% sodium perchlorate aqueous solution.

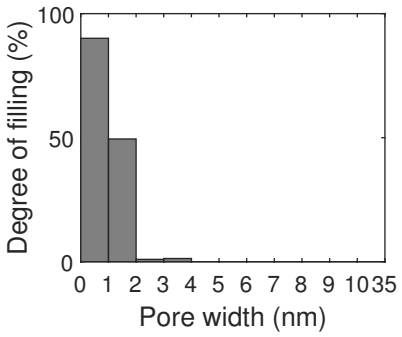

(a) FY5.

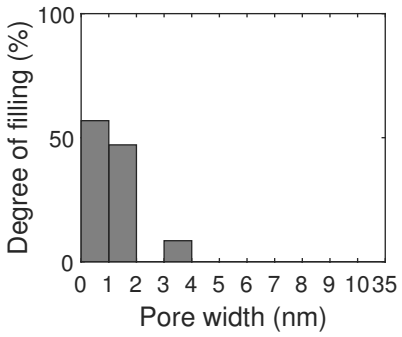

(b) FY5-21.

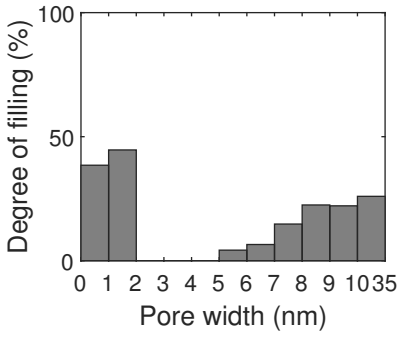

(c) FY5-57.

Figure 3.38: Degree of pore filling of carbon FY5 and its derivatives filled with $NaClO_4$.

Table 3.26: Characterization of the degree of pore filling of carbon FY5 and its derivatives filled with $NaClO_4$; (a) total pore volume at $P/P_0 = 0.985$; (b) by equilibrium QSDFT model; (c) based on MIP data; (d) assuming that the difference in total pore volume determined by N_2 adsorption between the filled and the pristine carbon is filled with $NaClO_4$ at its TMD; (e) assuming that all the salt is in the carbon particles.

Carbon	FY5	FY5-21	FY5-57
Yield (g/g)	0.46	0.72	1.08
Fraction of TPV filled[a] (%)	74	45	38
Fraction of micropores filled[b] (cm^3/g)	82	53	41
Fraction of mesopores filled[b] (cm^3/g)	-	-	6
Fraction of macropores filled[c]	58	47	10
Apparent density[c] (g/cm^3)	1.51	1.31	1.32
Calculated yield (g/g)[d]	0.57	0.52	0.78
Calculated apparent density[e] (g/cm^3)	1.44	1.43	1.36

Discussion

The significant difference in yield appears to be in very good agreement with the increase in total pore volume due to the overactivation. This supports the assumption, already mentioned in section 3.5.1, that the volume of the retained solution during the filtration step, and thus the yield, is governed by the pore volume of the carbon particles.

However, the overall pore filling efficiency of both overactivated carbons is significantly lower than that of the pristine carbon BPL even if the same preferential filling of the smallest pores is however observed for all carbons. For the overactivated derivatives, the calculated yield is significantly lower than the measured yield. This indicates the presence of a significant fraction of the salt in the macropores or on the surface. The estimated masses of salt in the macropores of about 0.25 and 0.50 g/g for carbons BPL-18 and BPL-37, respectively, are in very good agreement with the reported difference between the experimental and the calculated yield. This suggests that $NaClO_4$ is crystallized in the porosity of these carbons at a density close to its TMD. Even if pore blocking cannot be excluded on this basis, it appears not to be significant. The observed decrease in degree of pore filling between BPL and its overactivated derivatives is attributed to the modification of their surface chemistry during the thermal treatment. As detailed in section 3.2, this treatment partially de-functionalizes the carbon by removing most of the carboxylic acid, carbonyl and phenol surface functionalities. As discussed above in section 3.5.2, even a rather small difference in surface chemistry can have important consequences on the degree of pore filling. The carboxylic acid surface functionalities are also presumed to have a high affinity for the solution and to have a significant contribution to the improved wettability of the pore walls. In these conditions, it is difficult to discuss the development of the mesoporosity of BPL upon overactivation on the effectiveness of the pore filling process, as the modification of the surface chemistry interferes. These results however indicate that sodium perchlorate can effectively crystallize in micropores, as seen with pristine BPL, even if the mesopore volume is rather small. As the mesoporous volume increases with overactivation, a preferential filling of the smallest pores is moreover observed, as already reported in section 3.5.1. This supports the hypothesis that the higher degree of pore filling of the smallest pores is related to the stronger dispersive intermolecular interactions in these pores that promote the diffusion of the solution in these pore when the solvent is evaporated.

For FY5, the apparent overall pore filling efficiency of both overactivated carbons is significantly lower than that of the pristine carbon FY5. However, as discussed in section 3.5.1, the interpretation of the degree of pore filling of pristine carbon FY5 must be nuanced as pore blocking is significant. For the overactivated derivatives, the calculated yield is significantly lower than the measured yield. This indicates the presence of a significant fraction of the salt in the macropores or on the surface. The estimated masses of salt in the macropores of about 0.25 and 0.10 g/g for carbons FY5-21 and FY5-57, respectively, are of the same order of magnitude that the reported difference between the experimental and the calculated yield. This suggests that $NaClO_4$ is crystallized in the porosity of these carbons at a density close to its TMD. Even if pore blocking cannot be excluded on this basis, it appears not to be significant. The overactivation of FY5 led to an overall enlargement of the micropores, and to a broadening of the micropore size distribution which includes large micropores. Notwithstanding the effects of pore blocking which makes the comparison of the effectiveness of the pore filling process complex,

these result indicate that, whereas pore blocking was significant for a narrow distribution of micropores of width close to 1 nm, it was not observed when after that the porous network was widening upon overactivation. This supports the hypothesis that narrow micropores promote pore blocking during the crystallization of the salt.

3.6 Partial conclusions

The pore filling process by crystallization after solution contraction upon drying was deeply investigated. Even if the efficiency of the process strongly depends on the nature of the oxidizing salt and the carbon, it has been shown that this process successfully allows high degree of pore filling to be achieved with a selective filling of the micro and mesopores. Most of the salt crystallized was in pores of width smaller than 4 nm, which corresponds to the objective of this work of ensuring a homogeneous mixture of the oxidizing and the reducing agent at the nanometer scale.

When investigating the influence of the oxidizing agent, only sodium perchlorate has shown an ability to selectively crystallize in the smallest pores and to achieve a pore filling yield which confers a potential energetic character to the filled carbons. Only this salt is therefore further considered in this discussion.

The influences of infiltration time and heating rate on the efficiency of the pore filling process were also investigated and optimal values were defined.

The influence of the physicochemical properties of the pristine carbons was studied. However, the interpretation of the results is quite difficult, as the respective potential contributions of variable density and pore blocking to the pore filling characterization are interdependent and cannot be separately quantified. Generally speaking, the yield of the pore filling process is very well correlated with the pore volume of the pristine carbons, but both textural properties and surface chemistry appear to have a significant influence on the degree of pore filling. The results suggest that the crystallization of the salt occurs selectively in pore of width smaller than 3-4 nm, but than the capillary driving force becomes too weak in larger pores to effectively lead to a preferentially filling of these pores with respect to the macropores when the solvent is progressively evaporated. This is presumably related to the stronger dispersive intermolecular forces in the micropores and the smallest mesopores where the force fields of the opposite walls can superpose. Finally, the results show that the degree of pore filling depends significantly on the surface chemistry of the carbon materials. Even if the respective contribution of the different surface functionalities remain unclear, some results suggest that carboxylic acid may play an important role in improving the wettability of the carbon walls, hereby enhancing the effectiveness of the pore filling process. It has moreover been shown that some extent of polar functional groups appears to be needed to achieve a high degree of pore filling. This is presumably related to an overall lower interfacial free energy between the concentrated salt solution and the pore walls in the presence of polar surface groups which promotes the preferential filling of the micro and the mesopores when the solvent is evaporated.

Regarding the feasibility of the concept of energetic materials based on nanoporous carbon filled with an oxidizing salt, the pore filling yields of filled carbons C and F5001 and of some of their derivatives are in line with potential application as energetic materials in term of oxygen balance. Especially for carbon C, the smallest pores are selectively filled and the overall degree of pore filling is high. The pore filling process developed in this chapter therefore fulfils the defined objectives of a pore filling yield high enough for potential energetic applications and a selective filling of the nanopores.

Chapter 4

Energetic characterization

In this chapter, the energetic materials based on nanoporous carbon studied in this PhD thesis are first characterized by thermal analysis in section 4.1. Their sensitivities are then analyzed in section 4.2, and the basic detonation properties of a selected energetic material are evaluated in section 4.3. Partial conclusions (section 4.4) complete the chapter.

4.1 Thermal analysis

In this section, the thermal properties of nanoporous carbons filled with oxidizing agents are studied by differential scanning calorimetry (DSC) and thermogravimetric analysis (TGA). The experimental methods are detailed in chapter 2. All the experimental results are shown in annex H.

The same approach is followed in this section than in chapter 3. The thermal properties of carbons C and F5001 filled with sodium perchlorate, potassium nitrate and ammonium perchlorate are first investigated to highlight the influence of the oxidizing agent on the decomposition mechanism. Then, the thermal properties of the four commercial activated carbons (C, F5001, BPL and FY5) filled with sodium perchlorate are investigated to study the influence of both the nature of the carbon and the concentration of the solution used in the pore filling process. In order to investigate separately the influence of the surface chemistry and the textural properties of the carbons, the thermal properties of the carbon derivatives obtained by thermal reduction, chemical oxidation and overactivation are discussed. Finally, the decomposition kinetics of carbons C and F5001 filled with sodium perchlorate are investigated and compared to that of the corresponding physical mixtures at the μm scale to highlight the influence of the mixture at the nm scale.

4.1.1 Results

Figures 4.1 and 4.2 show the DSC curves of bare oxidizing agents ($NaClO_4$, KNO_3 and NH_4ClO_4) and of carbons C and F5001 filled with these oxidizing agents, respectively. During the infiltration step of the pore filling process, saturated solutions of KNO_3 and NH_4ClO_4 at room temperature and a 56 wt% solution of $NaClO_4$ are used. Tables 4.1 and 4.2 show the corresponding onset temperature, peak temperature and heat of decomposition calculated based on these results for the filled carbons.

Table 4.1: DSC analysis of carbon C filled with $NaClO_4$ (from a 56 wt% aqueous solution) and KNO_3 and NH_4ClO_4 (from saturated solutions).

Oxidizer	$NaClO_4$	KNO_3	NH_4ClO_4
Onset temperature[a] (°C)	299	344	265
Peak temperature[a] (°C)	352	360	316
Heat of decomposition[a] (J/g)	3545	1303	1399

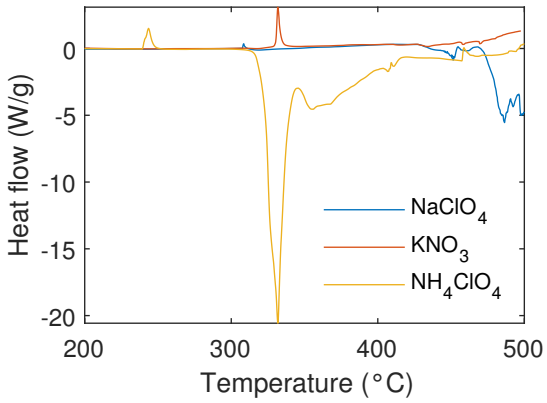

Figure 4.1: DSC results of bare oxidizers.

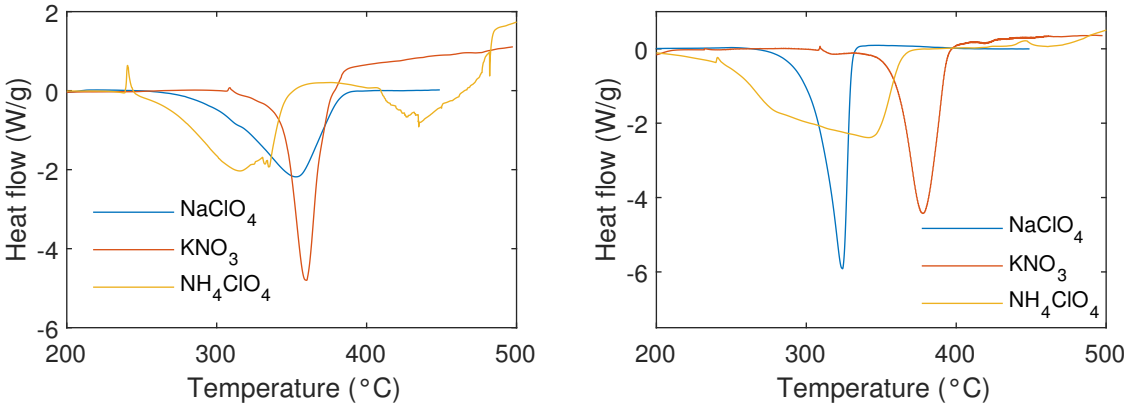

(a) C.

(b) F5001.

Figure 4.2: DSC results of carbon C and F5001 filled with $NaClO_4$ (from a 56 wt% aqueous solution) and KNO_3 and NH_4ClO_4 (from saturated solutions).

Table 4.2: DSC analysis of carbon F5001 filled with $NaClO_4$ (from a 56 wt% aqueous solution) and KNO_3 and NH_4ClO_4 (from saturated solutions).

Oxidizer	$NaClO_4$	KNO_3	NH_4ClO_4
Onset temperature[a] (°C)	306	345	243
Peak temperature[a] (°C)	326	378	342
Heat of decomposition[a] (J/g)	3210	1208	2005

It is observed that the melting of $NaClO_4$ and its decomposition occur almost simultaneously at a temperature of about 470 °C. For both carbons filled with $NaClO_4$, the onset temperatures are of about 300 °C, i.e. approximately 170 °C lower that bare $NaClO_4$.

The melting of KNO_3 takes place at 330 °C and its boiling and decomposition occur simultaneously from a temperature of about 420 °C. For both carbons filled with KNO_3, the results show that the onset of the decomposition occurs just after the melting of the bare KNO_3 at temperatures of about 345 °C.

The decomposition of NH_4ClO_4 takes place at 330 °C. For both carbons filled with NH_4ClO_4, the onset temperatures are of about 240-260 °C, i.e. approximately 70-90 °C lower that bare NH_4ClO_4.

These results show that the onset of the decomposition of the filled carbons occurs at a significantly lower temperature than that of the bare oxidizing agents. It is also observed that the decomposition peaks of both carbons present a long tail towards the low temperatures, with differences between the onset and the peak temperatures up to 50 °C. This effect is more significant for $NaClO_4$ and NH_4ClO_4 than for KNO_3. The results show that the heat of decomposition is significantly higher for $NaClO_4$ than for NH_4ClO_4 and KNO_3 for both carbons.

Figure 4.3 shows the DSC and DTG (derivative thermogravimetry) curves of the four commercial activated carbons (C, F5001, BPL and FY5) filled with $NaClO_4$ from a 56 wt% aqueous solution. The onset temperatures, the peak temperatures and the heat of decomposition determined based on the DSC curves are shown in figure 4.4 for these carbons filled with $NaClO_4$ at different concentrations (40, 50, 56 and 60 wt%). The mass loss after the decomposition (at 450 °C) and the peak temperature of the DTG curves based on the TGA analysis are shown in figure 4.5.

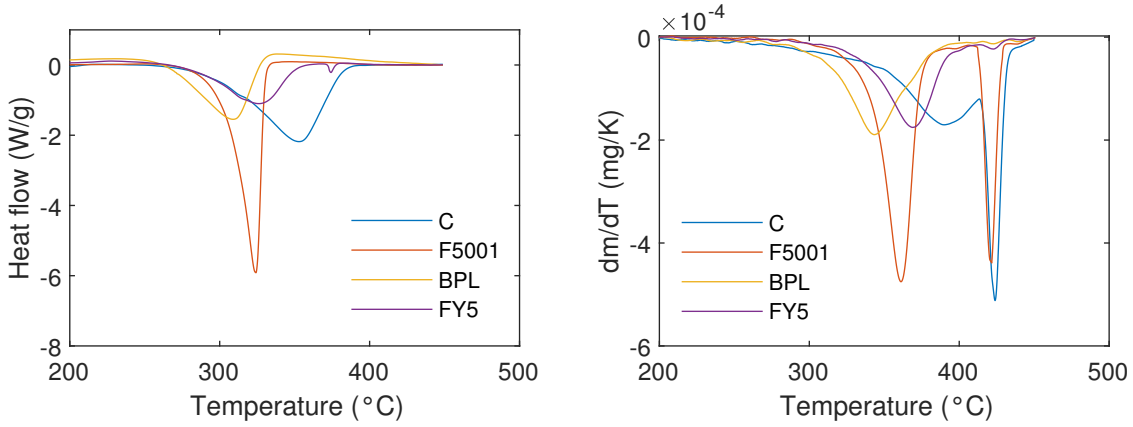

Figure 4.3: DSC and DTG results for carbons C, F5001, BPL and FY5 filled with sodium perchlorate from a 56 wt% aqueous solution.

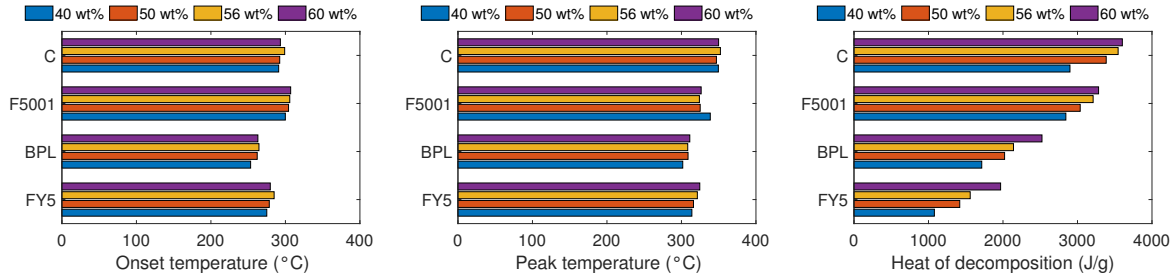

Figure 4.4: Onset temperature, peak temperature and heat of decomposition of carbons C, F5001, BPL and FY5 filled with sodium perchlorate from aqueous solutions of different concentrations determined by DSC.

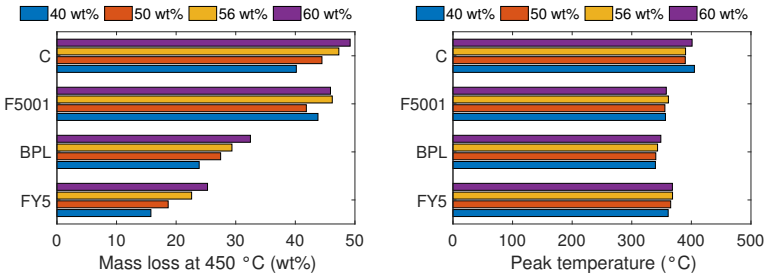

Figure 4.5: Mass loss after the decomposition (at 450 °C) determined by TGA and peak temperature of the corresponding DTG curves of carbons C, F5001, BPL and FY5 filled with sodium perchlorate from aqueous solutions of different concentrations.

For all carbons, it is first observed that the onset temperature determined by DSC and the peak temperatures determined by DSC and DTG do not depend on the concentration of the solution. However, both the heat of decomposition determined by DSC and the mass loss after decomposition progressively increase when the concentration of the solution increases, for all carbons.

Small differences in onset and peak temperatures are observed between the carbons, with a slightly earlier decomposition in the case of BPL. However, the decomposition temperature and the mass loss after decomposition significantly differ between the carbons for the same solution concentration. The DSC and DTG curves have very comparable aspects, with a global shift to higher temperatures observed for the DTG with respect to the DSC curves. A second peak is also observed for carbons C and F5001 at a temperature of about 420 °C. Such a peak is not observed on the DSC curves. It is also observed that the decomposition peaks of all carbons present a long tail towards the low temperatures, with differences between the onset and the peak temperatures up to 50 °C. This effect is more significant for carbons C, BPL and FY5 than for carbon F5001 for which the decomposition peak is sharper.

Figures 4.6 and table 4.3 show the results of the thermal analysis performed on carbon C and its derivatives obtained by thermal treatment (C-R300 and C-R600). These results show that the onset temperature of the decomposition becomes progressively higher with the degree of thermal reduction, which has a smaller effect on the peak temperatures. However, the heat of decomposition and the mass loss after decomposition are very comparable for carbon C and its derivatives. Whereas the decomposition peak of carbon C presents a long tail towards lower temperatures, the peaks become progressively sharper with the extent of the thermal reduction.

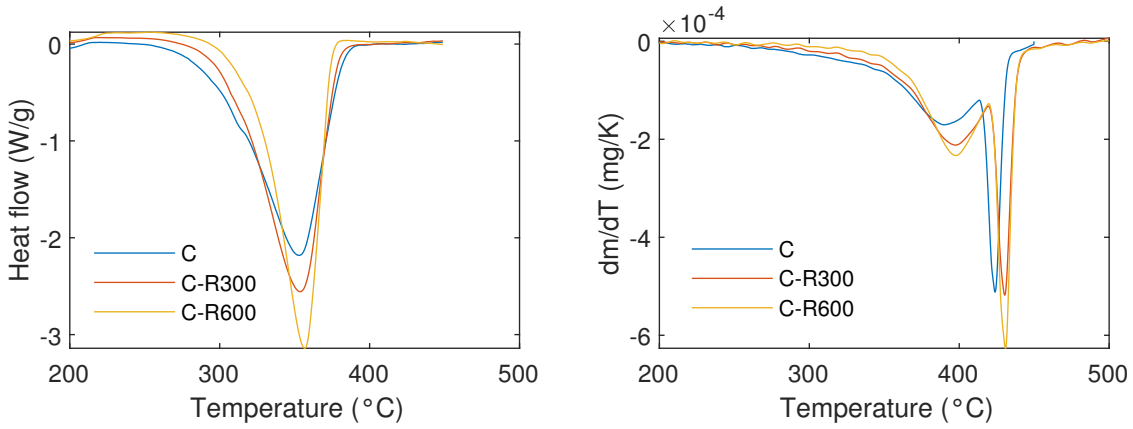

Figure 4.6: DSC and DTG results for carbon C and its derivatives obtained by thermal treatment filled with sodium perchlorate from a 56 wt% aqueous solution.

Table 4.3: Characterization of the thermal properties of carbon C and its derivatives obtained by thermal treatment filled with $NaClO_4$ from a 56 wt% aqueous solution ; (a) based on DSC data ; (b) based on TGA data ; (c) based on DTG curve.

Carbon	C	C-R300	C-R600
Onset temperature[a] (°C)	299	305	322
Peak temperature[a] (°C)	352	353	358
Heat of decomposition[a] (J/g)	3545	3530	3470
Mass loss[b] at 450 °C (wt%)	47	49	46
Peak temperature[c]	390	397	397

Figures 4.7 and table 4.4 show the results of the thermal analysis performed on carbon F5001 and its derivatives obtained by chemical oxidation (F5001-APS and F5001-HN). As for carbon C, the onset temperature of the decomposition appears to progressively decrease with the degree of chemical oxidation. For the strongly oxidized carbon F5001-APS, the onset of the decomposition occurs at a temperature 50 °C lower than for the pristine carbon F5001, whereas the moderately oxidized F5001-HN has an intermediate onset temperature. The peak temperatures of filled carbon F5001 and F5001-HN are very comparable, but that of carbon F5001-APS is moderately lower (of 20-40 °C). It is also observed that the decomposition peak of carbon F5001 is sharp, but as for carbon C it appears that the oxidized carbons present a long tail towards lower temperatures and the results show that the tail becomes progressively more pronounced with the extent of the chemical oxidation. The heat of decomposition and the mass

loss after decomposition are very comparable for carbon F5001 and its derivatives, with a slightly higher heat of decomposition and mass loss for carbon F5001-APS than for the two others.

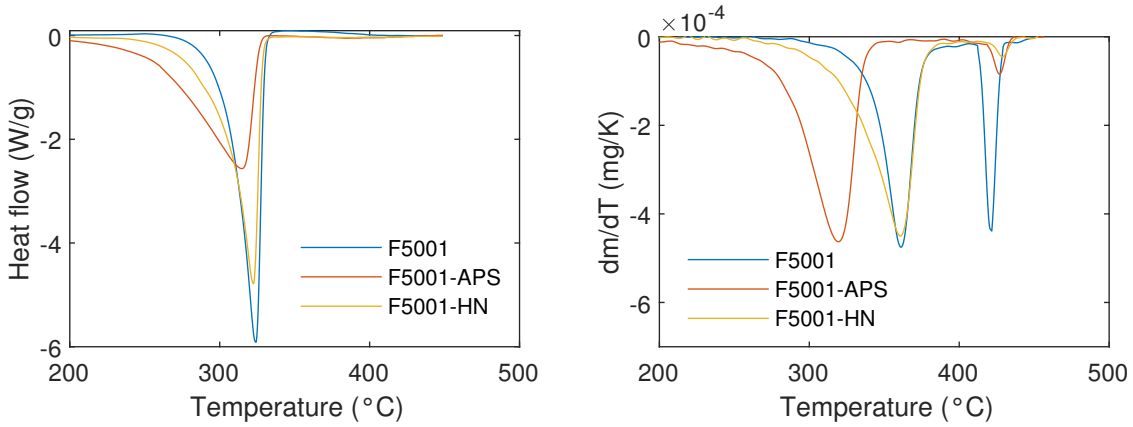

Figure 4.7: DSC and DTG results for carbon F5001 and its derivatives obtained by chemical oxidation filled with sodium perchlorate from a 56 wt% aqueous solution.

Table 4.4: Characterization of the thermal properties of carbon F5001 and its derivatives obtained by chemical oxidation filled with $NaClO_4$ from a 56 wt% aqueous solution ; (a) based on DSC data ; (b) based on TGA data ; (c) based on DTG curve.

Carbon	F5001	F5001-APS	F5001-HN
Onset temperature[a] (°C)	306	255	276
Peak temperature[a] (°C)	326	314	323
Heat of decomposition[a] (J/g)	3210	3461	3291
Mass loss[b] at 450 °C (wt%)	46	53	49
Peak temperature[c]	361	320	361

Figures 4.8 and table 4.5 show the results of the thermal analysis performed on carbon BPL and its derivatives obtained by overactivation (BPL-18 and BPL-37). It is observed that the peak temperature of decomposition is slightly lower for the overactivated derivatives than for the pristine carbon BPL, with a difference of about 10 °C. The mass loss after decomposition and the heat of decomposition seem to increase with the degree of overactivation, and the shape of the decomposition peaks is very comparable for all carbons.

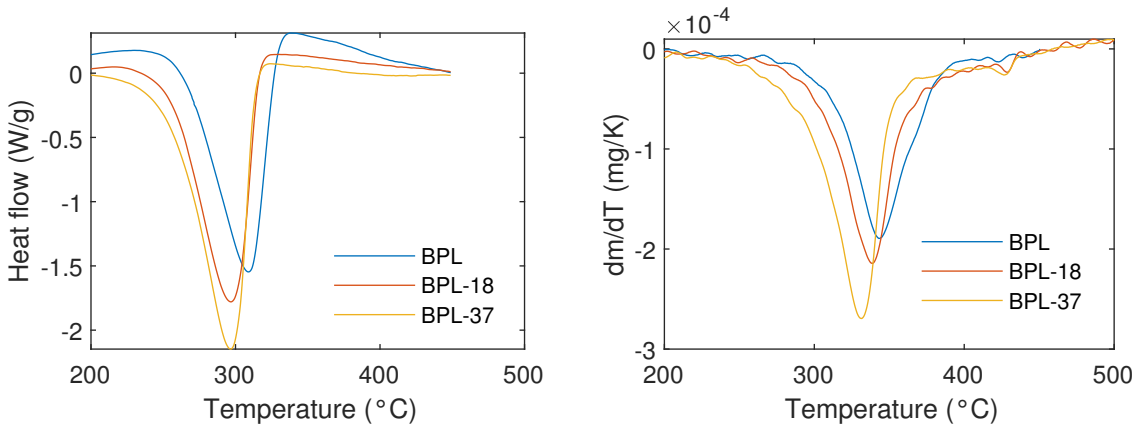

Figure 4.8: DSC and DTG results for carbon BPL and its derivatives obtained by overactivation filled with sodium perchlorate from a 56 wt% aqueous solution.

Table 4.5: Characterization of the thermal properties of carbon BPL and its derivatives obtained by overactivation filled with $NaClO_4$ from a 56 wt% aqueous solution ; (a) based on DSC data ; (b) based on TGA data ; (c) based on DTG curve.

Carbon	BPL	BPL-18	BPL-37
Onset temperature[a] (°C)	264	256	256
Peak temperature[a] (°C)	308	299	297
Heat of decomposition[a] (J/g)	2141	2137	2447
Mass loss[b] at 450 °C (wt%)	29	32	37
Peak temperature[c]	343	338	331

Figures 4.9 and table 4.6 show the results of the thermal analysis performed on carbon FY5 and its derivatives obtained by overactivation (FY5-21 and FY5-57). As for carbon BPL, the results show that the overactivated derivatives exhibit lower onset and peak temperatures for their decomposition reaction than the pristine carbon FY5, with a difference of about 30-40 °C. As already mentioned above, a higher degree of overactivation leads to a larger mass loss after decomposition and a higher heat of decomposition, and the decomposition peak of all carbons have a very comparable shape.

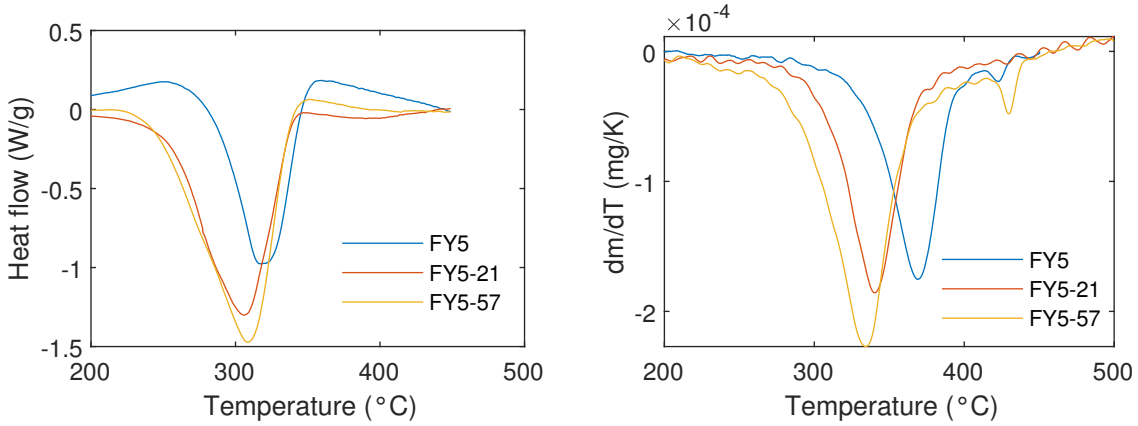

Figure 4.9: DSC and DTG results for carbon FY5 and its derivatives obtained by overactivation filled with sodium perchlorate from a 56 wt% aqueous solution.

Table 4.6: Characterization of the thermal properties of carbon FY5 and its derivatives obtained by overactivation filled with $NaClO_4$ from a 56 wt% aqueous solution ; (a) based on DSC data ; (b) based on TGA data ; (c) based on DTG curve.

Carbon	FY5	FY5-21	FY5-57
Onset temperature[a] (°C)	285	256	245
Peak temperature[a] (°C)	321	306	307
Heat of decomposition[a] (J/g)	1561	1912	2465
Mass loss[b] at 450 °C (wt%)	23	27	36
Peak temperature[c]	368	340	334

Tables 4.7 and 4.8 show the modelling of the decomposition kinetics based on TGA results of carbons C and F5001 filled with sodium perchlorate from a 56 wt% solution compared to that of the corresponding physical mixtures at the μm scale obtained by mixing carbon and oxidizing agent, both milled and sieved between 25 and 50 μm. These results are shown with the corresponding 95 % confidence intervals. This analysis shows that there is no significant difference in the decomposition kinetics between the filled carbons and the corresponding physical mixtures.

Table 4.7: Modelling of the decomposition kinetics of carbon C filled with sodium perchlorate from a 56 wt% aqueous solution, and of the corresponding physical mixture of carbon C and $NaClO_4$, both milled and sieved between 25 and 50 μm, based on TGA data.

Material	Filled carbon	Physical mixture
Activation energy (E_a) (kJ/mol)	163.8 ± 2.0	163.4 ± 6.3
Pre-exponential factor ($\ln A$) (1/min)	27.2 ± 0.4	27.6 ± 1.2

Table 4.8: Modelling of the decomposition kinetics of carbon F5001 filled with sodium perchlorate from a 56 wt% aqueous solution, and of the corresponding physical mixture of carbon F5001 and $NaClO_4$, both milled and sieved between 25 and 50 μm, based on TGA data.

Material	Filled carbon	Physical mixture
Activation energy (E_a) (kJ/mol)	135.3 ± 4.9	130.2 ± 3.6
Pre-exponential factor ($\ln A$) (1/min)	23.4 ± 0.9	22.1 ± 0.7

4.1.2 Discussion

The results globally show that the heat of decomposition and the mass loss after decomposition are in very good agreement with the yield of the pore filling process. This was qualitatively expected, as the yield is directly correlated with the oxygen balance of the materials and therefore to a higher degree of oxidation of the carbon matrix. For each carbon filled with sodium perchlorate, it was moreover shown that the onset temperature and the peak temperatures do not depend on the concentration of the solution used for the infiltration, and therefore do not depend on the yield of the pore filling process. This supports the hypothesis, already stated in chapter 3, of sodium perchlorate filling the pores as continuous blocks. Schematically, some parts of the porosity are presumably filled, whereas other parts are empty. Globally, the material would then present the same qualitative thermal behavior as the result of the contribution of the filled parts which have the same properties, independently of the yield. The empty parts would then be likely to not significantly contribute to the decomposition process, but to lead to lower mass loss and heat of decomposition.

For all oxidizers and carbons, the decomposition of the filled carbons occurs at significantly lower temperatures than that of the bare oxidizing agents, with differences ranging from 70 to 170 °C. The observed differences in the onset and peak temperatures between the different oxidizers moreover indicate that the nature of the oxidizer plays an important role in the decomposition mechanism. However, it appears that the nature of the carbon has also an influence, as moderate differences in thermal properties are observed between different carbons filled with sodium perchlorate. Whereas the decomposition peaks are sharp for carbons with a low extent of surface functionalities, a significant long tail towards the low temperatures appears when the amount of oxygen-containing surface groups increases. Even if the decomposition peak temperatures seem mostly unaffected, this leads to lower onset temperatures. This is presumably related to the thermal stability of the carbon surfaces. Interactions between the gaseous products resulting from the thermal reduction of the carbon surface and the oxidizing agent in the pores could play a role, as the empty carbons with a large amount of surface functionalities show a significant mass loss at temperatures close to the observed decomposition temperatures. Regarding the textural properties, overactivation to significant degree of burn-off have led to a moderate shift of the decomposition peak to lower temperatures, without noticeable difference in shape. This shows that the structure of the porous network of the carbons also play a role in the decomposition mechanism.

The influence of the nanometer scale on the physicochemical properties of the oxidizing agent is difficult to predict, as it could result in lower melting and decomposition temperatures of the oxidizing agents due to the presumably large contribution of the surface energy at this scale. This makes the analysis of the thermal properties of the nanoporous carbons filled with an oxidizing agent more complex. However, it was shown that not only the nature of the oxidizing agent but also that of the nanoporous carbon influence the decomposition mechanism, although to a lesser extent. Regarding the physicochemical properties of the carbons, the surface chemistry and the textural properties both play a role. Even if the confinement of the oxidizing agent in nanopores and the energetic heterogeneity of the nanoporous carbon surface add complexity to the analysis, this denotes a synergistic effect of both the oxidizing agent and the nanoporous carbon on the decomposition mechanism.

The modelling of the decomposition kinetics showed that there are no statistically relevant differences

in decomposition kinetics between the filled carbons and their corresponding physical mixture at the μm scale, for two carbons filled with sodium perchlorate at yields in line with potential applications as energetic materials. These results are quite surprising, as a mixture at nanometer scale was expected to lead to a faster decomposition of the material and to potential applications as energetic materials. It therefore seems that mass transfer is not the rate limiting step of the decomposition mechanism in these conditions. This affirmation must however be nuanced, as it is strictly only valid for a static decomposition in the temperature range of the model (i.e. between 330 and 400 °C), and it cannot be concluded on these bases that the nanometer scale of the mixture has no influence on the decomposition mechanism.

4.2 Sensitivities

The sensitivities of energetic materials are important features regarding their safety. As such, they are one of the most critical properties of energetic materials, in parallel to their performances and stability. The sensitivities to impact and friction and the temperature of ignition of the carbons C and F5001 and their derivatives filled with sodium perchlorate are studied. These carbons were chosen because they have oxygen balances in line with potential applications. The temperature of ignition is related to the thermal behavior of the materials, but is mostly considered as contributing to the characterization of the sensitivity to temperature of energetic materials and is therefore included in this section. The thermal ignition properties of carbons C and F5001 filled with sodium perchlorate are moreover investigated and compared to that of the corresponding physical mixtures at the μm scale to highlight the influence of the mixture at the nm scale on the decomposition mechanism.

4.2.1 Impact and friction sensitivities

Table 4.9 shows the impact and friction sensitivities of the selected filled carbons. The sensitivities of reference energetic materials measured in the same conditions are given for comparison purposes, as the sensitivity scales are semi-quantitative. TNT is considered as a very insensitive high explosive, and RDX and PETN are widely used in high explosive formulations, but in a flegmatized form. Values of 2 J and 80 N are moreover widely considered as thresholds [100, 101] for commercial applications.

Table 4.9: Sensitivities to impact and friction of carbons C and F5001, and of their derivatives filled with sodium perchlorate from a 56 wt% aqueous solution. Values for TNT, RDX and PETN measured in the same conditions are given for comparison purposes.

Material	Impact sensitivity (J)	Friction sensitivity (N)
C	10	48
C-R300	15	54
C-R600	15	60
F5001	7.5	168
F5001-APS	5	56
F5001-HN	20	160
TNT	10-20	240-360
RDX	5-10	80-120
PETN	2-4	36-48

The precision and the semi-quantitative nature of these sensitivities makes the analysis of the influence of the physicochemical properties of the carbons more difficult. Whereas the results shows that the thermal treatment of carbon C has only a limited effect on its impact and friction sensitivities, it seems that a strong oxidation of carbon F5001 led to a sensitization of the material. Generally speaking, all the carbons have sensitivities comparable to that of substances used as secondary explosives as TNT, RDX and PETN. Gas inclusion in materials is well-known to lead to materials very sensitive to impact as the result of adiabatic compression [102]. In the case of nanoporous carbons filled with an oxidizing agent, an empty pore could act accordingly and lead to the generation of a hot spot upon compression. The results show that this sensitization effect is not significant in these conditions, as the impact sensitivities

are globally low for all carbons. These observed moderate sensitivities are presumably related to the robustness of the materials, which limits their compressibility.

4.2.2 Temperature of ignition

Table 4.10 shows the temperature of ignition and the type of reaction of the selected filled carbons. It is first observed that the ignition temperatures are in very good agreement with the onsets of decomposition measured by DSC. In all cases, a very violent reaction was observed, which is qualified as an explosion according to the norm [90]. In all cases, the reaction is accompanied by a very loud noise and a very short and powerful flash, and the glass tubes were completely shattered due to the reaction.

Table 4.10: Temperatures of ignition of carbons C and F5001, and of their derivatives filled with sodium perchlorate from a 56 wt% aqueous solution.

Material	Temperature of ignition (°C)	Type of reaction
C	315	Explosion
C-R300	326	Explosion
C-R600	344	Explosion
F5001	332	Explosion
F5001-APS	279	Explosion
F5001-HN	309	Explosion

Table 4.11 shows the temperatures of ignition of carbons C and F5001 filled with sodium perchlorate from a 56 wt% aqueous solution and of the corresponding physical mixtures with the same yield of oxidizing salt. Physical mixtures at the mm scale consists of pristine carbon grains mixed homogeneously with $NaClO_4$ milled and sieved between 25 and 50 μm, and physical mixtures at the μm scale consists of homogeneous mixture of the carbon and $NaClO_4$, both milled and sieved between 25 and 50 μm.

Table 4.11: Temperatures of ignition of carbons C and F5001 filled with sodium perchlorate from a 56 wt% aqueous solution, and of the corresponding physical mixtures with the same yield of oxidizing salt. Mixtures at the mm scale consists of pristine carbon grains mixed homogeneously with $NaClO_4$ milled, and sieved between 25 and 50 μm. Mixtures at the μm scale consists of homogeneous mixture of the carbon and $NaClO_4$, both milled and sieved between 25 and 50 μm.

Material	Temperature of ignition (°C)	Type of reaction
C filled with $NaClO_4$	315	Explosion
Physical mixture of C and $NaClO_4$ (μm scale)	339	Ignition
Physical mixture of C and $NaClO_4$ (mm scale)	393	Ignition
F5001 filled with $NaClO_4$	332	Explosion
Physical mixture of F5001 and $NaClO_4$ (μm scale)	359	Ignition
Physical mixture of F5001 and $NaClO_4$ (mm scale)	412	Ignition

The results show that the scale of the mixture has a significant effect on the temperature of ignition and on the type of reaction. For both carbons, the temperature of ignition significantly increases with the scale of the mixture, and less violent reactions are observed for the mm and the μm scale (this observation can be clearly identified in the video of the experiment). In both cases, the reaction is accompanied by a loud noise and short flash, but the glass tubes were not damaged. These reactions are qualified as ignition. It is interesting to note that ignition is the most common type of reaction for energetic materials, whereas explosion is mainly observed for primary explosives. This contrasts with the discussion of the modelling of the decomposition kinetics (see section 4.1) where no influence of the scale on the decomposition kinetics was reported. This difference is presumably related to the different amount of material used in the experiments. In performing TGA experiments, great care is taken to prevent self-heating from damaging the instrument or interfering with the analysis. This

limits the amount of energetic material to about 1 mg. On the contrary, the temperature of ignition is determined with 200 mg and self-heating plays a key role. In these conditions, the heat transfer from the center of the mass to the surroundings is much slower than in a TGA experiment and depends on the thermal properties of the material. At a given temperature, the heat generated by the decomposition cannot be quickly transferred to the surroundings and the temperature increases faster than the heating rate of the experiment so that the decomposition accelerates and more heat is produced. Finally, as decomposition kinetics depend exponentially on temperature, this leads to a run-away behavior and the observed reactions of ignition and explosion. This is a short description of the well-known phenomenon of thermal ignition of energetic materials [103]. Both the lower temperatures and the differences in violence of reaction show that the nm scale leads to significantly faster decomposition kinetics in the conditions of the determination of the temperature of ignition. It is also well-known that the decomposition kinetics govern the run-away behavior of energetic materials, whereas the influence of the thermal properties is only marginal [103, 104]. Therefore, the observed results are presumably related to faster decomposition kinetics at higher temperatures, which lead to a faster acceleration of the decomposition during the run-away phase. Generally speaking and as self-heating is very important for characterizing the thermal ignition of energetic materials, the temperature of ignition experiment is considered as more relevant than the modelling of the kinetics based on TGA experiments to study the influence of the length scale of the mixtures of oxidizing and reducing agents on the decomposition kinetics. Therefore, these results suggest that the nm scale of the mixture well promotes the decomposition of the oxidizing agent confined in the nanopores of the carbon matrix in realistic conditions.

4.3 Detonation properties

4.3.1 Results

The results of chapter 3 and section 4.2 have shown that it was possible to fill the nanopores of carbons to a yield that corresponds to oxygen balance in line with potential applications as energetic materials, and that the decomposition is significantly promoted by the nanometer scale of the mixture when the oxidizing agent is confined in the nanopores. However, it is very difficult to predict the detonability and the detonation properties based on these observations, as they depend on real effects and local dynamic features as described in the theoretical description of the detonation process (see section 1.1.3). Dynamic detonation experiments are therefore carried out in this section to demonstrate the concept of detonable energetic materials based on a reducing nanoporous carbon matrix filled with a solid oxidizing agent. When designing the experimental set-up, it must be kept in mind that a large amount of parameters influences the detonation process, as the density of the material, its confinement, the charge dimension and the mean of initiation. To demonstrate the ability of a material to detonate and to characterize its basic detonation properties, numerous experiments must therefore be performed to take into account the influence of these parameters. Moreover, the charge dimensions cannot be too small to not prevent the detonation from being sustained because of real effects. This has for consequences that hundreds of grams of energetic materials are needed to carry out such an experiment campaign. As the synthesis is performed at the laboratory scale, only one carbon was investigated. Amongst the filled carbons with oxygen balances in line with potential applications as energetic material, the carbon C filled with sodium perchlorate from an aqueous solution at 56 wt% was chosen. This carbon has a high degree of pore filling with the majority of the salt in pores of width smaller than 4 nm, a small amount of salt in the macropores and on the surface, and an oxygen balance around -40 wt%. The experimental methods are detailed in chapter 2. All the experiments were performed with charges in heavy confinement (2 mm thick steel walls) and the charges are initiated with a standard military detonator. Figure 4.10 shows the results of the preliminary detonability study performed with this material. The charge diameter and length were set at 10 and 50 mm, and the indent depth on an aluminum witness plate was measured. As the depth of the indent is directly correlated with the brisance of a high explosive [12, 14, 15], this experiment allows evaluating if a material has detonated and to semi-quantitatively estimate its brisance. The smallest density of about 0.85 g/cm^3 corresponds to the density of the loose material, where the higher densities were obtained by pressing the material in tubes with a hydraulic press (see details in section A.5).

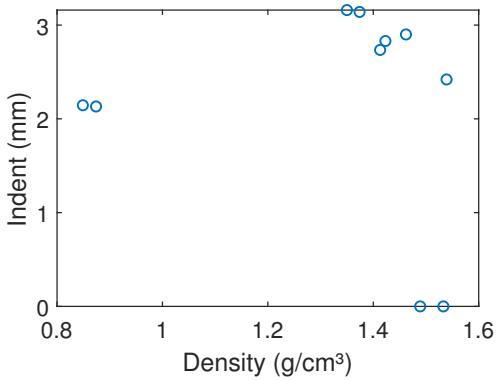

Figure 4.10: Results of the detonability preliminary study of carbon C filled with $NaClO_4$ from a 56 wt% aqueous solution, in a heavy confinement and initiated by a standard detonator.

The results show that an indent was observed for all densities except for the highest ones. The presence of such an indent indicates that the materials have detonated. It is observed that the indent depth increases from a density of 0.85 to 1.35 g/cm^3. It is then almost constant to a density of 1.40 g/cm^3, before suddenly dropping at higher densities until no indent is observed. For the highest densities, the results are not reproducible. Sometimes a clear indent is observed, and other times there is none for the same density.

Based on this preliminary study, three different densities (0.85, 1.35 and 1.40 g/cm^3) were selected to study the basic detonation properties of the material. The influence of the charge diameter was also studied to identify critical and ideal diameters in the experimental conditions. In all cases, a standard detonator was used as initiator and the confinement was heavy (2 mm thick steel walls). Table 4.12 and figure 4.11 show the measured detonation velocities for these different densities at different diameters.

Table 4.12: Measured detonation velocities, ideal diameters and critical diameters of carbon C filled with $NaClO_4$ from a 56 wt% aqueous solution compressed at different densities (ρ), in a heavy confinement and initiated by a standard detonator.

Density (g/cm^3)	0.85	1.35	1.40
Detonation velocity (km/s)	3.0	4.1	4.3
Critical diameter (mm)	8	6	6
Ideal diameter (mm)	10	8	8

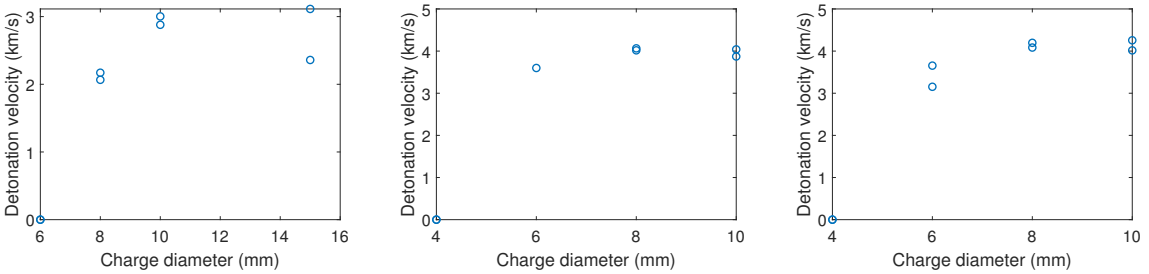

(a) $\rho = 0.85$ g/cm^3. (b) $\rho = 1.35$ g/cm^3. (c) $\rho = 1.40$ g/cm^3.

Figure 4.11: Measured detonation velocities in function of the charge diameter for carbon C filled with $NaClO_4$ from a 56 wt% aqueous solution compressed at different densities (ρ), in a heavy confinement and initiated by a standard detonator.

These results confirm that the material detonated when initiated by a standard detonator in heavy confinement and for charge diameters of the order of magnitude of 1 cm. The critical and ideal diameters measured in these conditions slightly decrease with the charge density, whereas the detonation velocity significantly increases between densities of 0.85 and 1.35 g/cm^3 and then only slightly increases between

densities of 1.35 and 1.40 g/cm^3.

Finally, additional detonation experiments were performed with bare sodium perchlorate and physical mixtures of the same composition as the studied composite material to demonstrate the influence of the confinement of the salt in the nanopores of the carbon matrix on the detonation process. The results are detailed in annex I. For the bare sodium perchlorate and the physical mixtures, they indicate that these materials were not able to sustain a detonation, even if the charge diameters were significantly larger (20-30 mm) and the initiation significantly stronger (15-30 g C-4 booster) than that used to perform the detonation experiments described in this section on the filled carbon.

4.3.2 Discussion

For densities between 0.85 and 1.40 g/cm^3, the results of the preliminary study and the measure of detonation velocities show that the brisance increases with the density, as expected according to the ideal detonation theory described in section 1.1.3.

At higher densities, the decrease of the brisance, the probabilistic behavior and the fact that no detonation is observed strongly indicate that shock desensitization occurs during pressing. This phenomenon is well-known, notably for primary explosives [105] or some non-ideal explosives [12]. For the highest densities for which the highest pressures were applied, this strongly suggests that the pressing of the material leads to a decrease of the density of hot spots in the material. In these conditions, the overall decomposition kinetics is so slow that the material is not able to sustain a detonation anymore.

The results show that the material is cap sensitive when confined in steel tubes and for charge diameters larger than 6-8 mm. This indicates that the material can be considered as a secondary explosive. The performed experiments aim at investigating only the brisance of this material. For comparison purposes, it is interesting to express the brisance of a high explosive with respect to that of a reference high explosive, mostly TNT. TNT with a density of 1.64 g/cm^3 and a detonation velocity of 6.95 km/s is considered in this work as reference [8]. To extend the scope of this comparison, a typical ANFO (an intimate mixture of ammonium nitrate and fuel oil) with a density of 0.9 g/cm^3 and a detonation velocity of 5 km/s is also considered in this work as reference for high explosives for civilian applications. As stated in the description of the detonation phenomenon (see section 1.1.3), the brisance of a high explosive is governed by its detonation pressure. The determination of the detonation pressure goes however beyond the basic characterization performed in this work, and it must therefore be estimated based on the available results. This can be done by comparing the indent depth, known to be proportional to the detonation pressure [12, 14, 15], or by using equation (1.16) which express that the detonation pressure is proportional to the product of the density and the square of the detonation velocity. Table 4.13 shows the relative brisance of the studied composite energetic material with respect to TNT and ANFO. For TNT, a plate-dent test was performed in the same conditions as in the preliminary study and an indent depth of 5 mm was measured. For ANFO, this was not relevant because of its large critical diameter.

Table 4.13: Relative brisance (%) of carbon C filled with $NaClO_4$ from a 56 wt% aqueous solution compressed at different densities (ρ), in a heavy 2 mm steel confinement and initiated by a standard military detonator, with respect to TNT (ρ = 1.64 g/cm^3, D (detonation velocity) = 6.95 km/s) and ANFO (ρ = 0.9 g/cm^3, D = 5.0 km/s). The relative brisance is calculated based on the value of the product ρD^2 or based on the indent depth measured in the same conditions.

Density (g/cm^3)	0.85	1.35	1.40
TNT, ρD^2 method	10	29	33
TNT, indent depth	43	63	56
ANFO, ρD^2 method	34	101	115

This comparison must however be nuanced. The method based on the product ρD^2 supposes that Γ, a parameter describing the non-ideality of the detonation gases in their simplest equation of state, is constant for all explosives. Even if this is true for most military explosives, this coefficient depends on the density of the explosive and globally on the nature of the detonation gases [8]. Comparing a composite energetic material containing an inorganic oxidizing agent and having a large fraction of solid detonation products with explosives as TNT and ANFO on this basis must therefore be done carefully. The method based on the comparison of the indent depth should also be nuanced for the same reason, as this is strictly valid for explosives with detonation products having comparable expansion isentropes [12].

The intrinsic differences between the composite energetic material investigated in this section and the reference explosives makes therefore any comparison of the brisance difficult. At best, the calculated relative brisances must be considered as order of magnitudes. In light of this, this analysis indicates that the carbon C filled with $NaClO_4$ from a 56 wt% aqueous solution at densities of 1.35-1.40 g/cm^3 has a brisance comparable to about 30-60 % of that of TNT and of the same order of magnitude than that of ANFO. These observations are atypical for heterogeneous fuel/oxidizer composites [71], especially with a large fraction of solid decomposition product, and denotes very fast dynamic decomposition kinetics promoted by the nanometer scale of the mixture.

Based on the presented results, it is not possible to conclude that a physical mixture of carbon C and sodium perchlorate cannot detonate in all circumstances. Nevertheless, the results show that these mixtures did not detonate even with a strong booster and a charge diameter 3 to 4 times larger than the critical diameter of the filled carbon described in this section. This confirms that the nanometer scale of the mixture plays a key role in allowing the material to sustain a detonation. The observed detonation properties are presumably strongly related to the fact that the mixture of oxidizing and reducing agents in the nanopores is in the immediate vicinity of the hot spots generated in the material by shock compression, and to the higher density achieved when the carbon particles are filled with the oxidizing agent than for the corresponding physical mixture. This is supposed to lead to a faster overall decomposition kinetics than in the case of a physical mixture, which is fast enough to allow the material to sustain a detonation in a heavy confinement and with a charge diameter of 6-8 mm.

4.4 Partial conclusions

The thermal analysis has shown that the nature of both the oxidizing agent and the nanoporous carbon has an influence on the decomposition mechanism, with a synergistic effect leading to decomposition temperature significantly lower than that of the oxidizing agents.

The study of the sensitivities to impact and friction of nanoporous carbons filled with an oxidizing agent are comparable with that of secondary explosives and are in line with potential applications.

The detonability of this composite energetic material has been experimentally demonstrated, and it was shown that this material has a brisance comparable to that of typical high explosives for civilian applications and to 30-60 % of that of TNT (for heavily confined charges of a diameter ranging from 6 to 10 mm). It was moreover shown that the nanoconfinement of the oxidizing agent in the pores of the carbon matrix plays a key role in enabling this material to sustain a detonation, by comparing the decomposition kinetics of the energetic materials characterized by thermal analysis, the type of reaction observed during the determination of its temperature of ignition, and its detonation properties with that of corresponding physical mixtures. These results are an experimental proof of the concept of this work.

Conclusions and perspectives

This work aimed at exploring a new family of energetic materials produced by filling the porosity of a nanoporous carbon with a solid oxidizing agent in order to obtain an energetic material which is able to detonate. This concept was novel and could lead to a new family of energetic materials with promising properties and applications as pyrotechnic composition, propellant or high explosive. A feasibility study was first performed and the theoretical feasibility of the concept demonstrated. Nevertheless, a pore filling process had to be developed to synthesize these composite energetic materials, and their ability to detonate had to be experimentally verified. Both of these aspects were experimentally investigated in details, and the most significant concluding remarks that can be inferred from this PhD thesis are summarized below:

- The objectives of the pore filling process were defined; the amount of oxidizer should be sufficient to achieve an oxygen balance to CO_2 in line with potential applications as energetic materials (the threshold was set at -75 wt% in this work), and the nanopores must be selectively filled, as the presence of oxidizer in larger pores or on the external surface is considered as detrimental for the detonation process.
- A pore filling process by crystallization after solution contraction upon drying was successfully developed. Even if the efficiency of the process strongly depends on the nature of the oxidizing salt and of that of the carbon, it has been shown that this process can successfully allow high degree of pore filling to be achieved with a selective filling of the micro and mesopores. Among the typical oxidizing agents in pyrotechnic applications and in the experimental conditions used in this work, only sodium perchlorate has shown an ability to selectively crystallize in the smallest pores and to achieve a pore filling yield which confers a potential energetic character to the filled carbons. Most of the oxidizing agent crystallized in pores of width smaller than 4 nm, which corresponds to the objective of this work of ensuring a homogeneous mixture of the oxidizing and the reducing agents at the nanometer scale to confer it an energetic character.
- The influence of the physicochemical properties of the carbons was investigated. As the respective potential contributions of variable density and pore blocking to the pore filling characterization are interdependent and cannot be separately quantified, the interpretation of the results is complex. In overall, the yield of the pore filling process (a measure of the amount of oxidizing agent per unit mass of carbon) is in very good agreement with the pore volume of the nanoporous carbons, but both textural properties and surface chemistry appear to have a significant influence on the location of the oxidizing agent in the porous network. It was shown that the crystallization of the salt occurs selectively in pore of width smaller than 3-4 nm, but the capillary driving force presumably becomes too weak in larger pores to effectively lead to a preferentially filling of these pores with respect to the larger pores when the solvent is progressively removed during the pore filling process. This is attributed to the stronger dispersive intermolecular forces in the micropores and the smallest mesopores where the force fields of the opposite walls can superpose. The results show also that the degree of pore filling is significantly dependent on the surface chemistry of the carbon materials. The respective contributions of the different surface functionalities remain unclear, but some results suggest that carboxylic acid may play an important role in improving the wettability of the carbon walls to enhance the effectiveness of the pore filling process. It has moreover been shown that some extent of polar surface groups appears to be needed to achieve a high degree of pore filling. This is presumably related to a lower interfacial free energy between the concentrated oxidizing salt solution and the pore walls in the presence of these groups, which promotes the preferential filling of the nanopores when the solvent is evaporated.
- The results suggest that sodium perchlorate fills the pores as continuous blocks. Schematically, some parts of the porosity are presumably filled, whereas other parts are empty. This hypothesis is supported by thermodynamic considerations, the characterization of the residual porosity of the

filled carbons, and the thermal analysis. The proposed mechanism is the following: the solution preferentially contracts upon drying in micropores and small mesopores by capillary effect; nucleation occurs at some degree of supersaturation, presumably on active sites as micropores or surface functional groups; crystal growth takes place as the ions diffuse through the pores to the nuclei and the water molecules diffuse out of the porosity to the external surface. The amount and location of nuclei are governed by the textural properties and the surface chemistry of the carbon material, and diffusion kinetics play a critical role. Nucleation could be promoted by heterogeneous ion concentration during drying, and additional nucleation on other sites may also occur if the diffusion in the porous network is too slow during the growth phase. Pore blocking may finally be observed is an empty space is completely enclosed by filled pores.

- The investigation of the decomposition mechanism of the synthesized composite energetic materials by thermal analysis indicated that the nature of both the oxidizing agent and the nanoporous carbon has an influence on the decomposition mechanism, with a synergistic effect leading to a decomposition temperature significantly lower than that of the bare oxidizing agent.
- The analysis of the sensitivities to impact and friction of nanoporous carbons filled with an oxidizing agent has shown that they are in line with potential applications as secondary explosive.
- The detonability of a selected composite energetic material made of a nanoporous carbon matrix filled with sodium perchlorate has been experimentally demonstrated. It was shown that this material is cap-sensitive, and has a brisance comparable to that of typical high explosives for civilian applications and to 30-60 % of that of TNT, when heavily confined charges of a diameter ranging from 6 to 10 mm are used. It was moreover observed by different means that the nanoconfinement of the oxidizing agent in the pores of the carbon matrix plays a key role in enabling this material to sustain a detonation.

In sum, a new pore filling process to synthesize novel energetic materials based on nanoporous carbons filled with an oxidizing agent was developed and investigated in this PhD thesis, and an experimental proof of the concept was provided.

In addition to this first exploratory study, the concept offers many degrees of freedom and opportunities for improvement. The process parameters could notably be further optimized, the nanoporous carbon could be tailored to applications, advanced characterization techniques could be applied to obtain a better understanding of the role of the properties of the nanoporous carbons, and the detonation properties of a wider range of composite energetic materials could be measured to investigate the relation between the detonatibility of the materials and their properties. These perspectives are summarized below:

- In overall, nanoporous carbons tailored to different applications could be purchased, synthesized or obtained by modification of commercial materials in order to achieve higher performance. Different specific applications could be investigated in detail, and the properties of the composite energetic materials optimized accordingly. The applications which should be studied as first based on the results presented in this work are applications as primary explosive (the deflagration-to-detonation transition should first be experimentally demonstrated), as component of priming charge, as secondary explosive (for specific applications, potentially with insensitive properties owing to the structure of the carbon materials), and as propellant (typically with ammonium cations).
- In addition to the TPDMS analysis performed in this work to characterize the surface chemistry of the carbon materials, XPS (X-ray photoelectron spectroscopy) could also be applied to provide more information about the nature and the chemical environment of the surface functional groups, and the wettability of the carbon surface could be assessed by measuring water adsorption isotherms. This latter method provides very relevant information about the accessibility and the affinity for water of the surface functional groups of carbon materials. The relation between the information provided by this method and the effect on the pore filling efficiency is however not straightforward and would have to be investigated in details.
- To clarify the effect of the nanometer size of the oxidizer particles on the decomposition mechanism, it would be useful to confine the salt on the same scale but in an inert material (e.g. nanoporous silica), and to study thermal properties of this composite material. This would help to identify the primary step of the decomposition mechanism. One of the possibilities is indeed a self-decomposition of the nanometric particles of oxidizing salt at a temperature significantly lower than the decomposition temperature of the bulk salt, owing to a significant contribution of surface energy. This would be comparable with the effect of the nanometer size on the melting point of metal nanoparticles, which is significantly lower than that of the bulk material.
- To get a better understanding of the role of the pore size on the selective crystallization in pores

smaller than 4 nm, it would be interesting to use ordered mesoporous carbons obtained by a hard-templating method using SBA-15 mesoporous silica of different pore size (e.g., 4, 6, 8 and 10 nm). This would help to determine a limiting pore width from which capillary effects are not sufficient to lead to contraction and subsequent selective crystallization in these pores.

- The materials could also be characterized by helium pycnometry to measure their true density. This method, coupled with the determination of the apparent density by mercury intrusion porosimetry, would allow to directly measure the mean density of the salt in the porosity. It would also be less subject to pore blocking, and would allow performing a more detailed analysis of the location of the salt in the porosity.
- Thermodynamic simulations of the detonation properties could be performed to explore the potential of this family of energetic materials. However, this necessitates two elements, namely an estimation of the apparent density of the material (which could be estimated based on the results presented in this work) and an accurate value for the standard enthalpy of formation of the energetic materials. This latter point is not straightforward, as the elemental composition of the material must be precisely known, and its heat of combustion experimentally determined by calorimetry. The usual practice consisting in additively calculating the standard heat of formation of a composite material based on the standard heat of formation of its constituents and their mass fraction does not seem appropriate in this case, because neglecting the surface energy between the carbon material and the oxidizing salt probably lead to a significant underestimation of this standard enthalpy of formation because of the nanometric scale of the mixture. This should at least be experimentally verified for a series of representative materials.
- The brisance and the power of the composite energetic materials could be experimentally investigated by advanced techniques (e.g., by determining the detonation pressure and/or by performing underwater detonation experiments) to improve the comparison of the performances with commercial or military high explosives, and the detonation properties of more composite energetic materials could be studied to investigate the relation between the structure of the material (i.e., the properties of the carbon material, the degree of pore filling, the amount of oxidizing agent, etc.) and these detonation properties. This latter point would necessitate to upscale the pore filling process (e.g. to batches of 100 g).
- The shock sensitivity and the sensitivity to electrostatic discharge could be investigated to obtain a global picture of the sensitivities of these materials. Moreover, the stability of the composite energetic materials could be investigated, for instance by vacuum stability or heat flow calorimetry to assess the thermal aging properties of these materials, and their chemical compatibility with typical contact materials found in ammunition could also be studied to identify potential issues at this level.
- The filtration step could be significantly optimized, namely by controlling directly the superficial velocity of the gas flow through the bed. For this purpose, an overpressure filtering set-up could be used, where the flow rate is controlled by means of a mass flow controller. This would allow investigating other flow rates during this step, and potentially enlarging the scope of the process to other particle sizes (e.g., powder), and to other salts (e.g. nitrate, chlorate, etc.). It would also be possible to carry out controlled reimpregnation of samples or impregnation in two steps with different salts, which is not possible with the current set-up, as it is operated at a fixed flow rate that is insufficient to properly remove the solution from a powder bed or from a material which has already been filled with an oxidizing agent (as its wettability is dramatically higher than that of the original carbon material).
- The use of molten salt was disregarded because the melting point of an oxidizing salt is usually very close to its decomposition temperature, which would result in a violent reaction if molten salts were brought into contact with carbon. However, eutectic mixtures of oxidizing salt (e.g., a eutectic mixture of ammonium nitrate and ammonium perchlorate) could allow circumventing this issue and might lead to a degree of pore filling close to 100 %.
- As oxidizing agents with very high water solubility are needed to achieve a high efficiency of the pore filling process, the resulting energetic materials will probably be too hygroscopic for applications. This could be improved by performing a cation exchange after the synthesis, for instance to replace sodium by potassium after pore filling with sodium perchlorate.
- As metal impregnation is a mature technique for infiltrating metal nanoparticles in the pore structure of activated carbon, this technique could be used to disperse catalyst nanoparticles in the carbon matrix in order to increase the overall decomposition kinetics of the material, for instance by using MnO_2, which is a known decomposition catalyst for the chlorate and perchlorate salts.

Bibliography

[1] NATO Standardization Office. NATOTerm, The official NATO Terminology Database, 2021.

[2] R. Meyer, J. Köhler, and A. Homburg. *Explosives*. Wiley-VCH, 7th edition, 2015.

[3] S.M. Kaye. Encyclopedia of explosives and related items. Technical report, US Army Research and Development Command, Picatinny Arsenal, 1978. Volume 8.

[4] N. Kubota. *Propellants and explosives: thermochemical aspects of combustion*. Wiley-VCH, 2001.

[5] J.M. Walsh and R.H. Christian. Equation of state of metals from shock wave measurements. *Physical Review*, 97:1544–1556, 1955.

[6] R.W. Goranson, D. Bancroft, B.L. Burton, T. Blechar, E.E. Houston, E.F. Gittings, and S.A. Landeen. Dynamic determination of the compressibility of metals. *Journal of Applied Physics*, 26:1472–1479, 1955.

[7] S.P. Marsh, editor. *LASL Shock Hugoniot Data*. University of Calofornia Press, 1980.

[8] P.W. Cooper. *Explosives Engineering*. Wiley-VCH, 1996.

[9] E. Jouguet. *Mécanique des explosifs*. Octave Doin et Fils, 1917.

[10] D.L. Chapman. On the rate of explosion in gases. *The London, Edinburgh, and Dublin Philosophical Magazine and Journal of Science*, 1899.

[11] M. Sućeska. *Explo5 user's guide*. 2014.

[12] C.L. Mader. *Numerical modeling of explosives and propellants*. CRC Press, 3rd edition, 2008.

[13] A.W. Campbell, W.C. Davis, J.B. Ramsay, and J.R. Travis. Shock initiation of solid explosives. *Physics of Fluids*, 4:511, 1961.

[14] M. Sućeska. *Test methods for explosives*. Springer, 1995.

[15] L.C. Smith. *On brisance, and a plate-denting test for the estimation of detonation pressure*. Los Alamos Scientific Laboratory, 1964.

[16] T.J. Bandosz, editor. *Activated Carbon Surfaces in Environmental Remediation*. Elsevier, 2006.

[17] C.O. Ania, P. Armstrong, T.J. Bandosz, F. Beguin, A. Carvalho, A. Celzard, E. Frackowiak, M. Gilarranz, K. Laszlo, J. Matos, and M.F.R. Pereira. Engaging nanoporous carbons in beyond adsorption applications: Characterization, challenges and performance. *Carbon*, 164:69–84, 2020.

[18] T.J. Bandosz. Nanoporous carbons: Looking beyond their perception as adsorbents, catalyst supports and supercapacitors. *The Chemical Record*, 16:205–218, 2015.

[19] J.M.D. Tascón, editor. *Novel carbon adsorbents*. Elsevier, 2012.

[20] H. Marsh and F. Rodríguez-Reinoso. *Activated carbon*. Elsevier, 2006.

[21] A. Oberlin and S. Bonnamy. A realistic approach to disordered carbons. In *Chemistry and physics of carbon*, volume 31. CRC Press, 2013.

[22] H.F. Stoeckli. Microporous carbons and their characterization: the present state of the art. *Carbon*, 28:1, 1990.

[23] P.J.F. Harris. Impact of the discovery of fullerenes on carbon science. In *Chemistry and physics of carbon*, volume 28. CRC Press, 2003.

[24] M. Inagaki, K. Kaneko, and T. Nishizawa. Nanocarbons - recent research in japan. *Carbon*, 42:1401, 2004.

[25] Q.-L. Yan, M. Gozin, F.-Q. Zhao, A. Cohen, and S.-P. Pang. Highly energetic compositions based on functionalized carbon nanomaterials. *Nanoscale*, 8:4799, 2016.

[26] M. Thommes, K. Kaneko, A.V. Neimark, J.P. Olivier, F. Rodriguez-Reinoso, J. Rouquerol, and K.S.W. Sing. Physisorption of gases, with special reference to the evaluation of surface area and pore size distribution (IUPAC technical report). *Pure and Applied Chemistry*, 87:1051–1069, 2015.

[27] E. Fitzer, K.-H. Köchling, H.P. Boehm, and H. Marsh. Recommended terminology for the description of carbon as a solid (IUPAC recommendations 1995). *Pure and Applied Chemistry*, 67:473–506, 1995.

[28] A.S. Mestre and A.P. Carvalho. Nanoporous carbon synthesis: An old story with exciting new chapters. In *Porosity: Process, Technologies and Applications*. IntechOpen, 2017.

[29] Y. Qiu, S. Moore, R. Hurt, and I. Külaots. Influence of external heating rate on the structure and porosity of thermally exfoliated graphite oxide. *Carbon*, 111:651–657, 2017.

[30] B.T. Fedoroff and O.E. Sheffield. Encyclopedia of explosives and related items. Technical report, US Army Research and Development Command, Picatinny Arsenal, 1962. Volume 2.

[31] E. Gray, H. Marsh, and M. McLauren. A short history of gunpowder and the roal of charcoal in its manufacture. *Journal of materials science*, 17:3385–3400, 1982.

[32] J.R. Schmidt and R.A. Pesce-Rodriguez. Review paper on black powder and benite igniter composition with emphasis on charcoal performance. Technical report, DEVCOM Army Research Laboratory, July 2021.

[33] R.A. Sasse. A comprehensive review on black powder. Technical report, US Army Ballistic Research Laboratory, January 1985.

[34] R.A. Sasse. The influence of physical properties on black powder combustion. Technical report, US Army Ballistic Research Laboratory, March 1981.

[35] A.D. Kirshenbaum. Effect of different carbons on ignition temperature and activation energy of black powder. *Thermochimica Acta*, 18(113-123), 1977.

[36] G. Hussain and G.J. Rees. Combustion of black powder. Part IV: Effect of carbon and other parameters. *Propellants, Explosives, Pyrotechnics*, 17(1-4), 1992.

[37] J.E. Rose. The role of charcoal in the combustion of black powder. Technical report, Naval Ordnance Station, 1980.

[38] J. Bate. *The second book of fireworkes*. London, 1635.

[39] B.S. Ermolaev, A.A. Belyaev, S.B. Viktorov, K.A. Sleptsov, and S.Yu. Zharikova. Nonideal regimes of deflagration and detonation of black powder. *Russian Journal of Physical Chemistry B*, 4:428–439, 2010.

[40] J.D. Blackwood and F.P. Bowden. The initiation, burning and thermal decomposition of gunpowder. *Proceedings of the Royal Society of London A*, 213:285–306, 1952.

[41] A.-M. Turcotte R. Turcotte, R.C. Fouchard and D.E.G. Jones. Thermal analysis of black powder. *Journal of Thermal Analysis and Calorimetry*, 73:105–118, 2003.

[42] M.E. Brown and R.A. Rugunanan. A temperature-profile study of the combustion of black powder and its constituent binary mixtures. *Propellants, Explosives, Pyrotechnics*, 14:69–75, 1989.

[43] J. Daniel. *Dictionnaire des matières explosives*. Dunod, 1902.

[44] A. Marshall. *Dictionary of Explosives*. P. Blakinston's son & co., 1920.

[45] B.T. Fedoroff, H.A. Aaronson, E.F. Reese, O.E. Sheffield, and G.D. Clift. Encyclopedia of explosives and related items. Technical report, US Army Research and Development Command, Picatinny Arsenal, 1960. Volume 1.

[46] B.T. Fedoroff. Dictionary of explosives, ammunition and weapons (German section). Technical report, US Army Research and Development Command, Picatinny Arsenal, 1958. PATR 2510.

[47] B.T. Fedoroff and O.E. Sheffield. Encyclopedia of explosives and related items. Technical report, US Army Research and Development Command, Picatinny Arsenal, 1962. Volume 7.

[48] B.T. Fedoroff and O.E. Sheffield. Encyclopedia of explosives and related items. Technical report, US Army Research and Development Command, Picatinny Arsenal, 1972. Volume 5.

[49] B.T. Fedoroff and O.E. Sheffield. Encyclopedia of explosives and related items. Technical report, US Army Research and Development Command, Picatinny Arsenal, 1974. Volume 6.

[50] S.M. Kaye. Encyclopedia of explosives and related items. Technical report, US Army Research and Development Command, Picatinny Arsenal, 1980. Volume 9.

[51] J.P. Cundill and J.H. Thomson. *Dictionary of explosives*. London, 1895.

[52] P.W. Streijffert. Procédé de fabrication d'explosifs, 1941. Patent FR861729A.

[53] J. Akhavan. *The chemistry of explosives*. RSC Paperbacks, 1998.

[54] G.P. Sutton and O. Biblarz. *Rocket Propulsion Elements*. John Wiley & Sons, 2001.

[55] N. Kubota, T.J. Ohlemiller, L.H. Caveny, and M. Summerfield. The mechanism of super-rate burning of catalysed burning rate propellants. Technical report, Office of Naval Research, 1973.

[56] M. Comet, V. Pichot, B. Siegert, D. Spitzer, J.-P. Moeglin, and Y. Boehrer. Use of nanodiamonds as a reducing agent in a chlorate-based energetic composition. *Propellants, Explosives, Pyrotechnics*, 34:166–173, 2009.

[57] N. Wang, J. Li, and G. Li. Synthesis of trinitrophenyl C60 derivative. *Propellants, Explosives, Pyrotechnics*, 21:317–319, 1996.

[58] X. Fu, Y. Zhu, J. Li, L. Jiang, X. Zhao, and X. Fan. Preparation, characterization and application of nano-graphene-based energetic materials. *Nanomaterials*, 11:2374, 2021.

[59] R. Li, J. Wang, J.-P. Shen, C. Hua, and G.C. Yang. Preparation and characterization of insensitive HMX/graphene oxide composites. *Propellants, Explosives, Pyrotechnics*, 38:798–804, 2013.

[60] L. Yu, H. Ren, X.-Y. Guo, X.-B. Jiang, and Q.-J. Jiao. A novel ϵ-HNIW-based insensitive high explosive incorporated with reduced graphene oxide. *Journal of Thermal Analysis and Calorimetry*, 117:1187–1199, 2014.

[61] R. Guo, Y. Hu, R. Shen, Y. Ye, and L. Wu. A micro initiator realized by integrating KNO3/CNTs nanoenergetic materials with a cu microbridge. *Chemical Engineering Journal*, 211:31–36, 2012.

[62] H. Cai, L. Tian, B. Huang, G. Yang, D. Guan, and H. Huang. 1,1-diamino-2,2-dinitroethene FOX-7, nano-crystals embedded in mesoporous carbon fdu-15. *Microporous and mesoporous materials*, 170:20–25, 2013.

[63] M.-K. Shin, M.-H. Kim, G.-Y. Kim, B. Kang, J.S. Chae, and S. Haam. Highly energetic materials-hosted 3D inverse opal-like porous carbon: stabilization/desensitization of explosives. *ACS applied materials & interfaces*, 10:43857–43864, 2018.

[64] M.K. Atamanov, R. Amrousse, J. Jandosov, K. Hori, A.R. Kerimkulova, D.I. Chenchik, and B.Y. Kolesnikov. Combustion characteristics of HAN-based green propellant assisted with nanoporous active carbons. *Eurasian Chemico-Technological Journal*, 19:215–222, 2017.

[65] M.K. Atamanov, R. Amrousse, K. Hori, B.Y. Kolesnikov, and Z.A. Mansurov. Influence of activated carbon on the thermal decomposition of hydroxylammonium nitrate. *Combustion, Explosion, and Shock Waves*, 54:316–324, 2018.

[66] Z.A. Mansurov, R. Amrousse, K. Hori, and M. Atamanov. Combustion/decomposition behavior of HAN under the effects of nanoporous activated carbon. In *Innovative Energetic Materials: Properties, Combustion Performance and Application*. Springer, 2020.

[67] A. Miyake and Y.-I. Izato. Thermal decomposition behaviors of ammonium nitrate and carbon mixtures. *International Journal of Energetic Materials and Chemical Propulsion*, 9:523–531, 2010.

[68] F.V. Mikulec, J.D. Kirtland, and M.J. Sailor. Explosive nanocrystalline porous silicon and its use in atomic emission spectroscopy,. *Advanced Materials*, 14:38–41, 2002.

[69] M. du Plessis. A decade of porous silicon as nano-explosive material. *Propellants, Explosives, Pyrotechnics*, 35:1–17, 2013.

[70] M. du Plessis. Energetics with porous silicon. In *Handbook of porous silicon*. Springer International, 2018.

[71] P.M. Guerieri, B. Fuchs, and W.A. Churaman. Feasibility of detonation in porous silicon nanoenergetics. *Propellants, Explosives, Pyrotechnics*, 46:1260–1275, 2021.

[72] R.V. Kent, T.P. Vaid, J.A. Boissonault, and A.J. Matzger. Adsorption of tetranitromethane in zeolitic imidazolate frameworks yields energetic materials. *Dalton Transactions*, 48:7509–7513, 2019.

[73] D. Spitzer, M. Comet, C. Baras, V. Pichot, and N. Piazzon. Energetic nano-materials: Opportunities for enhanced performances. *Journal of Physics and Chemistry of Solids*, 71:100–108, 2010.

[74] ICT-database of thermochemical values. Technical report, Fraunhofer Institude for Chemical Technology ICT.

[75] J.B. Parra, C.O. Ania, A. Arenillas, and J.J. Pis. Textural characterisation of activated carbons obtained from poly(ethylene terephthalate) by carbon dioxide activation. *Studies in Surface Science and Catalysis*, 144:537–543, 2002.

[76] W.M. Haynes, editor. *CRC handbook of chemistry and physics*. CRC press, 2016-2017.

[77] M.M. Dubinin. The potential theory of adsorption of gases and vapors for adsorbents with energetically nonuniform surfaces. *Chemical Reviews*, 60:235–241, 1960.

[78] J. Rouquerol, F. Rouquerol, K.S.W. Sing, P. Llewellyn, and G. Maurin. *Adsorption by powders and porous solids: principles, methodology and applications*. Academic Press, 2014.

[79] S. Lowell, J.E. Shields, M.A. Thomas, and M. Thommes. *Characterization of porous solids and powders: surface area, pore size and density*. Springer, 2004.

[80] A.V. Neimark, Y. Lin, P.I. Ravikovitch, and M. Thommes. Quenched solid density functional theory and pore size analysis of micro-mesoporous carbons. *Carbon*, 47:1617–1628, 2009.

[81] J. Roquerol, G. Baron, R. Denoyel, H. Giesche, J. Groen, P. Klobes, P. Levitz, A.V. Neimark, S. Rigby, R. Skudas, K. Sing, M. Thommes, and K. Unger. Liquid intrusion and aleternative methods for the characterization of macroporous materials (IUPAC technical report). *Pure and Applied Chemistry*, 84:107–136, 2012.

[82] J.L. Figueiredo, M.F.R. Pereira, M.M.A. Freitas, and J.J.M. Órfão. Characterization of active sites on carbon catalysts. *Industrial and Engineering Chemistry Research*, 46:4110–4115, 2007.

[83] J.L. Figueiredo, M.F.R. Pereira, M.M.A. Freitas, and J.J.M. Órfão. Modification of the surface chemistry of activated carbons. *Carbon*, 37:1379–1389, 1999.

[84] STANAG 4515 - explosives, thermal analysis using differential thermal analysis, differential scanning calorimetry, heat flow calorimetry and thermogravimetric analysis. NATO Standardization Office, 2015.

[85] H.E. Kissinger. Reaction kinetics in differential thermal analysis. *Analytical chemistry*, 29:1702–1706, 1957.

[86] STANAG 4147 - chemical compatibility of ammunition components with explosives. NATO Standardization Office, 2001.

[87] H.L. Friedman. Kinetic of thermal degradation of char-forming plastics from thermogravometry. application to a phenolic plastic. *Journal of Polymer Science Polymer Symposium*, 6:183–195, 1964.

[88] EN 13631-4 Explosives for civil uses - high explosives - part 4: Determination of sensitiveness to impact of explosives. European standard, 2002.

[89] EN 13631-3 Explosives for civil uses - high explosives - part 4: Determination of sensitiveness to friction of explosives. European standard, 2004.

[90] STANAG 4491 - explosives, thermal sensitiveness and explosiveness tests. NATO Standardization Office, 2002.

[91] R. Van Riet, E. Amayuelas, P. Lodewyckx, M.H. Lefebvre, and C.O. Ania. Novel opportunities for nanoporous carbons as energetic materials. *Carbon*, 164:129–132, 2020.

[92] M.G. Plazza, F. Rubiera, J.J. Pis, and C. Pevida. Ammoxidation of carbon materials for co2 capture. *Applied Surface Science*, 22:6843–6849, 2010.

[93] Y. Boutillara. *Application of activated carbons in the separation of toxic gas mixtures and optimisation of the impregnation process.* PhD thesis, Ecole Royale Militaire and Université de Mons, 2019.

[94] B. Fidalgo, A. Arenillas, and J.A. Menéndez. Synergetic effect of a mixture of activated carbon + Ni/Al2O3 used as catalysts for the CO2 reforming of CH4. *Applied Catalysis A: General*, 390:78–83, 2010.

[95] J. Jagiello, J. Kenvin, C.O. Ania, J.B. Parra, A. Celzard, and V. Fierro. Exploiting the adsorption of simple gases O2 and H2 with minimal quadrupole moments for the dual gas characterization of nanoporous carbons using 2D-NLDFT models. *Carbon*, 160:164–175, 2020.

[96] P. Tasker. The stability of ionic crystal surfaces. *Journal of Physics C: Solid state physics*, 12:4977–4984, 1979.

[97] J.M. Coulson and J.F. Richardson. *Chemical Engineering Volume 2: Particle technology and separation processes.* Butterworth-Heinemann, 2002.

[98] D.M. Ruthven. *Principles of adsorption and adsorption processes.* John Wiley & Sons, 1984.

[99] L. Liu, S. Tan, T. Horikawa, D.D. Do, D. Nicholson, and J. Liu. Water adsorption on carbon - a review. *Advances in Colloid and Interface Science*, 250:64–78, 2017.

[100] Recommendations on the transport of dangerous goods - manual of tests and criteria. United Nations, 2015.

[101] EN 13631 Explosives for civil uses - high explosives. European standard, 2005.

[102] C.H. Johanssonand P.A. Persson. *Detonics of high explosives.* Academic Press, 1970.

[103] J.A. Zukas and W.P. Walters, editors. *Explosive effects and applications.* Springer, 1997.

[104] R.N. Rogers. Thermochemistry of explosives. *Thermochimica Acta*, 11:131–139, 1975.

[105] R. Matyáš and J. Pachman. *Primary explosives.* Springer, 2013.

[106] N. Job, R. Pirard, J.-P. Pirard, and C. Alié. Non intrusive mercury porosimetry: pyrolysis of resorcinol-formaldehyde xerogels. *Particle and Particle Systems Characterization*, 23:72–81, 2006.

List of symbols

Symbol	Description
β	Heating rate
γ	Surface tension
Γ	Polytropic coefficient
ρ	Specific mass
θ	Contact angle
Ω	Oxygen balance
Ω^V	Volumetric oxygen balance
A	Pre-exponential factor (Arrhenius equation)
C_0	Bulk sound velocity (parameter of the empiric relation (Hugoniot) between D and v)
C_P^0	Standard heat capacity at constant pressure
D	Shock velocity / Velocity of detonation
d_p	Pore diameter
E_a	Activation energy (Arrhenius equation)
H	Enthalpy
$\Delta_r H^0$	Standard reaction enthalpy
m_a, m_b	Mass of sample after and before MIP experiment
P	Pressure
R	Universal gas constant
s	Parameter of the empiric relation (Hugoniot) between D and v
T	Temperature
T_m	Peak temperature
U	Internal energy
v	Particle velocity
V_{micro}	Micropore volume
V_{meso}	Mesopore volume
V_{macro}	Macropore volume
$V_{\text{Hg}}^{\text{entr}}$	Volume of entrapped mercury

List of abbreviations

Abbreviation	Description
ADN	Ammonium dinitramide
ANFO	Ammonium nitrate - fuel oil
APS	Ammonium persulfate
BAM	*Bundesanstalt für Materialforschung und -prüfung*
CJ	Chapman-Jouguet (state)
CNT	Carbon nanotube
DFT	Density functional theory
DMSO	Dimethyl sulfoxide
DR	Dubinin-Radushkevich (model)
DSC	Differential Scanning Calorimetry
DTG	Differentiate thermogravimetric analysis
GO	Graphite oxide
HAN	Hydroxylammonium nitrate
IUPAC	International union of pure and applied chemistry
MIP	Mercury intrusion porosimetry
MS	Mass spectrometry
MWCNT	Multi wall carbon nanotube
NATO	North Atlantic treaty organization
NGl	Nitroglycerine
NLDFT	Non-Linear density functional theory
PETN	Pentaerythritol tetranitrate
PTFE	Polytetrafluoroethylene
QSDFT	Quenched-state density functional theory
rGO	Reduced graphene oxide
STP	Standard conditions of temperature and pressure
TGA	Thermogravimetric analysis
TNT	Trinitrotoluene
TPD	Temperature programmed desorption
TPDMS	Temperature programmed desorption - mass spectrometry
TPV	Total pore volume
VN	von Neumann (state)
XPS	X-ray photoemission spectroscopy
ZIF	Zeolitic imidazolate framework

Appendix A

Materials and methods : Supplementary information

A.1 Choice of the overactivation temperature

The overactivation temperature was chosen from the point where the slope of the thermogravimetric profiles indicates the occurrence of the reaction with CO_2. Caution must be taken to control the kinetics of the reaction, thus avoid too fast activation that would render an external burnt-out of the carbon particles. Based on these requirements, overactivation temperatures of 875 and 840 °C were selected for BPL and FY5, respectively, based on the reactivity of the carbon in a CO_2 atmosphere shown in figure A.1. The reactivity was evaluated by performing a thermogravimetric analysis (TGA) under a CO_2 (99.99 vol%) flow of 10 Nml/min with approximatively 15 mg of carbon in 70 μl alumina crucibles at 10 K/min with a TGA/DSC 3+ instrument (Mettler Toledo). The CO_2 flow was inserted as reaction gas, directly on the top of the sample. The temperature at which the mass loss started to be significant (i.e. after a mass loss of 5 wt%) was selected as activation temperature by following guidelines of the literature [75].

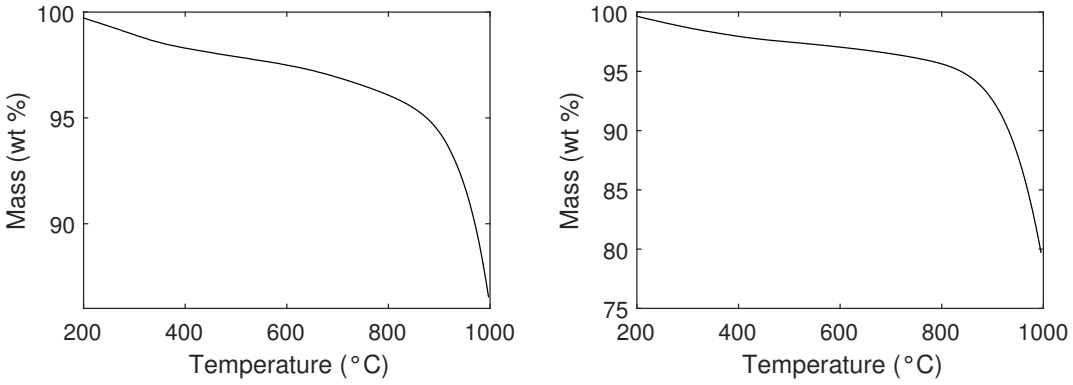

(a) BPL.

(b) FY5.

Figure A.1: CO_2 reactivity curves measured by TGA.

A.2 Classification of physisorption isotherms and types of hysteresis loops

The classification of physisorption isotherms and types of hysteresis loops are briefly described in this section.

Figure A.2 shows the classification of the physisorption isotherms recommended by IUPAC [26]:

- Type I isotherms are reversible and correspond to microporous adsorbent, for which micropore filling is observed at very low relative pressures. These materials have a relatively small external

surface. Type I(a) is observed for adsorbent with a narrow microporosity (mainly pores of width smaller than ± 1 nm). Type I(b) isotherm correspond to adsorbent with a broader micropore size distribution, and possibly narrow mesopores (of width smaller than ± 2.5 nm). Micropore filling is then observed on a wider range of relative pressure than for the type I(a).

- Type II isotherms are observed for nonporous or macroporous adsorbents, for which only monolayer and multilayer adsorption occurs. The knee observed on the isotherm (point B) usually corresponds to the completion of monolayer coverage.
- Type III isotherms are observed for nonporous or macroporous adsorbents for which adsorbent-adsorbate intermolecular interactions are relatively weak, so that the adsorbed molecules are preferentially adsorbed on the most energetically favorable sites on the surface. There is moreover no identifiable monolayer formation.
- Type IV isotherms are observed for mesoporous adsorbents, where monolayer and multilayer adsorption are followed by capillary condensation. In type IV(a) isotherms, capillary condensation is accompanied by adsorption hysteresis. This occurs when pores of widths larger than ± 4 nm are present. If the adsorbent has only mesopores of smaller widths, a reversible type IV(b) isotherm is observed.
- Type V isotherms are similar to type III isotherms for which adsorbent-adsorbate intermolecular interactions are relatively weak, but adsorption on preferential sites is followed by pore filling at higher relative pressure.
- Type VI isotherms are observed for highly uniform nonporous surface on which a distinct layer-by-layer adsorption occurs.

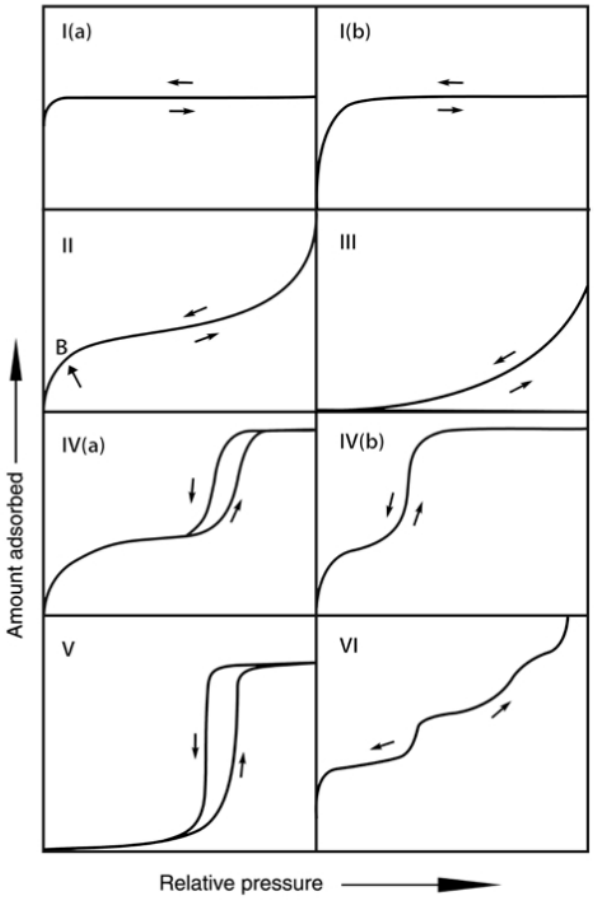

Figure A.2: Classification of gas adsorption isotherm [26].

Adsorption hysteresis is generally associated with capillary condensation in mesopores and its form is attributed to adsorption metastability and/or network effects [26]. A delayed condensation can result from metastability of the adsorbed multilayer, and it is generally considered that the adsorption branch of the hysteresis loop is not in thermodynamic equilibrium. However, the desorption process is reversible and thermodynamic equilibrium is well achieved on the desorption branch [26]. In complex pore structures,

the desorption process also depends on network effects and pore blocking, for instance if wide pores are only accessible through narrow necks. In this case, this is the size of the narrow neck that determines the pressure at which desorption occurs in the wider pores. For small neck diameters (ca. 5-6 nm for N_2 at 77 K), desorption from the wider pores involves cavitation [26], characterized by the homogeneous nucleation and growth of gas bubbles in the condensed fluid.

A.3 Charge confinement tubes used for detonation experiments

The dimensions of the steel tubes used to confine the charges during detonation experiments are shown on figure A.3 to A.9. The confinement tubes for charges of diameters ranging from 4 to 20 mm are made of stainless steel 316L, and that for charges of a diameter of 30 mm of stainless steel 321.

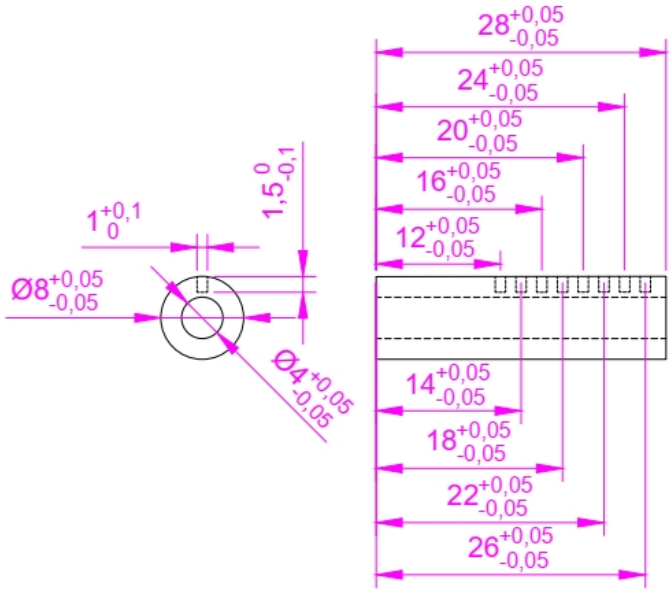

Figure A.3: Plan of the confinement tubes for charges with a diameter of 4 mm (dimensions in mm).

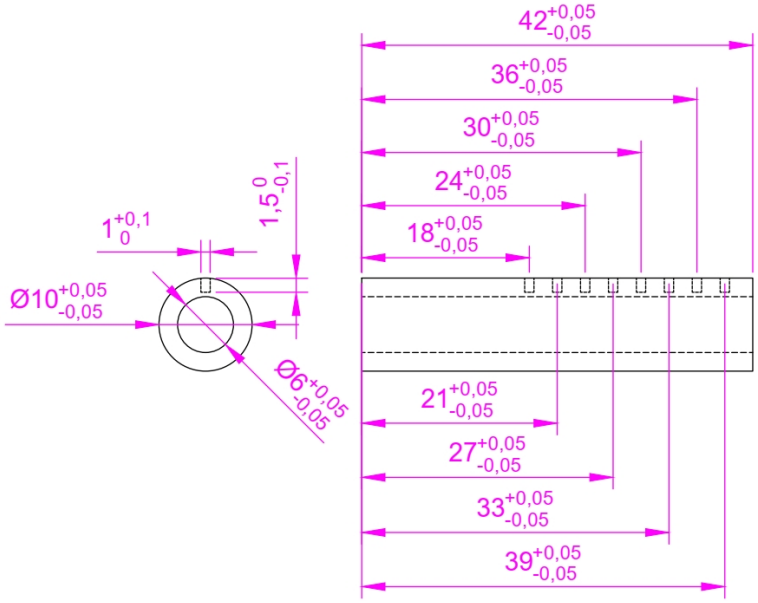

Figure A.4: Plan of the confinement tubes for charges with a diameter of 6 mm (dimensions in mm).

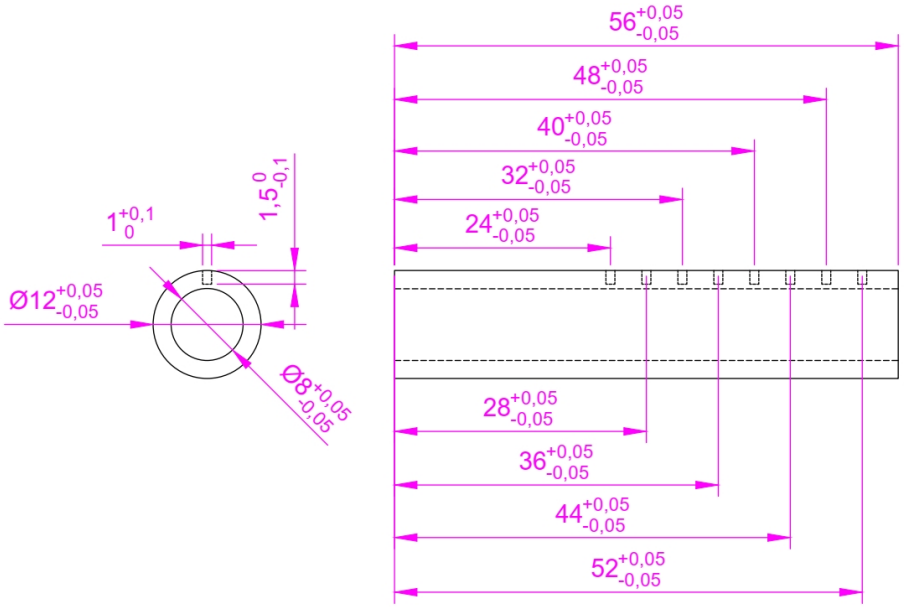

Figure A.5: Plan of the confinement tubes for charges with a diameter of 8 mm (dimensions in mm).

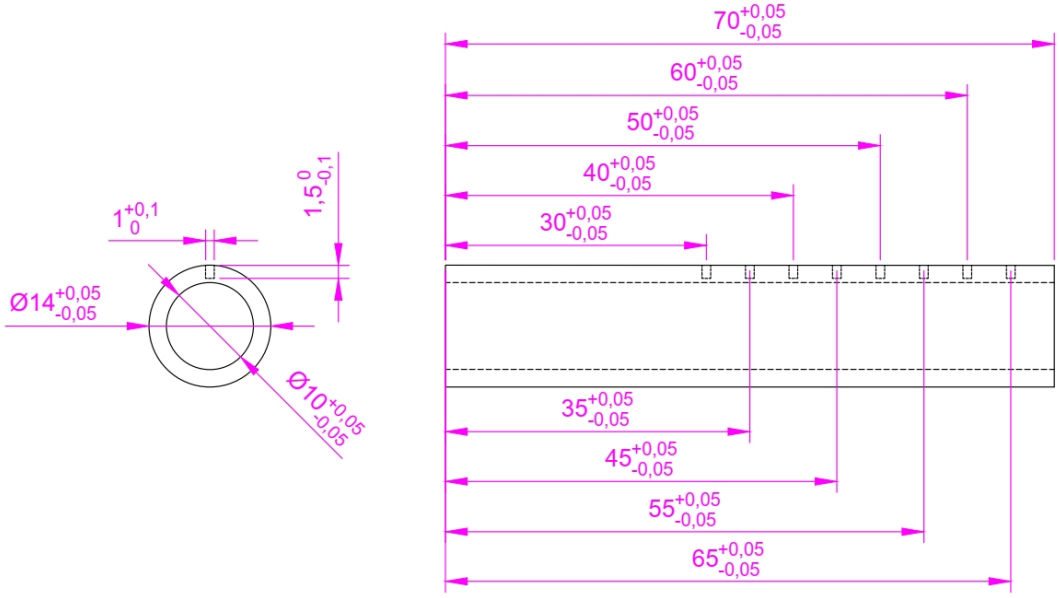

Figure A.6: Plan of the confinement tubes for charges with a diameter of 10 mm (dimensions in mm).

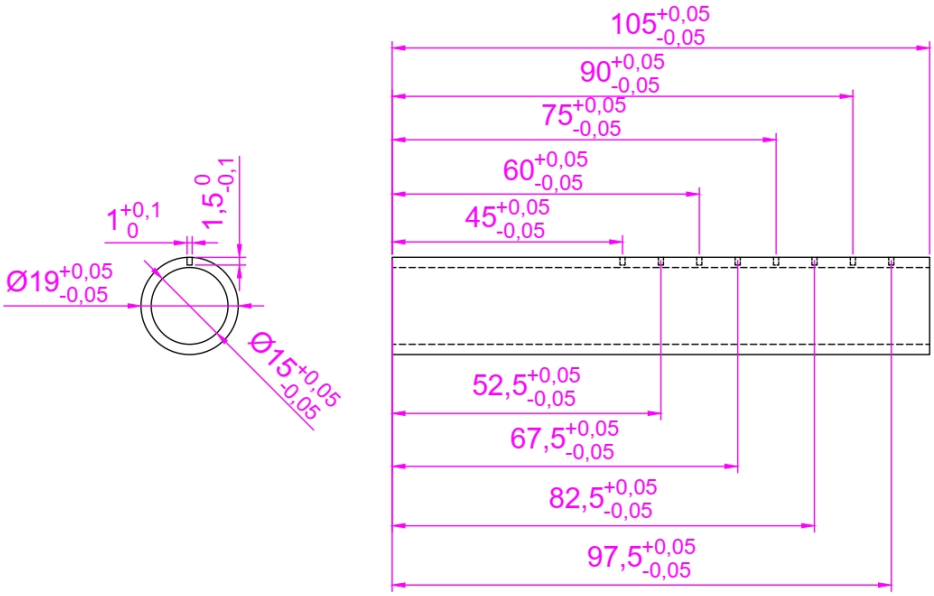

Figure A.7: Plan of the confinement tubes for charges with a diameter of 15 mm (dimensions in mm).

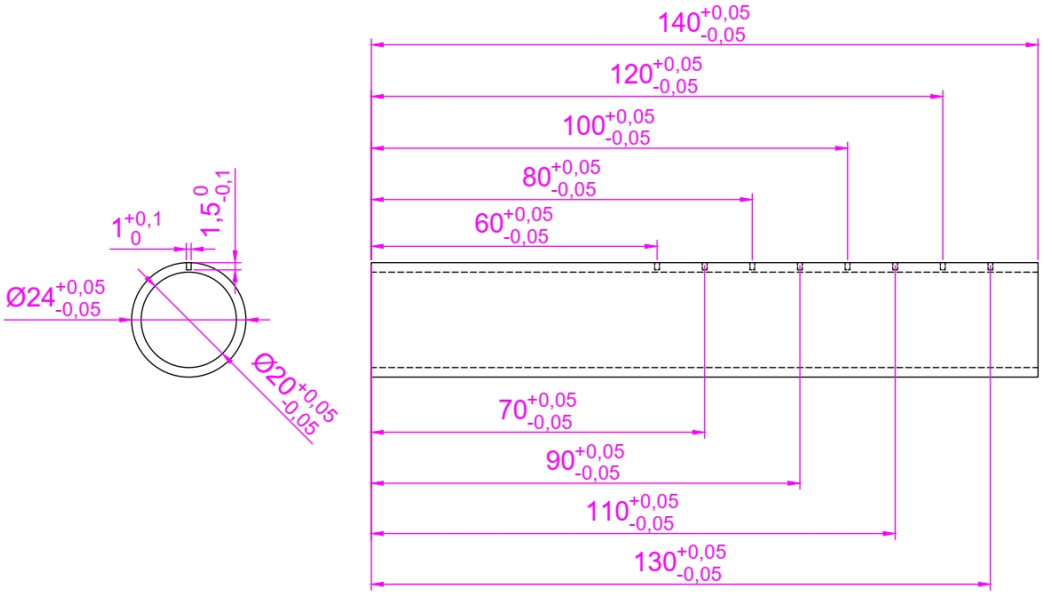

Figure A.8: Plan of the confinement tubes for charges with a diameter of 20 mm (dimensions in mm).

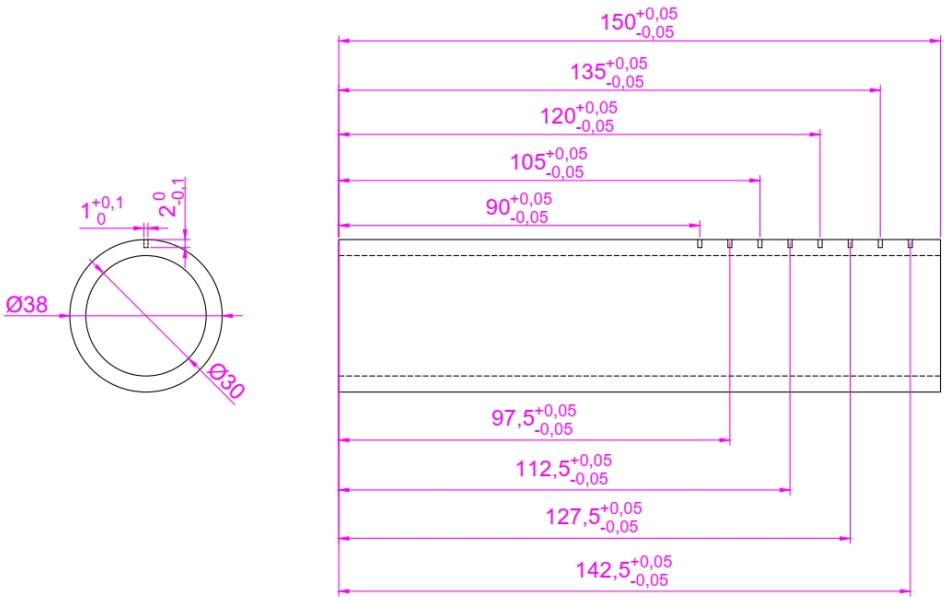

Figure A.9: Plan of the confinement tubes for charges with a diameter of 30 mm (dimensions in mm).

A.4 Determination of velocity of detonation based on arrival times

As described in chapter 2, the detonation velocities are determined by measuring the arrival times of a detonation wave at 8 different points in a high explosive charge. A typical recorded light signal is shown on figure A.10. The arrival time is clearly visible, as the signal shows a sharp increase at a relative time of 105.85 μs.

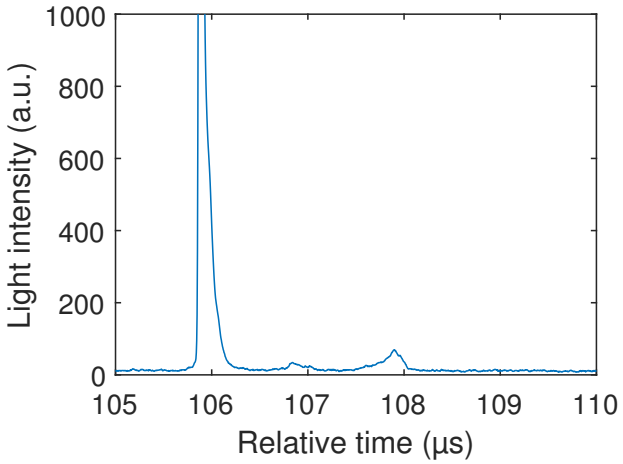

Figure A.10: Example of the light signal generated by the interaction between a shock wave travelling in the tube walls and generated by the detonation wave and the free surface at the bottom of a blind hole, transmitted by a glass optical fiber and recorded with an Optimex 64 Instrument (OZM Research).

Based on the determined arrival times and the known relative distances between the optical probes, the velocity of detonation is calculated by linear regression, as shown in figure A.11 for instance. The velocity of detonation is equal to the slope of the straight line, in this example 3.8 km/s for a charge diameter of 8 mm and a heavy steel confinement. The coefficient of determination (r^2) is 0.999 in this example, and is very close to 1 for all the presented results.

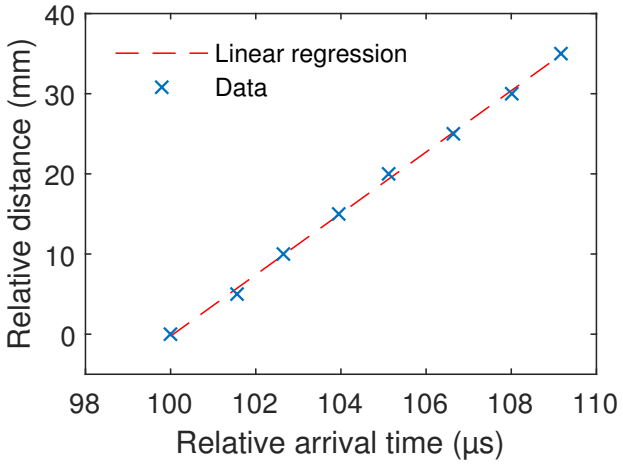

Figure A.11: Example of the linear regression performed to determine the velocity of detonation based on 8 measured arrival times at 8 different positions on a confinement tube wall.

A.5 Pressing of charge

The filled carbon investigated in section 4.3 is notably shaped into confinement tubes by means of hydraulic pressing. Figure A.12 shows the obtained density in function of the force applied on the charge by the press.

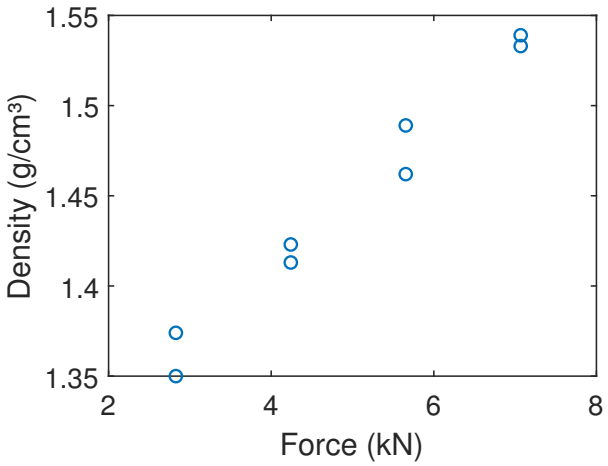

Figure A.12: Charge density in function of the force applied by means of a hydraulic press, for the filled carbon investigated in section 4.3.

Appendix B

Assessment of structural change during mercury intrusion

As high pressures are applied during mercury intrusion porosimetry, reversible and irreversible structural change may occur by compression, pore collapse or fracture of the material. Activated carbons are not usually considered as soft materials subject to these effects upon application of a high isostatic pressure. In order to verify this assumption, four representative activated carbon are selected (see Annex C for details):

- For carbon BPL and FY5, the overactivated derivatives with the highest burn-off (BPL-37 and FY5-57).
- For carbon C, the thermally reduced derivative at 600 °C (C-R600).
- For carbon F5001, the derivative chemically oxidized with ammonium persulfate (F5001-APS).

For carbons BPL, FY5 and C, these derivatives are selected as it is assumed that they are more prone to structural changes than the pristine carbons as their mechanical properties may have been affected by the thermal treatment. For carbon F5001, the chemically oxidized derivative is chosen because of a shortage of pristine carbon F5001, and as the chemical treatment is not supposed to significantly affect the mechanic properties of the carbon. The maximal pressure of the instrument (227 MPa) is used within the scope of this assessment. This is very conservative, as the intruded volume at ca. 30 MPa is used to determine the macroporous volume.

According to the IUPAC guidelines [81], two subsequent intrusion-extrusion cycles were recorded, and the results are shown in figure B.1 (only the high-pressure part of the curve is shown). It is observed that the hysteresis loops are reproducible during the second intrusion-extrusion cycle, indicating that there is no fracture of the material and that its structure is not irreversibly affected during the first cycle. The slightly less reproducible hysteresis loop of BPL-37 is attributed to a measurement error due to the limited accuracy of the method, as the intruded volume is very low owing to the relatively small macroporous volume of this carbon and to its low apparent density limiting the sample mass in the penetrometer to approximatively 0.15 g.

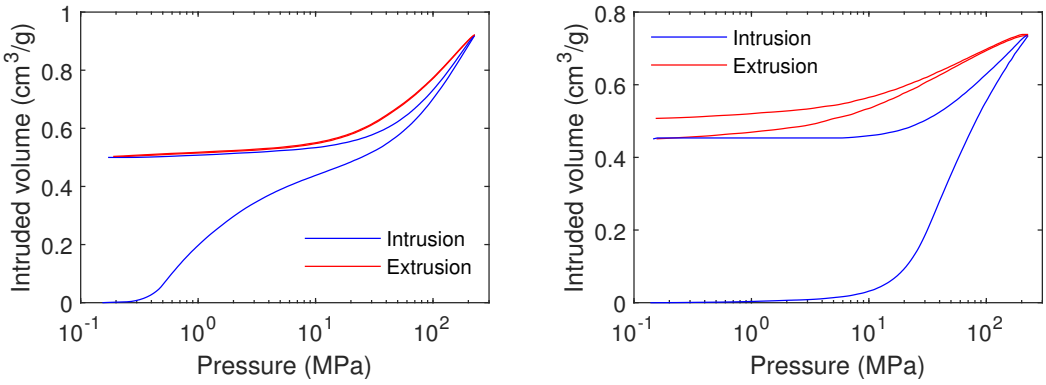

(a) C-R600.

(b) F5001-APS.

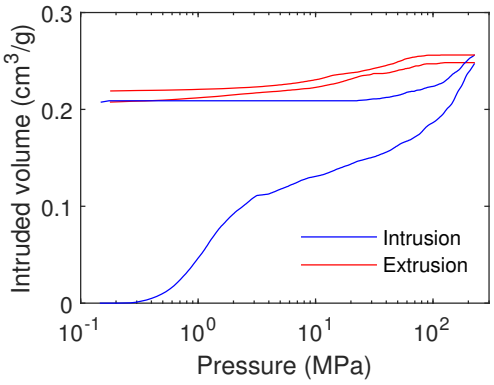

(c) BPL-37.

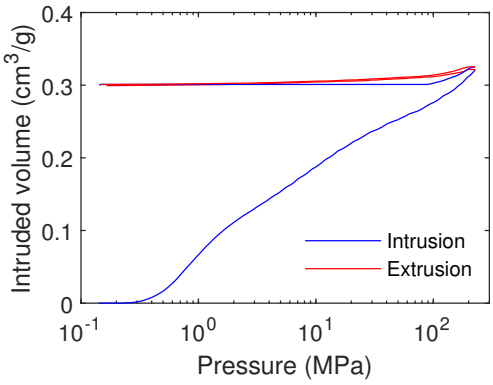

(d) FY5-57.

Figure B.1: Repeated mercury intrusion-extrusion cycles on different carbons.

Reversible compression or pore collapse can be significant and prevent the Washburn equation from being directly applied to the intrusion curve to determine the macroporous volume [106]. To assess the significance of these effects, the volume of entrapped mercury ($V_{\mathrm{Hg}}^{\mathrm{entr}}$) is obtained from the weighing of the recovered sample, following a procedure described in details elsewhere [106]:

$$V_{\mathrm{Hg}}^{\mathrm{entr}} = \frac{m_a - m_b}{\rho_{\mathrm{Hg}} \cdot m_b} \tag{B.1}$$

where m_a and m_b are the masses of the sample after and before the experiment, and ρ_{Hg} the density of mercury at room temperature (13.5 g/cm^3). The comparison of this volume of entrapped mercury with the residual volume, i.e. the last point of the extrusion curve recorded after depressurization, allows determining if mercury was effectively intruded in the pore structure and if irreversible compression occurs [106]. For the carbons selected for the assessment, this comparison is shown in table B.1.

Table B.1: Comparison between the calculated volume of mercury entrapped and the residual volume of mercury after extrusion, for different carbons. * Very difficult separation between the carbon beads and mercury.

Carbon	Mass before mass (g)	Mass after intrusion (g)	Volume of mercury entrapped (cm^3/g)	Residual volume (cm^3/g)
C-R600	0.2489	2.6984	0.729	0.672
F5001-APS	0.2565	3.3782*	0.901	0.508
BPL-37	0.1513	0.5501	0.195	0.173
FY5-57	0.1180	0.7427	0.392	0.343

It is observed that the calculated volume of entrapped mercury is in good agreement with the residual volume of mercury, excepted for the carbon F5001-APS, for which the separation between the mercury

and the small carbon beads was very difficult. The slight differences are attributed to traces of residual mercury weighed with the sample and to kinetic effects, as the mercury extrusion from the pores has been reported as a slow process that continues after depressurization [106]. These results show that mercury intrusion in the porous structure occurs, at least in a part of the pressure domain. They also suggest that no irreversible shrinkage occurred at high-pressure. It was also observed that the samples had exactly the same visual aspect after the experiment than before, which supports the assumption that no fracture occurred. However, a reversible compression followed by mercury intrusion cannot be excluded based on these results, as the mercury intrusion is not completely irreversible. The observation of the curves displaying the volume variation upon pressurization and depressurization (see figure B.2) is likewise not sufficient to confirm that no reversible compression occurs. It is however observed that the reversible part of the mercury intrusion is relatively limited. Given the rigid three-dimensional structure of the materials used in this work [20], i.e. activated carbon with biomass, coal or synthetic polymer as precursors, a significant reversible shrinkage seems nevertheless unlikely to occur. The Washburn equation is therefore used to determine the macroporous volume of the used carbon materials.

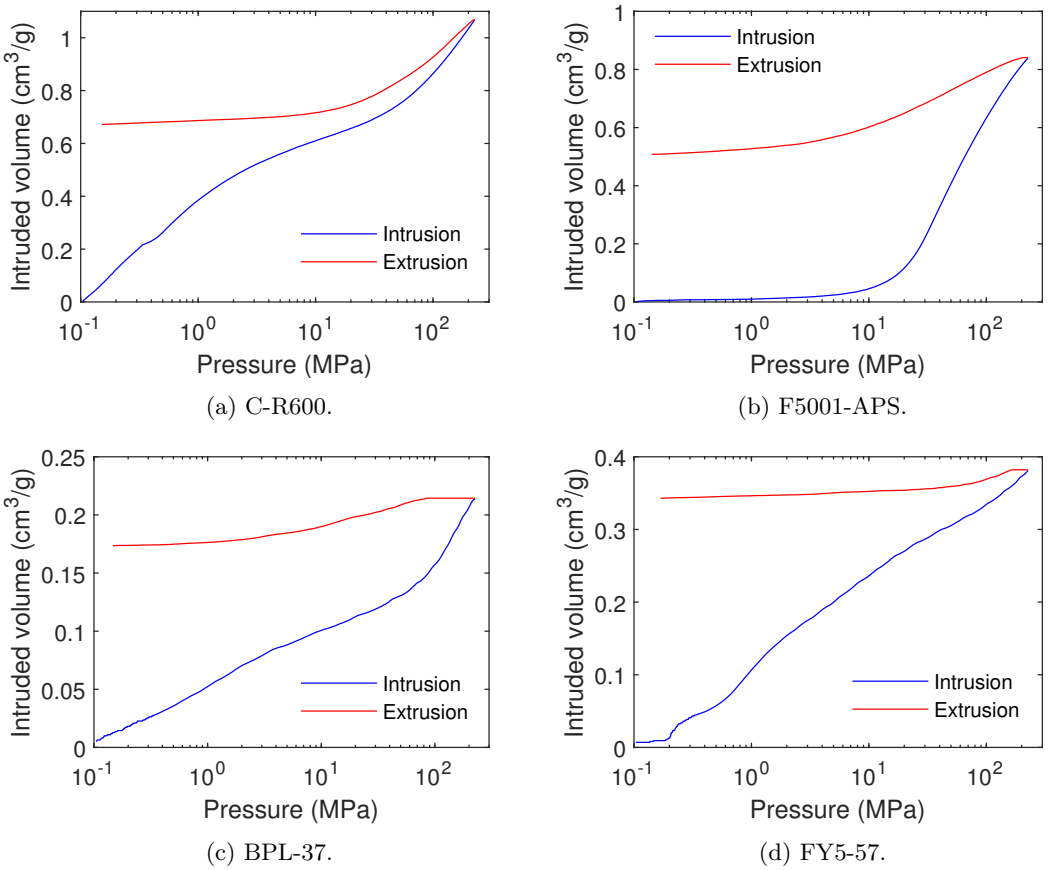

(a) C-R600.

(b) F5001-APS.

(c) BPL-37.

(d) FY5-57.

Figure B.2: Mercury intrusion-extrusion cycle measured for different carbons, to determine the volume of entrapped mercury and the residual mercury volume.

Appendix C

Characterization of pristine nanoporous carbons and derivatives

This annex presents all the experimental data about the characterization of the physicochemical properties of the pristine and modified carbons, described in section 3.2. The following results are shown:

- The N_2 adsorption/desorption isotherm measured at 77 K.
- The Ar adsorption/desorption isotherm measured at 87 K (only for pristine carbons).
- The CO_2 adsorption/desorption isotherm measured at 273 K (only for pristine carbons).
- The pore size distribution modelled from the N_2, Ar and CO_2 adsorption/desorption isotherm data.
- The mercury intrusion porosimetry (MIP) data.
- A summary of the main textural properties.
- The data of the temperature-programmed desorption analysis coupled with a mass spectrometer (TPDMS).
- An analysis of the TPDMS data to qualitatively identify the functional groups present on the surface of the carbon.
- The elemental analysis.
- The ash content.

The materials and the experimental methods are described in chapter 2.

C.1 Carbon C and derivatives

C.1.1 Pristine C

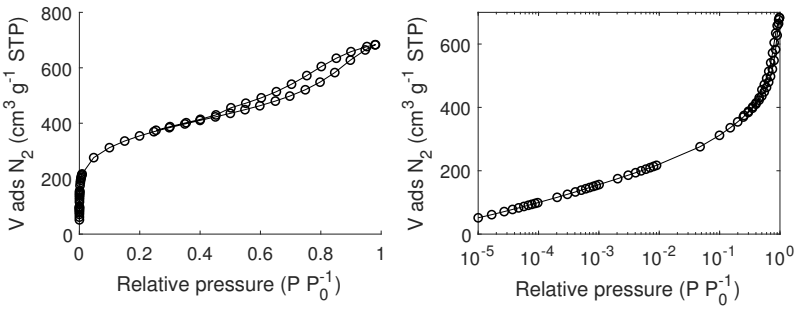

Figure C.1: N_2 adsorption/desorption isotherm of carbon C measured at 77 K.

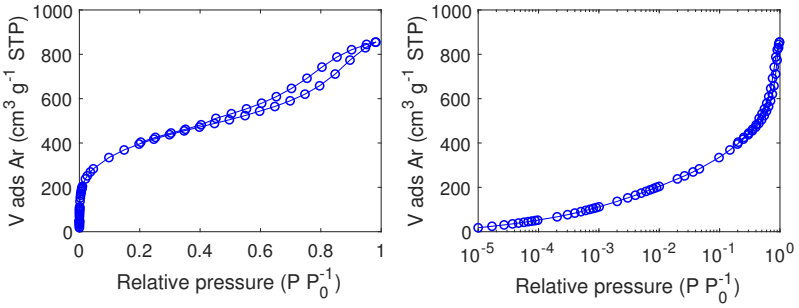

Figure C.2: Ar adsorption/desorption isotherm of carbon C measured at 87 K.

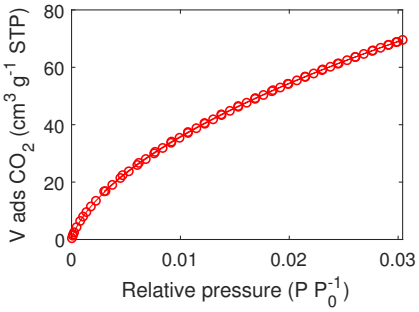

Figure C.3: CO_2 adsorption/desorption isotherm of carbon C measured at 273 K.

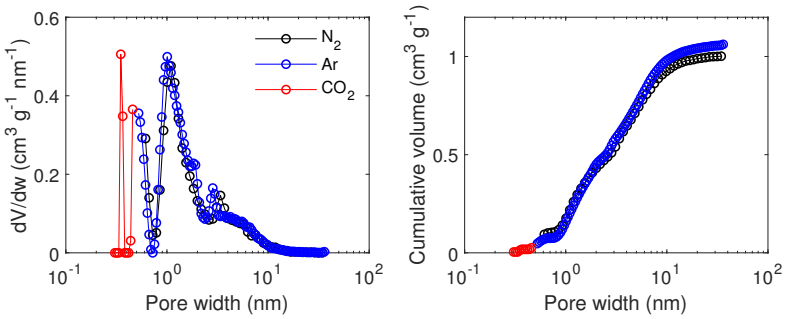

Figure C.4: Pore size distribution modelled by QSDFT for N_2 and Ar adsorption/desorption isotherms and NLDFT for adsorption/desorption CO_2 isotherm for carbon C.

Table C.1: Selected textural properties of carbon C; (a) total pore volume at $P/P_0 = 0.985$; (b) by NLDFT model; (c) by equilibrium QSDFT model; (d) by DR model; (e) based on MIP data; (1) N_2 adsorption isotherm at 77 K; (2) Ar adsorption isotherm at 87 K; (3) CO_2 adsorption isotherm at 273 K.

TPV^a (cm^3/g)	1.06[1] / 1.09[2]
Surface area^b (m^2/g)	1160[1] / 1165[2]
$V^b_{\text{ultramicro}}$ (cm^3/g)	0.12[3]
V^c_{micro} (cm^3/g)	0.43[1] / 0.45[2]
W^d_0 (cm^3/g)	0.44[1] / 0.43[2]
V^c_{meso} (cm^3/g)	0.57[1] / 0.61[2]
V^e_{macro} (cm^3/g)	0.67
Apparent density^e (g/cm^3)	0.41

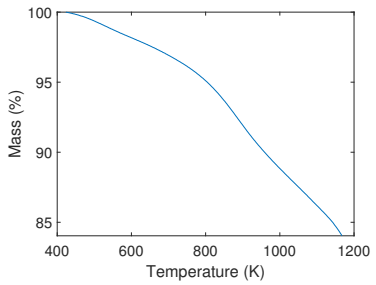

(a) TGA.

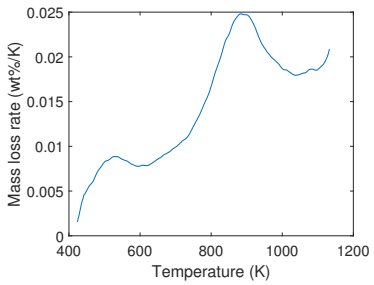

(b) DTG.

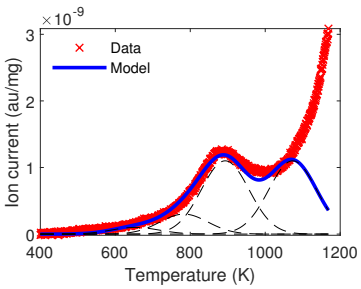

(c) CO profile.

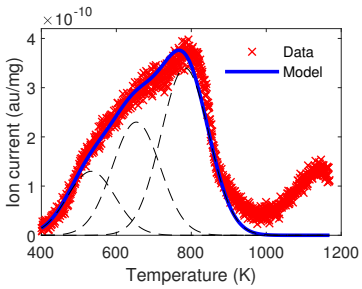

(d) CO_2 profile.

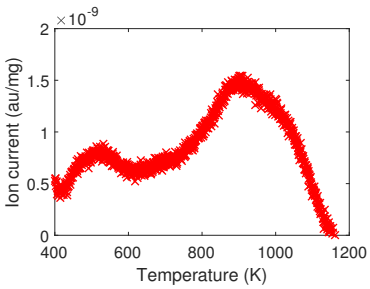

(e) H_2O profile.

Figure C.5: TPDMS data of carbon C.

Table C.2: Peak attribution based on TPDMS analysis of carbon C; (1) decomposition in α-substituted ketones and aldehydes.

Gas evolved	Peak temperature (K)	Peak width (K)	Peak area (a.u./mg)	Attribution
CO_2	533	150	$2.1 \cdot 10^{-8}$	Carboxylic acid
CO_2	653	150	$3.3 \cdot 10^{-8}$	Carboxylic acid
CO	653	150	$1.6 \cdot 10^{-8}$	Carbonyl[1]
CO_2	783	160	$5.8 \cdot 10^{-8}$	Carboxylic anhydride
CO	783	160	$5.1 \cdot 10^{-8}$	Carboxylic anhydride
CO	893	150	$1.8 \cdot 10^{-7}$	Phenol
CO	1073	150	$1.8 \cdot 10^{-7}$	Carbonyl/quinones

Table C.3: Elemental analysis and ash content (wt%) of carbon C.

C	H	O	N	S	Sum CHONS	Ash content
82.2	2.5	7.5	0.3	0.0	92.5	5.0

C.1.2 C-R300

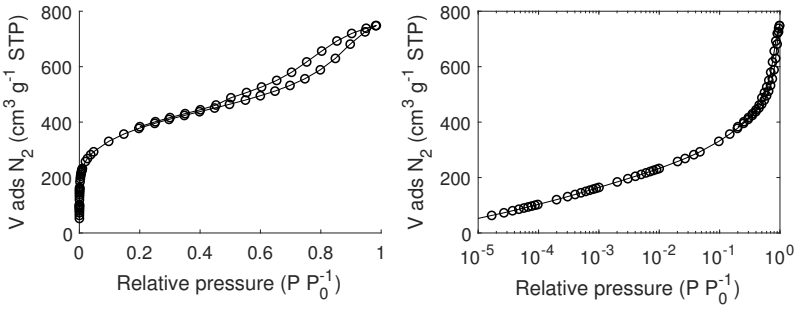

Figure C.6: N_2 adsorption/desorption isotherm of carbon C-R300 measured at 77 K.

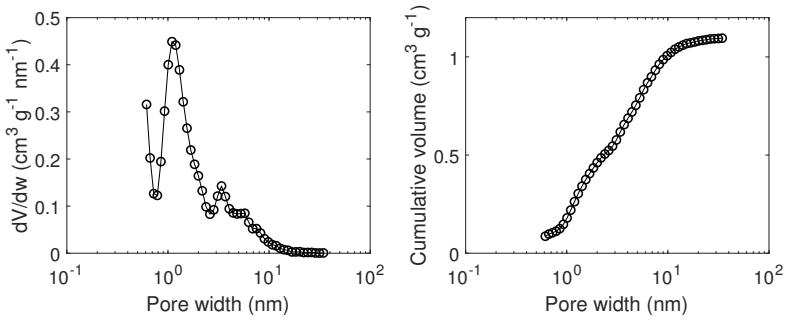

Figure C.7: Pore size distribution modelled by QSDFT based on N_2 adsorption/desorption isotherm for carbon C-R300.

Table C.4: Selected textural properties of carbon C-R300; (a) total pore volume at $P/P_0 = 0.985$; (b) by equilibrium QSDFT model; (c) by DR model; (d) based on MIP data.

TPV^a (cm^3/g)	1.16
Surface area^b (m^2/g)	1215
V^b_{micro} (cm^3/g)	0.46
W^c_0 (cm^3/g)	0.45
V^b_{meso} (cm^3/g)	0.63
V^d_{macro} (cm^3/g)	0.93
Apparent density^d (g/cm^3)	0.40

Table C.5: Peak attribution based on TPDMS analysis of carbon C-R300; (1) decomposition in α-substituted ketones and aldehydes.

Gas evolved	Peak temperature (K)	Peak width (K)	Peak area (a.u./mg)	Attribution
CO_2	533	150	$6.4 \cdot 10^{-9}$	Carboxylic acid
CO_2	673	150	$3.0 \cdot 10^{-8}$	Carboxylic acid
CO	673	150	$8.0 \cdot 10^{-9}$	Carbonyl[1]
CO_2	783	160	$5.8 \cdot 10^{-8}$	Carboxylic anhydride
CO	783	160	$6.8 \cdot 10^{-8}$	Carboxylic anhydride
CO	893	150	$2.4 \cdot 10^{-7}$	Phenol
CO	1073	150	$2.1 \cdot 10^{-7}$	Carbonyl/quinones

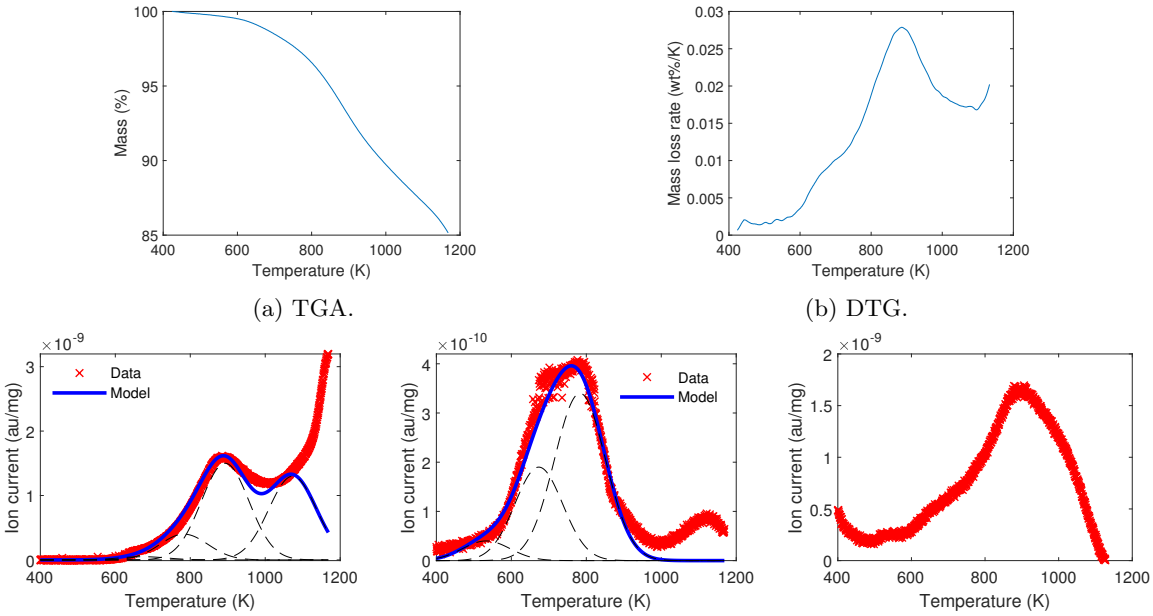

(a) TGA. (b) DTG.

(c) CO profile. (d) CO_2 profile. (e) H_2O profile.

Figure C.8: TPDMS data of carbon C-R300.

Table C.6: Elemental analysis (wt%) of carbon C-R300.

C	H	O	N	S	Sum CHONS
79.9	2.1	6.6	0.2	0.0	88.8

C.1.3 C-R600

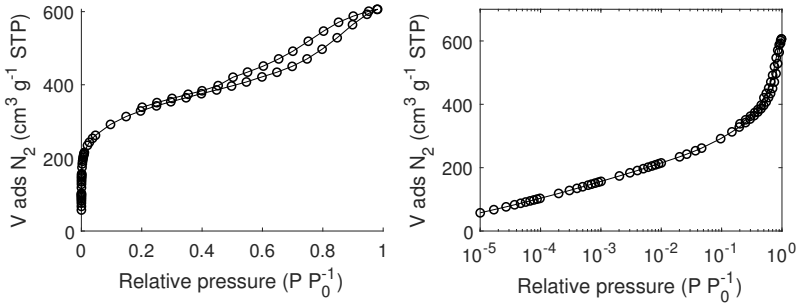

Figure C.9: N_2 adsorption/desorption isotherm of carbon C-R600 measured at 77 K.

Table C.7: Selected textural properties of carbon C-R600; (a) total pore volume at $P/P_0 = 0.985$; (b) by equilibrium QSDFT model; (c) by DR model; (d) based on MIP data.

TPV^a (cm^3/g)	0.94
Surface area^b (m^2/g)	1131
V^b_{micro} (cm^3/g)	0.41
W^c_0 (cm^3/g)	0.40
V^b_{meso} (cm^3/g)	0.47
V^d_{macro} (cm^3/g)	0.78
Apparent density^d (g/cm^3)	0.46

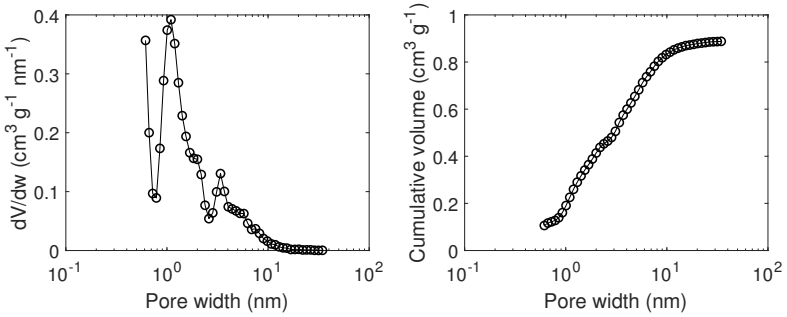

Figure C.10: Pore size distribution modelled by QSDFT based on N_2 adsorption/desorption isotherm for carbon C-R600.

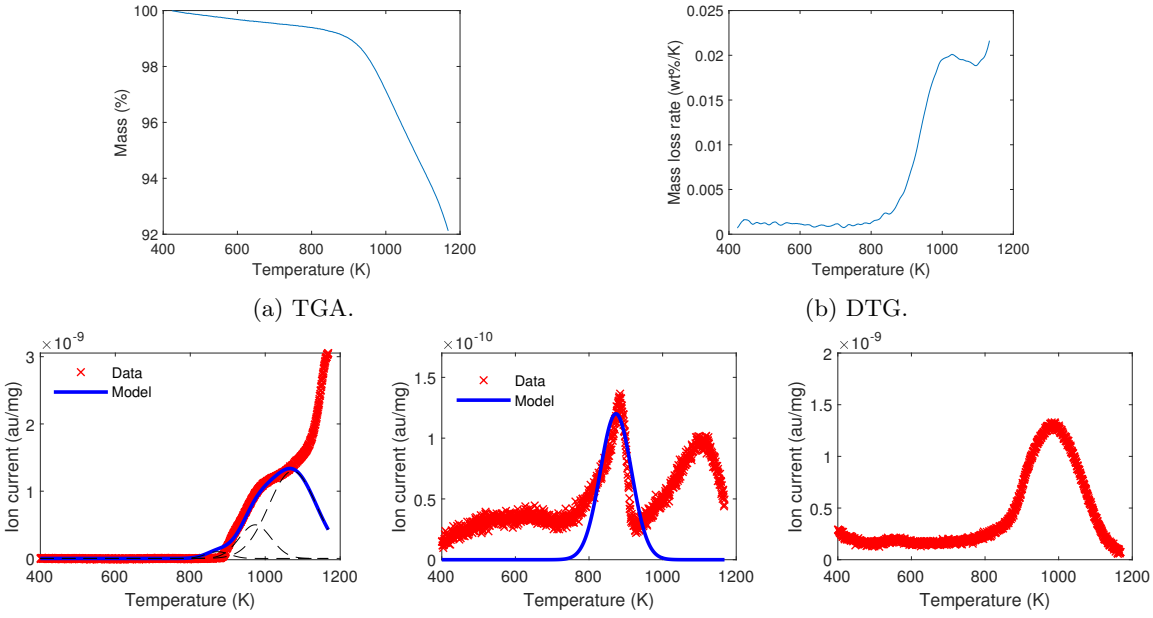

(a) TGA.

(b) DTG.

(c) CO profile.

(d) CO_2 profile.

(e) H_2O profile.

Figure C.11: TPDMS data of carbon C-R600.

Table C.8: Peak attribution based on TPDMS analysis of carbon C-R600.

Gas evolved	Peak temperature (K)	Peak width (K)	Peak area (a.u./mg)	Attribution
CO_2	873	75	$9.6 \cdot 10^{-9}$	Carboxylic anhydride
CO	873	75	$8.0 \cdot 10^{-9}$	Carboxylic anhydride
CO	973	100	$5.3 \cdot 10^{-8}$	Phenol
CO	1073	150	$2.1 \cdot 10^{-7}$	Carbonyl/quinones

Table C.9: Elemental analysis (wt%) of carbon C-R600.

C	H	O	N	S	Sum CHONS
80.6	1.7	4.6	0.2	0.0	87.1

C.2 Carbon F5001 and derivatives

C.2.1 Pristine F5001

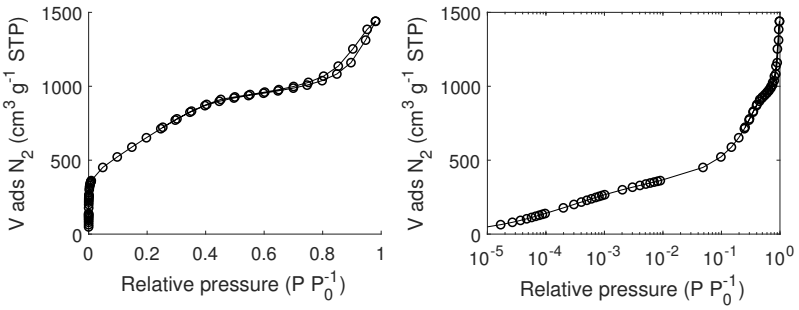

Figure C.12: N_2 adsorption/desorption isotherm of carbon F5001 measured at 77 K.

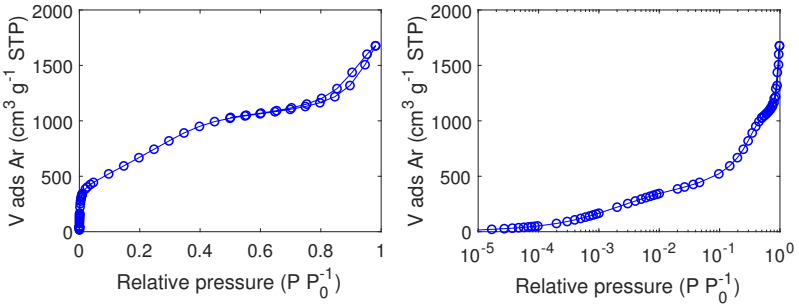

Figure C.13: Ar adsorption/desorption isotherm of carbon F5001 measured at 87 K.

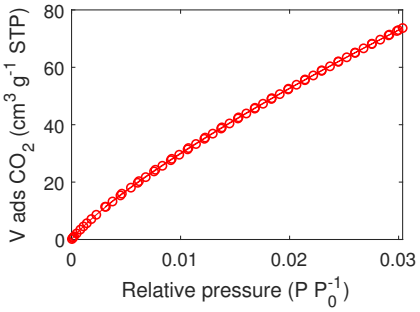

Figure C.14: CO_2 adsorption/desorption isotherm of carbon F5001 measured at 273 K.

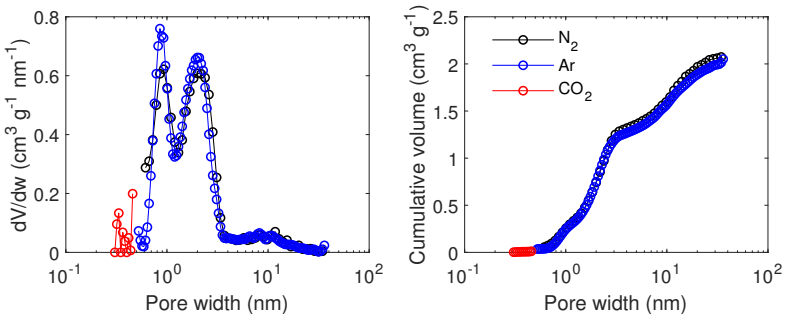

Figure C.15: Pore size distribution modelled by QSDFT for N_2 and Ar adsorption/desorption isotherms and NLDFT for CO_2 adsorption/desorption isotherm for carbon F5001.

Table C.10: Selected textural properties of carbon F5001; (a) total pore volume at P/P_0 = 0.985; (b) by NLDFT model; (c) by equilibrium QSDFT model; (d) by DR model; (e) based on MIP data; (1) N_2 adsorption isotherm at 77 K; (2) Ar adsorption isotherm at 87 K; (3) CO_2 adsorption isotherm at 273 K.

TPV^a (cm^3/g)	2.23^1 / 2.14^2
Surface area^b (m^2/g)	1890^1 / 1879^2
$V^b_{ultramicro}$ (cm^3/g)	0.11^3
V^c_{micro} (cm^3/g)	0.74^1 / 0.75^2
W^d_0 (cm^3/g)	0.99^1 / 0.75^2
V^c_{meso} (cm^3/g)	1.33^1 / 1.30^2
V^e_{macro} (cm^3/g)	0.43
Apparent density^e (g/cm^3)	0.37

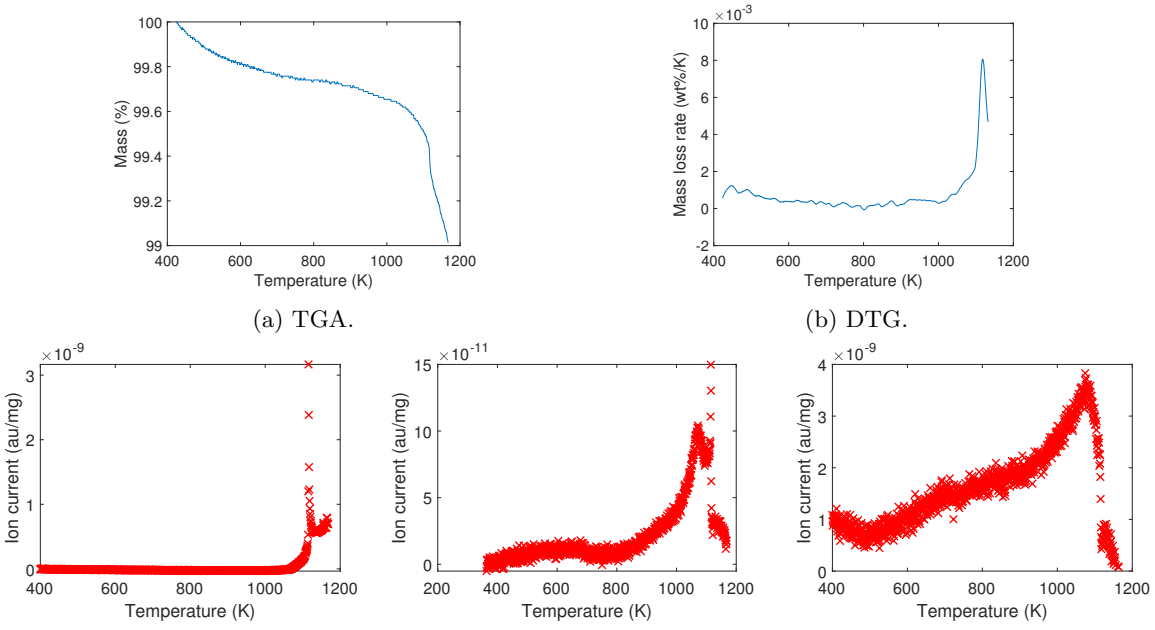

(a) TGA.

(b) DTG.

(c) CO profile.

(d) CO_2 profile.

(e) H_2O profile.

Figure C.16: TPDMS data of carbon F5001.

Table C.11: Elemental analysis and ash content (wt%) of carbon F5001.

C	H	O	N	S	Sum CHONS	Ash content
97.1	0.7	1.6	0.1	0.7	100.2	0.5

C.2.2 F5001-APS

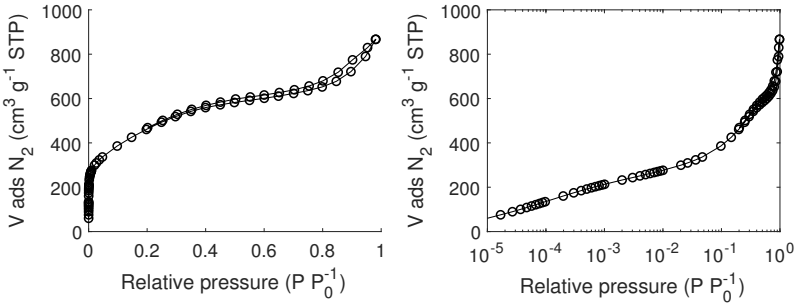

Figure C.17: N_2 adsorption/desorption isotherm of carbon F5001-APS measured at 77 K.

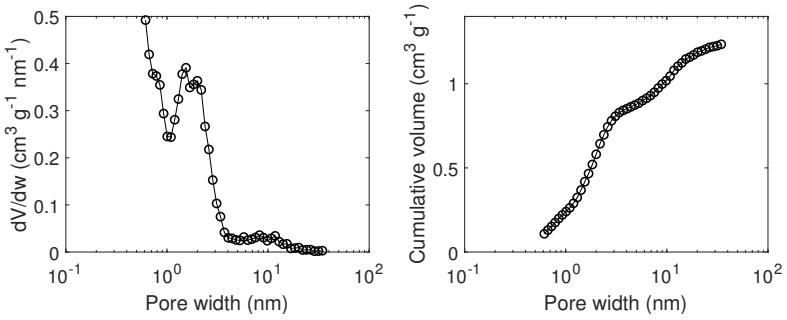

Figure C.18: Pore size distribution modelled by QSDFT based on N_2 adsorption/desorption isotherm for carbon F5001-APS.

Table C.12: Selected textural properties of carbon F5001-APS; (a) total pore volume at P/P_0 = 0.985; (b) by equilibrium QSDFT model; (c) by DR model; (d) based on MIP data.

TPV^a (cm^3/g)	1.34
Surface area^b (m^2/g)	1258
V^b_{micro} (cm^3/g)	0.58
W^c_0 (cm^3/g)	0.63
V^b_{meso} (cm^3/g)	0.65
V^d_{macro} (cm^3/g)	0.21
Apparent density^d (g/cm^3)	0.61

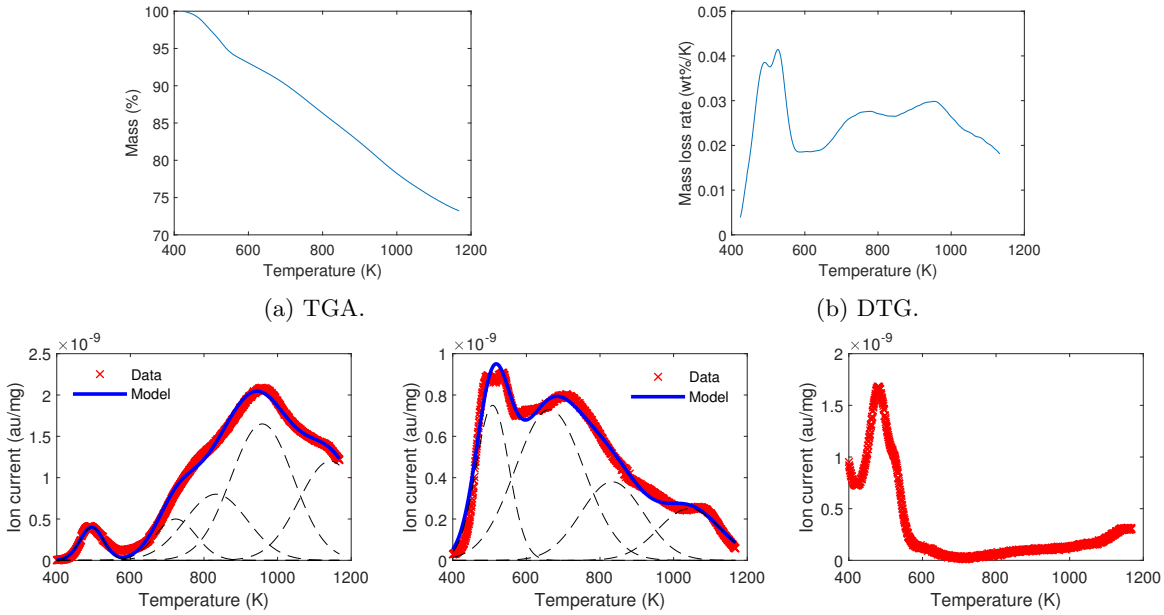

(a) TGA. (b) DTG.

(c) CO profile. (d) CO_2 profile. (e) H_2O profile.

Figure C.19: TPDMS data of carbon F5001-APS.

Table C.13: Peak attribution based on TPDMS analysis of carbon F5001-APS; (1) decomposition in α-substituted ketones and aldehydes.

Gas evolved	Peak temperature (K)	Peak width (K)	Peak area (a.u./mg)	Attribution
CO_2	508	105	$8.4 \cdot 10^{-8}$	Carboxylic acid
CO	495	75	$3.2 \cdot 10^{-8}$	Carbonyl[1]
CO_2	663	220	$1.7 \cdot 10^{-7}$	Carboxylic acid
CO	723	130	$6.9 \cdot 10^{-8}$	Carbonyl[1]
CO_2	833	200	$8.1 \cdot 10^{-8}$	Carboxylic anhydride
CO	733	200	$1.7 \cdot 10^{-7}$	Carboxylic anhydride
CO	958	200	$3.5 \cdot 10^{-7}$	Phenol
CO_2	1043	200	$5.3 \cdot 10^{-8}$	Lactone
CO	1143	200	$2.6 \cdot 10^{-7}$	Carbonyl/quinones

Table C.14: Elemental analysis (wt%) of carbon F5001-APS.

C	H	O	N	S	Sum CHONS
76.0	1.0	14.8	1.3	0.4	93.5

C.2.3 F5001-HN

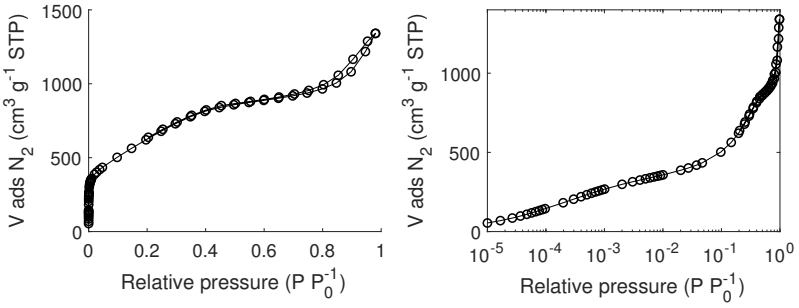

Figure C.20: N_2 adsorption/desorption isotherm of carbon F5001-HN measured at 77 K.

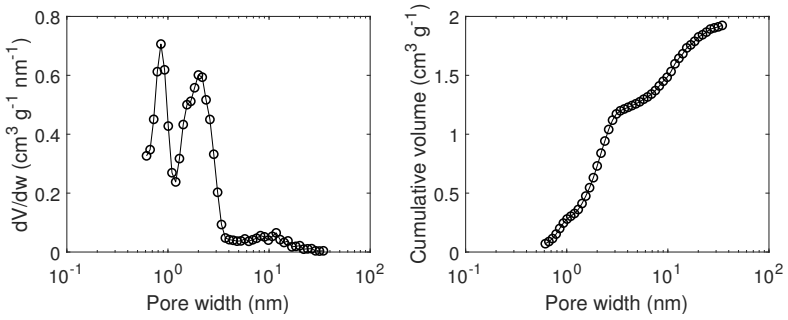

Figure C.21: Pore size distribution modelled by QSDFT based on N_2 adsorption/desorption isotherm for carbon F5001-HN.

Table C.15: Selected textural properties of carbon F5001-HN; (a) total pore volume at P/P_0 = 0.985; (b) by equilibrium QSDFT model; (c) by DR model; (d) based on MIP data.

TPV^a (cm^3/g)	2.07
Surface area^b (m^2/g)	1850
V^b_{micro} (cm^3/g)	0.73
W^c_0 (cm^3/g)	0.96
V^b_{meso} (cm^3/g)	1.19
V^d_{macro} (cm^3/g)	0.37
Apparent density^d (g/cm^3)	0.41

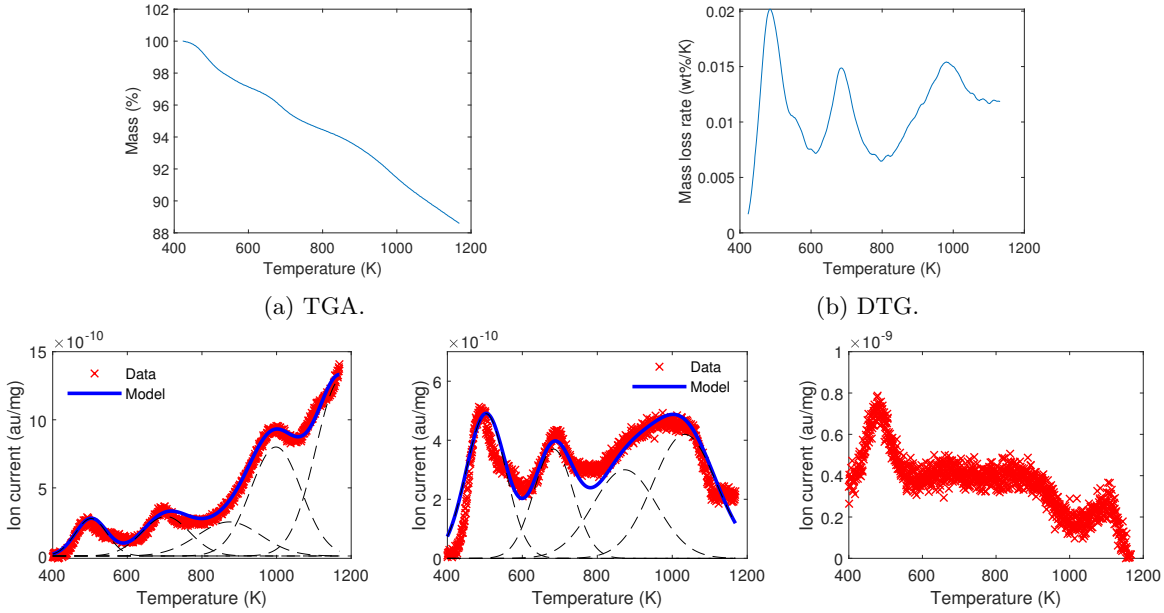

(a) TGA. (b) DTG.

(c) CO profile. (d) CO_2 profile. (e) H_2O profile.

Figure C.22: TPDMS data of carbon F5001-HN.

Table C.16: Peak attribution based on TPDMS analysis of carbon F5001-HN; (1) decomposition in α-substituted ketones and aldehydes.

Gas evolved	Peak temperature (K)	Peak width (K)	Peak area (a.u./mg)	Attribution
CO_2	503	125	$6.5 \cdot 10^{-8}$	Carboxylic acid
CO	503	100	$2.9 \cdot 10^{-8}$	Carbonyl[1]
CO_2	683	125	$4.9 \cdot 10^{-8}$	Carboxylic acid
CO	703	150	$4.6 \cdot 10^{-8}$	Carbonyl[1]
CO_2	873	200	$6.4 \cdot 10^{-8}$	Carboxylic anhydride
CO	873	200	$5.3 \cdot 10^{-8}$	Carboxylic anhydride
CO	998	160	$1.4 \cdot 10^{-7}$	Phenol
CO_2	1033	200	$8.9 \cdot 10^{-8}$	Lactone
CO	1173	160	$2.2 \cdot 10^{-7}$	Carbonyl/quinones

Table C.17: Elemental analysis (wt%) of carbon F5001-HN.

C	H	O	N	S	Sum CHONS
85.8	0.4	4.5	1.0	0.6	92.3

C.3 Carbon BPL and derivatives

C.3.1 Pristine BPL

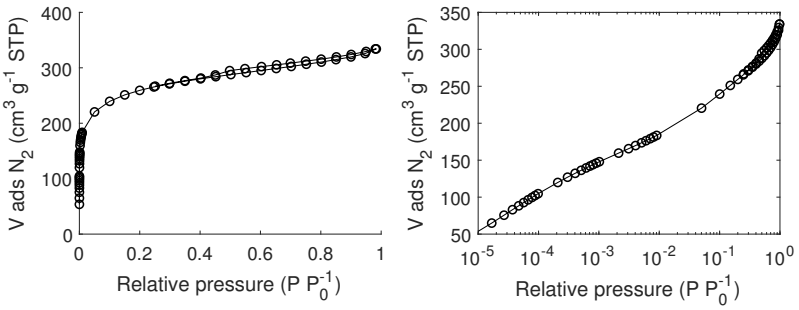

Figure C.23: N_2 adsorption/desorption isotherm of carbon BPL measured at 77 K.

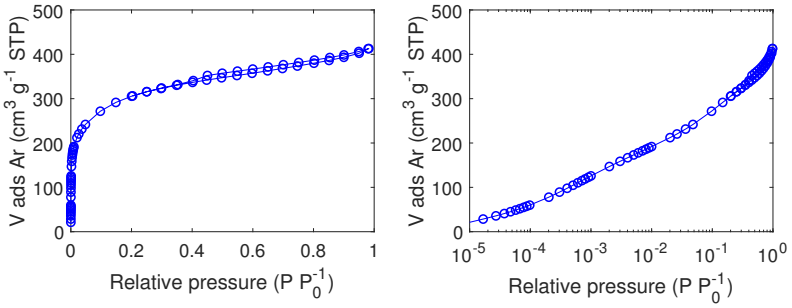

Figure C.24: Ar adsorption/desorption isotherm of carbon BPL measured at 87 K.

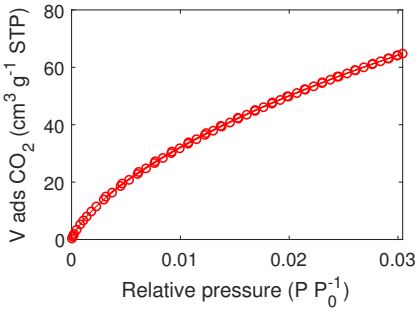

Figure C.25: CO_2 adsorption/desorption isotherm of carbon BPL measured at 273 K.

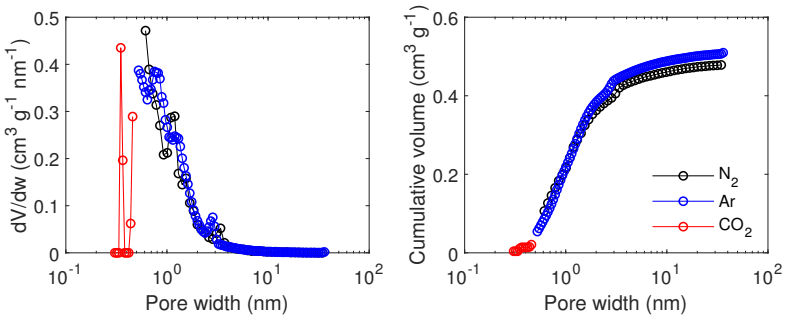

Figure C.26: Pore size distribution modelled by QSDFT for N_2 and Ar adsorption/desorption isotherms and NLDFT for CO_2 adsorption/desorption isotherm for carbon BPL.

Table C.18: Selected textural properties of carbon BPL; (a) total pore volume at $P/P_0 = 0.985$; (b) by NLDFT model; (c) by equilibrium QSDFT model; (d) by DR model; (e) based on MIP data; (1) N_2 adsorption isotherm at 77 K; (2) Ar adsorption isotherm at 87 K; (3) CO_2 adsorption isotherm at 273 K.

TPV^a (cm^3/g)	0.58^1 / 0.53^2
Surface area^b (m^2/g)	955^1 / 990^2
$V^b_{ultramicro}$ (cm^3/g)	0.11^3
V^c_{micro} (cm^3/g)	0.40^1 / 0.38^2
W^d_0 (cm^3/g)	0.40^1 / 0.34^2
V^c_{meso} (cm^3/g)	0.14^1 / 0.13^2
V^e_{macro} (cm^3/g)	0.31
Apparent density^e (g/cm^3)	0.73

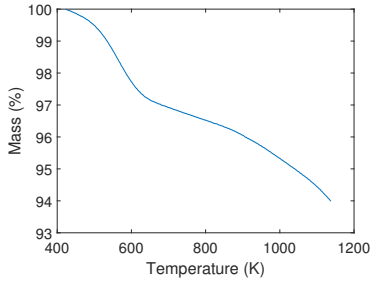

(a) TGA.

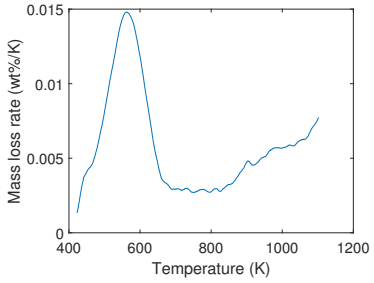

(b) DTG.

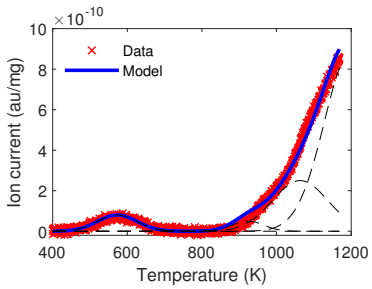

(c) CO profile.

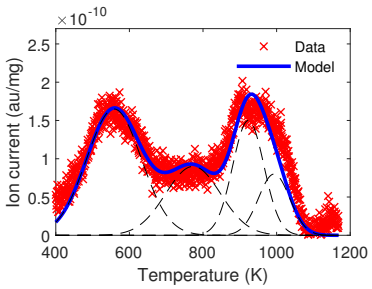

(d) CO_2 profile.

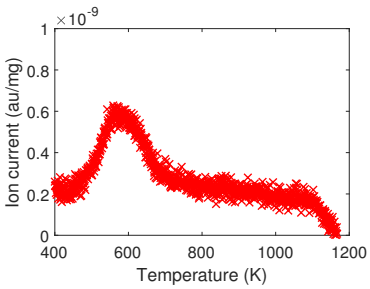

(e) H_2O profile.

Figure C.27: TPDMS data of carbon BPL.

Table C.19: Peak attribution based on TPDMS analysis of carbon BPL; (1) decomposition in α-substituted ketones and aldehydes.

Gas evolved	Peak temperature (K)	Peak width (K)	Peak area (a.u./mg)	Attribution
CO_2	558	175	$3.1 \cdot 10^{-8}$	Carboxylic acid
CO	573	125	$1.1 \cdot 10^{-8}$	Carbonyl[1]
CO_2	773	175	$1.7 \cdot 10^{-8}$	Carboxylic acid
CO_2	923	100	$1.6 \cdot 10^{-8}$	Carboxylic anhydride
CO	923	100	$5.3 \cdot 10^{-9}$	Carboxylic anhydride
CO_2	993	100	$8.5 \cdot 10^{-9}$	Lactone
CO	1063	175	$4.7 \cdot 10^{-8}$	Phenol
CO	1203	175	$1.7 \cdot 10^{-7}$	Carbonyl/quinones

Table C.20: Elemental analysis and ash content (wt%) of carbon BPL.

C	H	O	N	S	Sum CHONS	Ash content
78.6	1.0	2.6	0.3	0.3	82.8	11.8

C.3.2 BPL-18

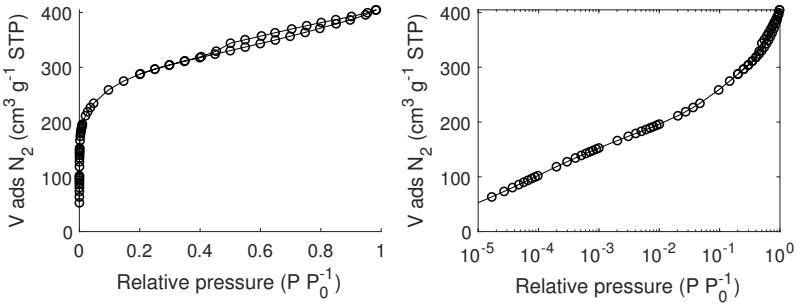

Figure C.28: N_2 adsorption/desorption isotherm of carbon BPL-18 measured at 77 K.

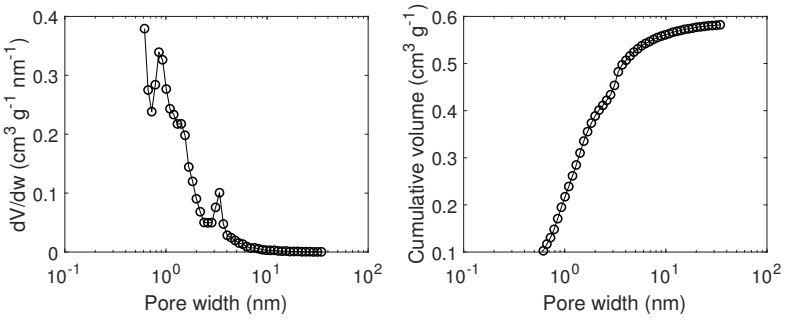

Figure C.29: Pore size distribution modelled by QSDFT based on N_2 adsorption/desorption isotherm for carbon BPL-18.

Table C.21: Selected textural properties of carbon BPL-18; (a) total pore volume at $P/P_0 = 0.985$; (b) by equilibrium QSDFT model; (c) by DR model; (d) based on MIP data.

TPV^a (cm^3/g)	0.63
Surface area^b (m^2/g)	1015
V^b_{micro} (cm^3/g)	0.39
W^c_0 (cm^3/g)	0.40
V^b_{meso} (cm^3/g)	0.19
V^d_{macro} (cm^3/g)	0.32
Apparent density^d (g/cm^3)	0.70

Table C.22: Peak attribution based on TPDMS analysis of carbon BPL-18.

Gas evolved	Peak temperature (K)	Peak width (K)	Peak area (a.u./mg)	Attribution
CO_2	1053	100	$8.5 \cdot 10^{-9}$	Lactone
CO	1203	150	$1.1 \cdot 10^{-7}$	Carbonyl/quinones

Table C.23: Elemental analysis (wt%) of carbon BPL-18.

C	H	O	N	S	Sum CHONS
79.2	0.5	0.9	0.4	0.4	81.4

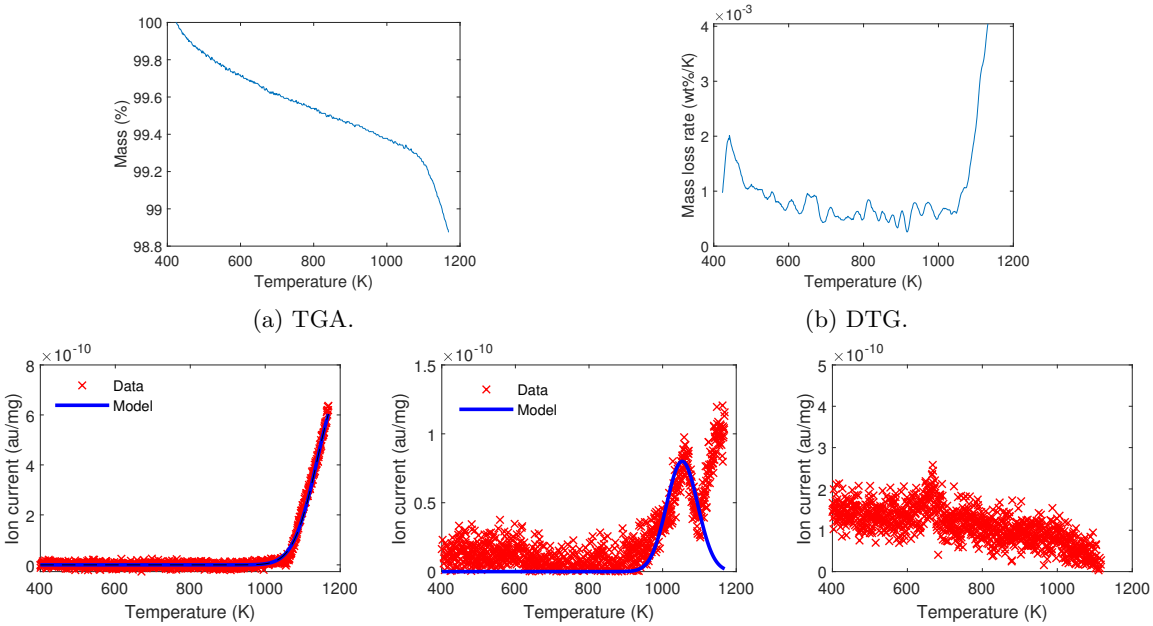

(a) TGA. (b) DTG.

(c) CO profile. (d) CO_2 profile. (e) H_2O profile.

Figure C.30: TPDMS data of carbon BPL-18.

C.3.3 BPL-37

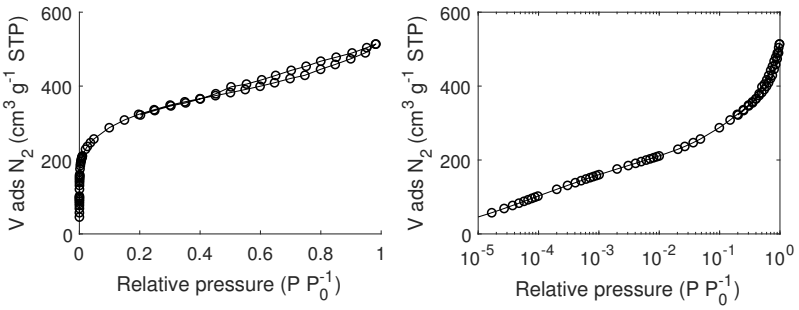

Figure C.31: N_2 adsorption/desorption isotherm of carbon BPL-37 measured at 77 K.

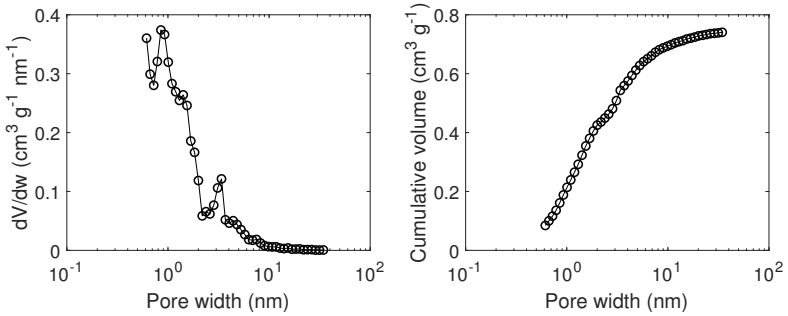

Figure C.32: Pore size distribution modelled by QSDFT based on N_2 adsorption/desorption isotherm for carbon BPL-37.

Table C.24: Selected textural properties of carbon BPL-37; (a) total pore volume at P/P_0 = 0.985; (b) by equilibrium QSDFT model; (c) by DR model; (d) based on MIP data.

TPV^a (cm^3/g)	0.79
Surface area^b (m^2/g)	1075
V^b_{micro} (cm^3/g)	0.43
W^c_0 (cm^3/g)	0.45
V^b_{meso} (cm^3/g)	0.31
V^d_{macro} (cm^3/g)	0.48
Apparent density^d (g/cm^3)	0.57

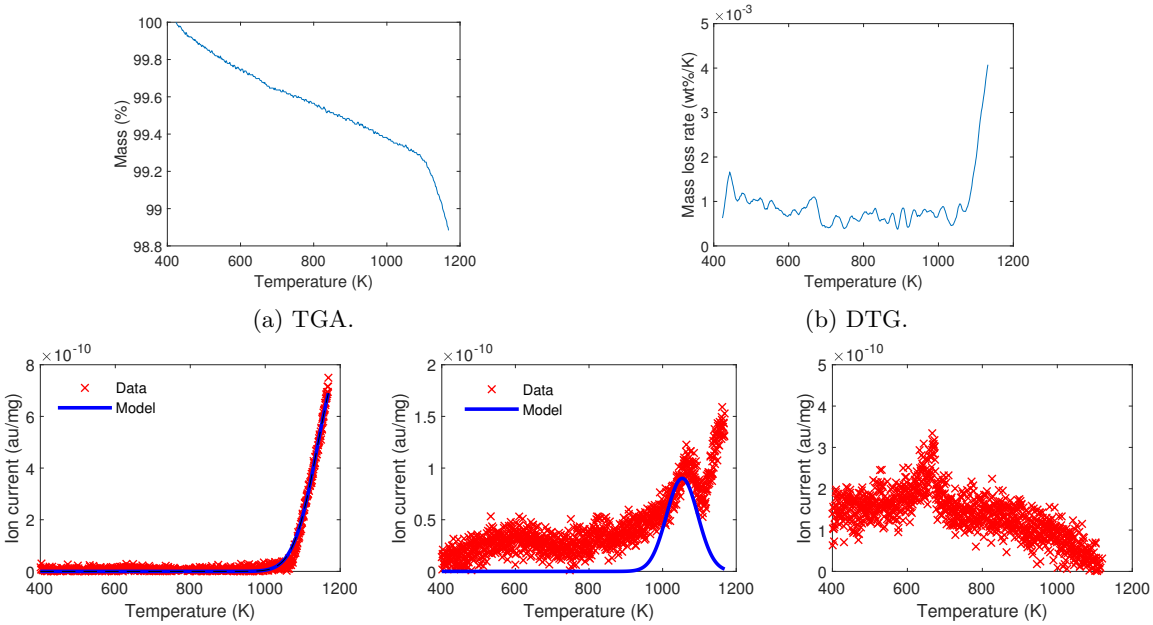

(a) TGA. (b) DTG.

(c) CO profile. (d) CO_2 profile. (e) H_2O profile.

Figure C.33: TPDMS data of carbon BPL-37.

Table C.25: Peak attribution based on TPDMS analysis of carbon BPL-37.

Gas evolved	Peak temperature (K)	Peak width (K)	Peak area (a.u./mg)	Attribution
CO_2	1053	100	$8.5 \cdot 10^{-9}$	Lactone
CO	1203	150	$1.1 \cdot 10^{-7}$	Carbonyl/quinones

Table C.26: Elemental analysis (wt%) of carbon BPL-37.

C	H	O	N	S	Sum CHONS
82.8	0.6	1.0	0.9	0.0	85.3

C.4 Carbon FY5 and derivatives

C.4.1 Pristine FY5

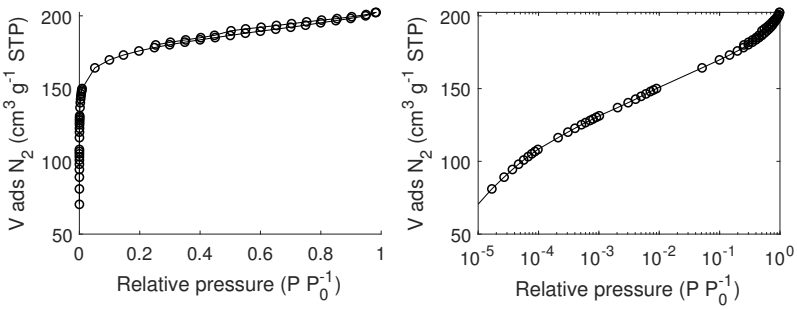

Figure C.34: N_2 adsorption/desorption isotherm of carbon FY5 measured at 77 K.

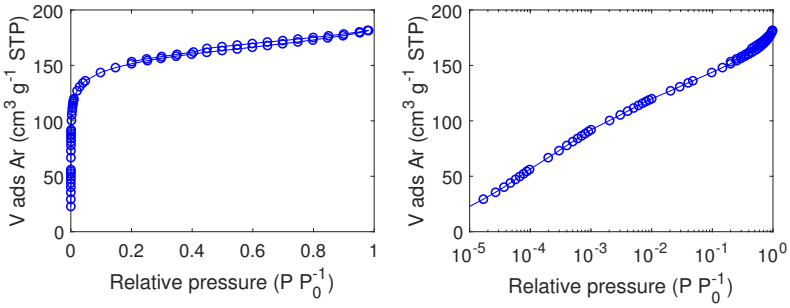

Figure C.35: Ar adsorption/desorption isotherm of carbon FY5 measured at 87 K.

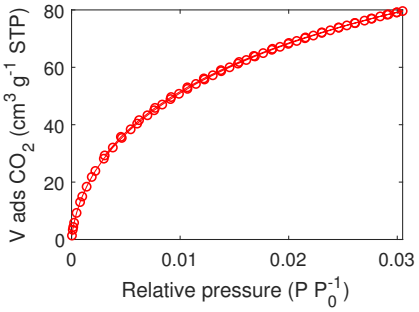

Figure C.36: CO_2 adsorption/desorption isotherm of carbon FY5 measured at 273 K.

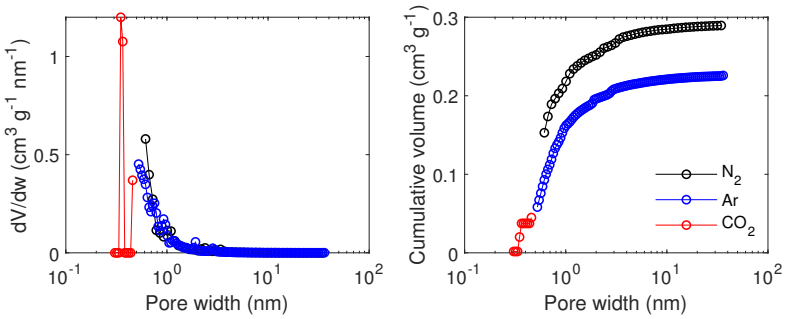

Figure C.37: Pore size distribution modelled by QSDFT for N_2 and Ar adsorption/desorption isotherms and NLDFT for CO_2 adsorption/desorption isotherm for carbon FY5.

Table C.27: Selected textural properties of carbon FY5; (a) total pore volume at P/P_0 = 0.985; (b) by NLDFT model; (c) by equilibrium QSDFT model; (d) by DR model; (e) based on MIP data; (1) N_2 adsorption isotherm at 77 K; (2) Ar adsorption isotherm at 87 K; (3) CO_2 adsorption isotherm at 273 K.

TPV^a (cm^3/g)	0.31[1] / 0.23[2]
Surface area^b (m^2/g)	835[1] / 617[2]
$V^b_{\text{ultramicro}}$ (cm^3/g)	0.16[3]
V^c_{micro} (cm^3/g)	0.25[1] / 0.20[2]
W^d_0 (cm^3/g)	0.27[1] / 0.19[2]
V^c_{meso} (cm^3/g)	0.04[1] / 0.03[2]
V^e_{macro} (cm^3/g)	0.18
Apparent density^e (g/cm^3)	0.98

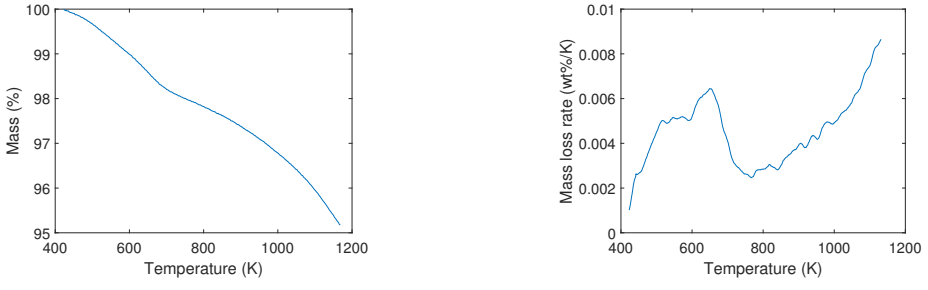

(a) TGA. (b) DTG.

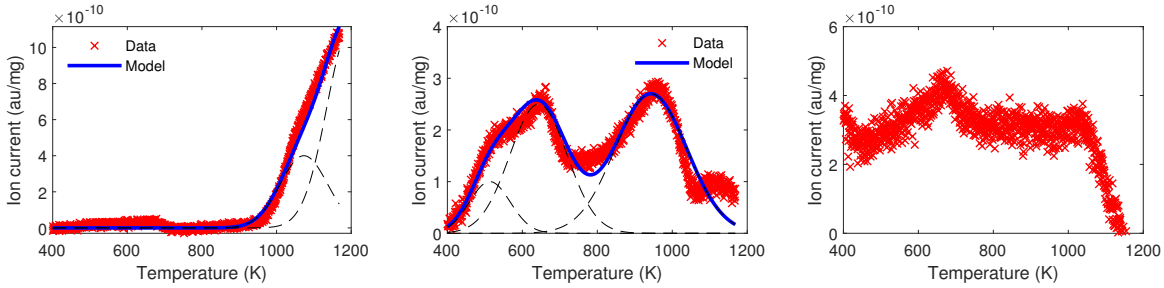

(c) CO profile. (d) CO_2 profile. (e) H_2O profile.

Figure C.38: TPDMS data of carbon FY5.

Table C.28: Peak attribution based on TPDMS analysis of carbon FY5.

Gas evolved	Peak temperature (K)	Peak width (K)	Peak area (a.u./mg)	Attribution
CO_2	513	125	$1.3 \cdot 10^{-8}$	Carboxylic acid
CO_2	643	180	$4.8 \cdot 10^{-8}$	Carboxylic acid
CO_2	943	225	$6.5 \cdot 10^{-8}$	Lactone
CO	1073	150	$6.4 \cdot 10^{-8}$	Phenol
CO	1198	150	$1.8 \cdot 10^{-7}$	Carbonyl/quinones

Table C.29: Elemental analysis and ash content (wt%) of carbon FY5.

C	H	O	N	S	Sum CHONS	Ash content
86.2	0.6	2.2	0.2	0.1	89.3	3.2

C.4.2 FY5-21

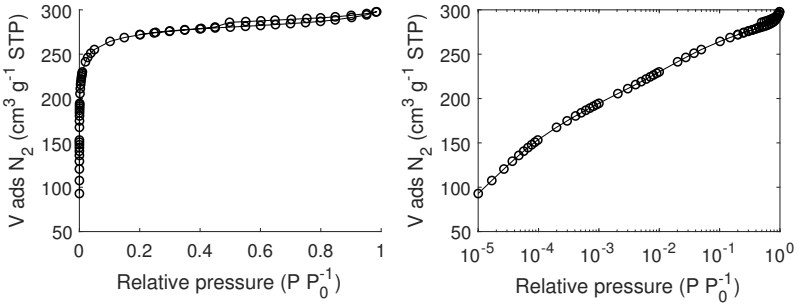

Figure C.39: N_2 adsorption/desorption isotherm of carbon FY5-21 measured at 77 K.

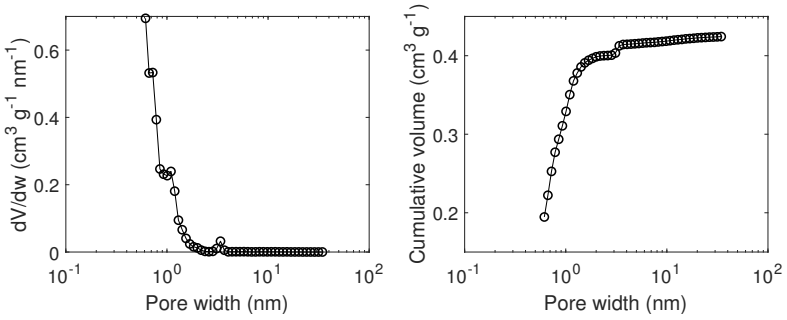

Figure C.40: Pore size distribution modelled by QSDFT based on N_2 adsorption/desorption isotherm for carbon FY5-21.

Table C.30: Selected textural properties of carbon FY5-21; (a) total pore volume at $P/P_0 = 0.985$; (b) by equilibrium QSDFT model; (c) by DR model; (d) based on MIP data.

TPV^a (cm^3/g)	0.46
Surface area^b (m^2/g)	1188
V^b_{micro} (cm^3/g)	0.40
W^c_0 (cm^3/g)	0.42
V^b_{meso} (cm^3/g)	0.03
V^d_{macro} (cm^3/g)	0.23
Apparent density^d (g/cm^3)	0.83

Table C.31: Peak attribution based on TPDMS analysis of carbon FY5-21.

Gas evolved	Peak temperature (K)	Peak width (K)	Peak area (a.u./mg)	Attribution
CO_2	513	125	$1.3 \cdot 10^{-8}$	Carboxylic acid
CO_2	643	180	$1.9 \cdot 10^{-8}$	Carboxylic acid
CO_2	998	225	$3.8 \cdot 10^{-8}$	Lactone
CO	1073	75	$1.6 \cdot 10^{-8}$	Phenol
CO	1198	150	$2.2 \cdot 10^{-7}$	Carbonyl/quinones

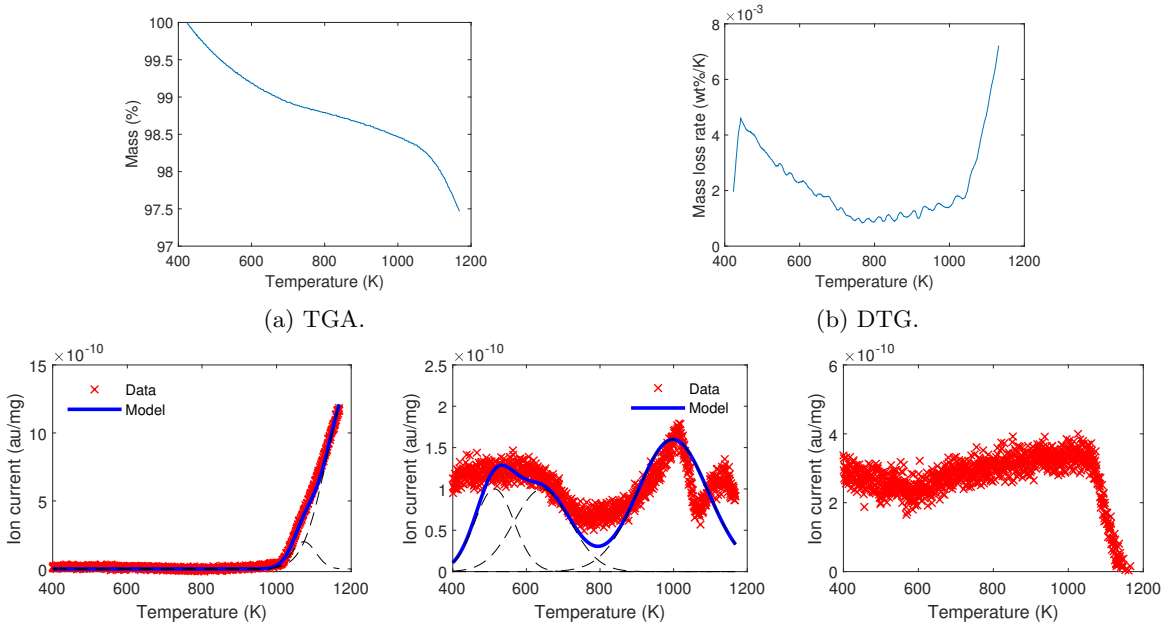

(a) TGA. (b) DTG.

(c) CO profile. (d) CO_2 profile. (e) H_2O profile.

Figure C.41: TPDMS data of carbon FY5-21.

Table C.32: Elemental analysis (wt%) of carbon FY5-21.

C	H	O	N	S	Sum CHONS
91.9	0.5	1.3	0.2	0.1	94.0

C.4.3 FY5-57

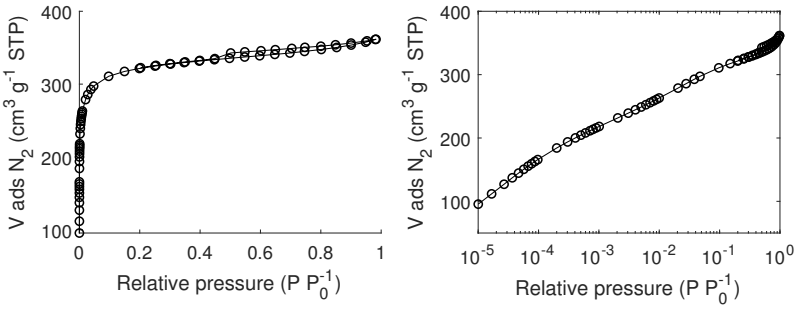

Figure C.42: N_2 adsorption/desorption isotherm of carbon FY5-57 measured at 77 K.

Table C.33: Selected textural properties of carbon FY5-57; (a) total pore volume at P/P_0 = 0.985; (b) by equilibrium QSDFT model; (c) by DR model; (d) based on MIP data.

TPV^a (cm^3/g)	0.82
Surface area^b (m^2/g)	1369
V^b_{micro} (cm^3/g)	0.67
W^c_0 (cm^3/g)	0.68
V^b_{meso} (cm^3/g)	0.08
V^d_{macro} (cm^3/g)	0.29
Apparent density^d (g/cm^3)	0.64

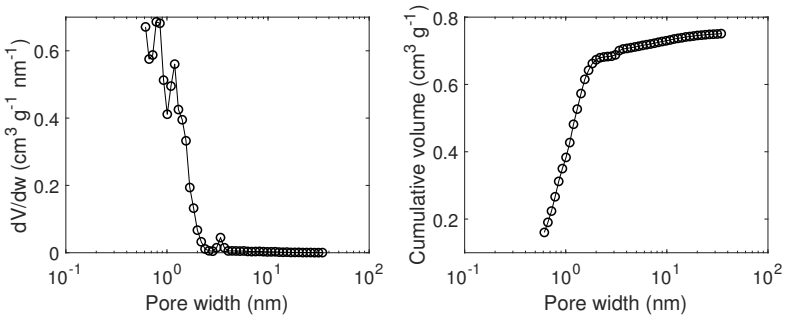

Figure C.43: Pore size distribution modelled by QSDFT based on N_2 adsorption/desorption isotherm for carbon FY5-57.

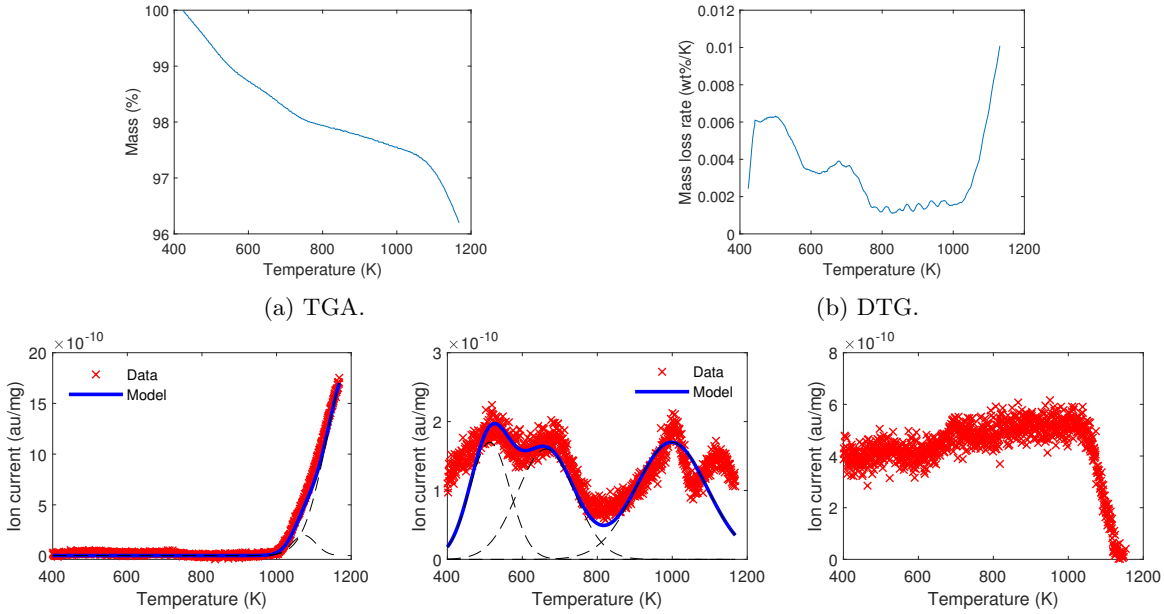

(a) TGA.

(b) DTG.

(c) CO profile.

(d) CO_2 profile.

(e) H_2O profile.

Figure C.44: TPDMS data of carbon FY5-57.

Table C.34: Peak attribution based on TPDMS analysis of carbon FY5-57.

Gas evolved	Peak temperature (K)	Peak width (K)	Peak area (a.u./mg)	Attribution
CO_2	513	125	$2.3 \cdot 10^{-8}$	Carboxylic acid
CO_2	663	180	$3.1 \cdot 10^{-8}$	Carboxylic acid
CO_2	998	225	$4.1 \cdot 10^{-8}$	Lactone
CO	1073	75	$1.6 \cdot 10^{-8}$	Phenol
CO	1198	150	$3.0 \cdot 10^{-7}$	Carbonyl/quinones

Table C.35: Elemental analysis and ash content (wt%) of carbon FY5-57.

C	H	O	N	S	Sum CHONS
89.5	0.5	1.8	0.4	0.3	92.5

Appendix D

Comparison of pore size analysis based on N_2 and Ar adsorption/desorption isotherms

This annex presents all the experimental data of the comparison between the pore size distribution and the cumulative pore volume modelled by QSDFT based on N_2 and Ar adsorption/desorption isotherms, in order to assess if specific interactions between the adsorbate and the oxidizing salt are significant and affect the pore size analysis. This comparison relies on the difference in quadrupole moment between the adsorbate. As N_2 presents a significant quadrupole moment, its specific interactions with polar sites on the surface should be stronger than in the case of Ar, which has no quadrupole moment. If no significant different is observed between the pore size analysis based on N_2 and Ar adsorption/desorption isotherm data, this would suggest that these specific interactions are not significant enough to affect the pore size analysis. The interpretation is however difficult, as kinetics effects, material inhomogeneity or experimental error interfere.

The experimental results presented in annex C show that the pore size analysis based on the N_2 and the Ar adsorption/desorption isotherm data are in very good agreement for all the commercial pristine carbons, except for the FY5. As this carbon is characterized by a very narrow microporosity which makes the measurement of its adsorption isotherm difficult because of a very slow diffusion kinetics, the observed difference is attributed to kinetic effects and not to specific interactions with the surface. This carbon will therefore not been considered within the scope of this evaluation.

A representative list of filled carbons is used to compare the results of the pore size analyses based on N_2 and Ar adsorption/desorption isotherm data. The differences in total pore volumes (TPV) and in micro- and mesoporous volumes of these carbons between the pore size analysis based on N_2 and Ar are shown in table D.1.

Data shows that the differences are very small with respect to the precision of the experimental measurement and the modelling. The microporous volume from the Ar pore size analysis appears to be slightly larger than that which results from the N_2 analysis, which could also be related to kinetic effects and differences in pore filling pressures between Ar and N_2.

In summary, the pore size analysis based on N_2 and Ar adsorption/desorption isotherm data are in very good agreement, indicating that potential specific interactions between N_2 and the polar sites resulting from the presence of salt in the porosity significantly do not affect the pore size analysis in a greater extent than the experimental and modelling errors.

Table D.1: Comparison of the pore size analysis based on N_2 and Ar adsorption/desorption isotherm data for selected carbons. The differences are shown (Ar - N_2).

Carbon	Solution concentration (wt%)	Total pore volume (g/cm^3)	Microporous volume (g/cm^3)	Mesoporous volume (g/cm^3)
C	40	0.00	0.01	0.00
C	60	0.00	0.01	0.00
C-R300	56	0.00	0.01	0.00
C-R600	56	0.01	0.01	0.01
F5001	40	0.11	0.06	0.06
F5001	60	-0.01	0.01	0.00
F5001-APS	56	-0.01	0.00	-0.01
F5001-HN	56	0.01	0.00	0.00
BPL	40	0.00	0.00	0.00
BPL	60	-0.01	0.00	0.01
BPL-37	56	0.00	0.02	-0.01

D.1 C and derivatives

The results of the pore size analysis of carbon C filled with $NaClO_4$ from an aqueous solution with a $NaClO_4$ concentration of 40 wt% are shown in figure D.1, D.2, D.3 and table D.2.

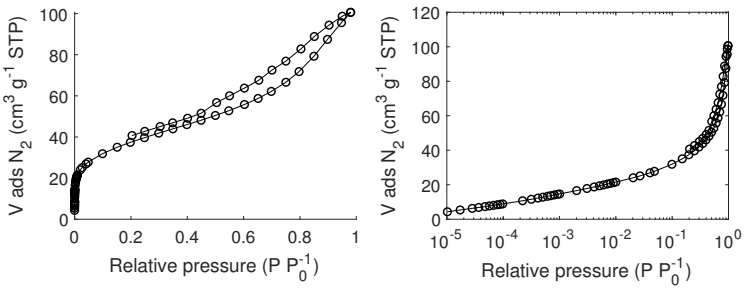

Figure D.1: N_2 adsorption/desorption isotherm of carbon C filled with $NaClO_4$ from a 40 wt% aqueous solution measured at 77 K.

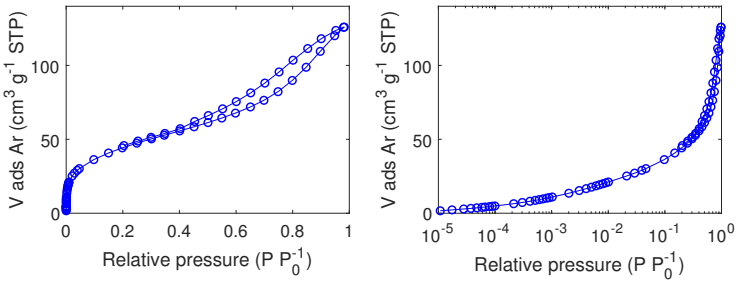

Figure D.2: Ar adsorption/desorption isotherm of carbon C filled with $NaClO_4$ from a 40 wt% aqueous solution measured at 87 K.

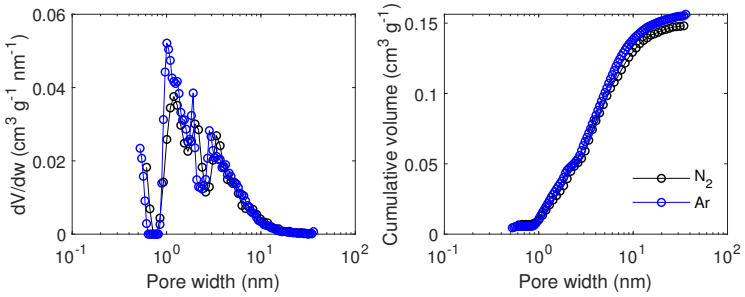

Figure D.3: Pore size distribution modelled by QSDFT based on N_2 at 77 K and Ar at 87 K adsorption/desorption isotherms for carbon C filled with $NaClO_4$ from a 40 wt% aqueous solution.

Table D.2: Comparison of the pore size analysis based on N_2 at 77 K and Ar at 88 K adsorption/desorption isotherms for carbon C filled with $NaClO_4$ from a 40 wt% aqueous solution; (a) total pore volume at $P/P_0 = 0.985$; (b) by equilibrium QSDFT model.

Adsorbate	N_2	Ar
TPV^a (cm^3/g)	0.16	0.16
V^b_{micro} (cm^3/g)	0.04	0.05
V^b_{meso} (cm^3/g)	0.11	0.11

The results of the pore size analysis of carbon C filled with $NaClO_4$ from an aqueous solution with a $NaClO_4$ concentration of 60 wt% are shown in figure D.4, D.5, D.6 and table D.3.

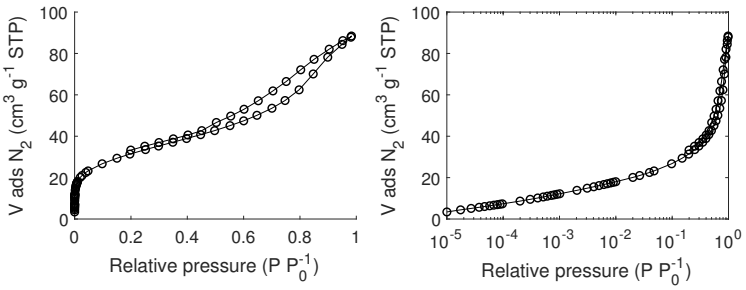

Figure D.4: N_2 adsorption/desorption isotherm of carbon C filled with $NaClO_4$ from a 60 wt% aqueous solution measured at 77 K.

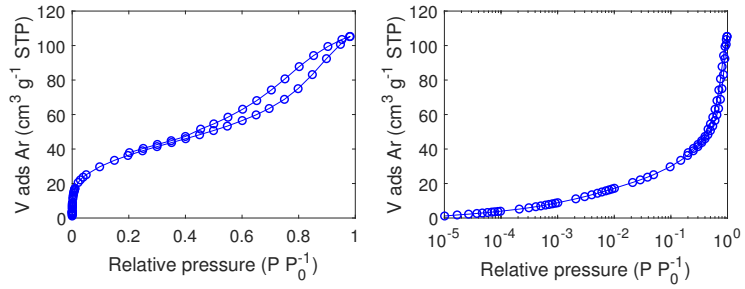

Figure D.5: Ar adsorption/desorption isotherm of carbon C filled with $NaClO_4$ from a 60 wt% aqueous solution measured at 87 K.

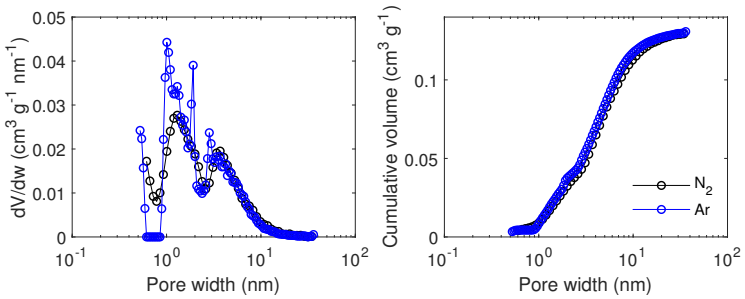

Figure D.6: Pore size distribution modelled by QSDFT based on N_2 at 77 K and Ar at 87 K adsorption/desorption isotherms for carbon C filled with $NaClO_4$ from a 60 wt% aqueous solution.

Table D.3: Comparison of the pore size analysis based on N_2 at 77 K and Ar at 88 K adsorption/desorption isotherms for carbon C filled with $NaClO_4$ from a 60 wt% aqueous solution; (a) total pore volume at $P/P_0 = 0.985$; (b) by equilibrium QSDFT model.

Adsorbate	N_2	Ar
TPV^a (cm^3/g)	0.14	0.13
V^b_{micro} (cm^3/g)	0.03	0.04
V^b_{meso} (cm^3/g)	0.10	0.09

The results of the pore size analysis of carbon C-R300 filled with $NaClO_4$ from an aqueous solution with a $NaClO_4$ concentration of 56 wt% are shown in figure D.7, D.8, D.9 and table D.4.

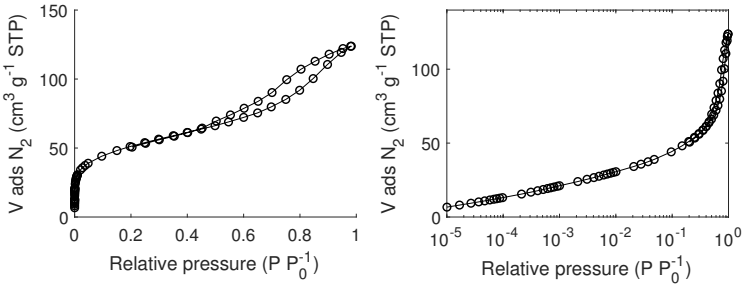

Figure D.7: N_2 adsorption/desorption isotherm of carbon C-R300 filled with $NaClO_4$ from a 56 wt% aqueous solution measured at 77 K.

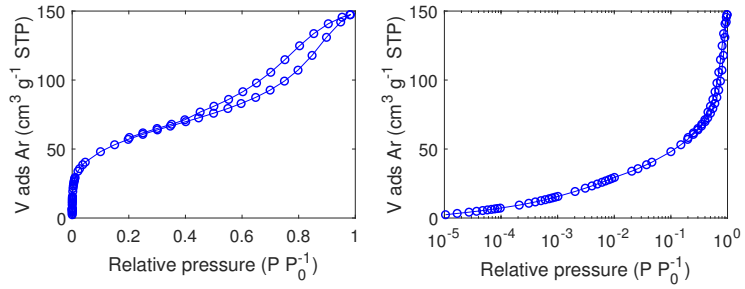

Figure D.8: Ar adsorption/desorption isotherm of carbon C-R300 filled with $NaClO_4$ from a 56 wt% aqueous solution measured at 87 K.

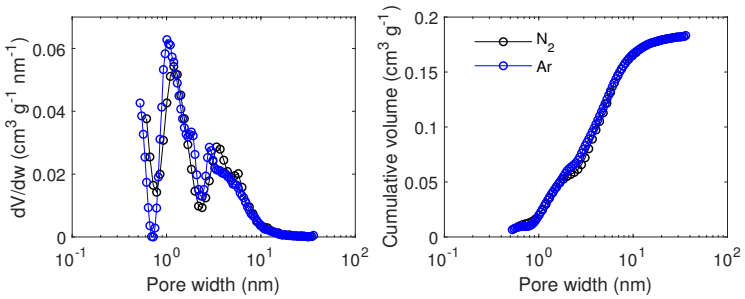

Figure D.9: Pore size distribution modelled by QSDFT based on N_2 at 77 K and Ar at 87 K adsorption/desorption isotherms for carbon C-R300 filled with $NaClO_4$ from a 56 wt% aqueous solution.

Table D.4: Comparison of the pore size analysis based on N_2 at 77 K and Ar at 88 K adsorption/desorption isotherms for carbon C-R300 filled with $NaClO_4$ from a 56 wt% aqueous solution; (a) total pore volume at $P/P_0 = 0.985$; (b) by equilibrium QSDFT model.

Adsorbate	N_2	Ar
TPV^a (cm^3/g)	0.19	0.19
V^b_{micro} (cm^3/g)	0.05	0.06
V^b_{meso} (cm^3/g)	0.13	0.12

The results of the pore size analysis of carbon C-R600 filled with $NaClO_4$ from an aqueous solution with a $NaClO_4$ concentration of 56 wt% are shown in figure D.10, D.11, D.12 and table D.5.

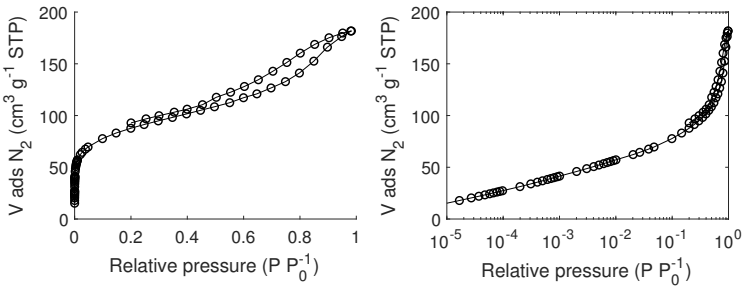

Figure D.10: N_2 adsorption/desorption isotherm of carbon C-600 filled with $NaClO_4$ from a 56 wt% aqueous solution measured at 77 K.

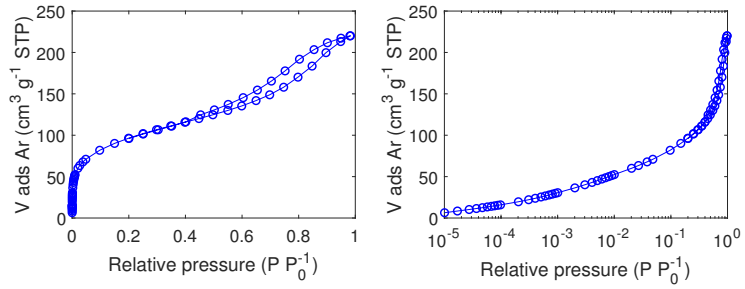

Figure D.11: Ar adsorption/desorption isotherm of carbon C-R600 filled with $NaClO_4$ from a 56 wt% aqueous solution measured at 87 K.

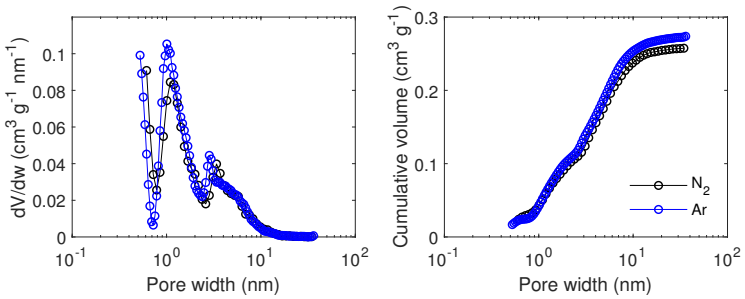

Figure D.12: Pore size distribution modelled by QSDFT based on N_2 at 77 K and Ar at 87 K adsorption/desorption isotherms for carbon C-R600 filled with $NaClO_4$ from a 56 wt% aqueous solution.

Table D.5: Comparison of the pore size analysis based on N_2 at 77 K and Ar at 88 K adsorption/desorption isotherms for carbon C-R600 filled with $NaClO_4$ from a 56 wt% aqueous solution; (a) total pore volume at $P/P_0 = 0.985$; (b) by equilibrium QSDFT model.

Adsorbate	N_2	Ar
TPV^a (cm^3/g)	0.27	0.28
V^b_{micro} (cm^3/g)	0.10	0.10
V^b_{meso} (cm^3/g)	0.16	0.17

D.2 F5001 and derivatives

The results of the pore size analysis of carbon F5001 filled with $NaClO_4$ from an aqueous solution with a $NaClO_4$ concentration of 40 wt% are shown in figure D.13, D.14, D.15 and table D.6.

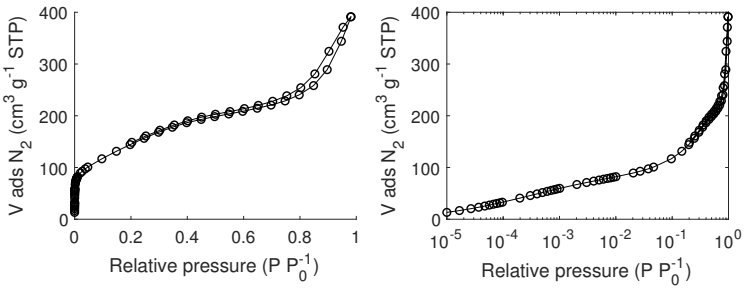

Figure D.13: N_2 adsorption/desorption isotherm of carbon F5001 filled with $NaClO_4$ from a 40 wt% aqueous solution measured at 77 K.

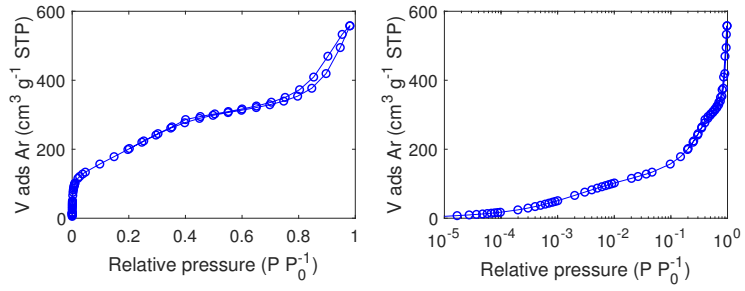

Figure D.14: Ar adsorption/desorption isotherm of carbon F5001 filled with $NaClO_4$ from a 40 wt% aqueous solution measured at 87 K.

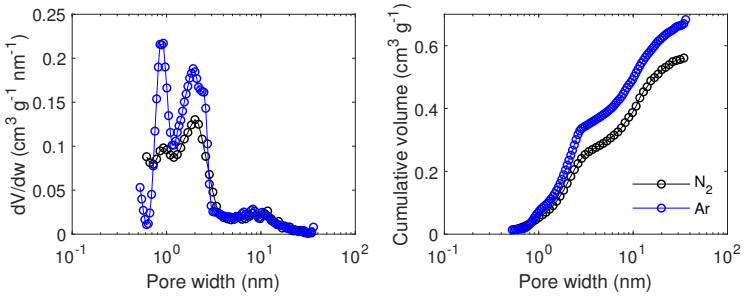

Figure D.15: Pore size distribution modelled by QSDFT based on N_2 at 77 K and Ar at 87 K adsorption/desorption isotherms for carbon F5001 filled with $NaClO_4$ from a 40 wt% aqueous solution.

Table D.6: Comparison of the pore size analysis based on N_2 at 77 K and Ar at 88 K adsorption/desorption isotherms for carbon F5001 filled with $NaClO_4$ from a 40 wt% aqueous solution; (a) total pore volume at $P/P_0 = 0.985$; (b) by equilibrium QSDFT model.

Adsorbate	N_2	Ar
TPV^a (cm^3/g)	0.61	0.71
V^b_{micro} (cm^3/g)	0.16	0.22
V^b_{meso} (cm^3/g)	0.40	0.46

The results of the pore size analysis of carbon F5001 filled with $NaClO_4$ from an aqueous solution with a $NaClO_4$ concentration of 60 wt% are shown in figure D.16, D.17, D.18 and table D.7.

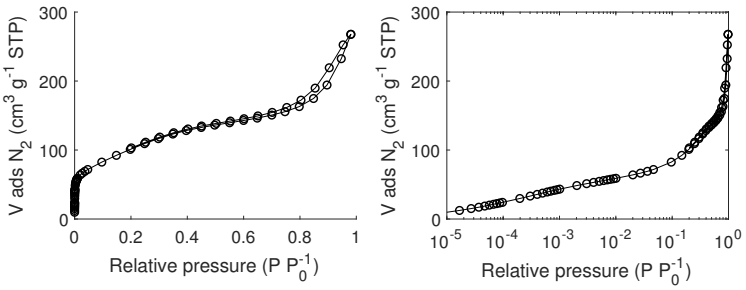

Figure D.16: N_2 adsorption/desorption isotherm of carbon F5001 filled with $NaClO_4$ from a 60 wt% aqueous solution measured at 77 K.

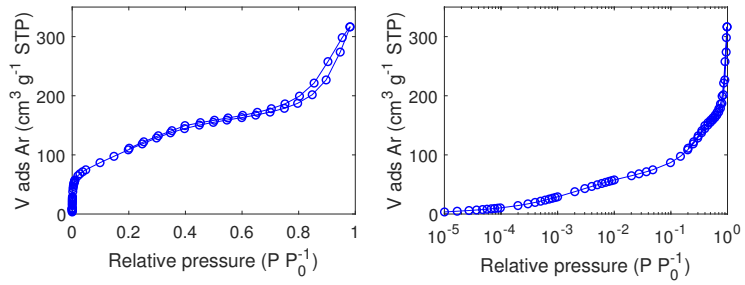

Figure D.17: Ar adsorption/desorption isotherm of carbon F5001 filled with $NaClO_4$ from a 60 wt% aqueous solution measured at 87 K.

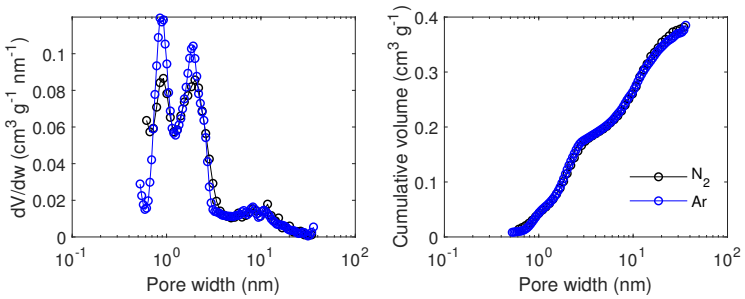

Figure D.18: Pore size distribution modelled by QSDFT based on N_2 at 77 K and Ar at 87 K adsorption/desorption isotherms for carbon F5001 filled with $NaClO_4$ from a 60 wt% aqueous solution.

Table D.7: Comparison of the pore size analysis based on N_2 at 77 K and Ar at 88 K adsorption/desorption isotherms for carbon F5001 filled with $NaClO_4$ from a 60 wt% aqueous solution; (a) total pore volume at $P/P_0 = 0.985$; (b) by equilibrium QSDFT model.

Adsorbate	N_2	Ar
TPV^a (cm^3/g)	0.41	0.40
V^b_{micro} (cm^3/g)	0.11	0.12
V^b_{meso} (cm^3/g)	0.27	0.26

The results of the pore size analysis of carbon F5001-APS filled with $NaClO_4$ from an aqueous solution with a $NaClO_4$ concentration of 56 wt% are shown in figure D.19, D.20, D.21 and table D.8.

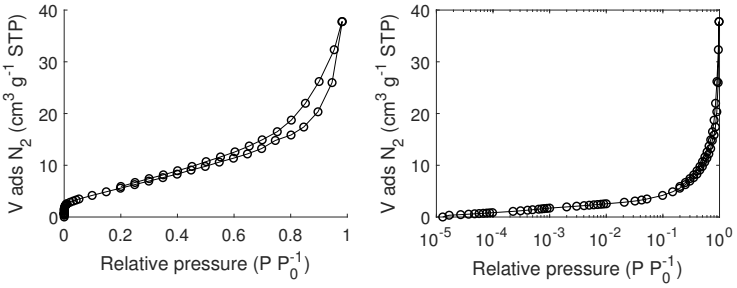

Figure D.19: N_2 adsorption/desorption isotherm of carbon F5001-APS filled with $NaClO_4$ from a 56 wt% aqueous solution measured at 77 K.

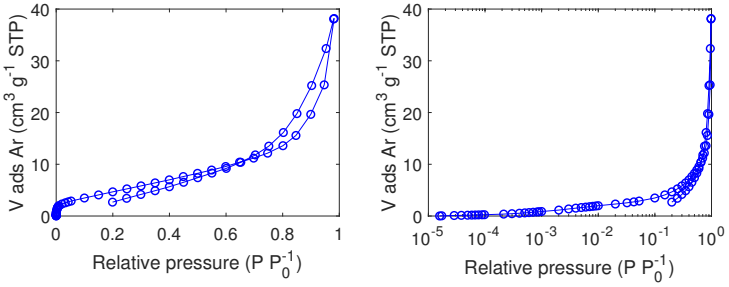

Figure D.20: Ar adsorption/desorption isotherm of carbon F5001-APS filled with $NaClO_4$ from a 56 wt% aqueous solution measured at 87 K.

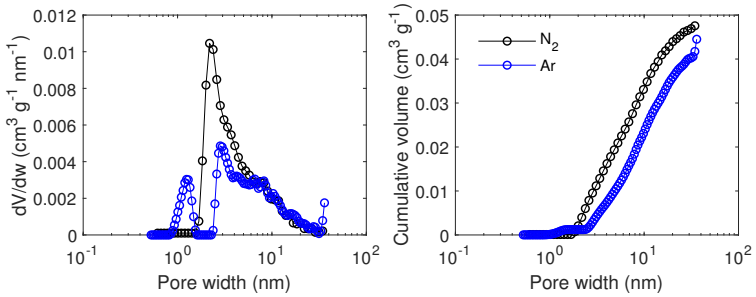

Figure D.21: Pore size distribution modelled by QSDFT based on N_2 at 77 K and Ar at 87 K adsorption/desorption isotherms for carbon F5001-APS filled with $NaClO_4$ from a 56 wt% aqueous solution.

Table D.8: Comparison of the pore size analysis based on N_2 at 77 K and Ar at 88 K adsorption/desorption isotherms for carbon F5001-APS filled with $NaClO_4$ from a 56 wt% aqueous solution; (a) total pore volume at $P/P_0 = 0.985$; (b) by equilibrium QSDFT model.

Adsorbate	N_2	Ar
TPV^a (cm^3/g)	0.06	0.05
V^b_{micro} (cm^3/g)	0.00	0.00
V^b_{meso} (cm^3/g)	0.05	0.04

The results of the pore size analysis of carbon F5001-HN filled with $NaClO_4$ from an aqueous solution with a $NaClO_4$ concentration of 56 wt% are shown in figure D.22, D.23, D.24 and table D.9.

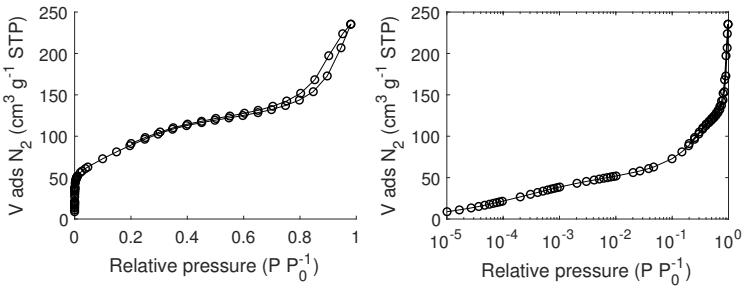

Figure D.22: N_2 adsorption/desorption isotherm of carbon F5001-HN filled with $NaClO_4$ from a 56 wt% aqueous solution measured at 77 K.

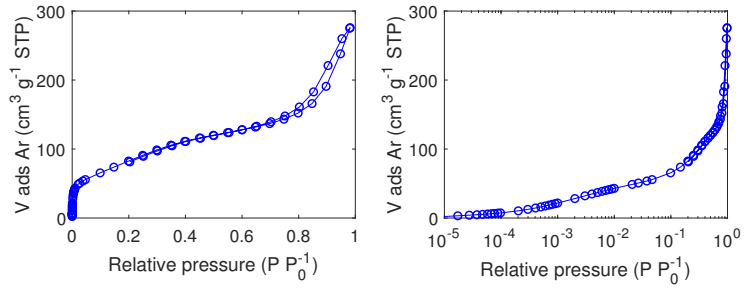

Figure D.23: Ar adsorption/desorption isotherm of carbon F5001-HN filled with $NaClO_4$ from a 56 wt% aqueous solution measured at 87 K.

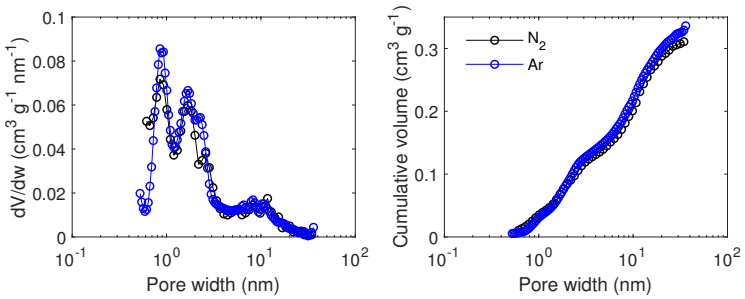

Figure D.24: Pore size distribution modelled by QSDFT based on N_2 at 77 K and Ar at 87 K adsorption/desorption isotherms for carbon F5001-HN filled with $NaClO_4$ from a 56 wt% aqueous solution.

Table D.9: Comparison of the pore size analysis based on N_2 at 77 K and Ar at 88 K adsorption/desorption isotherms for carbon F5001-HN filled with $NaClO_4$ from a 56 wt% aqueous solution; (a) total pore volume at $P/P_0 = 0.985$; (b) by equilibrium QSDFT model.

Adsorbate	N_2	Ar
TPV^a (cm^3/g)	0.34	0.35
V^b_{micro} (cm^3/g)	0.08	0.08
V^b_{meso} (cm^3/g)	0.26	0.25

D.3 BPL and derivatives

The results of the pore size analysis of carbon BPL filled with $NaClO_4$ from an aqueous solution with a $NaClO_4$ concentration of 40 wt% are shown in figure D.25, D.26, D.27 and table D.10.

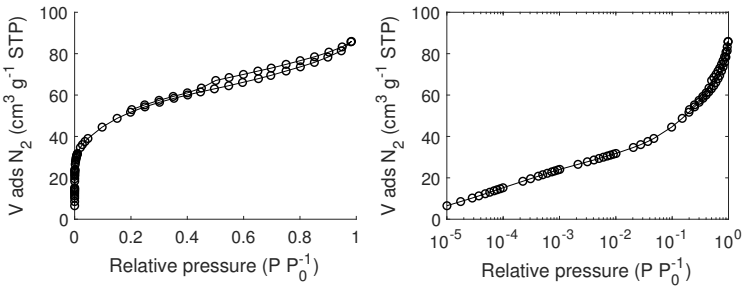

Figure D.25: N_2 adsorption/desorption isotherm of carbon BPL filled with $NaClO_4$ from a 40 wt% aqueous solution measured at 77 K.

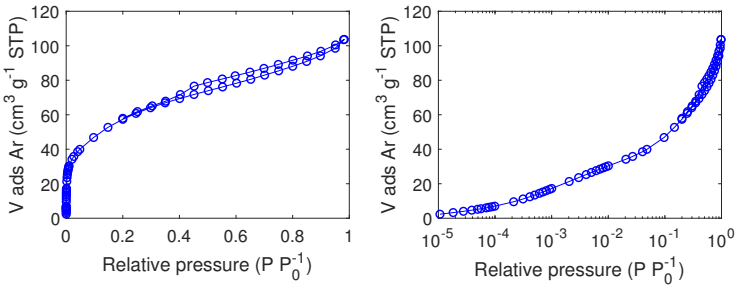

Figure D.26: Ar adsorption/desorption isotherm of carbon BPL filled with $NaClO_4$ from a 40 wt% aqueous solution measured at 87 K.

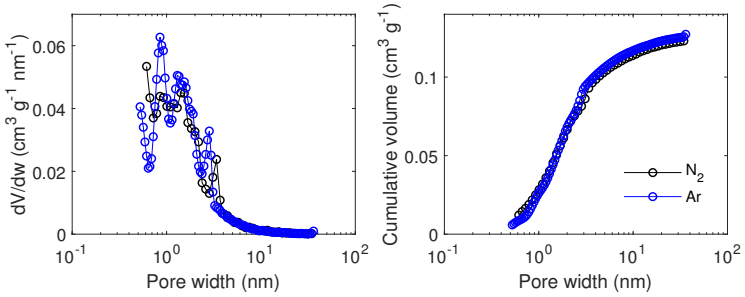

Figure D.27: Pore size distribution modelled by QSDFT based on N_2 at 77 K and Ar at 87 K adsorption/desorption isotherms for carbon BPL filled with $NaClO_4$ from a 40 wt% aqueous solution.

Table D.10: Comparison of the pore size analysis based on N_2 at 77 K and Ar at 88 K adsorption/desorption isotherms for carbon BPL filled with $NaClO_4$ from a 40 wt% aqueous solution; (a) total pore volume at $P/P_0 = 0.985$; (b) by equilibrium QSDFT model.

Adsorbate	N_2	Ar
TPV^a (cm^3/g)	0.13	0.13
V^b_{micro} (cm^3/g)	0.07	0.07
V^b_{meso} (cm^3/g)	0.06	0.06

The results of the pore size analysis of carbon BPL filled with $NaClO_4$ from an aqueous solution with a $NaClO_4$ concentration of 60 wt% are shown in figure D.28, D.29, D.30 and table D.11.

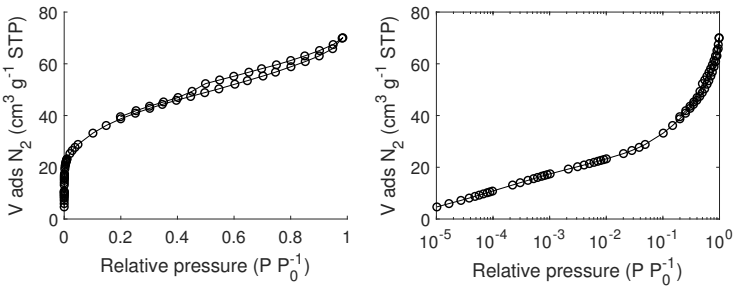

Figure D.28: N_2 adsorption/desorption isotherm of carbon BPL filled with $NaClO_4$ from a 60 wt% aqueous solution measured at 77 K.

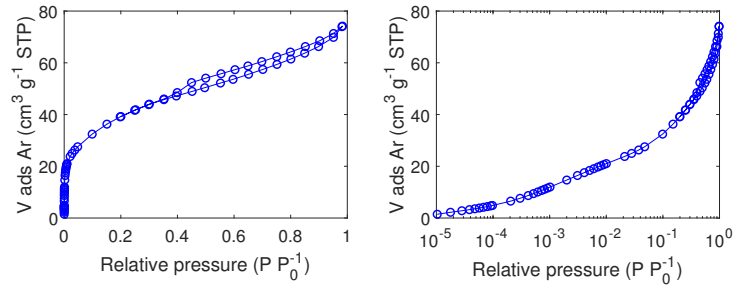

Figure D.29: Ar adsorption/desorption isotherm of carbon BPL filled with $NaClO_4$ from a 60 wt% aqueous solution measured at 87 K.

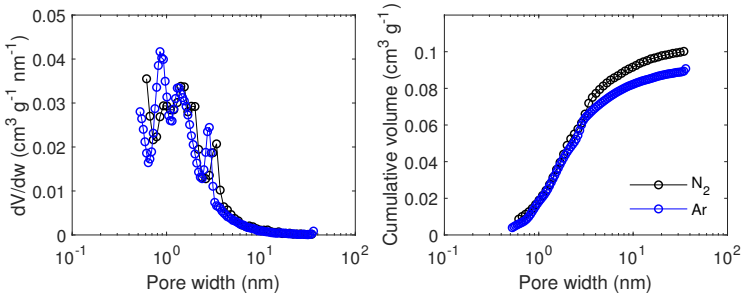

Figure D.30: Pore size distribution modelled by QSDFT based on N_2 at 77 K and Ar at 87 K adsorption/desorption isotherms for carbon BPL filled with $NaClO_4$ from a 60 wt% aqueous solution.

Table D.11: Comparison of the pore size analysis based on N_2 at 77 K and Ar at 88 K adsorption/desorption isotherms for carbon BPL filled with $NaClO_4$ from a 60 wt% aqueous solution; (a) total pore volume at $P/P_0 = 0.985$; (b) by equilibrium QSDFT model.

Adsorbate	N_2	Ar
TPV^a (cm^3/g)	0.11	0.94
V^b_{micro} (cm^3/g)	0.05	0.05
V^b_{meso} (cm^3/g)	0.05	0.05

The results of the pore size analysis of carbon BPL-37 filled with $NaClO_4$ from an aqueous solution with a $NaClO_4$ concentration of 56 wt% are shown in figure D.31, D.32, D.33 and table D.12.

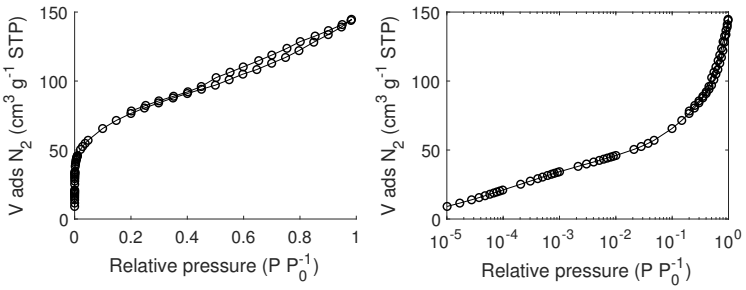

Figure D.31: N_2 adsorption/desorption isotherm of carbon BPL-37 filled with $NaClO_4$ from a 56 wt% aqueous solution measured at 77 K.

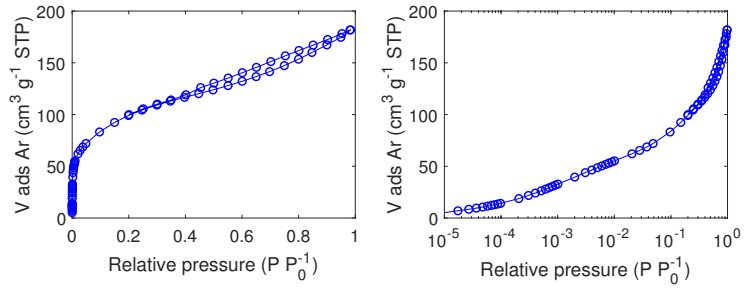

Figure D.32: Ar adsorption/desorption isotherm of carbon BPL-37 filled with $NaClO_4$ from a 56 wt% aqueous solution measured at 87 K.

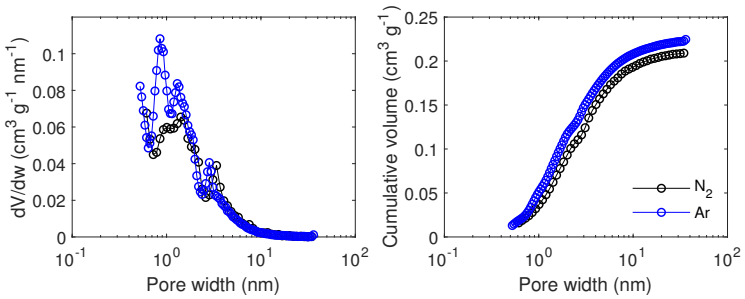

Figure D.33: Pore size distribution modelled by QSDFT based on N_2 at 77 K and Ar at 87 K adsorption/desorption isotherms for carbon BPL-37 filled with $NaClO_4$ from a 56 wt% aqueous solution.

Table D.12: Comparison of the pore size analysis based on N_2 at 77 K and Ar at 88 K adsorption/desorption isotherms for carbon BPL-37 filled with $NaClO_4$ from a 56 wt% aqueous solution; (a) total pore volume at $P/P_0 = 0.985$; (b) by equilibrium QSDFT model.

Adsorbate	N_2	Ar
TPV^a (cm^3/g)	0.22	0.22
V^b_{micro} (cm^3/g)	0.09	0.12
V^b_{meso} (cm^3/g)	0.12	0.11

Appendix E

Characterization of the textural properties of the oxidizing agents

This annex presents the characterization of the textural properties of the oxidizing agents used in this work, in order to demonstrate that they can be considered as non-porous materials within the scope of the calculation of theoretical adsorption isotherms.

Figures E.1, E.2 and E.3 show the N_2 adsorption isotherm of sodium perchlorate, potassium nitrate and ammonium perchlorate. The three isotherms are of type II and corresponds to nonporous material. The surface area of sodium perchlorate, potassium nitrate and ammonium perchlorate is 1.1, 1.1 and 1.4 m^2/g, respectively, and reflect the mono and multilayer adsorption of N_2 on the external surface of the salt particles.

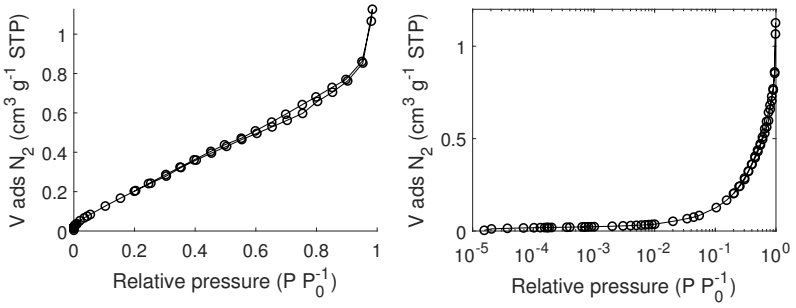

Figure E.1: N_2 adsorption/desorption isotherm of sodium perchlorate measured at 77 K.

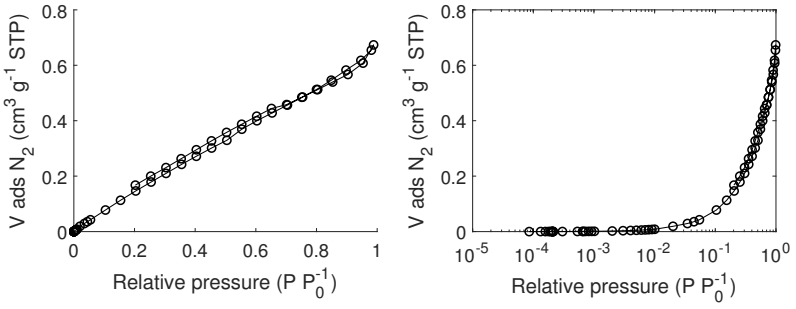

Figure E.2: N_2 adsorption/desorption isotherm of potassium nitrate measured at 77 K.

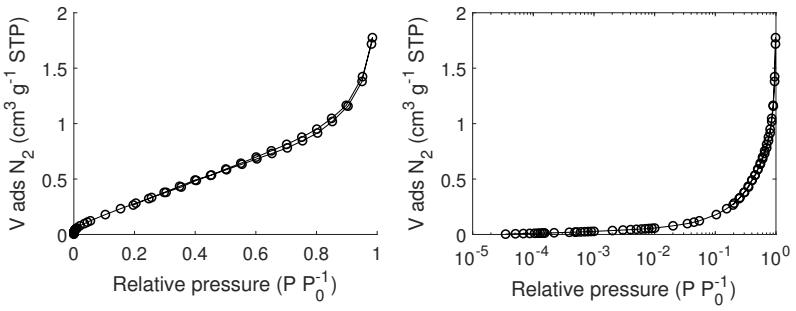

Figure E.3: N_2 adsorption/desorption isotherm of ammonium perchlorate measured at 77 K.

Appendix F

Properties of the filled carbons

In this annex, the experimental results and the textural properties of the filled carbons discussed in section 3.5 are presented. The methods are described in chapter 2. All the syntheses were carried out at least by duplicate. N_2 adsorption/desorption isotherms and mercury intrusion (MIP) were measured for each carbon. For the carbon FY5 for which the measurement of the N_2 adsorption/desorption isotherms was very long and practically difficult, only the isotherm of one repetition was measured. For the vast majority of the cases, the reproducibility is very good and corresponds to the expected experimental error of the method. Given the destructive character of the MIP analysis, a very few experimental results are not available in duplicate.

F.1 Carbon C and derivatives

F.1.1 Influence of concentration

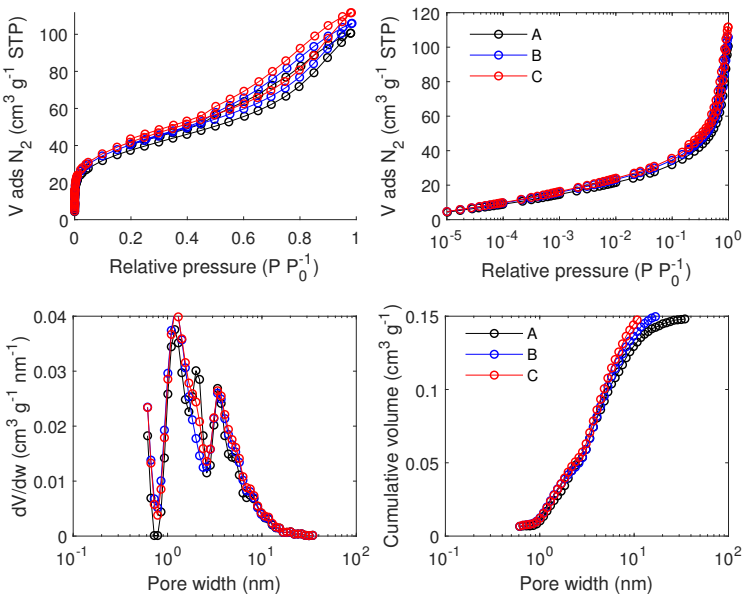

Figure F.1: N_2 adsorption/desorption isotherm data measured at 77 K and pore size analysis by equilibrium QSDFT for carbon C filled with $NaClO_4$ from a 40 wt% aqueous solution. A, B and C are repetitions (from the synthesis).

Table F.1: Selected textural properties based on N_2 isotherm at 77 K and MIP data for carbon C filled with $NaClO_4$ from a 40 wt% aqueous solution; (a) total pore volume at $P/P_0 = 0.985$; (b) by equilibrium QSDFT model; (c) based on MIP data. A, B and C are repetitions (from the synthesis).

Experiment	A	B	C
Yield (g/g)	1.21	1.21	1.23
TPV^a (cm^3/g)	0.16	0.16	0.17
V^b_{micro} (cm^3/g)	0.04	0.04	0.04
V^b_{meso} (cm^3/g)	0.11	0.11	0.12
V^c_{macro} (cm^3/g)	0.28	0.28	0.27
Apparent density (g/cm^3)	1.04	1.01	1.07

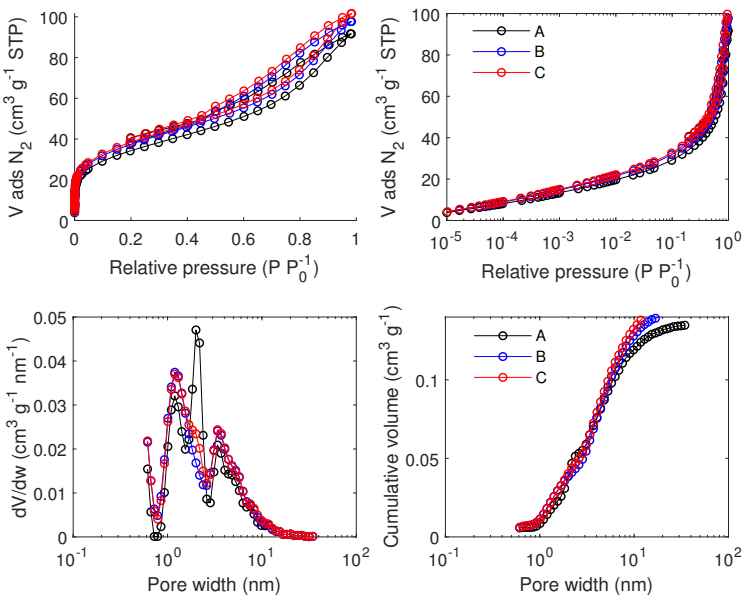

Figure F.2: N_2 adsorption/desorption isotherm data measured at 77 K and pore size analysis by equilibrium QSDFT for carbon C filled with $NaClO_4$ from a 50 wt% aqueous solution. A, B and C are repetitions (from the synthesis).

Table F.2: Selected textural properties based on N_2 isotherm at 77 K and MIP data for carbon C filled with $NaClO_4$ from a 50 wt% aqueous solution; (a) total pore volume at $P/P_0 = 0.985$; (b) by equilibrium QSDFT model; (c) based on MIP data. A, B and C are repetitions (from the synthesis).

Experiment	A	B	C
Yield (g/g)	1.53	1.52	1.49
TPV^a (cm^3/g)	0.14	0.15	0.16
V^b_{micro} (cm^3/g)	0.04	0.04	0.04
V^b_{meso} (cm^3/g)	0.10	0.10	0.11
V^c_{macro} (cm^3/g)	0.25	0.26	0.18
Apparent density (g/cm^3)	1.12	1.10	1.12

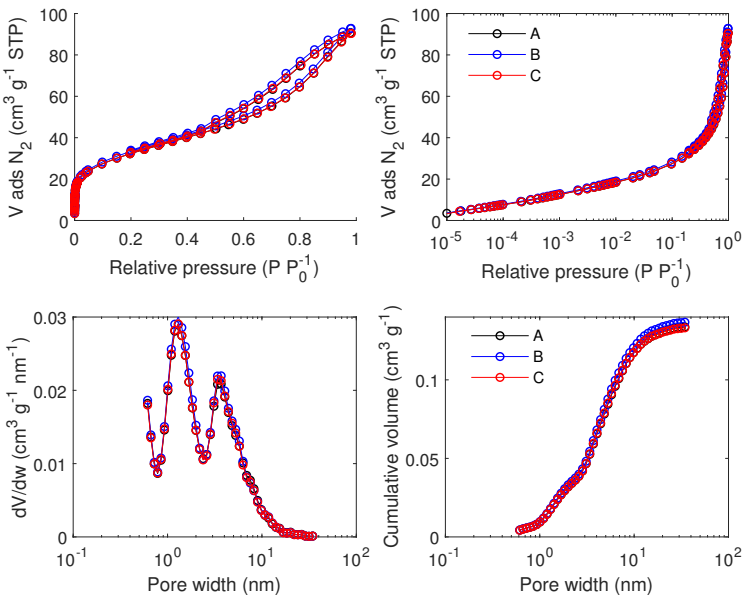

Figure F.3: N_2 adsorption/desorption isotherm data measured at 77 K and pore size analysis by equilibrium QSDFT for carbon C filled with $NaClO_4$ from a 56 wt% aqueous solution. A, B and C are repetitions (from the synthesis).

Table F.3: Selected textural properties based on N_2 isotherm at 77 K and MIP data for carbon C filled with $NaClO_4$ from a 56 wt% aqueous solution; (a) total pore volume at $P/P_0 = 0.985$; (b) by equilibrium QSDFT model; (c) based on MIP data. A, B and C are repetitions (from the synthesis).

Experiment	A	B	C
Yield (g/g)	1.79	1.81	1.76
TPV^a (cm^3/g)	0.14	0.14	0.14
V^b_{micro} (cm^3/g)	0.03	0.03	0.03
V^b_{meso} (cm^3/g)	0.10	0.10	0.10
V^c_{macro} (cm^3/g)	0.20	0.18	0.17
Apparent density (g/cm^3)	1.18	1.20	1.21

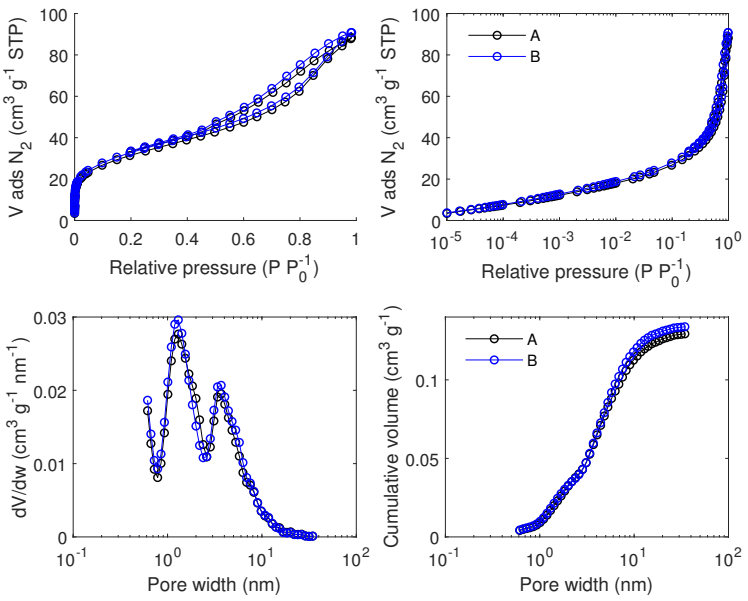

Figure F.4: N_2 adsorption/desorption isotherm data measured at 77 K and pore size analysis by equilibrium QSDFT for carbon C filled with $NaClO_4$ from a 60 wt% aqueous solution. A and B are repetitions (from the synthesis).

Table F.4: Selected textural properties based on N_2 isotherm at 77 K and MIP data for carbon C filled with $NaClO_4$ from a 60 wt% aqueous solution; (a) total pore volume at $P/P_0 = 0.985$; (b) by equilibrium QSDFT model; (c) based on MIP data. A and B are repetitions (from the synthesis).

Experiment	A	B	C
Yield (g/g)	2.03	2.08	1.99
TPV^a (cm^3/g)	0.14	0.14	-
V^b_{micro} (cm^3/g)	0.03	0.03	-
V^b_{meso} (cm^3/g)	0.10	0.10	-
V^c_{macro} (cm^3/g)	0.19	0.18	0.21
Apparent density (g/cm^3)	1.22	1.21	1.21

F.1.2 Thermal reduction

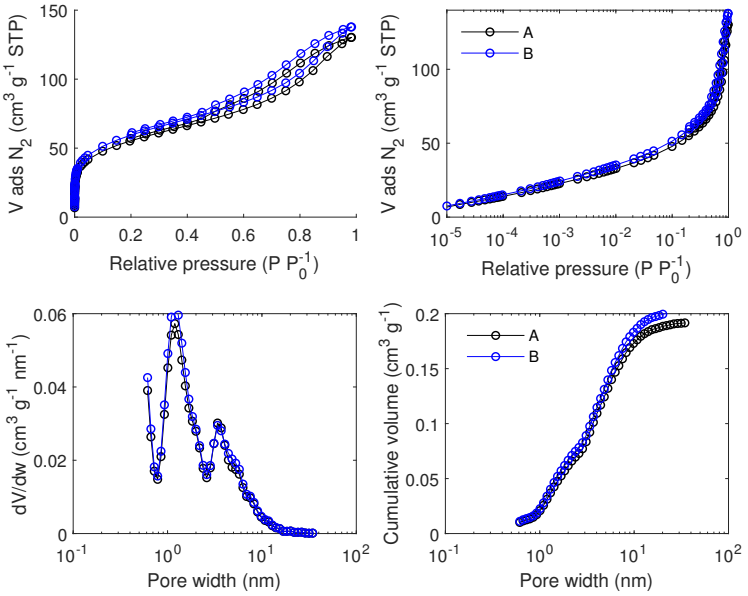

Figure F.5: N_2 adsorption/desorption isotherm data measured at 77 K and pore size analysis by equilibrium QSDFT for carbon C-R300 filled with $NaClO_4$ from a 56 wt% aqueous solution. A and B are repetitions (from the synthesis).

Table F.5: Selected textural properties based on N_2 isotherm at 77 K and MIP data for carbon C-R300 filled with $NaClO_4$ from a 56 wt% aqueous solution; (a) total pore volume at P/P_0 = 0.985; (b) by equilibrium QSDFT model; (c) based on MIP data. A and B are repetitions (from the synthesis).

Experiment	A	B
Yield (g/g)	2.16	2.08
TPV^a (cm^3/g)	0.20	0.21
V^b_{micro} (cm^3/g)	0.06	0.07
V^b_{meso} (cm^3/g)	0.13	0.14
V^c_{macro} (cm^3/g)	-	0.24
Apparent density (g/cm^3)	1.27	1.28

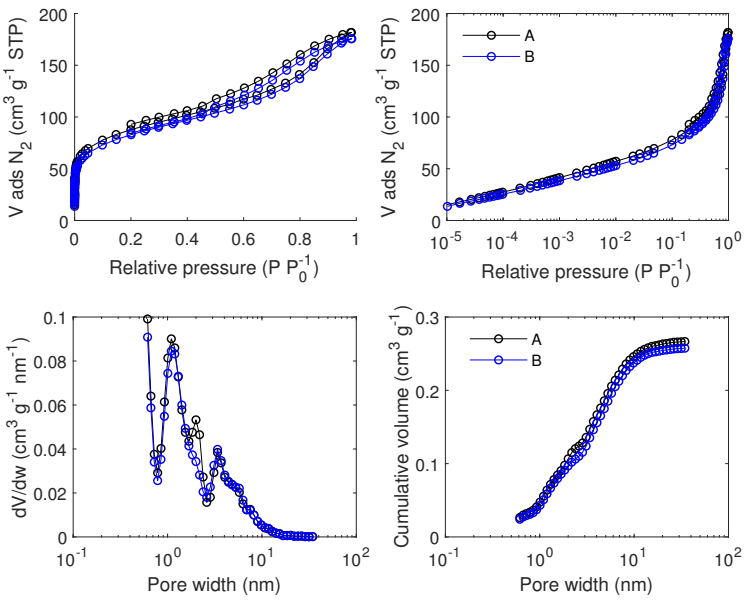

Figure F.6: N_2 adsorption/desorption isotherm data measured at 77 K and pore size analysis by equilibrium QSDFT for carbon C-R600 filled with $NaClO_4$ from a 56 wt% aqueous solution. A and B are repetitions (from the synthesis).

Table F.6: Selected textural properties based on N_2 isotherm at 77 K and MIP data for carbon C-R600 filled with $NaClO_4$ from a 56 wt% aqueous solution; (a) total pore volume at P/P_0 = 0.985; (b) by equilibrium QSDFT model; (c) based on MIP data. A and B are repetitions (from the synthesis).

Experiment	A	B
Yield (g/g)	1.50	1.51
TPV^a (cm^3/g)	0.28	0.27
V^b_{micro} (cm^3/g)	0.11	0.10
V^b_{meso} (cm^3/g)	0.16	0.16
V^c_{macro} (cm^3/g)	0.22	0.20
Apparent density (g/cm^3)	0.99	1.03

F.2 Carbon F5001 and derivatives

F.2.1 Influence of concentration

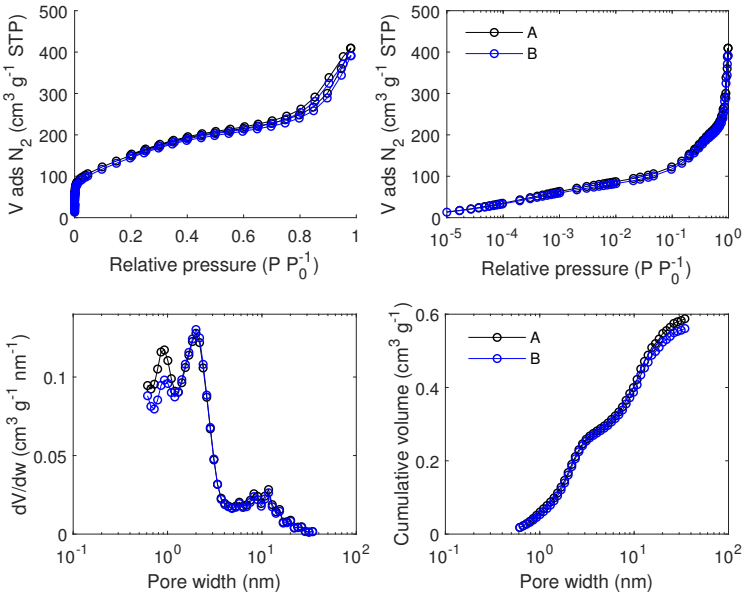

Figure F.7: N_2 adsorption/desorption isotherm data measured at 77 K and pore size analysis by equilibrium QSDFT for carbon F5001 filled with $NaClO_4$ from a 40 wt% aqueous solution. A and B are repetitions (from the synthesis).

Table F.7: Selected textural properties based on N_2 isotherm at 77 K and MIP data for carbon F5001 filled with $NaClO_4$ from a 40 wt% aqueous solution; (a) total pore volume at $P/P_0 = 0.985$; (b) by equilibrium QSDFT model; (c) based on MIP data. A and B are repetitions (from the synthesis).

Experiment	A	B
Yield (g/g)	1.38	1.38
TPV^a (cm^3/g)	0.63	0.61
V^b_{micro} (cm^3/g)	0.17	0.16
V^b_{meso} (cm^3/g)	0.42	0.40
V^c_{macro} (cm^3/g)	0.17	0.19
Apparent density (g/cm^3)	0.88	0.89

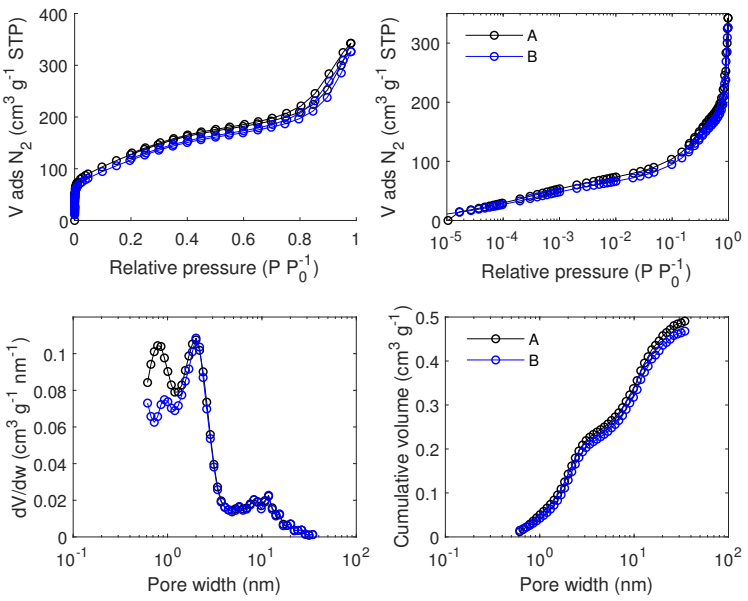

Figure F.8: N_2 adsorption/desorption isotherm data measured at 77 K and pore size analysis by equilibrium QSDFT for carbon F5001 filled with $NaClO_4$ from a 50 wt% aqueous solution. A and B are repetitions (from the synthesis).

Table F.8: Selected textural properties based on N_2 isotherm at 77 K and MIP data for carbon F5001 filled with $NaClO_4$ from a 50 wt% aqueous solution; (a) total pore volume at $P/P_0 = 0.985$; (b) by equilibrium QSDFT model; (c) based on MIP data. A and B are repetitions (from the synthesis).

Experiment	A	B
Yield (g/g)	1.77	1.78
TPV^a (cm^3/g)	0.53	0.51
V^b_{micro} (cm^3/g)	0.14	0.13
V^b_{meso} (cm^3/g)	0.35	0.34
V^c_{macro} (cm^3/g)	0.15	0.15
Apparent density (g/cm^3)	0.95	0.96

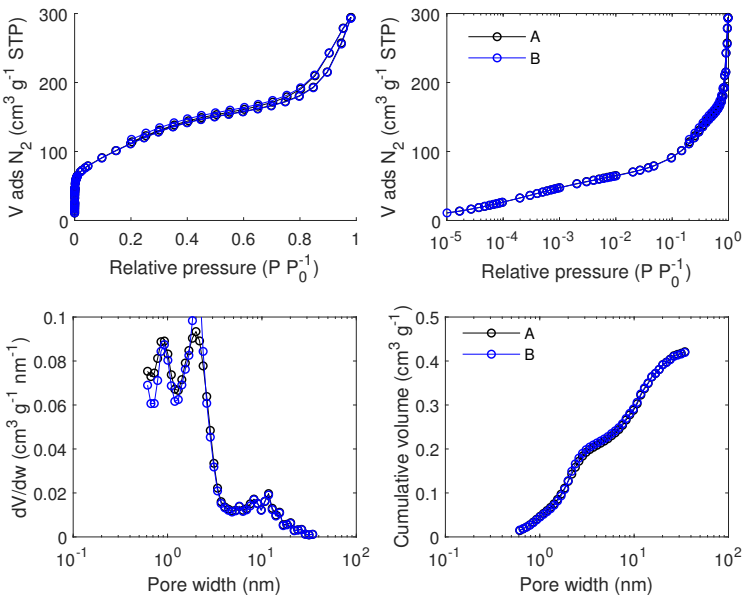

Figure F.9: N_2 adsorption/desorption isotherm data measured at 77 K and pore size analysis by equilibrium QSDFT for carbon F5001 filled with $NaClO_4$ from a 56 wt% aqueous solution. A and B are repetitions (from the synthesis).

Table F.9: Selected textural properties based on N_2 isotherm at 77 K and MIP data for carbon F5001 filled with $NaClO_4$ from a 56 wt% aqueous solution; (a) total pore volume at $P/P_0 = 0.985$; (b) by equilibrium QSDFT model; (c) based on MIP data. A and B are repetitions (from the synthesis).

Experiment	A	B
Yield (g/g)	2.15	2.14
TPV^a (cm^3/g)	0.45	0.45
V^b_{micro} (cm^3/g)	0.13	0.13
V^b_{meso} (cm^3/g)	0.30	0.29
V^c_{macro} (cm^3/g)	0.12	0.11
Apparent density (g/cm^3)	1.06	1.06

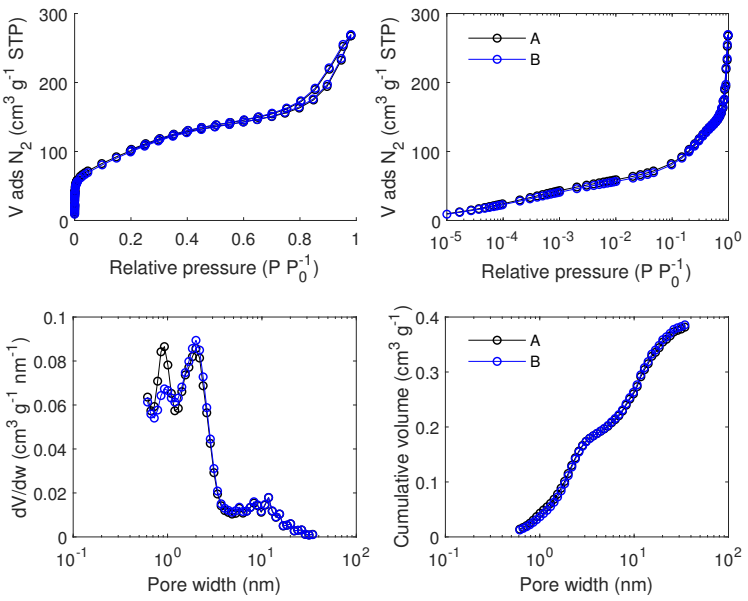

Figure F.10: N_2 adsorption/desorption isotherm data measured at 77 K and pore size analysis by equilibrium QSDFT for carbon F5001 filled with $NaClO_4$ from a 60 wt% aqueous solution. A and B are repetitions (from the synthesis).

Table F.10: Selected textural properties based on N_2 isotherm at 77 K and MIP data for carbon F5001 filled with $NaClO_4$ from a 60 wt% aqueous solution; (a) total pore volume at $P/P_0 = 0.985$; (b) by equilibrium QSDFT model; (c) based on MIP data. A and B are repetitions (from the synthesis).

Experiment	A	B
Yield (g/g)	2.27	2.27
TPV^a (cm^3/g)	0.41	0.42
V^b_{micro} (cm^3/g)	0.11	0.11
V^b_{meso} (cm^3/g)	0.27	0.27
V^c_{macro} (cm^3/g)	0.09	0.10
Apparent density (g/cm^3)	1.11	1.10

F.2.2 Chemical oxidation

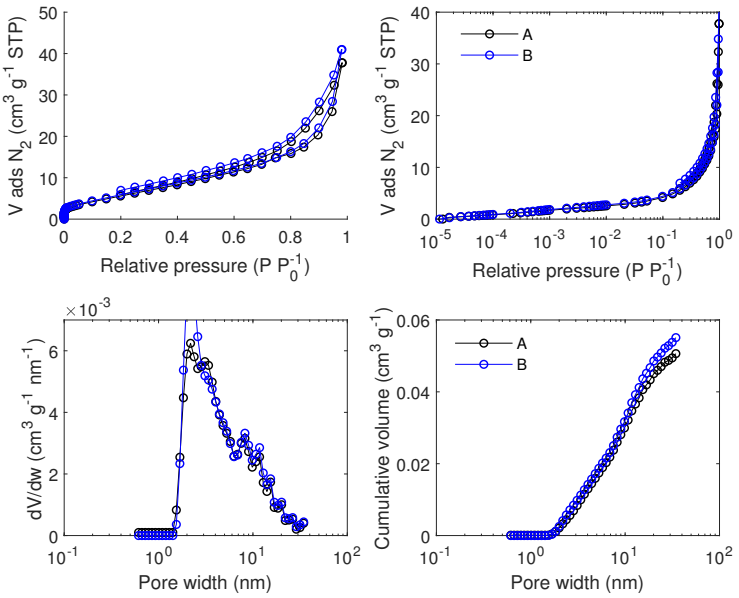

Figure F.11: N_2 adsorption/desorption isotherm data measured at 77 K and pore size analysis by equilibrium QSDFT for carbon F5001-APS filled with $NaClO_4$ from a 56 wt% aqueous solution. A and B are repetitions (from the synthesis).

Table F.11: Selected textural properties based on N_2 isotherm at 77 K and MIP data for carbon F5001-APS filled with $NaClO_4$ from a 56 wt% aqueous solution; (a) total pore volume at $P/P_0 = 0.985$; (b) by equilibrium QSDFT model; (c) based on MIP data. A and B are repetitions (from the synthesis).

Experiment	A	B
Yield (g/g)	1.65	1.78
TPV^a (cm^3/g)	0.06	0.06
V^b_{micro} (cm^3/g)	0.00	0.00
V^b_{meso} (cm^3/g)	0.05	0.05
V^c_{macro} (cm^3/g)	0.01	0.01
Apparent density (g/cm^3)	1.89	1.86

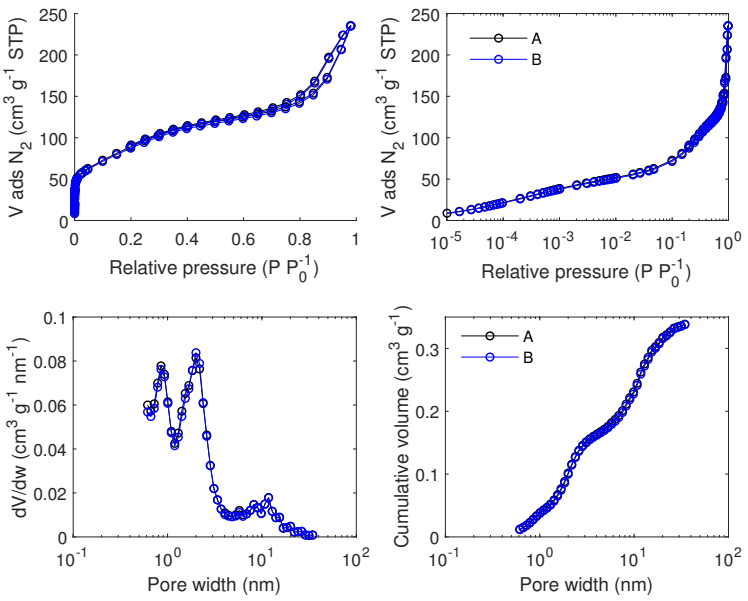

Figure F.12: N_2 adsorption/desorption isotherm data measured at 77 K and pore size analysis by equilibrium QSDFT for carbon F5001-HN filled with $NaClO_4$ from a 56 wt% aqueous solution. A and B are repetitions (from the synthesis).

Table F.12: Selected textural properties based on N_2 isotherm at 77 K and MIP data for carbon F5001-HN filled with $NaClO_4$ from a 56 wt% aqueous solution; (a) total pore volume at $P/P_0 = 0.985$; (b) by equilibrium QSDFT model; (c) based on MIP data. A and B are repetitions (from the synthesis).

Experiment	A	B
Yield (g/g)	2.04	2.04
TPV^a (cm^3/g)	0.36	0.36
V^b_{micro} (cm^3/g)	0.10	0.10
V^b_{meso} (cm^3/g)	0.24	0.24
V^c_{macro} (cm^3/g)	0.06	0.06
Apparent density (g/cm^3)	1.25	1.31

F.3 Carbon BPL and derivatives

F.3.1 Influence of concentration

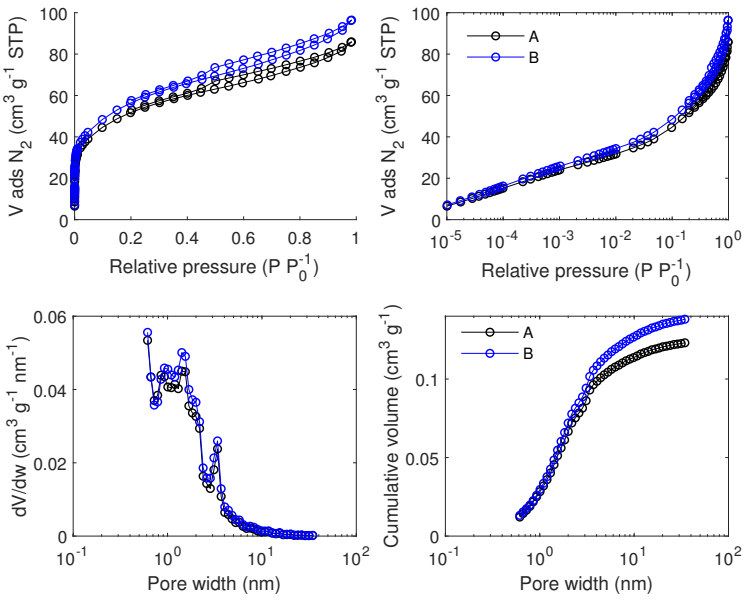

Figure F.13: N_2 adsorption/desorption isotherm data measured at 77 K and pore size analysis by equilibrium QSDFT for carbon BPL filled with $NaClO_4$ from a 40 wt% aqueous solution. A and B are repetitions (from the synthesis).

Table F.13: Selected textural properties based on N_2 isotherm at 77 K and MIP data for carbon BPL filled with $NaClO_4$ from a 40 wt% aqueous solution; (a) total pore volume at $P/P_0 = 0.985$; (b) by equilibrium QSDFT model; (c) based on MIP data. A and B are repetitions (from the synthesis).

Experiment	A	B
Yield (g/g)	0.53	0.53
TPV^a (cm^3/g)	0.13	0.15
V^b_{micro} (cm^3/g)	0.07	0.07
V^b_{meso} (cm^3/g)	0.06	0.07
V^c_{macro} (cm^3/g)	0.20	0.20
Apparent density (g/cm^3)	1.21	1.23

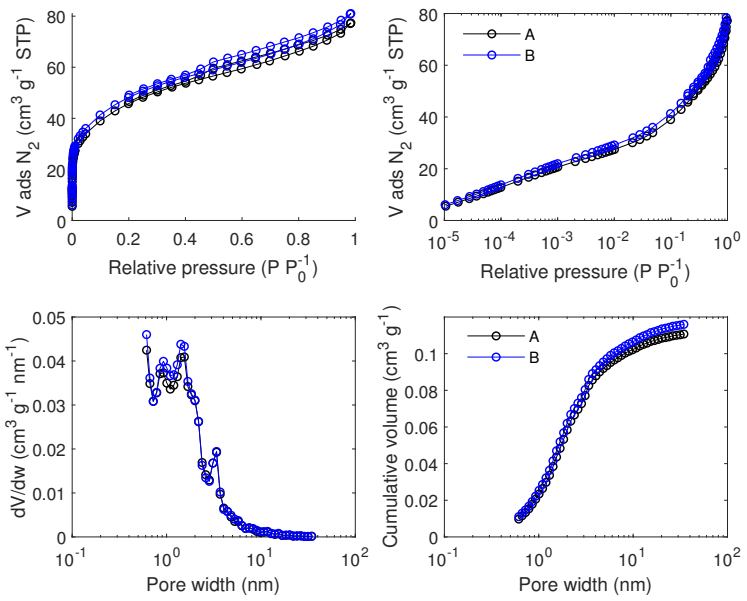

Figure F.14: N_2 adsorption/desorption isotherm data measured at 77 K and pore size analysis by equilibrium QSDFT for carbon BPL filled with $NaClO_4$ from a 50 wt% aqueous solution. A and B are repetitions (from the synthesis).

Table F.14: Selected textural properties based on N_2 isotherm at 77 K and MIP data for carbon BPL filled with $NaClO_4$ from a 50 wt% aqueous solution; (a) total pore volume at $P/P_0 = 0.985$; (b) by equilibrium QSDFT model; (c) based on MIP data. A and B are repetitions (from the synthesis).

Experiment	A	B
Yield (g/g)	0.67	0.67
TPV^a (cm^3/g)	0.12	0.13
V^b_{micro} (cm^3/g)	0.06	0.06
V^b_{meso} (cm^3/g)	0.05	0.05
V^c_{macro} (cm^3/g)	0.17	0.17
Apparent density (g/cm^3)	1.30	1.31

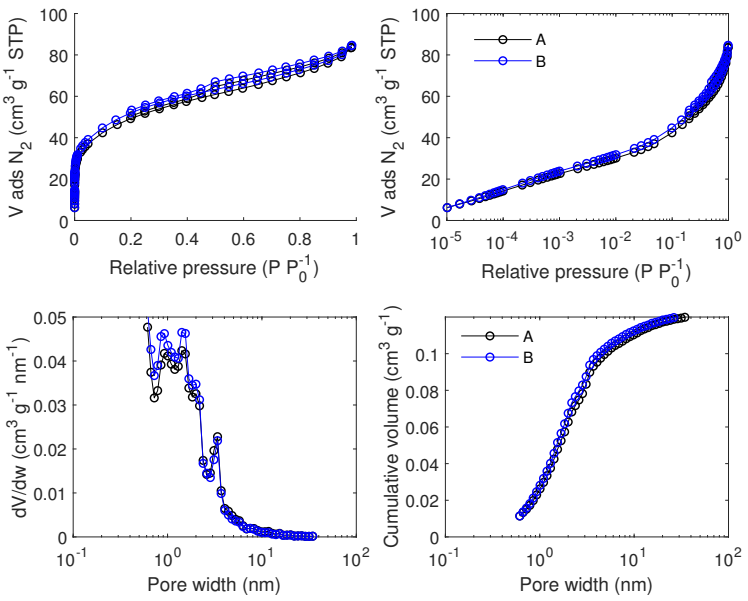

Figure F.15: N_2 adsorption/desorption isotherm data measured at 77 K and pore size analysis by equilibrium QSDFT for carbon BPL filled with $NaClO_4$ from a 56 wt% aqueous solution. A and B are repetitions (from the synthesis).

Table F.15: Selected textural properties based on N_2 isotherm at 77 K and MIP data for carbon BPL filled with $NaClO_4$ from a 56 wt% aqueous solution; (a) total pore volume at $P/P_0 = 0.985$; (b) by equilibrium QSDFT model; (c) based on MIP data. A and B are repetitions (from the synthesis).

Experiment	A	B
Yield (g/g)	0.68	0.66
TPV^a (cm^3/g)	0.13	0.13
V^b_{micro} (cm^3/g)	0.06	0.07
V^b_{meso} (cm^3/g)	0.06	0.05
V^c_{macro} (cm^3/g)	0.14	0.14
Apparent density (g/cm^3)	1.42	1.31

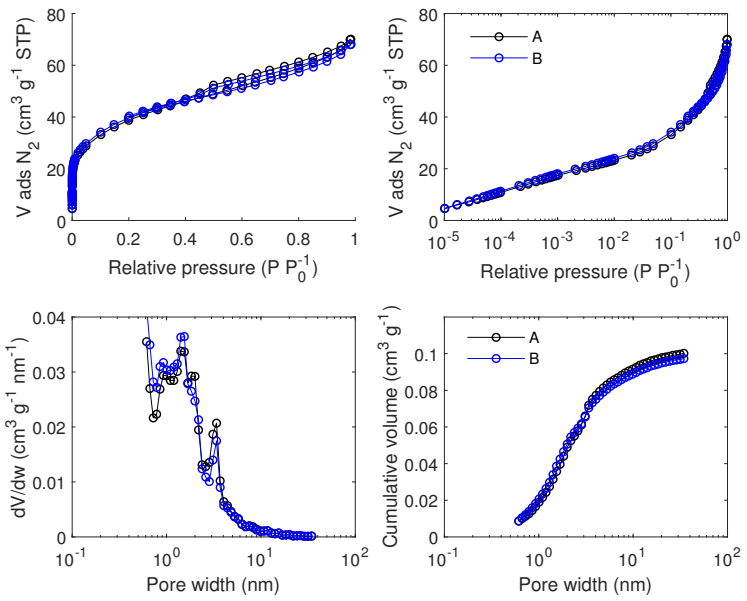

Figure F.16: N_2 adsorption/desorption isotherm data measured at 77 K and pore size analysis by equilibrium QSDFT for carbon BPL filled with $NaClO_4$ from a 60 wt% aqueous solution. A and B are repetitions (from the synthesis).

Table F.16: Selected textural properties based on N_2 isotherm at 77 K and MIP data for carbon BPL filled with $NaClO_4$ from a 60 wt% aqueous solution; (a) total pore volume at $P/P_0 = 0.985$; (b) by equilibrium QSDFT model; (c) based on MIP data. A and B are repetitions (from the synthesis).

Experiment	A	B
Yield (g/g)	0.81	0.81
TPV^a (cm^3/g)	0.11	0.10
V^b_{micro} (cm^3/g)	0.05	0.05
V^b_{meso} (cm^3/g)	0.05	0.05
V^c_{macro} (cm^3/g)	0.12	0.11
Apparent density (g/cm^3)	1.42	1.40

F.3.2 Overactivation

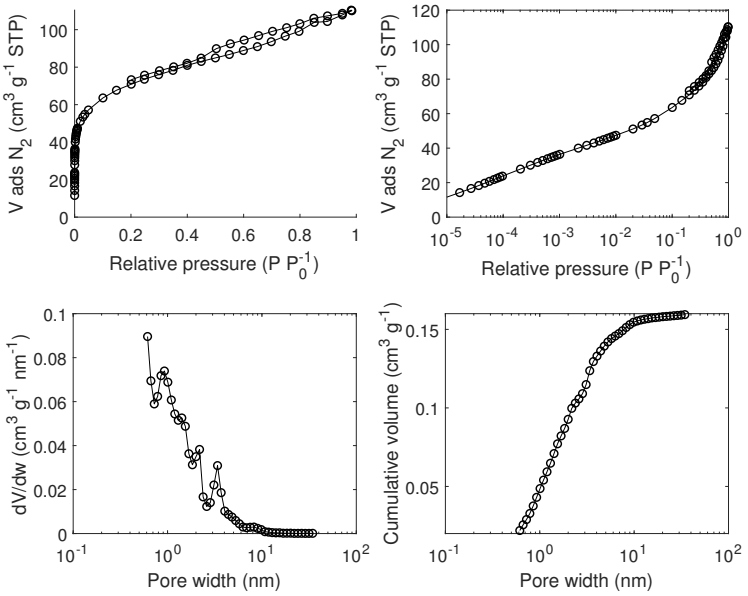

Figure F.17: N_2 adsorption/desorption isotherm data measured at 77 K and pore size analysis by equilibrium QSDFT for carbon BPL-18 filled with $NaClO_4$ from a 56 wt% aqueous solution.

Table F.17: Selected textural properties based on N_2 isotherm at 77 K and MIP data for carbon BPL-18 filled with $NaClO_4$ from a 56 wt% aqueous solution; (a) total pore volume at P/P_0 = 0.985; (b) by equilibrium QSDFT model; (c) based on MIP data. A and B are repetitions (from the synthesis).

Experiment	A	B
Yield (g/g)	0.99	0.97
TPV^a (cm^3/g)	0.17	-
V^b_{micro} (cm^3/g)	0.09	-
V^b_{meso} (cm^3/g)	0.07	-
V^c_{macro} (cm^3/g)	0.11	0.16
Apparent density (g/cm^3)	1.37	1.33

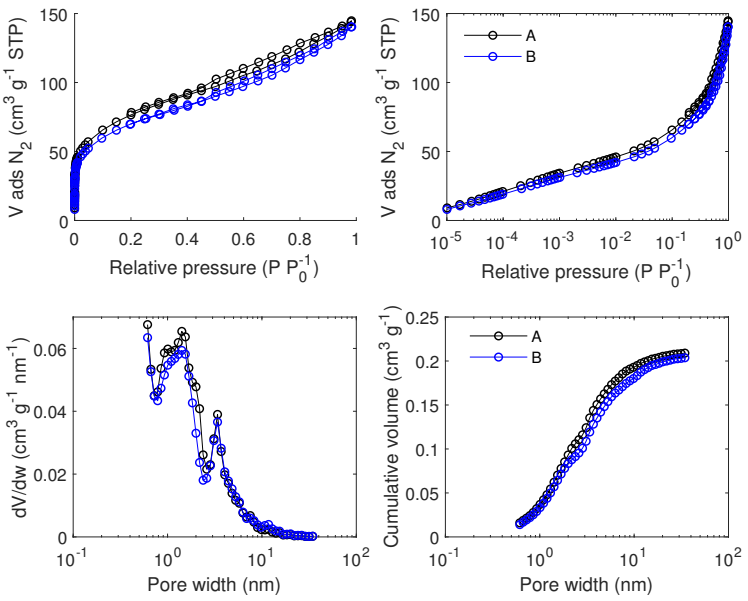

Figure F.18: N_2 adsorption/desorption isotherm data measured at 77 K and pore size analysis by equilibrium QSDFT for carbon BPL-37 filled with $NaClO_4$ from a 56 wt% aqueous solution. A and B are repetitions (from the synthesis).

Table F.18: Selected textural properties based on N_2 isotherm at 77 K and MIP data for carbon BPL-37 filled with $NaClO_4$ from a 56 wt% aqueous solution; (a) total pore volume at P/P_0 = 0.985; (b) by equilibrium QSDFT model; (c) based on MIP data. A and B are repetitions (from the synthesis).

Experiment	A	B
Yield (g/g)	1.28	1.27
TPV^a (cm^3/g)	0.22	0.22
V^b_{micro} (cm^3/g)	0.09	0.08
V^b_{meso} (cm^3/g)	0.12	0.12
V^c_{macro} (cm^3/g)	0.13	0.18
Apparent density (g/cm^3)	1.25	1.26

F.4 Carbon FY5 and derivatives

F.4.1 Influence of concentration

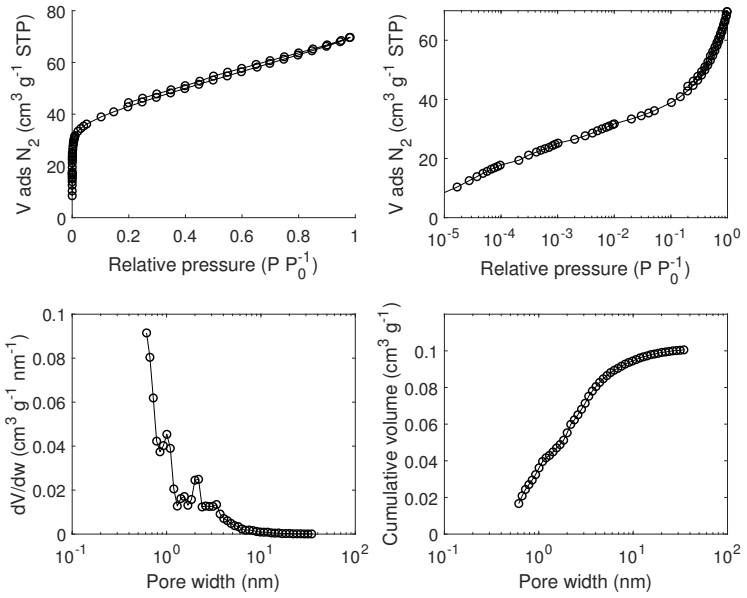

Figure F.19: N_2 adsorption/desorption isotherm data measured at 77 K and pore size analysis by equilibrium QSDFT for carbon FY5 filled with $NaClO_4$ from a 40 wt% aqueous solution.

Table F.19: Selected textural properties based on N_2 isotherm at 77 K and MIP data for carbon FY5 filled with $NaClO_4$ from a 40 wt% aqueous solution; (a) total pore volume at $P/P_0 = 0.985$; (b) by equilibrium QSDFT model; (c) based on MIP data. A and B are repetitions (from the synthesis).

Experiment	A	B
Yield (g/g)	0.32	0.32
TPV^a (cm^3/g)	0.11	-
V^b_{micro} (cm^3/g)	0.05	-
V^b_{meso} (cm^3/g)	0.05	-
V^c_{macro} (cm^3/g)	0.08	0.08
Apparent density (g/cm^3)	1.38	1.48

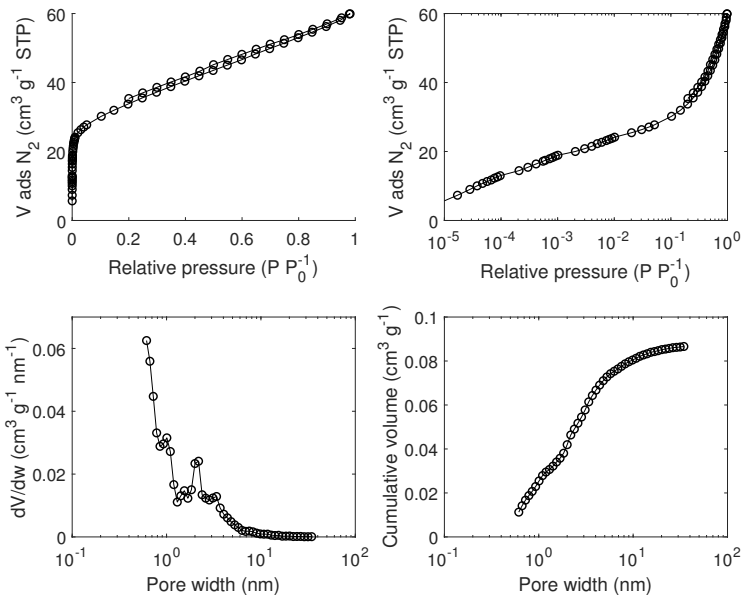

Figure F.20: N_2 adsorption/desorption isotherm data measured at 77 K and pore size analysis by equilibrium QSDFT for carbon FY5 filled with $NaClO_4$ from a 50 wt% aqueous solution.

Table F.20: Selected textural properties based on N_2 isotherm at 77 K and MIP data for carbon FY5 filled with $NaClO_4$ from a 50 wt% aqueous solution; (a) total pore volume at $P/P_0 = 0.985$; (b) by equilibrium QSDFT model; (c) based on MIP data. A and B are repetitions (from the synthesis).

Experiment	A	B
Yield (g/g)	0.38	0.43
TPV^a (cm^3/g)	0.09	-
V^b_{micro} (cm^3/g)	0.04	-
V^b_{meso} (cm^3/g)	0.05	-
V^c_{macro} (cm^3/g)	0.07	0.06
Apparent density (g/cm^3)	1.49	1.35

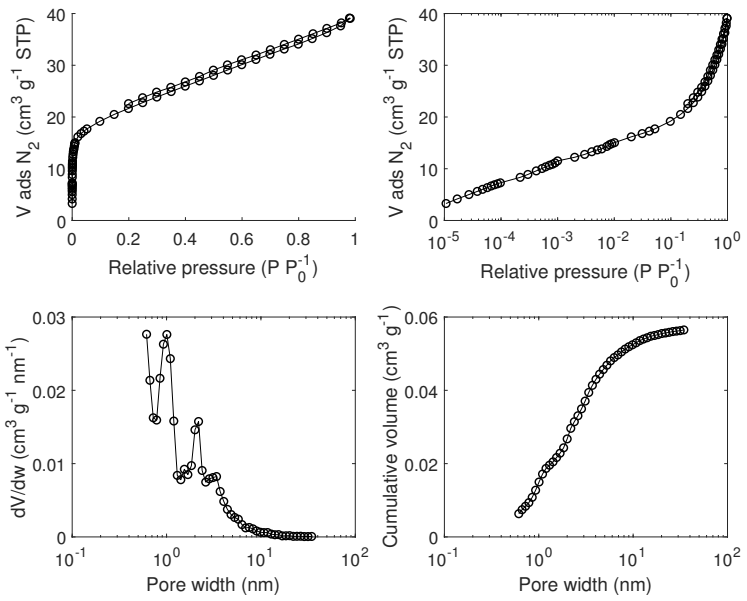

Figure F.21: N_2 adsorption/desorption isotherm data measured at 77 K and pore size analysis by equilibrium QSDFT for carbon FY5 filled with $NaClO_4$ from a 56 wt% aqueous solution.

Table F.21: Selected textural properties based on N_2 isotherm at 77 K and MIP data for carbon FY5 filled with $NaClO_4$ from a 56 wt% aqueous solution; (a) total pore volume at $P/P_0 = 0.985$; (b) by equilibrium QSDFT model; (c) based on MIP data. A and B are repetitions (from the synthesis).

Experiment	A	B
Yield (g/g)	0.46	0.48
TPV^a (cm^3/g)	0.06	-
V^b_{micro} (cm^3/g)	0.03	-
V^b_{meso} (cm^3/g)	0.03	-
V^c_{macro} (cm^3/g)	0.05	0.05
Apparent density (g/cm^3)	1.51	1.52

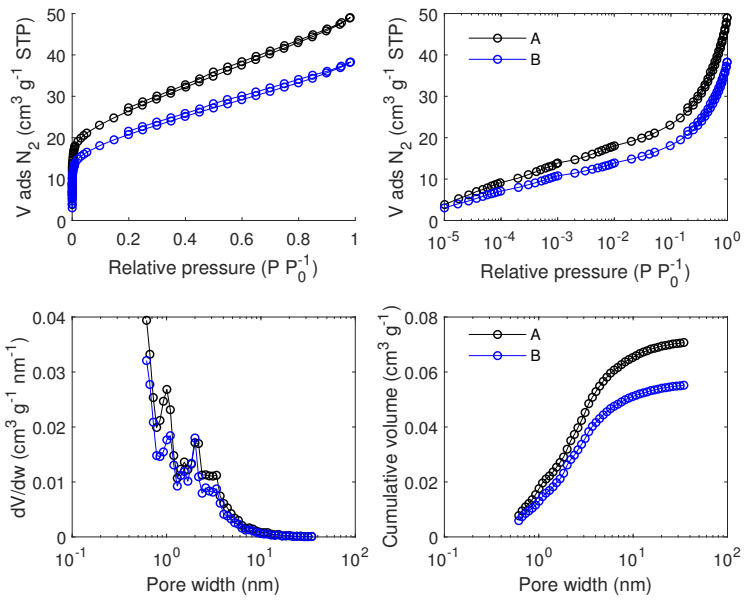

Figure F.22: N_2 adsorption/desorption isotherm data measured at 77 K and pore size analysis by equilibrium QSDFT for carbon FY5 filled with $NaClO_4$ from a 60 wt% aqueous solution. A and B are repetitions (from the synthesis).

Table F.22: Selected textural properties based on N_2 isotherm at 77 K and MIP data for carbon FY5 filled with $NaClO_4$ from a 60 wt% aqueous solution; (a) total pore volume at $P/P_0 = 0.985$; (b) by equilibrium QSDFT model; (c) based on MIP data. A and B are repetitions (from the synthesis).

Experiment	A	B
Yield (g/g)	0.54	0.47
TPV^a (cm^3/g)	0.08	0.06
V^b_{micro} (cm^3/g)	0.03	0.03
V^b_{meso} (cm^3/g)	0.04	0.03
V^c_{macro} (cm^3/g)	0.06	0.05
Apparent density (g/cm^3)	1.53	1.52

F.4.2 Overactivation

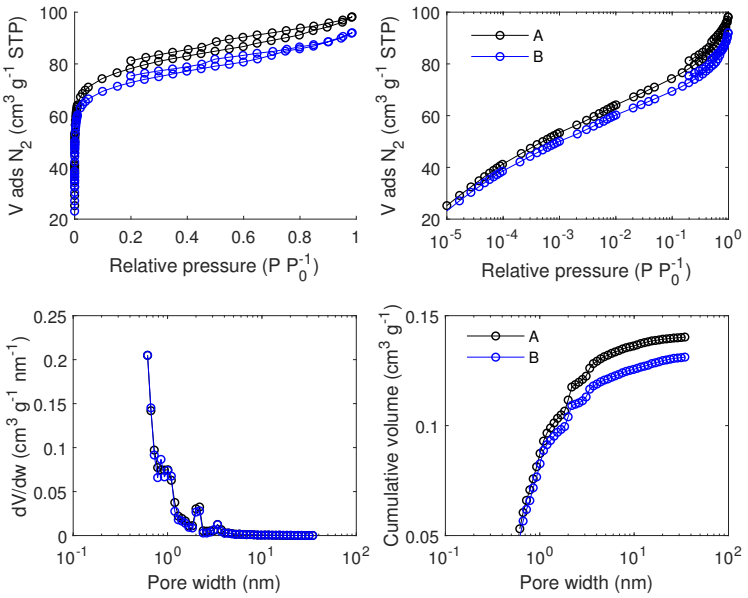

Figure F.23: N_2 adsorption/desorption isotherm data measured at 77 K and pore size analysis by equilibrium QSDFT for carbon FY5-21 filled with $NaClO_4$ from a 56 wt% aqueous solution. A and B are repetitions (from the synthesis).

Table F.23: Selected textural properties based on N_2 isotherm at 77 K and MIP data for carbon FY5-21 filled with $NaClO_4$ from a 56 wt% aqueous solution; (a) total pore volume at P/P_0 = 0.985; (b) by equilibrium QSDFT model; (c) based on MIP data. A and B are repetitions (from the synthesis).

Experiment	A	B
Yield (g/g)	0.72	0.72
TPV^a (cm^3/g)	0.15	0.14
V^b_{micro} (cm^3/g)	0.11	0.10
V^b_{meso} (cm^3/g)	0.03	0.03
V^c_{macro} (cm^3/g)	0.07	0.06
Apparent density (g/cm^3)	1.31	1.31

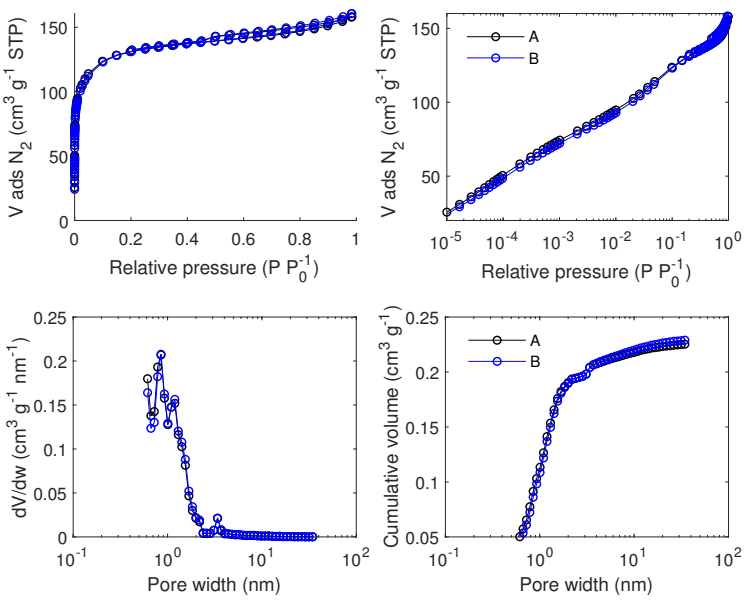

Figure F.24: N_2 adsorption/desorption isotherm data measured at 77 K and pore size analysis by equilibrium QSDFT for carbon FY5-57 filled with $NaClO_4$ from a 56 wt% aqueous solution. A and B are repetitions (from the synthesis).

Table F.24: Selected textural properties based on N_2 isotherm at 77 K and MIP data for carbon FY5-57 filled with $NaClO_4$ from a 56 wt% aqueous solution; (a) total pore volume at P/P_0 = 0.985; (b) by equilibrium QSDFT model; (c) based on MIP data. A and B are repetitions (from the synthesis).

Experiment	A
Yield (g/g)	1.08
TPV^a (cm^3/g)	0.24
V^b_{micro} (cm^3/g)	0.19
V^b_{meso} (cm^3/g)	0.03
V^c_{macro} (cm^3/g)	0.13
Apparent density (g/cm^3)	1.32

Appendix G

Visual aspect of filled carbons

Figures G.1, G.2, G.3 and G.4 show optical microscope pictures of pristine and filled carbons C, F5001 BPL and FY5, respectively, for comparison purposes. The carbons are filled with $NaClO_4$ from a 56 wt% aqueous solution (see section 3.5.1). These result show that the aspect of the carbon grains remains unchanged after pore filling, except for carbon F5001 where $NaClO_4$ crystals are visible on the external surface, which also leads to agglomeration of the beads.

(a) Pristine carbon C.

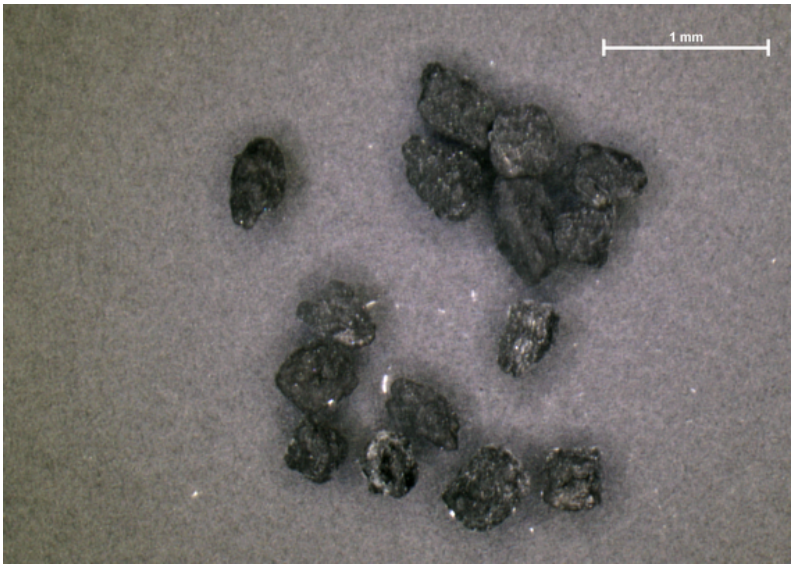

(b) Carbon C filled with $NaClO_4$ from a 56 wt% aqueous solution.

Figure G.1: Optical microscope picture of pristine and filled carbon C.

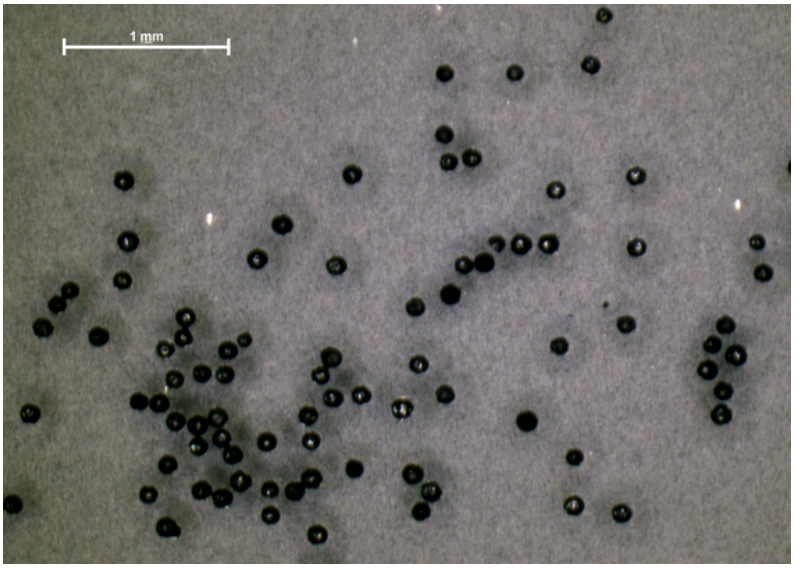

(a) Pristine carbon F5001.

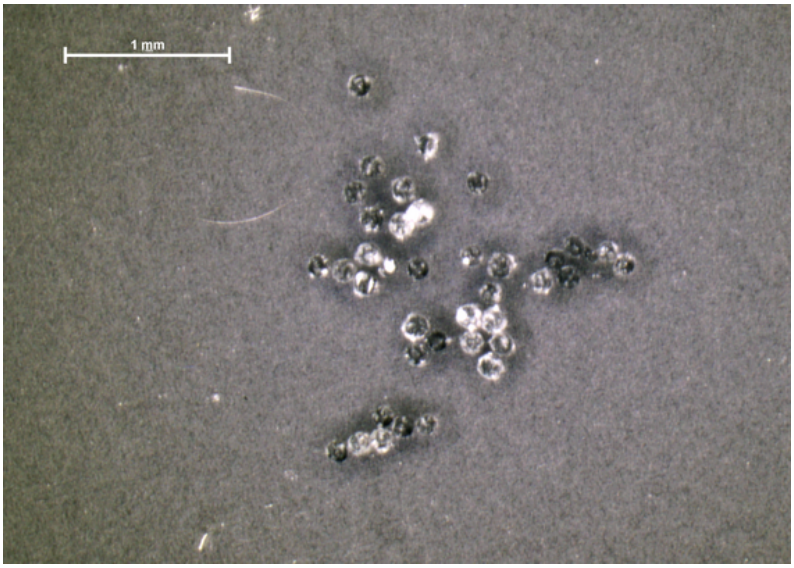

(b) Carbon F5001 filled with $NaClO_4$ from a 56 wt% aqueous solution.

Figure G.2: Optical microscope picture of pristine and filled carbon F5001.

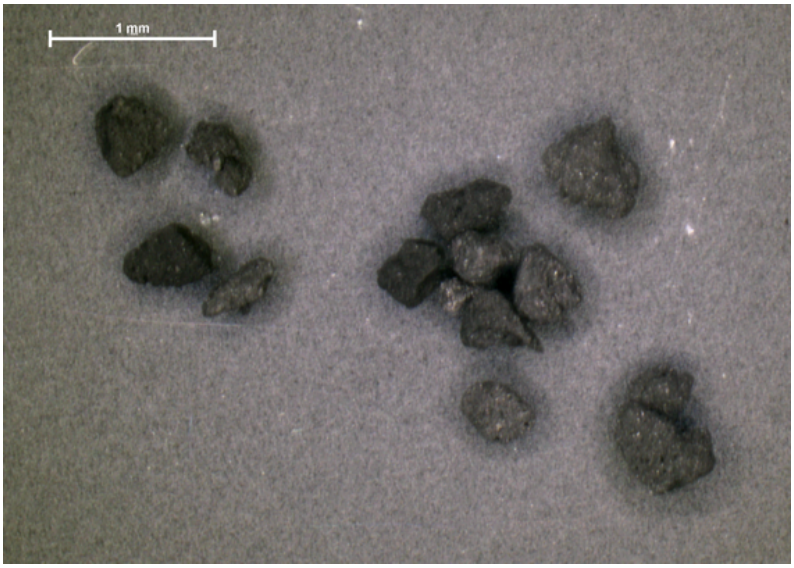

(a) Pristine carbon BPL.

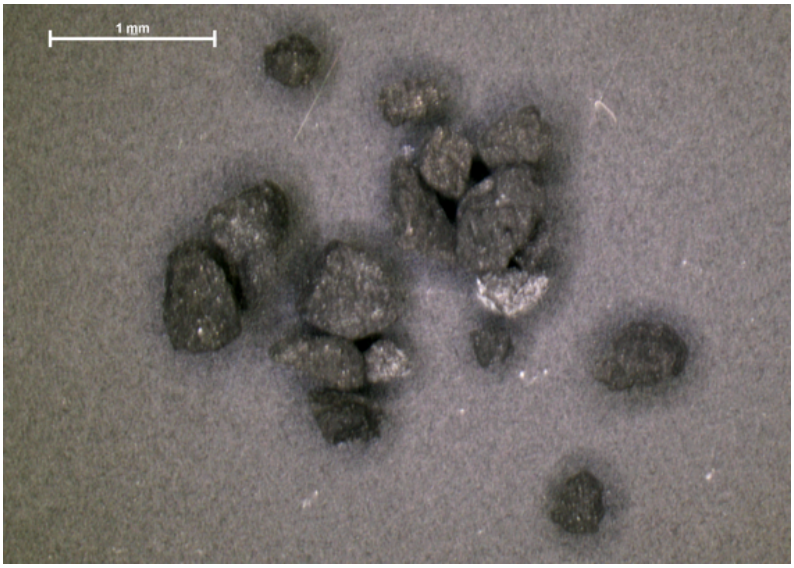

(b) Carbon BPL filled with $NaClO_4$ from a 56 wt% aqueous solution.

Figure G.3: Optical microscope picture of pristine and filled carbon BPL.

(a) Pristine carbon FY5.

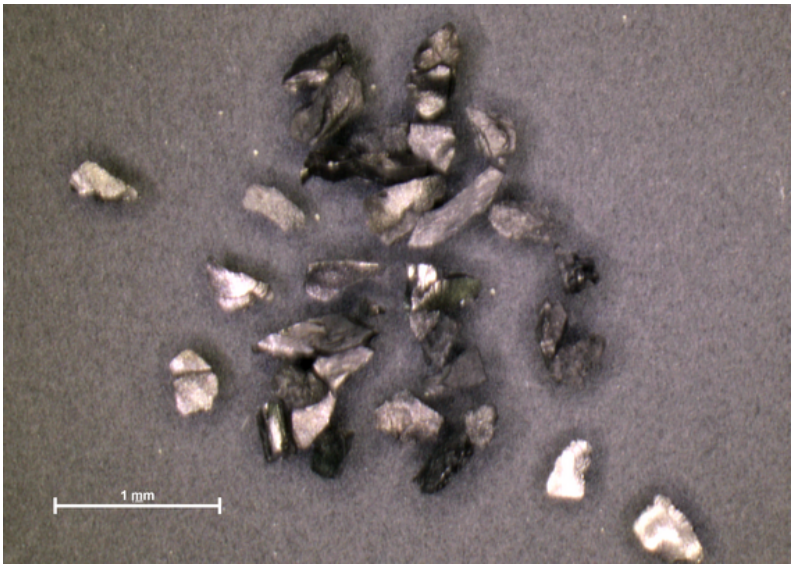

(b) Carbon FY5 filled with $NaClO_4$ from a 56 wt% aqueous solution.

Figure G.4: Optical microscope picture of pristine and filled carbon FY5.

Appendix H

Thermal analysis results

In this annex, the experimental results of the thermal analysis of pristine carbons and carbons filled with an oxidizing agent are shown. The TGA results of the pristine carbons were already shown in annex C. The experimental methods are detailed in chapter 2. The experiments replicated on the same material are labelled A and B if the experiment was repeated twice, and A, B and C if the experiment was repeated three times.

H.1 Thermal analysis of filled carbons

H.1.1 C and derivatives

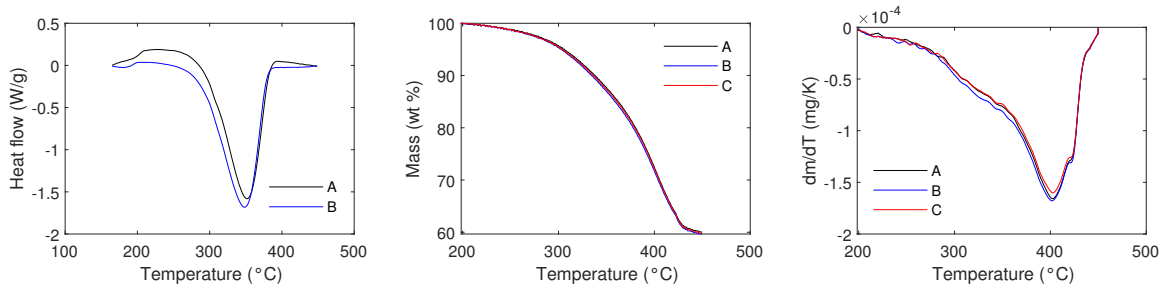

(a) 40 wt%.

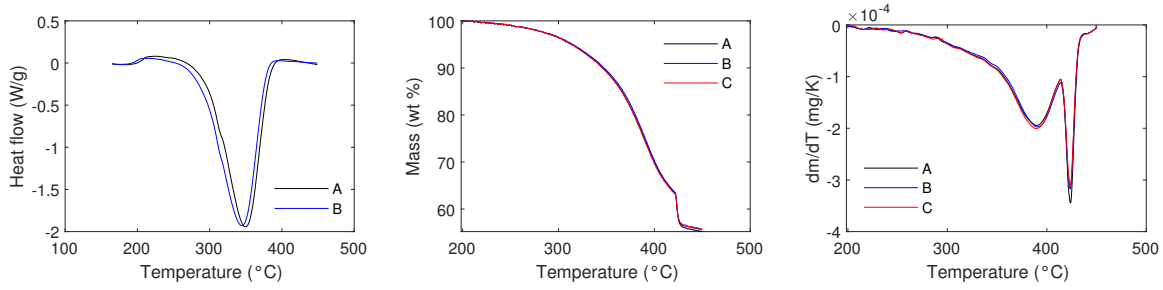

(b) 50 wt%.

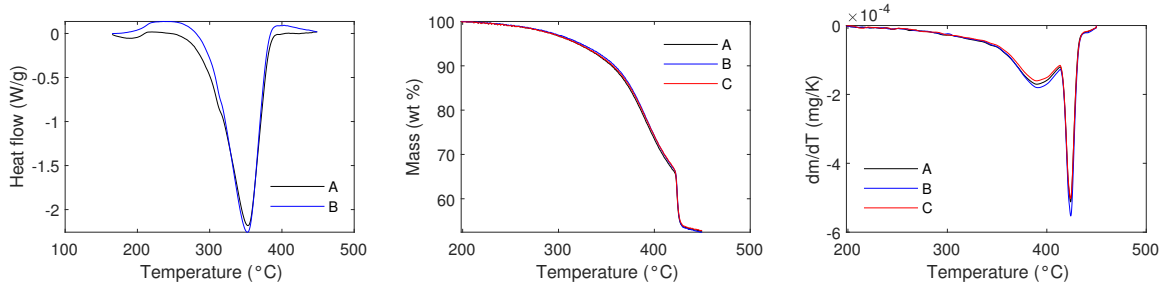

(c) 56 wt%.

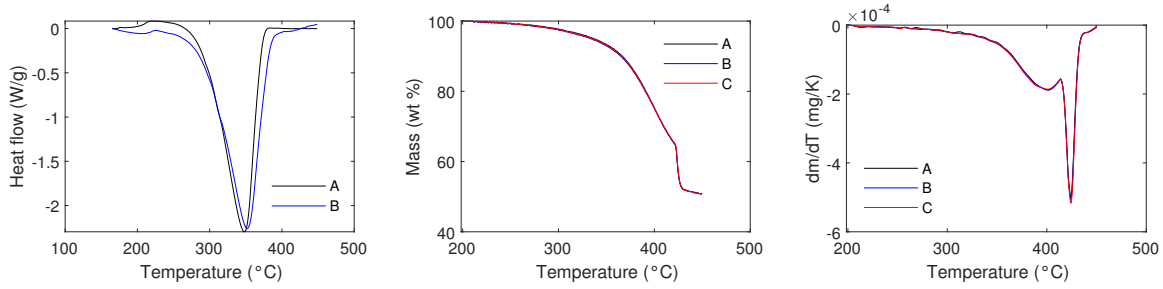

(d) 60 wt%.

Figure H.1: DSC (left), TGA (middle) and DTG (right) results of carbon C filled with $NaClO_4$ from solution at different concentrations (40, 50, 56 and 60 wt%).

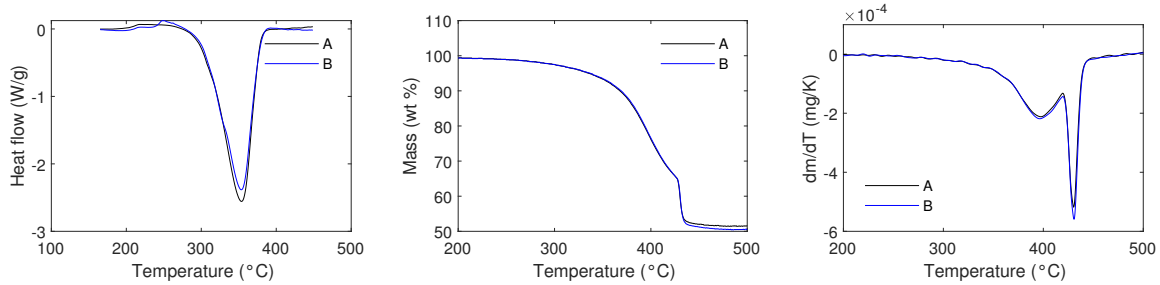

(a) C-R300.

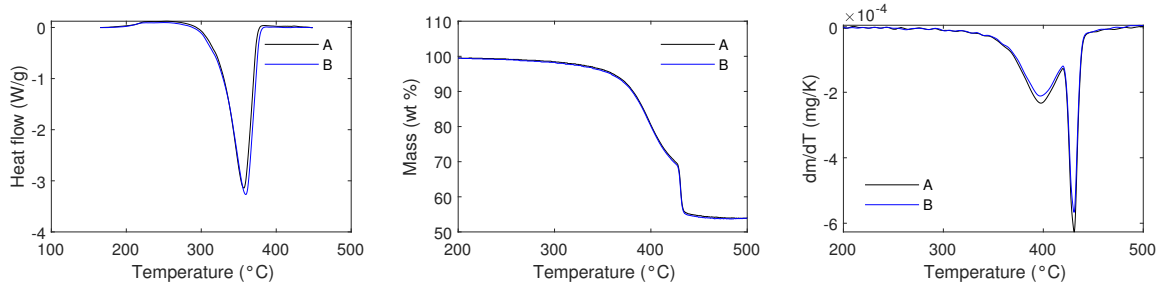

(b) C-R600.

Figure H.2: DSC (left), TGA (middle) and DTG (right) results of carbon C and its derivatives obtained by thermal reduction filled with $NaClO_4$ from a 56 wt% solution.

H.1.2 F5001 and derivatives

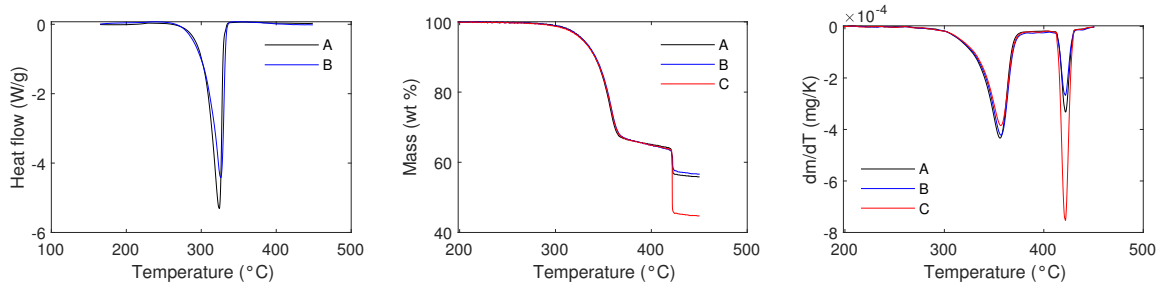

(a) 40 wt%.

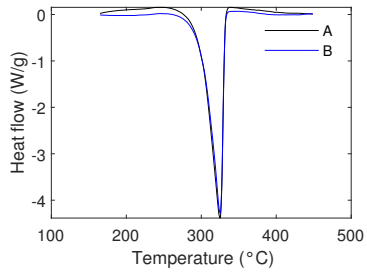

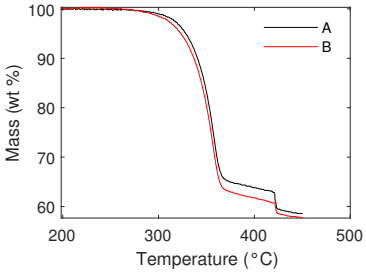

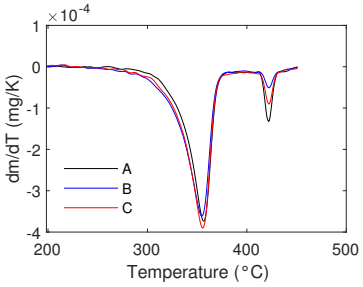

(b) 50 wt%.

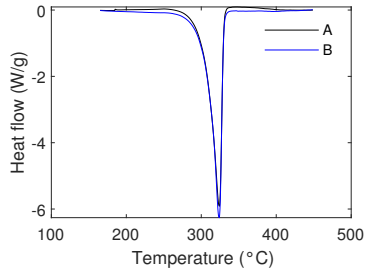

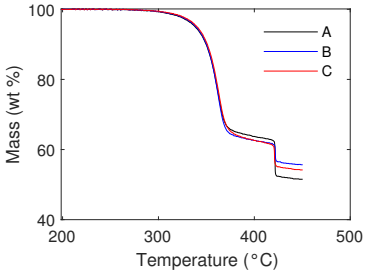

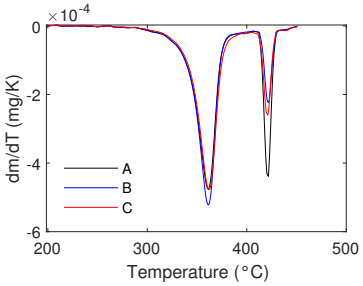

(c) 56 wt%.

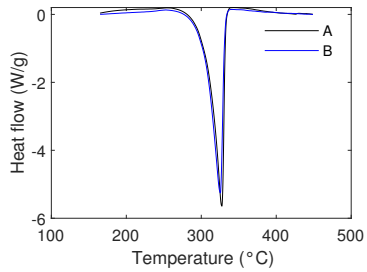

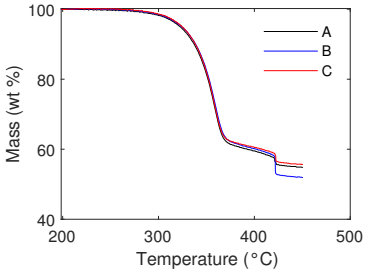

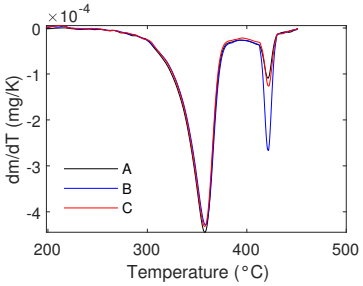

(d) 60 wt%.

Figure H.3: DSC (left), TGA (middle) and DTG (right) results of carbon F5001 filled with $NaClO_4$ from solution at different concentrations (40, 50, 56 and 60 wt%).

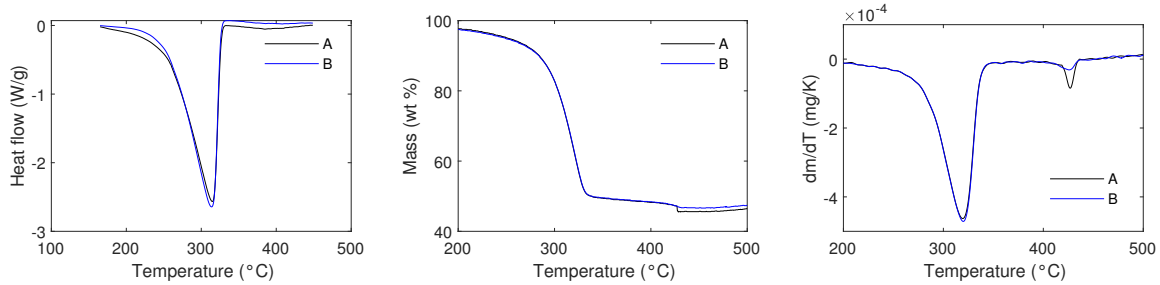

(a) F5001-APS.

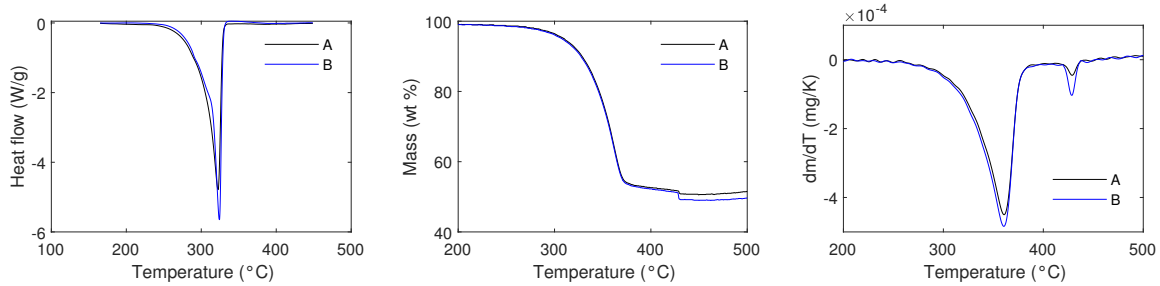

(b) F5001-HN.

Figure H.4: DSC (left), TGA (middle) and DTG (right) results of carbon F5001 and its derivatives obtained by chemical oxidation filled with $NaClO_4$ from a 56 wt% solution.

H.1.3 BPL and derivatives

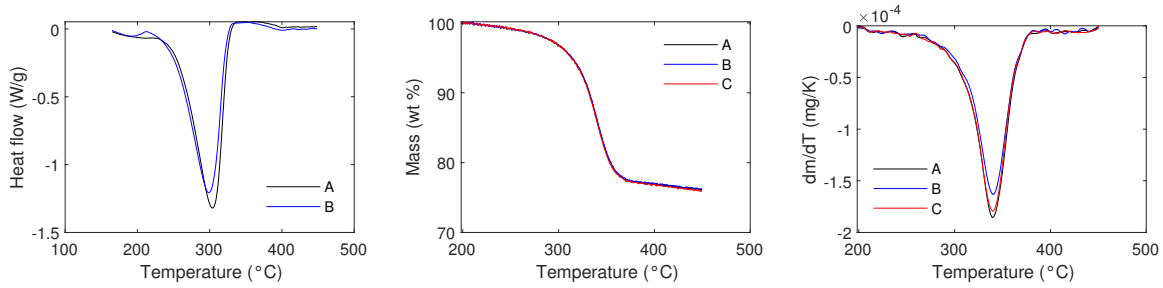

(a) 40 wt%.

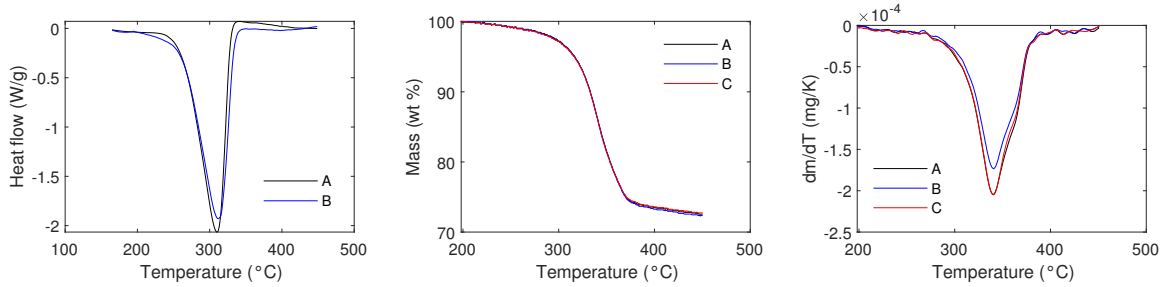

(b) 50 wt%.

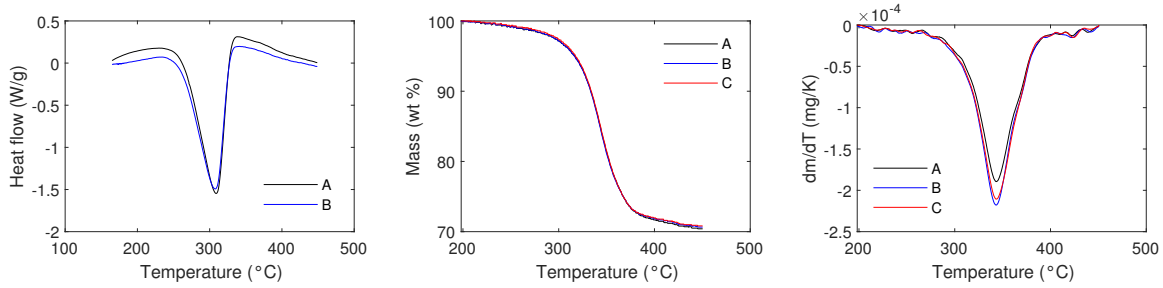

(c) 56 wt%.

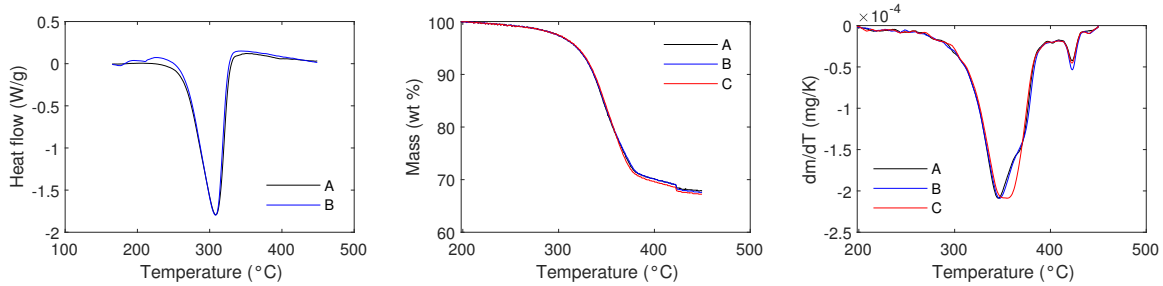

(d) 60 wt%.

Figure H.5: DSC (left), TGA (middle) and DTG (right) results of carbon BPL filled with $NaClO_4$ from solution at different concentrations (40, 50, 56 and 60 wt%).

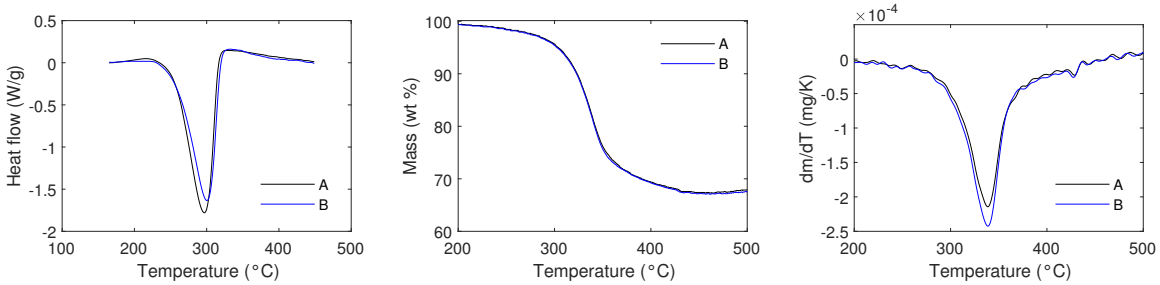

(a) BPL-18.

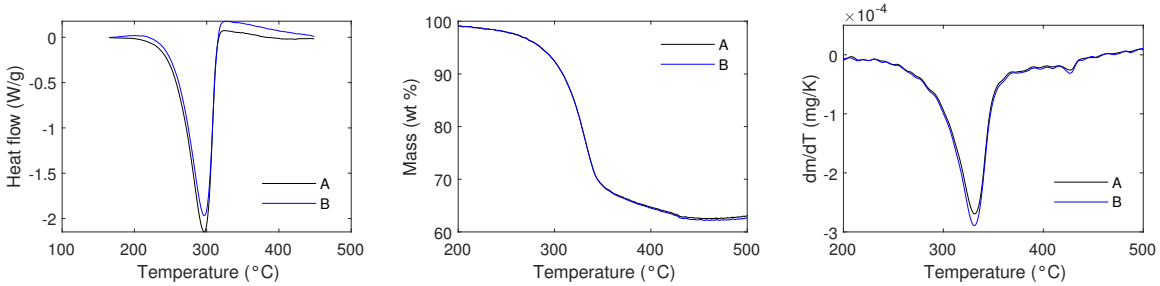

(b) BPL-37.

Figure H.6: DSC (left), TGA (middle) and DTG (right) results of carbon BPL and its derivatives obtained by overactivation filled with $NaClO_4$ from a 56 wt% solution.

H.1.4 FY5 and derivatives

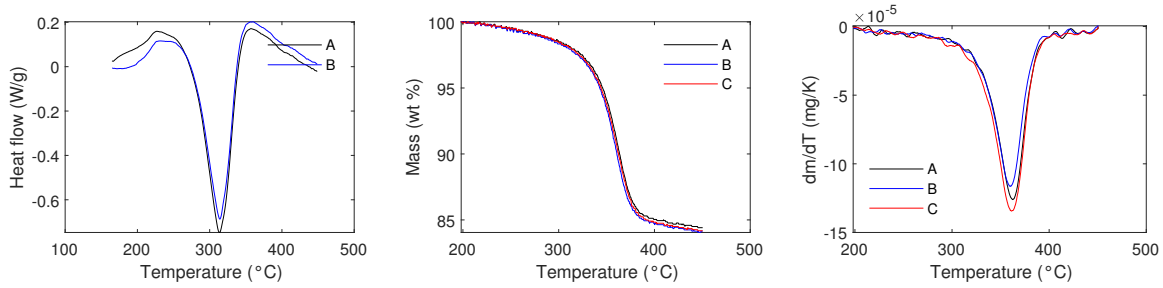

(a) 40 wt%.

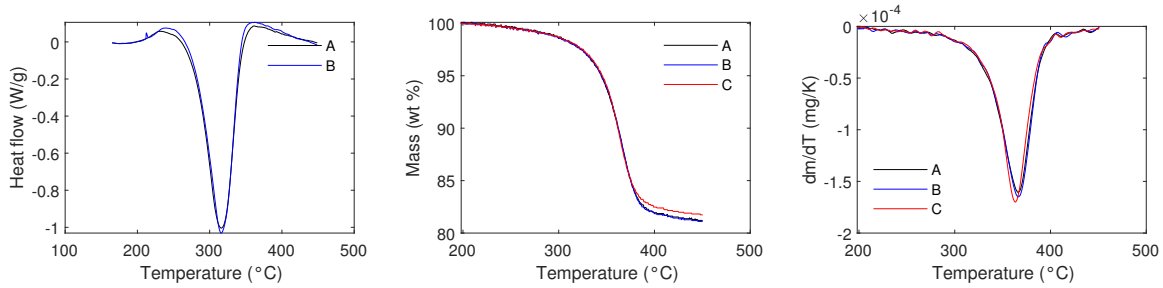

(b) 50 wt%.

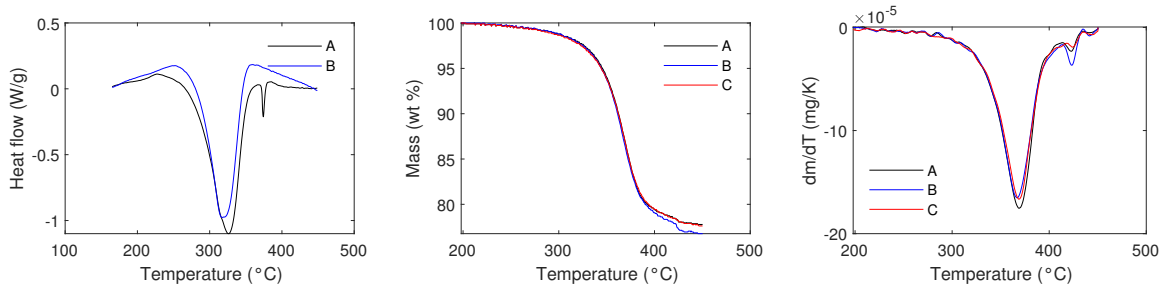

(c) 56 wt%.

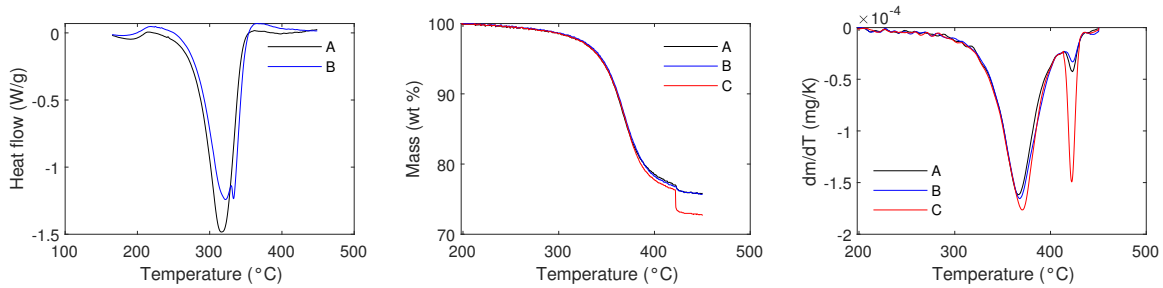

(d) 60 wt%.

Figure H.7: DSC (left), TGA (middle) and DTG (right) results of carbon FY5 filled with $NaClO_4$ from solution at different concentrations (40, 50, 56 and 60 wt%).

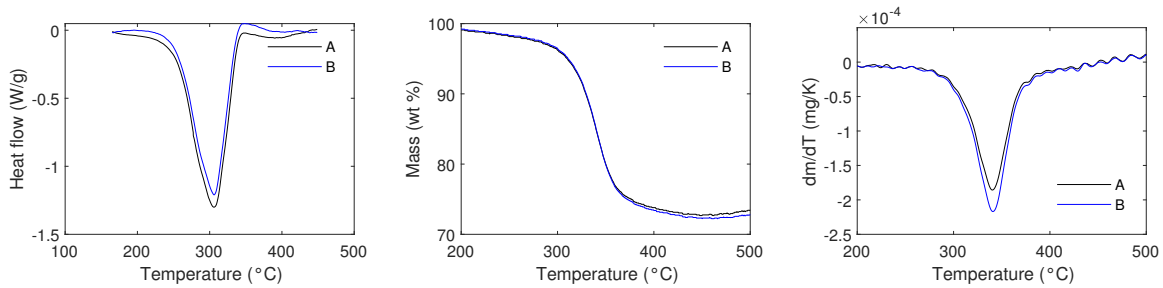

(a) FY5-21.

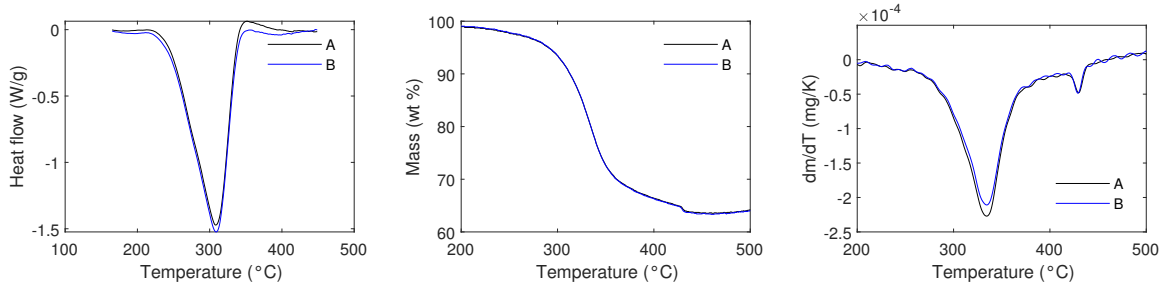

(b) FY5-57.

Figure H.8: DSC (left), TGA (middle) and DTG (right) results of carbon FY5 and its derivatives obtained by overactivation filled with $NaClO_4$ from a 56 wt% solution.

H.2 DSC analysis of pristine carbons

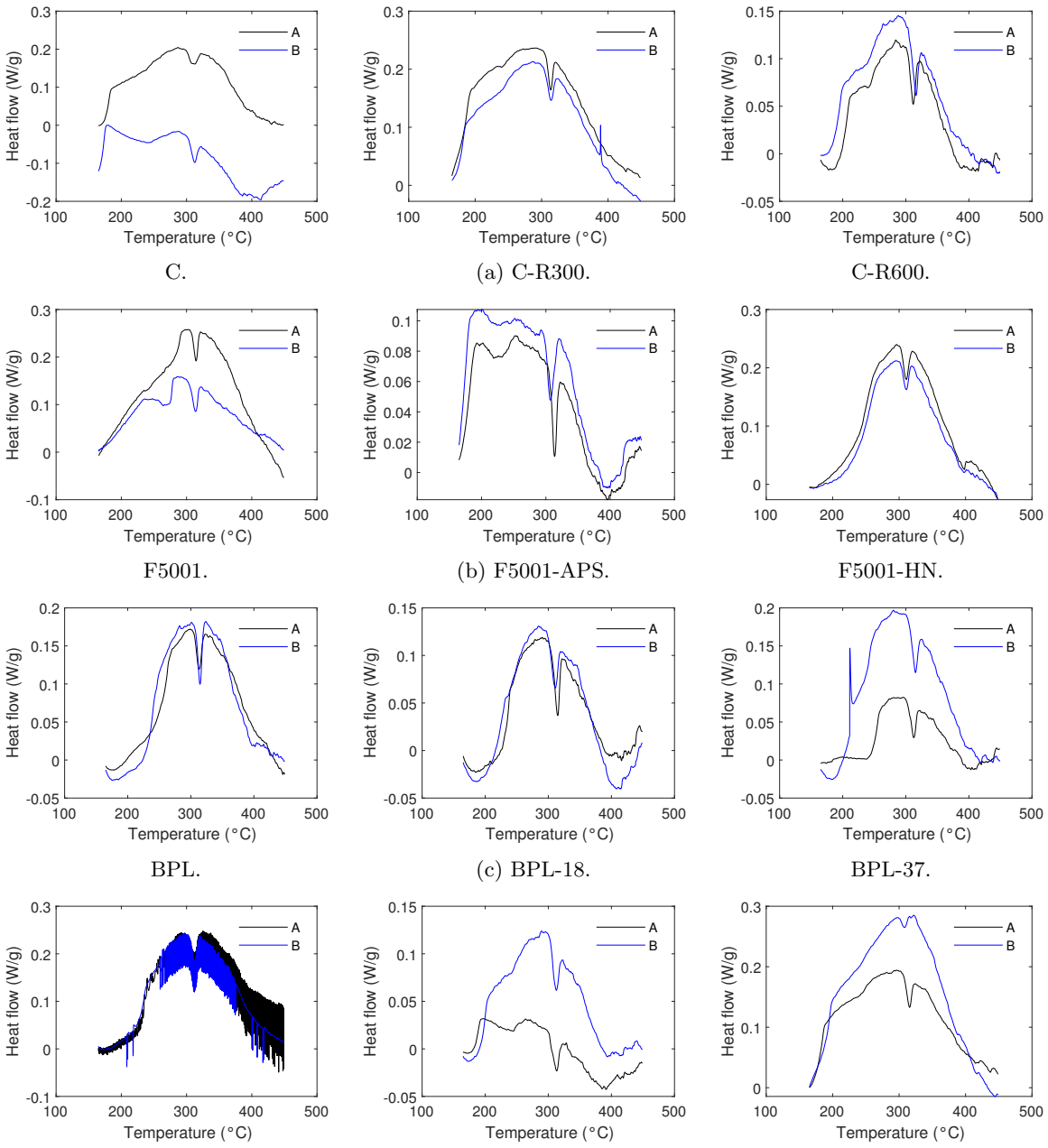

C. (a) C-R300. C-R600.

F5001. (b) F5001-APS. F5001-HN.

BPL. (c) BPL-18. BPL-37.

FY5. (d) FY5-21. FY5-57.

Figure H.9: DSC curves of pristine carbons.

H.3 Decomposition kinetics

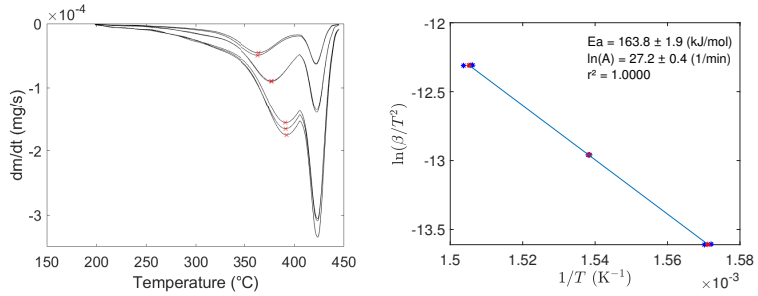

Figure H.10: TGA results (at 0.5, 1 and 2 K/min) of carbon C filled with sodium perchlorate from a 56 wt% aqueous solution and decomposition kinetics modelling.

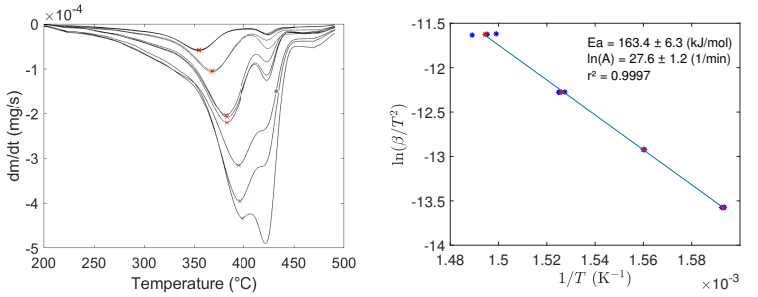

Figure H.11: TGA results (at 0.5, 1, 2, 4 and 7 K/min) of a physical mixture of carbon C and sodium perchlorate at 1.79 g/g, both milled and sieved between 25 and 50 μm, and decomposition kinetics modelling.

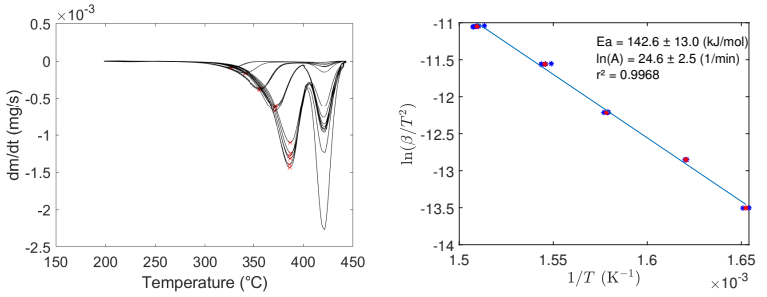

Figure H.12: TGA results (at 0.5, 1, 2, 4 and 7 K/min) of carbon F5001 filled with sodium perchlorate from a 56 wt% aqueous solution and decomposition kinetics modelling.

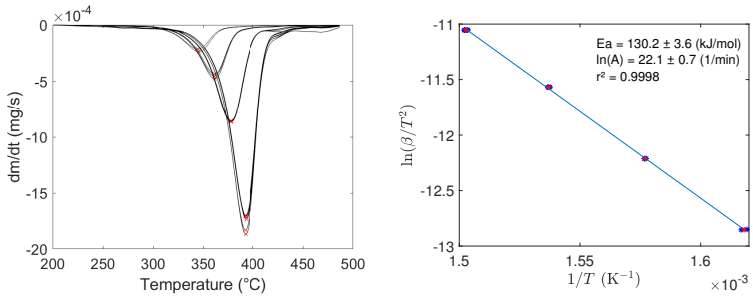

Figure H.13: TGA results (at 1, 2, 4 and 7 K/min) of a physical mixture of carbon F5001 and sodium perchlorate at 2.15 g/g, both milled and sieved between 25 and 50 μm, and decomposition kinetics modelling.

Appendix I

Detonation experiments performed on oxidizing agent and mixtures

As described in section 4.3, detonation experiments were performed with bare sodium perchlorate and physical mixture of the same composition as the studied composite material (carbon C filled with sodium perchlorate) in order to be used as reference of bare oxidizer and physical mixture.

Anhydrous sodium perchlorate was crushed in a ball mill and subsequently sieved. The fraction between 25 and 100 μm was used. The charge had a diameter of 30 mm, a height of 150 mm and was heavily confined in a steel tube (see Annex A). A sieve shaker was used to vibrate the charge in order to reach a reproducible tapped density, and sodium perchlorate was loaded in the tubes in steps in order to achieve a homogeneous density. A density of 1.39 g/cm^3 was obtained. The charge was initiated with a booster of 30 g of M112 (Composition C-4, supplied by LOP). The booster had a diameter of 30 mm, a height of 30 mm and was initiated by an electrical detonator, as described in chapter 2. The experiment was carried out by duplicate. In both cases, no sustained detonation was observed, as shown in figure I.1. The damage to the upper side of the tube is caused by the detonation of the booster charge. No sodium perchlorate was recovered after the experiment, and no indent was observed on the aluminum witness plate. No light signals associated with a detonation were recorded. These results indicate that the bare sodium perchlorate did not detonate, but only deflagrated in these conditions.

Figure I.1: Fragmentation pattern obtained after the initiation of bare sodium perchlorate at a density of 1.39 g/cm^3 and heavily confined in a 30 mm steel tube (a pristine tube is shown on the left side of the picture).

A physical mixture of carbon C and sodium perchlorate, in the same weight fraction as the filled carbon tested in section 4.3 was prepared by mixing carbon C and sodium perchlorate, both previously

dried and crushed in a ball mill before being sieved between 25 and 100 μm. The mixing was performed with a three-dimensional mixer for powders that uses an oloid rotary mechanism. Experiments were first performed by preparing and initiating the charges in the very same way as described above for sodium perchlorate. A density of 0.73 g/cm^3 was achieved. The experiment was carried out by duplicate and the results are shown in figure I.2. The tube was fragmented in large fragments only, and a very shallow indent was observed on the aluminum plate. The indent is nearly flat, with a depth of 3.5 mm. Despite the observation of an indent, the fragmentation pattern is typical of a deflagration and no light signals associated with a detonation were recorded. In the very same experimental conditions, velocity of detonation as low a 2.0 km/s and associated with calculated detonation pressure of 1.5 GPa were previously recorded. These results suggest that no sustained detonation occurred, and the observations are therefore attributed to a violent deflagration.

Figure I.2: Fragmentation pattern obtained after the initiation of a physical mixture of carbon C and sodium perchlorate at a density of 0.73 g/cm^3 and heavily confined in a 30 mm steel tube (a pristine tube is shown on the left side of the picture). The recovered witness plate is also shown on the right side of the picture.

Finally, the same physical mixture was pressed with a hydraulic press to the same force as that applied to achieve a density of 1.35 g/cm^3 with the filled carbon described in section 4.3. Because of practical safety limitations, the diameter of the charge was 20 mm. A density of 1.00 g/cm^3 was obtained. The charge was initiated with a booster of 15 g of M112 (Composition C-4, supplied by LOP). The booster had a diameter of 20 mm, a height of 30 mm and was initiated by an electrical detonator, as described in chapter 2. The experiment was carried out by duplicate. In both case, no sustained detonation was observed, as shown in figure I.3. No indent was observed on the aluminum witness plate, and no light signals associated with a detonation were recorded. These results indicate that the considered physical mixture did not detonate, but only deflagrated in these conditions.

Figure I.3: Fragmentation pattern obtained after the initiation of a physical mixture of carbon C and sodium perchlorate at a density of 1.00 g/cm^3 and heavily confined in a 20 mm steel tube (a pristine tube is shown on the left side of the picture).

Appendix J

Dissemination results

Article published (1)
R. Van Riet, E. Amayuelas, P. Lodewyckx, M.H. Lefebvre and C.O. Ania. Novel opportunities for nanoporous carbons as energetic materials. *Carbon*, 164:129-132, 2020. *doi: 10.1016/j.carbon.2020.03.061.* (`https://www.sciencedirect.com/science/article/pii/S0008622320303158`)

Patent filed (1)
R. Van Riet, P. Lodewyckx, C.O. Ania, M.H. Lefebvre. New energy-releasing composite material and method for manufacturing same. Filing date: 09 April 2020. Publication number: WO2020/208195. Application number: PCT/EP2020/060267.
(`https://patentscope.wipo.int/search/en/detail.jsf?docId=WO2020208195`)

Communications to conferences (3)

- R. Van Riet*, P. Lodewyckx, C.O. Ania, M.H. Lefebvre. A novel energetic material based on nanoporous carbons. 22th International Seminar on New Trends in Research of Energetic Materials, Pardubice, Czech-Republic, April 2019 [oral presentation].
- R. Van Riet*, P. Lodewyckx, M.H. Lefebvre, C.O. Ania. Nanoporous carbons as energetic nanomaterials. International Carbon Conference, Lexington (KY), USA, 2019 [oral presentation].
- R. Van Riet, P. Lodewyckx, M.H. Lefebvre, C.O. Ania*. An emerging application of nanoporous carbons as component of energetic nanomaterials. Beyond adsorption II Workshop, New York City, USA, 2019 [oral presentation].

* Presenting author.

Romuald VAN RIET

Nouveaux matériaux énergétiques à base de carbone nanoporeux rempli d'agent oxydant

Résumé : Ce travail explore une nouvelle famille de matériaux énergétiques produits en remplissant la porosité d'un carbone nanoporeux agissant comme un agent réducteur avec un agent oxydant solide. Un nouveau procédé de remplissage des pores par cristallisation après contraction de la solution lors du séchage est proposé pour remplir efficacement la porosité des carbones nanoporeux avec des agents oxydants solides. Il est démontré que l'efficacité de ce procédé dépend fortement de la nature du sel oxydant et du carbone, et que la plus grande partie de l'oxydant est cristallisé sélectivement dans des pores de largeur inférieure à 4 nm, ce qui assure un mélange homogène de l'agent oxydant et de l'agent réducteur à l'échelle nanométrique. Le concept est ensuite démontré expérimentalement en prouvant la capacité des carbones nanoporeux remplis d'agent oxydant à détoner et en évaluant leurs propriétés fondamentales en tant que matériaux énergétiques. Dans un confinement fort en acier, il est démontré qu'un matériau sélectionné est capable de détoner lorsqu'il est initié par un simple détonateur, avec des vitesses de détonation mesurées allant de 3000 à 4200 m/s pour différentes densités et des diamètres de 6 à 10 mm. Ces propriétés sont impressionnantes pour un matériau énergétique composite comportant une fraction très importante de produits de décomposition solides, ce qui dénote une cinétique de décomposition dynamique très rapide favorisée par l'échelle nanométrique du mélange. En conclusion, le concept d'une nouvelle famille de matériaux énergétiques basés sur des carbones nanoporeux remplis d'oxydants a été démontré dans ce travail, ouvrant de nouveaux horizons dans la voie vers des nanomatériaux énergétiques performants, sûrs et non toxiques avec un large spectre d'applications. Les propriétés uniques et la versatilité des carbones nanoporeux, combinées au grand nombre de degrés de liberté du procédé de remplissage des pores développé dans ce travail, offrent en outre des perspectives prometteuses dans ce domaine.

Mots clés : carbone nanoporeux, matériau énergétique, charbon actif.

New energetic materials based on nanoporous carbon filled with an oxidizing agent

Summary: This work explores a new family of energetic materials produced by filling the porosity of a nanoporous carbon acting as a reducing agent with a solid oxidizing agent. A new pore filling process by crystallization after solution contraction upon drying is proposed to efficiently fill the porosity of nanoporous carbons with solid oxidizing agents. It is shown that the efficiency of this process is highly dependent on both the nature of the oxidizing salt and the carbon, and that most of the oxidizing agent is selectively crystallized in pores of widths less than 4 nm, thus ensuring a homogeneous mixing of the oxidizing and reducing agent at the nanoscale. The concept is then demonstrated experimentally by proving the ability of nanoporous carbons filled with an oxidizing agent to detonate and by assessing their fundamental properties as energetic materials. In a heavy steel containment, it is demonstrated that a selected material is capable of detonating when initiated by a standard detonator, with measured detonation velocities ranging from 3000 to 4200 m/s for different densities and diameters of 6 to 10 mm. These properties are impressive for a composite energetic material with a very high fraction of solid decomposition products, indicating very fast dynamic decomposition kinetics favored by the nanoscale of the mixture. In conclusion, the concept of a new family of energetic materials based on nanoporous carbons filled with an oxidizing agent has been demonstrated in this work, opening new horizons in the path towards efficient, safe and non-toxic energetic nanomaterials with a wide spectrum of applications. The unique properties and versatility of nanoporous carbons, combined with the large number of degrees of freedom of the pore filling process developed in this work, further offer promising perspectives in this field.

Keywords: nanoporous carbon, energetic material, activated carbon.

CEMHTI - UPR3079 CNRS
Site Haute Température
CS 90055
1D avenue de la Recherche Scientifique
45071 Orléans Cedex 2
France

Département de Chimie
Faculté Polytechnique
École Royale Militaire
30 avenue de la Renaissance
1000 Bruxelles
Belgique